Search for multiple Higgs boson production in hadronic final states at the Large Hadron Collider

Chitroda, Bhakti Kanulal

Doctoral thesis / Doktorski rad

2024

Degree Grantor / Ustanova koja je dodijelila akademski / stručni stupanj: **University of Zagreb, Faculty of Science / Sveučilište u Zagrebu, Prirodoslovno-matematički fakultet**

Permanent link / Trajna poveznica: https://urn.nsk.hr/urn:nbn:hr:217:911256

Rights / Prava: In copyright/Zaštićeno autorskim pravom.

Download date / Datum preuzimanja: **2025-03-17**

University of Zagreb

FACULTY OF SCIENCE

Bhakti Kanulal Chitroda

Search for multiple Higgs boson production in hadronic final states at the Large Hadron Collider

DOCTORAL DISSERTATION

Zagreb, 2024.

University of Zagreb

FACULTY OF SCIENCE

Bhakti Kanulal Chitroda

Search for multiple Higgs boson production in hadronic final states at the Large Hadron Collider

DOCTORAL DISSERTATION

Supervisor:
Dinko Ferenček, Ph.D.

Zagreb, 2024.

Sveučilište u Zagrebu

PRIRODOSLOVNO MATEMATIČKI FAKULTET

Bhakti Kanulal Chitroda

Potraga za višestrukom produkcijom Higgsovih bozona u hadronskim konačnim stanjima na Velikom hadronskom sudarivaču

DOKTORSKI RAD

Mentor:
dr. sc. Dinko Ferenček

Zagreb, 2024.

Dinko Ferenček

Education

2006–2011	**Ph.D.**, **Physics**, University of Maryland, USA
2001–2006	**M.Sc.**, **Physics**, University of Zagreb, Croatia

Work Experience

2021–Present	**Senior Research Associate**, Ruđer Bošković Institute, Zagreb, Croatia
2015–2021	**Research Associate**, Ruđer Bošković Institute, Zagreb, Croatia
2011–2015	**Postdoctoral Research Associate**, Rutgers, The State University of New Jersey, USA
2007–2011	**Research Assistant**, University of Maryland, USA
2006–2007	**Teaching Assistant**, University of Maryland, USA

Selected Publications

1. CMS Collaboration, "Measurement of simplified template cross sections of the Higgs boson produced in association with W or Z bosons in the H $\to$ b$\bar{\text{b}}$ decay channel in proton-proton collisions at $\sqrt{s}$ = 13 TeV", *Phys. Rev. D* **109** (2024) 092011, arXiv:2312.07562

2. CMS Collaboration, "Search for a massive scalar resonance decaying to a light scalar and a Higgs boson in the four b quarks final state with boosted topology", *Phys. Lett. B* **842** (2023) 137392, arXiv:2204.12413

3. Ferenček D., Roguljić M., Starodumov A., "Production, calibration, and performance of the layer 1 replacement modules for the CMS pixel detector", *Proceedings of The 29th International Workshop on Vertex Detectors (VERTEX2020)*, JPS Conf. Proc. **34** (2021) 010023

4. Roguljić M., Starodumov A., Karadzhinova-Ferrer A., Ferenček D., Ahmed A. A., Jara-Casas L. M., "Low dose rate ^{60}Co facility in Zagreb", *Proceedings of The 28th International Workshop on Vertex Detectors (VERTEX2019)*, PoS Vertex2019 (2020) 066

5. Majer M., Roguljić M., Knežević, Ž., Starodumov A., Ferenček D., Brigljević V., Mihaljević B., "Dose mapping of the panoramic ^{60}Co gamma irradiation facility at the Ruđer Bošković Institute – Geant4 simulation and measurements", *Appl. Radiat. Isot.* **154** (2019) 108824

6. CMS Collaboration, "Identification of heavy-flavour jets with the CMS detector in pp collisions at 13 TeV", *JINST* **13** (2018) P05011, arXiv:1712.07158

7. CMS Collaboration, "Search for dijet resonances in proton-proton collisions at $\sqrt{s} =$ 13 TeV and constraints on dark matter and other models", *Phys. Lett. B* **769** (2017) 520, arXiv:1611.03568

8. CMS Collaboration, "Search for narrow resonances in dijet final states at $\sqrt{s} = 8$ TeV with the novel CMS technique of data scouting", *Phys. Rev. Lett.* **117** (2016) 031802, arXiv:1604.08907

9. CMS Collaboration, "Search for heavy resonances decaying to two Higgs bosons in final states containing four b quarks", *Eur. Phys. J. C* **76** (2016) 371, arXiv:1602.08762

10. CMS Collaboration, "Search for narrow resonances decaying to dijets in proton-proton collisions at $\sqrt{s} = 13$ TeV", *Phys. Rev. Lett.* **116** (2016) 071801, arXiv:1512.01224

11. CMS Collaboration, "Search for pair-produced vector-like B quarks in pp collisions at $\sqrt{s} = 8$ TeV", *Phys. Rev. D* **93** (2016) 112009, arXiv:1507.07129

12. CMS Collaboration, "Search for vector-like T quarks decaying to top quarks and Higgs bosons in the all-hadronic channel using jet substructure", *JHEP* **06** (2015) 080, arXiv:1503.01952

13. CMS Collaboration, "Search for resonances and quantum black holes using dijet mass spectra in proton-proton collisions at $\sqrt{s} = 8$ TeV", *Phys. Rev. D* **91** (2015) 052009, arXiv:1501.04198

14. CMS Collaboration, "Search for pair-produced resonances decaying to jet pairs in proton-proton collisions at $\sqrt{s} = 8$ TeV", *Phys. Lett. B* **747** (2015) 98, arXiv:1412.7706

15. CMS Collaboration, "Search for narrow resonances and quantum black holes in inclusive and b-tagged dijet mass spectra from pp collisions at $\sqrt{s} = 7$ TeV", *JHEP* **01** (2013) 013, arXiv:1210.2387

16. CMS Collaboration, "Search for First Generation Scalar Leptoquarks in the $evjj$ Channel in pp Collisions at $\sqrt{s} = 7$ TeV", *Phys. Lett. B* **703** (2011) 246, arXiv:1105.5237

17. CMS Collaboration, "Missing transverse energy performance of the CMS detector", *JINST* **6** (2011) 09001, arXiv:1106.5048

18. CMS Collaboration, "Search for Pair Production of First-Generation Scalar Leptoquarks in pp Collisions at $\sqrt{s} = 7$ TeV", *Phys. Rev. Lett.* **106** (2011) 201802, arXiv:1012.4031

19. V. Brigljević et. al., "Study of di-boson production with the CMS detector at LHC", *J. Phys. G* **34** (2007) N269-N295

Acknowledgements

This thesis work is the result of numerous people's encouragement and advice. I am extremely grateful of each and every one of them.

First and foremost, I would like to sincerely thank my supervisor, Dr. Dinko Ferenček, for his unwavering support and motivation, without which this research project would not have been feasible. Thank you for helping me become a more confident person and for enhancing my communication skills. His thoughtfully organised digital and physical life, coupled with his curiosity to understand the core reason behind any odd outcomes, will always serve as an inspiration to me. You are excellent mentor and I am grateful for the opportunity to learn as much from you. There is much more to say, but to sum up, I would say that because it was such an exciting period overall, five years did not seem like a long journey.

Along with my supervisor, I am grateful to Dr. Vuko Brigljević, Dr. Andrey Starodumov, and Dr. Devdatta Majumdar for their advice and assistance during the early stages of my research. I appreciate their tolerance for my shoddy communication skills. All of them have helped me understand the physics concepts I needed. Thank you for always believing in me and correcting me on my mistakes.

I want to thank my senior PhD fellows, Dr. Matej Roguljić and Dr. Saswat Mishra for their discussions and help. I'll always be envious of Matej's discipline, organized days, and presentation skills. I still have a lot to learn from him. I thank Tanja and Antonija for great coffees with interesting conversations from which I have learnt different things. I will always be grateful for the group at IRB for helping me during my sick days and giving me time to recover. They have been tremendously helpful in making my first time living abroad feel like home.

This research is a result of collaboration with the CMS in association with CERN. I want to thank all of the engineers, scientists, and students for their hard work and pro-activeness in solving any technical difficulties we face during this research. I would also like to express my gratitude to the CMS collaboration for providing opportunities to participate in various physics collaborative research activities to advance my career as an experimental high-energy physicist. And personally, I want to thank Chris, Alessandro,

Abstract

After the discovery of the Higgs boson, one of the main purposes of the physics program at the LHC has been a thorough characterization of its properties. Among important properties of Higgs lies trilinear and quartic Higgs self-coupling, accessible through di-Higgs and triple Higgs production respectively. This thesis primarily reports on two highly significant and intriguing studies that were performed utilizing data from the Run-2(2016–2018) proton–proton collision at a center-of-mass energy of 13 TeV collected by the CMS experiment at the LHC. The first study concerns the search for the non-resonant H pair produced through gluon-gluon fusion (ggF) and Vector Boson Fusion (VBF) modes in two photons and two b-jets final state. The $b\bar{b}\gamma\gamma$ final state is one of the most sensitive channels to the HH signal thanks to a relatively clean signature of two high-energy photons and large branching ratio of two heavy-flavor high-energy jets (b-jets). A 95% confidence level (CL) upper limit on the product of Higgs boson pair production cross section and branching fraction are derived as a function of κ_λ parameter. The constraints on the anomalous coupling of a pair of H with a pair of gauge bosons was determined for the first time by the CMS collaboration.

The second study focuses on the search for triple Higgs boson production in three b-jet pairs final state. Given the extremely low standard model (SM) cross-section for triple-Higgs production, the Two-Real Singlet Model (TRSM) is considered as an extension of SM. TRSM introduces two real scalars X and Y, which decay to three SM Higgs bosons which decays further to three pair of b-quarks through the process $X \rightarrow YH \rightarrow HHH \rightarrow b\bar{b}b\bar{b}b\bar{b}$. The search is performed in mass ranges of X (1–4 TeV) and Y (300–2800 GeV) where the H is highly Lorentz-boosted. In this kinematic regime, decayed b-quark pairs are collimated enough to allow the reconstruction of H using single large-area jets. We have considered two topologies: one topology where all three Higgs bosons are boosted and another where two of the three Higgs bosons are boosted. This analysis is still ongoing. A scan will be performed in a two dimensional plane spanned by the invariant mass of the two large-area jets associated to Y, and the invariant mass of three large-area jets used to reconstruct X.

Keywords: LHC, CMS, standard model, Higgs boson, Higgs self-coupling, TRSM, boosted objects, b-quarks, photons, Higgs-pair, triple Higgs

Prošireni sažetak rada

Uvod

Postoje četiri temeljne sile koje upravljaju svim interakcijama u svemiru, a rezultirale su stvaranjem svijeta u kojem živimo. To su – jaka nuklearna, elektromagnetska, slaba nuklearna, i gravitacijska sila, u padajućem redoslijedu relativnih jakosti. Zajedno, te sile čine manje od 5% ukupnog maseno-energetskog sadržaja svemira, u obliku obične materije i energije. To znači da je više od 95% svemira neistraženo područje koje ljudi vrlo malo ili nimalo ne razumiju.

Standardni model (SM) elementarnih čestica vrhunac je znanstvenih napora da se tri od četiri temeljne sile prirode (sve osim gravitacije) usklade u zajednički teorijski okvir. To je pomoglo u razumijevanju zakona koji upravljaju različitim temeljnim interakcijama i evolucije svemira od vremena Velikog praska do njegovog današnjeg oblika. U SM-u postoje tri generacije fermiona koji sačinjavaju materiju, a svaka se sastoji od nabijenog leptona (elektron, mion i tau), leptonskog neutrina i para kvarkova (u i d; s i c; t i b) . Dakle, postoji šest leptona i šest kvarkova; svaka od ovih dvanaest čestica ima svoju antičesticu. Osim toga, postoji ukupno pet bozona nositelja sile ($W\pm$, Z, γ, g) sa spinom 1, koji odgovaraju trima silama prirode. Naposljetku, skalarni Higgsov bozon stupa u interakciju kroz svoje polje s ostalim elementarnim česticama i dodjeljuje im njihove mase. Međutim, Higgsov bozon ne stupa u interakciju s neutrinima i stoga su neutrini bez mase u SM.

SM je vrlo uspješna prekretnica u našem trenutnom razumijevanju različitih pojava koje se događaju u našem svemiru. Kompletan okvir SM-a, koji danas poznajemo, razvio se tijekom proteklih 50 godina eksperimenata, uspješno prolazeći kroz nebrojena rigorozna testiranja različitih pretpostavki modela. Od uspješnog opisa elektronskog magnetskog dipolnog momenta do preciznosti od 11 signifikantnih znamenki, do predviđanja postojanja novih čestica, SM je nastavio držati svoje mjesto u polju fizike čestica kada je riječ o opisivanju zakona svemira. Međutim, to još uvijek nije potpuna opis prirode.

Dokazi o oscilacijama neutrina iz eksperimenta Super Kamiokande utvrdili su da najmanje dva od tri neutrina moraju imati vrlo malu masu različitu od nule. Mehanizam kojim SM neutrini postižu svoju masu, i koji ju čini iznimno malom, trenutno je misterija. 27%

maseno-energijskog sadržaja svemira je u obliku tamne tvari, za što postoje neizravni kozmološki dokazi iz rotacijskih krivulja galaksija ili gravitacijskih leća, za koju nema izravnog objašnjenja ili čestice kandidata u SM-u. Preostalih 68% svemira zajednički se naziva tamnom energijom, za koju ne postoje ni izravni ni neizravni zaključci o njezinu podrijetlu i mikroskopska svojstvima. To bi mogla biti potpuno nova, peta temeljna sila prirode, s vrlo potisnutom interakcijom s česticama iz SM-a. Zanimljivo je da SM također ne uključuje četvrtu temeljnu interakciju, gravitacijsku silu, u svoj okvir kvantne teorije polja i stoga ne može objasniti zašto je gravitacija $\mathcal{O}(10^{-38})$ puta slabija od jake sile. Osim ovih, postoje i nepotpuna i nezadovoljavajuća objašnjenja koja stoje iza asimetrije materije i antimaterije u svemiru, činjenice da postoje tri generacije fermiona materije i hijerarhija mase među njima i još mnogo toga. Sve to ukazuju na činjenicu da bi SM mogao biti efektivna teorija ili niskoenergetska manifestacija još temeljnije teorije prirode koja djeluje na mnogo višim energetskim skalama.

Gornji nedostaci dokazuju da smo, čak i nakon što smo na pravom putu da razumijemo svemir, još uvijek daleko od temeljne znanosti koja stoji iza svega. Zbog toga fizičari razvijaju nove teorije koje bi mogle reproducirati opažanja SM-a uz pružanje objašnjenja gore navedenih tajanstvenih pojava. One su poznate kao teorije izvan Standardnog modela (BSM). U tu skupinu spadaju supersimetrija (SUSY), iskrivljene ekstra dimenzije (WED) i mnogi drugi modeli. Međutim, postavlja se pitanje gdje tražiti novu fiziku? Jedna od mogućnosti je da koristimo Higgsov bozon kao stepenicu za dolazak do vrata nove fizike.

Nakon otkrića Higgsovog bozona, jedna od glavnih svrha istraživakog programa na LHC-u bila je temeljita karakterizacija njegovih svojstava. Razlika između mjerenja i odgovarajućih očekivanja standardnog modela (SM) bila bi jasan znak nove fizike. Među najosjetljivijim parametrima za novu fiziku, dostupnima na LHC-u, su trilinearno samosprezanje Higgsovog bozona λ_{HHH}, kvartično samosprezanje Higgsovog bozona λ_{HHHH}, vezanje Higgsovog bozona na top kvark y_{t}, i sprezanje između dva vektorska bozona i dva Higgsova bozona $c_{2\mathrm{v}}$. Parametri λ_{HHH} i λ_{HHHH} nastaju u Standardnom modelu iz razvoja potencijala polja Higgsovog bozona oko njegove vakuumske očekivane vrijednosti. Stoga njihovo izravno mjerenje pruža temeljni test predviđanja SM-a za oblik potencijala polja Higgsovog bozona. Najprikladniji procesi za izravno mjerenje λ_{HHH} i λ_{HHHH} su produkcija para i tipleta Higgsovih bozona. Parametar y_t definira najjaču spregu Higgsovog

bozona s fermionima i temeljan je, primjerice, za određivanje (meta)stabilnosti vakuuma SM-a. Dva procesa osjetljiva na y_t su produkcija $t\bar{t}H$ i para Higgsovih bozona. Sprezanje c_{2V} očekuje se u SM-u kao posljedica mehanizma spontanog narušavanja simetrije. Produkcija para Higgsovih bozona putem fuzije vektorskih bozona najosjetljiviji je proces na parametar c_{2V} dostupan na LHC-u.

Višestruke produkcije Higgsovog bozona ključne su za mjerenja važnih parametara. Ovaj rad sastoji se od dva glavna dijela: 1) potrage za nerezonantnom produkcijom para Higgsovih bozona i 2) rezonantne produkcije tripleta Higgsovih bozona. U SM-u moguća je samo nerezonantna produkcija tripleta Higgsovih bozona s vrlo malim udarnim presjekom. Stoga se razmatraju modifikacije SM-a, kao što su EFT vezanja i modifikatori za produkciju para Higgsovih bozona te Two-Real Singlet Model (TRSM) za rezonantnu produkciju tripleta Higgsovih bozona što predstavlja proširenje SM-a s dva dodatna realna skalara. U SM-u na izmjerenoj masi Higgsovog bozona, $H{\rightarrow}b\bar{b}$ kanal raspada ima najveći omjer grananja. Dakle, da bi se poboljšala statistika za produkciju tripleta Higgsovih bozona, razmatra se konačno stanje gdje se sva tri Higgsova bozona raspadaju u par b kvarkova parova ($X{\rightarrow}YH{\rightarrow}HHH{\rightarrow}b\bar{b}b\bar{b}b\bar{b}$). S druge strane, konačno stanje $b\bar{b}\gamma\gamma$ jedan je od najosjetljivijih kanala za HH signal zahvaljujući relativno čistom potpisu dva fotona visoke energije i dva visokoenergetska mlaza teškog okusa (b-mlazovi) ($pp{\rightarrow}HH{\rightarrow}b\bar{b}\gamma\gamma$).

Eksperimentalni postav

LHC je najveći i najsnažniji akcelerator čestica na svijetu te može postići sudare protona s energijom centra mase ($\sqrt{s}$) do 14 TeV i sudare teških iona s energijom centra mase do 2,76 TeV po nukleonu. Među glavnim ciljevima istraživačkog programa LHC-a bila je potraga za Higgsovim bozonom koji je prvi put uočen 2012. godine. LHC je kružni akcelerator s opsegom od oko 27 km. Nalazi se u blizini Ženeve na granici Francuske i Švicarske u tunelu na dubini između 50 i 175 m ispod zemlje.

Jedan od detektora dizajniranih za rekonstrukciju sudara s LHC-a je Compact Muon Solenoid (CMS). CMS detektor nalazi se u jednoj od četiri točke interakcije duž prstena LHC-a. Trenutačni istraživački program CMS-a usmjeren je na karakterizaciju Higgsovog bozona kao i na precizna mjerenja parametara SM-a, posebno elektroslabog sektora. U isto vrijeme, potrage za BSM fenomenima do energetske skale TeV također su ključne u istraživačkom programu CMS-a. CMS detektor ima 13 m dug supravodljivi solenoid s

unutarnjim polumjerom od 5,9 m. Solenoid može osigurati jednolično magnetsko polje od 3,8 T unutar svog cilindra. Ovo snažno magnetsko polje omogućuje visokoprecizna mjerenja količine gibanja nabijenih čestica.

Komponente CMS detektora počevši od točke interakcije su:

- Unutarnji detektor tragova: visoko segmentirani detektor napravljen od silicijskih piksela koristi se za rekonstrukciju primarnih točaka sudara i moguće sekundarnih vrhova nastalih raspadima kratkoživućih čestica. Izvan piksel detektora nalazi se detektor sa silicijskim trakama za praćenje putanja nabijenih čestica unutar magnetskog polja i mjerenje njihove transverzalne količine gibanja.

- Elektromagnetski kalorimetar (ECAL): homogeni kalorimetar napravljen od scintilirajućeg kristala za mjerenje energije elektromagnetskog pljuska potaknutog fotonima i elektronima.

- Hadronski kalorimetar (HCAL): uzorkujući kalorimetar sa slojevima mjedenog radijatora koji se izmjenjuju sa slojevima plastičnog scintilatora. Svrha HCAL-a je mjerenje energije hadrona.

- Mionski sustav: sustav od tri različite detektorske tehnologije za učinkovitu rekonstrukciju miona kao i precizno mjerenje njihove količine gibanja, posebice za mione s visokim p_T. Mionske komore nalazi se izvan solenoida, uglavljene u željezni jaram za povrat magnetskog toka.

Analiza podataka

Ovaj doktorski rad usredotočen je na potrage za produkcijom parova i tripleta Higgsovih bozona. Istraživački rad možemo podijeliti u dva dijela:

1. nerezonantna produkcija para Higgsovih bozona u konačnom stanju $b\bar{b}\gamma\gamma$,

2. rezonantna produkcija tripleta Higgsovih bozona u konačnom stanju $b\bar{b}b\bar{b}b\bar{b}$.

Nerezonantna produkcija para Higgsovih bozona i kasniji raspad na par fotona i b kvarkova

Potraga za nerezonantnom produkcijom parova Higgsovih bozona u konačnom stanju $b\bar{b}\gamma\gamma$ iskorištava podatke koje je prikupio CMS detektor u sudarima protona s energijom u centru mase od 13 TeV, za ukupni integrirani luminozitet od 137 fb^{-1}. Utvrđeno je da je produkcija HH u skladu sa SM-om. Postavljene su granice na anomalne vrijednosti parametara Higgsovih vezanja. Parametri koji se razmatraju su trilinearno samosprezanje Higgsovog bozona λ_{HHH}, konstanta vezanja dva Higgsova bozona s dva vektorska bozona c_{2V} i Yukawino vezanje Higgsovog bozona s top kvarkom y_t.

Postoje dva glavna načina produkcije, fuzija gluona (ggF HH) i fuzija vektorskih bozona (VBF HH) koji se razmatraju s nekim modificiranim EFT parametrima. $HH{\rightarrow}b\bar{b}\gamma\gamma$ konačno stanje sastoji se od dva fotona visoke energije i dva b-mlaza visoke energije. Za VBF HH topologiju, dva dodatna mlaza s velikom razlikom u pseudorapiditetu su producirana u konačnom stanju. Glavni izvori pozadine su procesi $\gamma\gamma$+mlaz proces i γ+mlaz s jednim mlazom pogrešno identificiranim kao foton. Drugi važni izvori pozadine su procesi $t\bar{t}\gamma\gamma$ i $t\bar{t}\gamma$. Događaji pojedinačne produkcije Higgsovog bozona koji se raspada u par fotona predstavljaju dodatni važan izvor pozadine za HH pretragu. Posebno je izražena kontaminacija događaja $t\bar{t}H(\gamma\gamma)$, koji u konačnom stanju imaju dva fotona i dva b-mlaza, u područjima HH signala.

Kandidati su prvenstveno odabrani zahtijevajući dva rekonstruirana fotona visoke energije. Kako bi se povećala osjetljivost na HH signal, događaji su klasificirani u ekskluzivne kategorije od kojih svaka cilja na specifičan mehanizam produkcije para Higgsovih bozona, tj. ggF HH i VBF HH. Osim toga, razvijeni su klasifikatori multivarijatne analize (MVA) za izolaciju svakog signala od njegove pozadine u ciljanoj kategoriji. Radi jasnoće, tijek analize sažet je na Slici 1. Potklasifikacija događaja na temelju rezultata MVA klasifikatora provodi se u svakoj kategoriji. U kategorijama ggF HH i VBF HH, događaji se dalje klasificiraju korištenjem invarijantne mase sustava četiri tijela koji se sastoji od para fotona i para mlazova koji tvore $H{\rightarrow}\gamma\gamma$ i $H{\rightarrow}b\bar{b}$ kandidate za poboljšanje osjetljivosti na nekoliko BSM scenarija.

Signal se identificira kao vrh u distribuciji $m_{\gamma\gamma}$ i vrh u distribuciji m_{jj}, oba na vrijednosti m_H. Za oba procesa, pozadina se modelira iz podataka korištenjem parametarskog modela pozadine. Kako bi se izmjerili parametri od interesa, provodi se istovremena prilagodba raspodjelama $m_{\gamma\gamma}$ i m_{jj}, za koje se pretpostavlja da nisu u korelaciji, u svakoj od kategorija
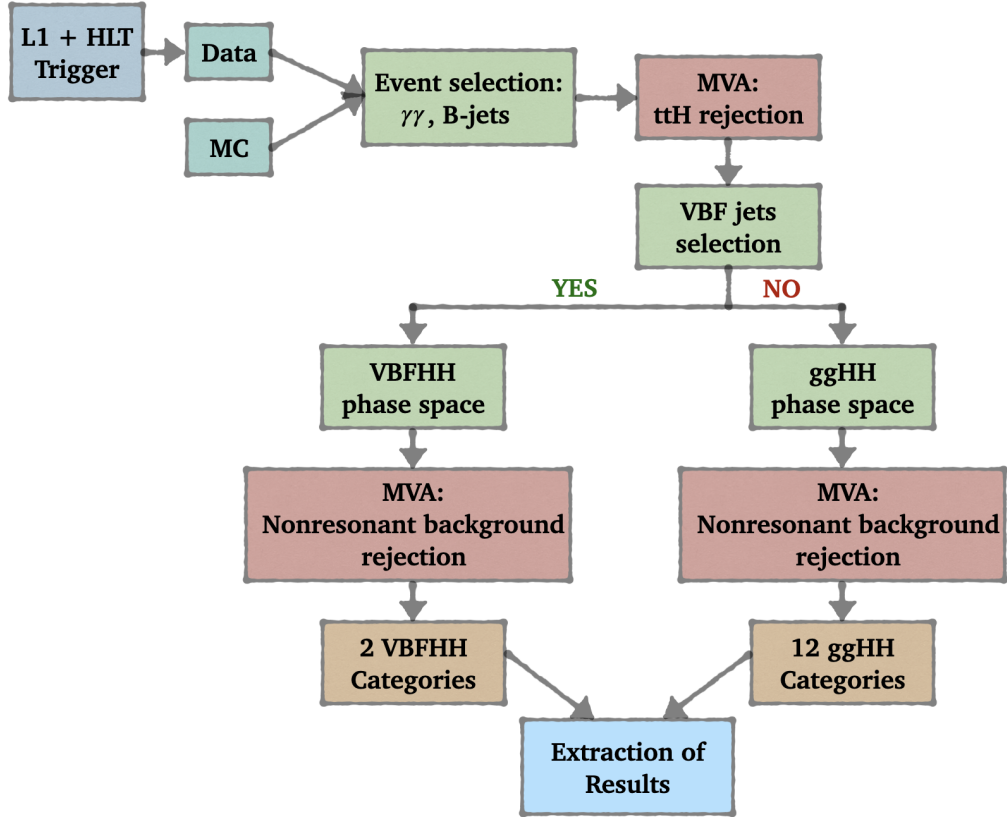
L1 + HLT Trigger

Data

MC

Event selection: $\gamma\gamma$, B-jets

MVA: ttH rejection

VBF jets selection

YES   NO

VBFHH phase space

ggHH phase space

MVA: Nonresonant background rejection

MVA: Nonresonant background rejection

2 VBFHH Categories

12 ggHH Categories

Extraction of Results

Figure 1: Shematski prikat tijeka analize.

obogaćenih HH signalom.

Rezultati

HH kategorije (dvanaest ggF HH i dvije VBF HH kategorije) uključene su u ekstrakciju jakosti HH signala. Očekivane i opažene jakosti signala navedene su u Tab. 1.

Parametar	Očekivano	Opaženo
μ_{HH}	$1.0^{+2.7}_{-1.9}$	$2.7^{+2.6}_{-2.0}$
$\mu_{ggF\ HH}$ fixing $\mu_{VBF\ HH} = 1$	$1.0^{+2.7}_{-1.9}$	$2.8^{+2.7}_{-2.0}$
$\mu_{VBF\ HH}$ fixing $\mu_{ggF\ HH} = 1$	$1.0^{+91.3}_{-65.1}$	$10.2^{+97.21}_{-61.6}$

Table 1: Očekivana i opažena jakost signala za ukupni HH signal (ggF HH + VBF HH), ggF HH i VBF HH.

Budući da nema naznaka HH signala, 95% C.L. gornje granice na $\sigma_{ggF\ HH} \times \mathrm{BR}(HH \to \gamma\gamma b\bar{b})$ izvedene su kao funkcija parametra κ_λ, kao što je prikazano na lijevom panelu Slike 2. Ovisnost gornje granice o κ_λ određena je varijacijom distribucije $\widetilde{M}_x$ signala ggF HH koja modificira populaciju kategorija, a time i osjetljivost na taj signal. Konkretno, kate-

gorije s visokim $\widetilde{M}_x$ pružaju veću osjetljivost od kategorija s niskim $\widetilde{M}_x$ jer imaju manju kontaminaciju pozadinom. Za κ_λ vrijednosti u intervalu [0,6], destruktivna interferencija između dijagrama proizvodnje ggF HH s "kutijastom" petljom top kvarkova i onog s tro-Higgsovim vrhom je maksimalna. To uzrokuje snažnu varijaciju distribucije $\widetilde{M}_x$ koja migrira od najvišeg energetskog spektra na oko $\kappa_\lambda = 2$ do najmekšeg spektra na oko κ_λ = 5. Uspoređujući s teorijskim predviđanjem, rezultirajuće granice na parametar κ_λ su:

$$\text{Opaženo: } -3{,}26 < \kappa_\lambda < 8{,}48 \text{ na 95\% C.L.}$$
$$\text{Očekivano: } -2{,}61 < \kappa_\lambda < 8{,}28 \text{ na 95\% C.L.}$$
$$(1)$$

Isti postupak se provodi za dobivanje granica na parametar c_{2V}, kao što je vidljivo na desnom panelu Slike 2. U ovom slučaju gornja granica je izvedena na $\sigma_{VBF\ HH} \times$ BR($HH \rightarrow \gamma\gamma b\bar{b}$) jer je osjetljivost na c_{2V} u potpunosti ograničena na VBF HH proces. Kao i za parametar κ_λ, varijacija gornje granice kao funkcija vrijednosti c_{2V} određena je odgovarajućom varijacijom distribucije $\widetilde{M}_x$. U ovom slučaju, interferencija između tri dijagrama proizvodnje VBF HH čini da spektar distribucije $\widetilde{M}_x$ migrira na visoke energije čim c_{2V} odstupi od svog SM predviđanja, povećavajući osjetljivost na VBF HH signal. Rezultirajuća granice na parametar c_{2V} su:

$$\text{Opaženo: } -1{,}31 < c_{2V} < 3{,}45 \text{ na 95\% C.L.}$$
$$\text{Očekivano: } -0{,}96 < c_{2V} < 3{,}07 \text{ na 95\% C.L.}$$
$$(2)$$

Ovo je prva granica na parametar c_{2V} postavljena od strane eksperimenta CMS. Kanal $HH \rightarrow \gamma\gamma b\bar{b}$ pruža dobru osjetljivost i na parametar c_V.

Ukratko, utvrđeno je da su svi rezultati kompatibilni s predviđanjima SM-a. HH procesu nije opažen i postavljen je gornja granica za njegov udarni presjek. Dodatni podaci bit će prikupljeni detektorom CMS tijekom Run 3 faze LHC-a, što je ekvivalentno integriranom luminozitetu od oko 300 fb^{-1}. Ovaj skup podataka će poboljšati osjetljivost na HH signal i na parametre vezanja. Preliminarne studije daju projiciranu granicu (očekivani SM) na inkluzivni udarni presjek za ggF HH od oko 3,6×SM za kraj Runa 3. Run 3 neće dati potrebnu količinu podataka za naznaku HH procesa. Naznaka (SM) HH procesa očekuju se tijekom faze visokog luminoziteta LHC-a.
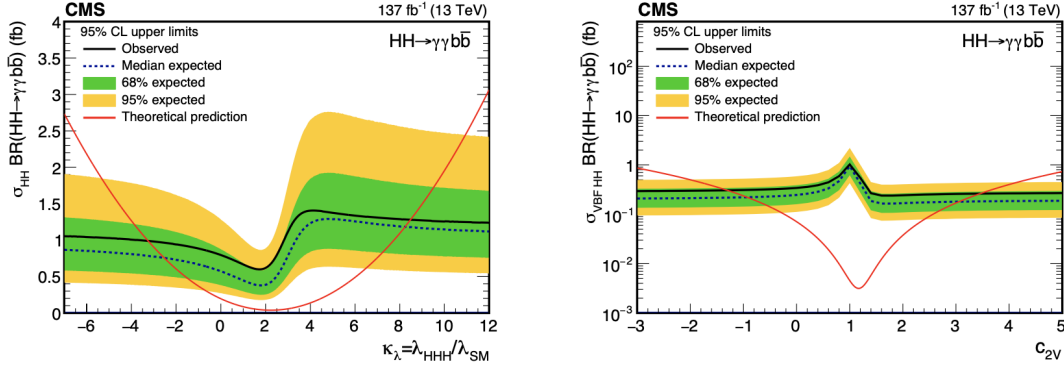
Figure 2: Očekivane i opažene gornje granice na 95% C.L. na udarni presjek za HH produkciju pomnožen s BR($HH{\rightarrow}\gamma\gamma b\bar{b}$) dobivene za različite vrijednosti κ_λ i c_{2V} na lijevoj odnosno desnoj strani. Zelena i žuta vrpca predstavljaju odstupanje očekivane granice za jednu odnosno dvije standardne devijacije. Crvene linije prikazuju teorijska predviđanja.

Rezonantna produkcija tripleta Higgsovih bozona i raspad na šest b kvarkova

Kvartično samosprezanje Higgsovog bozona može se izmjeriti iz produkcije tripleta Higgsovih bozona. Međutim, zbog vrlo malog udarnog presjeka ($\sim$80 ab pri $\sqrt{s} = 13$ TeV), potraga za produkcijom tripleta Higgsovih bozona u kontekstu SM-a izvan je dosega LHC-a.

TRSM ekstenzija SM-a proširuje skalarni sektor SM-a dodatnim skalarnim poljima koja se transformiraju kao singleti u odnosu na baždarne grupe SM-a. U TRSM-u udarni presjek za gluonsku fuziju $pp{\rightarrow}HHH$ pojačan je rezonantnom produkcijom skalara X. Fokusiramo se na scenarij u kojem se stanje H identificira s Higgsovim bozonom iz SM-a, a Y i X su dva nova teža skalara koji zadovoljavaju sljedeću hijerarhiju masa

$$2m_H < m_Y < (m_X - m_H). \tag{3}$$

To rezultira s dva skalarna singleta X i Y koji se raspadaju na Higgsov bozon H iz SM-a. Budući da $H{\rightarrow}b\bar{b}$ ima najveći omjer grananja, da bismo povećali statistiku, razmatramo slučaj kad se sva tri Higgsova bozona raspadaju na parove b kvarkova. Ovo daje $X{\rightarrow}Y(HH)H{\rightarrow}b\bar{b}b\bar{b}b\bar{b}$. Ovi b kvarkovi se eksperimentalno opažaju kao hadronski mlazovi. Ako Higgsov bozon miruje ili ima malu količinu gibanja, dva su b kvarka iz njegova raspada dobro odvojena i bit će detektirana kao dva različita mlaza. Međutim, ako Higgsov bozon ima veliku količinu gibanja, dva mlaza će biti kolimirana u smjeru gibanja

Higgsovog bozona. Ako je količina gibanja Higgsovog bozona dovoljno velika, dva mlaza će se stopiti u jedan veliki mlaz ("debeli" mlaz). Potraga se provodi u rasponima masa X (1-4 TeV) i Y (300-2800 GeV) gdje je H u ultrarelativističkom režimu. U ovom kinematičkom režimu parovi b kvarkova su dovoljno kolimirani da omoguće rekonstrukciju H pomoću jednog "debelog" mlaza. Ovdje će kombinacija tri Higgsova bozona dati različite topologije, od kojih nas zanimaju topologije u kojima su sva tri ili dva od tri Higgsova bozona u ultrarelativističkom režimu.

Glavna pozadina ovog procesa su višestruka produkcija hadronskih mlazova unutar SM-a te produkcija para top kvarkova. Koristili smo *2D-alphabet* metodu za procjenu oblika i normalizacije pozadine u signalnom području. Ova analiza je još u tijeku. Skeniranje će se izvršiti u dvodimenzionalnoj ravnini razapetoj masama skalara X i Y.

Contents

List of Tables

List of Figures

Chapter 1

Introduction

The universe has always been like a mystery box for us. The deeper we dig into it, our curiosity gets increased. Humans have been attempting to unravel this mystery for many ages. The foremost curiosity is the science behind the origin of the universe that could explain all the observed physics phenomena.

After studying the results from many experiments, scientists have constructed a particle theory named the Standard Model (SM) that describes elementary constituents of the universe and their interactions. There is no doubt that SM is the most successful theory so far after the discovery of Higgs particle by the two largest collaborations ATLAS [1] and CMS [2, 3], at CERN. However, SM only explains about 5% of the universe; the remaining 95% indicates that SM might be an effective theory that shows a low energy signature of physics existing at a high energy scale [4]. It does not explain many physics observations, e.g., the gravitational force does not fit within it. However, this is not the only drawback. The SM also does not provide any explanation for dark matter and dark energy [5, 6, 7], hierarchy problem of the electroweak SM [8], neutrino masses [9], amongst others.

The above drawbacks prove that even after being on the right track to unravel the universe, we are still far from the fundamental science behind it. This is why physicists are developing new theories that could reproduce the SM observations with providing an explanation of the above mysterious phenomena. These are known as beyond the Standard Model (BSM) theories. It comprises super-symmetry (SUSY) [10], warped extra dimen-

sion (WED) [11] and many other models. However, the question is where to look for new physics? One possibility is that we use the Higgs boson as a stairway to reach the door of new physics.

After discovering Higgs boson at the Large Hadron Collider (LHC) [12], the SM has become a complete theory. The couplings of Higgs boson with the SM gauge bosons and fermions (known as Yukawa couplings) have also been measured within a certain uncertainty by studying various production and decay modes. Considering these uncertainties, we still have experimentally allowed phase space supporting the existence of the BSM physics as extension of SM. Hence, SM precision measurements are essential in this prospect.

Following direct and indirect search techniques, colliders can play a crucial role in the search for the new physics (might appear at a very high energy scale) and SM precision measurements (any observed deviation from the SM predictions will be an indication for the new physics). Thus, the goals of LHC include new physics searches at high energy scales and SM precision measurements, including studies related to the self-interactions of the Higgs boson as the SM predicts that Higgs boson interacts with itself via trilinear and quartic self-coupling. However, these self couplings are yet to be determined. Experimentally, the trilinear coupling can be directly measured using the Higgs boson pair production mode $pp \rightarrow HH$, also known as **Di-Higgs production** and quartic coupling can be measured using **Triple Higgs production**.

Within SM, non-resonant production is the only process for multiple-Higgs production, while the resonant multiple-Higgs production has its own importance to look for the new BSM particles. Briefly, we can understand the importance of multiple-Higgs production in two ways:

1. Non-resonant multiple-Higgs production: It is a direct probe for the SM Higgs trilinear self-coupling. This approach is also suitable for BSM effective field theory (EFT) searches where resonance might appear at the large TeV scale, but we look for its low energy signatures.

2. Resonant multiple-Higgs production: There are BSM theories that provide the solutions to the SM inconsistencies like hierarchy problems, dark matter, etc. The

2

predicted resonances by these BSM models with an enhanced cross section directly couple to Higgs boson, which might be easier to probe using the direct search methods.

We have explored the non-resonant di-Higgs production mode with the decay channel, one Higgs boson decays into a pair of the bottom quark, and another one decays into a pair of photon resulting in $b\bar{b}\gamma\gamma$ final state. The $H \to b\bar{b}$ has the large branching fraction among all Higgs boson decay modes, but the SM multi-jet backgrounds make it a challenging final state to perform any study. On the other side, despite of low $H \to \gamma\gamma$ branching ratio, it has very low background contamination. Thus, $HH \to b\bar{b}\gamma\gamma$ keeps benefit of high purity and selection efficiency.

And for the resonant triple-Higgs production mode, the cross section is very small that it is better to have large branching ratio and thus, the decay channel, $HHH \to b\bar{b}b\bar{b}b\bar{b}$ is preferred. This search is motivated by the BSM theories such as Two-real-scalar-singlet extension of the SM (TRSM) [13] which provide explanation for some of the shortcomings of the SM and, among others, postulate additional scalar particles.

This thesis work focuses on the searches using both the di-Higgs production and triple-Higgs production. We can divide this research work into two parts,

1. non-resonant di-Higgs study in $b\bar{b}\gamma\gamma$ final state with proton-proton collision data.

2. resonant triple-Higgs study in boosted $b\bar{b}b\bar{b}b\bar{b}$ final state.

Two primary production modes, vector boson fusion (VBF) and gluon-gluon fusion (ggF), are investigated in non-resonant di-Higgs research. SM Higgs couplings such as the coupling between the Higgs boson and the top quark (y_t) and the trilinear Higgs self-coupling λ_{HHH} are accessible through both production modes. Simultaneously, considering production modes modified by BSM allows access to EFT couplings. Study of the production of Higgs boson pairs via BSM ggF gives access to two Higgs bosons and two gluons (c_{2g}), between one Higgs boson and two gluons (c_g), and between two Higgs bosons and two top quarks (c_2). Additionally, via BSM VBF gives access to the coupling of Higgs bosons pair with vector bosons pair, $C_{2V} \sim$HHVV and the coupling of a single H with a pair of vector bosons $C_V \sim$HVV. The couplings are further explained with Feynman diagrams in

section 2.4. When required, $t\bar{t}H$ production results were incorporated with ggF HH and VBF HH data in order to increase the sensitivity of y_t coupling at the end.

The search for di-Higgs production has two major obstacles: a small cross-section and irreducible background. To separate signal events from background events, MVAs were trained and the signal was divided into different categories to increase sensitivity. Despite this, no significant excesses over the background of double Higgs production events were found, thus upper limits on the HH cross sections were extracted. The observed upper limit on the inclusive HH production cross section is 7.7 times SM and corresponds to the most stringent result achieved by the CMS experiment to date [14]. In addition, constraints on Higgs coupling parameters were put with 95% confidence level, which is the most stringent constraint among the published results. Current results show no significant deviation from SM. An evidence of a SM HH process is expected during the high-luminosity phase of the LHC. The non-resonant HH analysis was published in 2021:

- CMS Collaboration, **Search for non-resonant Higgs boson pair production in final states with two bottom quarks and two photons in proton-proton collisions at $\sqrt{s} = 13$ TeV**, JHEP 03 (2021) 257, DOI 10.1007 / JHEP03(2021)257

The triple-Higgs production analysis is still under process. The event selection and boosted categories are defined for the selected channel. The 2D-Alphabet method is used to model background [15, 16]. The next steps are to define systematic uncertainties for theory model and experimental setup and extract the signal or extract upper limit for the cross-section.

This thesis is structured as follows. Chapter 1 aims to introduce the theory of elementary particle physics, focusing on its aspects relevant to the Higgs boson sector as it is directly related to the search for a signature of new physics presented in this thesis. The Higgs boson at LHC and the phenomenology of multiple-Higgs production is described in Chapter 2. Chapter 3 convey the details of the collider and experiment that provide us data used for the research work. Chapter 4 explains how to identify and measure particles present in the event using the signals left in the detector. Chapter 5 contains the first part of research work where non-resonant HH production in $b\bar{b}\gamma\gamma$ final state is described with the results. Chapter 6 details the second part of the research work, the search for

resonant triple-Higgs production in boosted 6*b* final state. In Chapter 7, we conclude with a detailed summary of the main results from both the analyses performed in Chapters 5 and 6. The Appendix A describes additional work I have done apart from multiple-Higgs analysis. It includes my work on Higgs bosons decaying into a $b\bar{b}$ quark pair, produced in association with a vector boson (VHbb analysis) which is not part of the main thesis. This analysis was published in 2024:

- CMS Collaboration, **Measurement of simplified template cross sections of the Higgs boson produced in association with W or Z bosons in the** $H \to b\bar{b}$ **decay channel in proton-proton collisions at** $\sqrt{s} = $ **13 TeV**, Phys. Rev. D 109 (2024) 092011, DOI 10.1103/PhysRevD.109.092011

1.1 The Standard Model of Elementary Particle Physics

The SM of particle physics was developed throughout the second half of the 20th century and provides a description of the elementary particles and their fundamental interactions [17]. Its theoretical framework is built upon the mathematical foundations of quantum field theory (QFT) and gauge symmetries, refined by the constant back and forth between theory and experiment. It is well corroborated by the experimental observations, and its predictive power was further consolidated with the discovery of the Higgs boson by the ATLAS and CMS experiments at the LHC on the 4th July 2012 [1, 2], almost half a century after it was postulated.

The SM is the name given to a theory of fundamental particles back in the 1970s. It incorporated all that was known about subatomic particles at the time and predicted the existence of additional particles as well. Two types of particles are included in the SM: the building blocks of matter, also known as *matter* particles, and the intermediate interaction particles, or *force carriers*. The first group is composed of *fermions*, whereas the second group is composed by *bosons*, which are the particles exchanged by the fermions during interactions.

Every elementary particle in the SM is characterized by a few quantum numbers which are conserved in the fundamental interactions. These are unique invariant masses, an electric charge (in the units of e), and a spin quantum number, which is equal to half integral $(\frac{1}{2}, \frac{3}{2}, \frac{5}{2}, \text{etc.})$ for fermions, whereas a whole integer (0, 1, 2, etc.) for bosons. The modern-day visualization of the SM, where all the fundamental particles are strategically placed, according to their designated roles in the nature, is shown in Fig. 1.1.
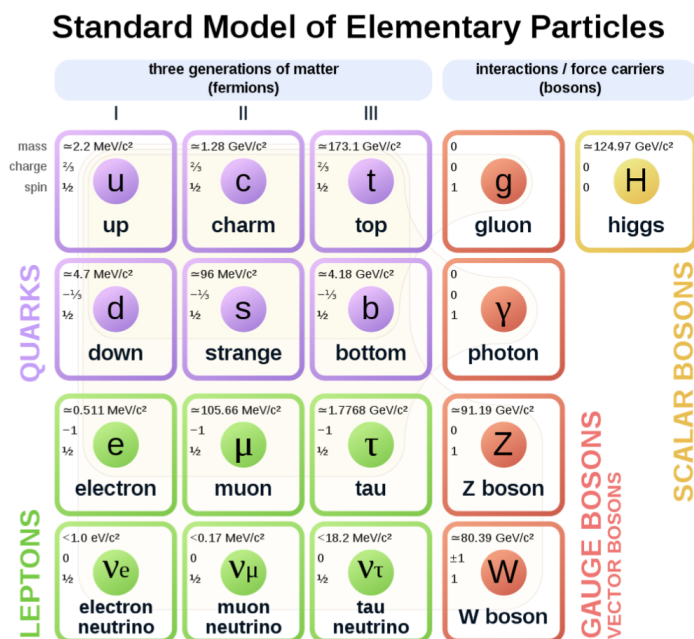
Figure 1.1: Diagram representing the elementary particles of the Standard Model. Matter is constituted by three generations of quarks (in purple) and leptons (in green), while the interactions amongst them are governed by the gauge bosons (in red). The Higgs boson (in yellow) is responsible for the masses of the particles.

Quarks are the only SM particles that are subject to the three forces: the electromagnetic, the weak and the strong. Each quark carries a flavour, which is subject to the electroweak interaction, and a colour, which is subject to the strong interaction. The latter is described by the Quantum Chromodynamics (QCD) theory. A property of this theory is the colour confinement, through which quarks do not exist as free states and can only be experimentally observed as bound states. Hence, they form mesons, which are quark-antiquark states, and baryons, which are composed by three quarks. Both bound states are denoted as hadrons. Although quarks are confined in hadrons, they are asymptotically free particles, meaning the strong coupling becomes weaker when the momentum transfer is large. This property allows the fundamental interactions between them to be studied in proton colliders such as the LHC.

The leptons, as the quarks, are divided in three families, but they are only subject to the electromagnetic and the weak interactions. The charged leptons of the three families are the electron (e), muon (μ) and tau lepton (τ), respectively. The electron is the lightest one and is stable. Each lepton is paired to a neutrino of the same flavour (ν_e, ν_μ, ν_τ), which is electrically neutral and is massless in the classical SM formulation. However, the observation of neutrino flavour oscillations implies that neutrinos have non-zero masses. Being electrically neutral, neutrinos interact with the matter only via the weak force, and consequently they are not directly detectable at collider experiments. Their presence can nonetheless be inferred via the energy imbalance of the event.

There are two types of bosons in the SM: vector bosons ($W\pm$, Z, γ) with spin = 1 and a scalar Higgs boson (H) with spin = 0. The vector bosons are the force-carrier particles of the fundamental interactions, viz. γ for electromagnetic interaction, eight types of gluons (g) for the strong interaction, and $W\pm$ or Z boson for the weak interaction. Last but not the least, the Higgs boson is responsible for generating masses to all the SM particles (including itself). The generation of the mass of the bosons and fermions is explained by the phenomenon of spontaneous symmetry breaking of the electroweak theory, which results from the postulation of the existence of the Higgs boson. The phenomenon of spontaneous symmetry breaking is presented in Section 1.2.

Any system is described by a Lagrangian density, or simply Lagrangian, which encodes the propagation of these fields and the interactions between them, based on a basic underlying symmetry, the gauge invariance. This invariance means the Lagrangian is invariant under local transformations which form certain Lie groups. The Lie groups which give rise to the interactions described by the SM are the SU(2)$\bigotimes$U(1) and SU(3) corresponding to electroweak and strong interactions, respectively. The SM does not include the description of the gravitational interaction, but this force can be neglected at the considered energies: its intensity is 25 orders of magnitude lower than the weak force, the weakest within the SM. The interactions between SM particles are described by a Lagrangian involving the corresponding quantum fields. The SM Lagrangian can be described as a sum of Lagrangian for the three interactions: Electromagnetic, strong and weak interactions. Throughout this thesis, natural units ($\hbar = c = 1$) are used.

1.1.1   Electromagnetic Interactions

The electromagnetic interaction is described by Quantum Electrodynamics (QED). It explains phenomena involving electrically charged particles interacting by means of exchange of a photon. It is an abelian gauge theory with the symmetry group U(1).

The Lagrangian of the QED is given as,

$$\mathcal{L}_{QED} = i\bar{\psi}\gamma^{\mu}\partial_{\mu}\psi - m\bar{\psi}\psi - eQ\bar{\psi}\gamma^{\mu}\psi A_{\mu} - \frac{1}{4}F_{\mu\nu}F^{\mu\nu}, \tag{1.1}$$

where ψ is a fermionic field, involving both quarks and leptons. The first term corresponds to the free Lagrangian of a massive spin - $\frac{1}{2}$ field, whereas the second term is the mass term. The third term arises from the introduction of the U(1) covariant derivative, namely

$$D_{\mu} = \partial_{\mu} + ieQA_{\mu}, \tag{1.2}$$

and corresponds to the interaction between the photon, represented by the gauge potential A_{μ}, and the fermion. The strength of the interaction is proportional to the charge eQ of the fermion, Q being the quantum number associated to this interaction and e the electron charge. The last term in Eq. 1.1 corresponds to the free propagation of the photon, where $F_{\mu\nu}$ is the electromagnetic or Maxwell tensor defined as $F_{\mu\nu} = \partial_{\mu}A_{\nu} - \partial_{\nu}A_{\mu}$. The photon is massless, but it does not interact with itself, since QED is an abelian theory.

1.1.2   Strong Interactions

The strong interaction is governed by QCD, the theory that describes the interactions between quarks and gluons. QCD is a non-abelian gauge theory based on a local gauge symmetry group called SU(3). It describes the Colour charge (C) associated to this group, and it can take three values: red, green and blue. Quarks being spin - $\frac{1}{2}$ fermions, they satisfy the Dirac equation and hence the free-field Lagrangian is given by the Dirac Lagrangian

8

$$\mathcal{L} = \bar{q}(i\gamma^\mu \partial_\mu - m)q, \tag{1.3}$$

where q corresponds to the quark field, m to its mass and γ^μ to the Dirac matrices. The symbol ∂_μ denotes the partial derivative with respect to the spacetime coordinates.

In order for the Lagrangian to be invariant under the transformation, the derivative ∂_μ has to be re-defined to the so-called covariant derivative D_μ as

$$D_\mu = \partial_\mu + ig_s \frac{\lambda_a}{2} G_\mu^a, \tag{1.4}$$

where g_s is a real constant in the parameters of the transformation. The term $\frac{\lambda_a}{2}$ corresponds to 3×3 traceless herminitian matrices, the so-called Gell-Mann matrices, which generate the group, the gauge vector fields G_μ^a correspond to the eight gluons that mediate the strong force. The overall QCD Lagrangian is

$$\mathcal{L}_{\mathrm{QCD}} = i\bar{q}\gamma^\mu \partial_\mu q - m\bar{q}q - g_s\bar{q}\gamma^\mu \frac{\lambda_a}{2} q G_\mu^a - \frac{1}{4} G_a^{\mu\nu} G_{\mu\nu}^a \tag{1.5}$$

with the summation over all quark fields involved. The first two terms in Eq. 1.5 are as described in Eq. 1.1.2. The third term arises from the introduction of the covariant derivative and describes interaction of the gluon with a quark and an antiquark. The strength of the interaction is parametrized by the constant g_s, usually redefined as the strong coupling constant $\alpha_s = g_s^2/4\pi$. This constant has the property of asymptotic freedom: it becomes very small when the energy transfer is large enough, leading to a quasi-free behaviour of the quarks and gluons. Finally, the fourth term represents the propagation of the gluons; upon expansion, it leads to 3-gluons and 4-gluons self-interactions. Gluons must be massless, otherwise adding a mass term $m^2 G_a^\mu G_\mu^a$ would lead to a gauge non-invariant Lagrangian.

1.1.3 Weak Interactions

The weak interaction is described with the non-abelian gauge group SU(2) group. It is a unique theory: unlike other interactions, it has the peculiarity that it violates parity. This is accounted for in the theoretical description by the property of the chirality of a fermion field, which introduces a vector-axial structure in the Lagrangian of the weak force. The chirality is a Lorentz-invariant quantity corresponding to the eigenvalues of the operator $\gamma^5 = i\gamma^0\gamma^1\gamma^2\gamma^3$, which can be -1 or +1 , giving rise to the so-called left (ψ_L) and right (ψ_R) chirality fields, represented as SU(2) doublets and SU(2) singlets, respectively. The left and right components of a fermion field ψ are obtained by applying the P_L and P_R projectors

$$
\begin{aligned}
\psi &= \psi_L + \psi_R \\
\psi_L &= P_L\psi = \frac{1}{2}\left(1 - \gamma^5\right)\psi \\
\psi_R &= P_R\psi = \frac{1}{2}\left(1 + \gamma^5\right)\psi.
\end{aligned}
\tag{1.6}
$$

where $\frac{1}{2}\left(1 - \gamma^5\right)$ and $\frac{1}{2}\left(1 + \gamma^5\right)$ are the left- and right-handed projection operators respectively. Each fermionic field of the SM is represented as one left chirality doublet (Ψ_L) and two right chirality singlets (ψ_R, ψ'_R). For the first family of fermions, the fields of the electron-neutrino pair are expressed as

$$
\Psi_L(x) = \begin{pmatrix} \nu_{eL} \\ e_L \end{pmatrix}; \quad \psi_R(x) = \nu_{eR}, \quad \psi'_R(x) = e_R;
\tag{1.7}
$$

the up-down quark pair is expressed as

$$
\Psi_L(x) = \begin{pmatrix} u_L \\ d_L \end{pmatrix}; \quad \psi_R(x) = u_R, \quad \psi'_R(x) = d_R.
\tag{1.8}
$$

The same holds for the other two families. Under this notation, the weak Lagrangian for a spin - $\frac{1}{2}$ field can be written as

$$
\mathcal{L}_{\text{weak}} = i\bar{\Psi}_L\gamma^\mu D_\mu\Psi_L + i\bar{\psi}_R\gamma^\mu D_\mu\psi_R + i\bar{\psi}'_R\gamma^\mu D_\mu\psi'_R - \frac{1}{4}W^i_{\mu\nu}W^{\mu\nu}_i,
\tag{1.9}
$$

The quantum number associated to the SU(2) group is the weak isospin, which has three components $I_{1,2,3}$. The right chirality fields ψ_R and ψ'_R have a third isospin component of $I_3 = 0$ as they are singlets under SU(2); the left-handed field Ψ_L has $I_3 = +1/2$ and $I_3 = -1/2$ for the upper and lower components, since they form a doublet under SU(2).

1.2 The Brout-Englert-Higgs Mechanism

Higgs field and electroweak symmetry breaking (EWSB) was first proposed in the mid-sixties by three independent groups: Robert Brout and François Englert;[18] by Peter Higgs;[19] and by Gerald Guralnik, C. R. Hagen, and Tom Kibble.[20, 21, 22]. The Brout-Englert-Higgs (BEH) mechanism was introduced as a solution to generate the gauge boson masses and explain the fermion masses, which were not accounted for in the electroweak gauge formalism. It is based on the concept of spontaneous symmetry breaking, a phenomenon that is often observed in nature in which a physical system whose equations of motion are symmetric, ends up in an asymmetric state. In particular, it describes systems where the Lagrangian obeys certain symmetries, but an individual ground state of the system does not exhibit the symmetries of the system itself.

The Lagrangian mass terms for the fermions, for the $W^{\pm}$, and for the Z bosons should be:

$$
\begin{aligned}
\mathcal{L}_{mf} &= m_f \left(\bar{\Psi}_L \Psi_R + \bar{\Psi}_R \Psi_L \right) \text{ for the fermions} \\
\mathcal{L}_{mV} &= m_{\mathrm{W}} W^{\mu+} W^-_\mu + \frac{m_{\mathrm{Z}}}{2} Z^\mu Z_\mu \text{ for the gauge bosons}
\end{aligned}
\tag{1.10}
$$

However, the $\mathcal{L}_{mf}$ term violates the SU(2) gauge symmetry while the $\mathcal{L}_{mV}$ term violates both the SU(2) and the U(1) gauge symmetries that were assumed to build the electroweak model. The Brout-Englert-Higgs mechanism allows to naturally introduce the mass terms in the SM Lagrangian within the initial assumption of the gauge symmetries. In particular, a new SU(2) doublet Φ is defined as:

$$
\Phi = \begin{pmatrix} \Phi^+ \\ \Phi^0 \end{pmatrix}
\tag{1.11}
$$

The Φ^+ and Φ^0 are complex scalar fields. Their superscripts correspond to their electric

11

1104 charge as it will be proven later on. The Φ field is introduced in the Lagrangian through
1105 a kinetic term:

$$\mathcal{L}_{\Phi kin} = D_\mu \Phi D^\mu \Phi \tag{1.12}$$

1106 and a "potential" term:

$$V(\Phi) = -\mu^2 \Phi^\dagger \Phi + \lambda \left(\Phi^\dagger \Phi \right)^2 \text{ with } \mu^2 > 0 \text{ and } \lambda > 0 \tag{1.13}$$

1107 The $V(\Phi)$ potential has a set of degenerate minima defined by the condition:

$$|\Phi|^2 = \frac{\mu^2}{2\lambda} = \frac{v^2}{2} \text{ with } v = \mu/\sqrt{\lambda} \tag{1.14}$$

1108 Therefore, $v/\sqrt{2}$ is the vacuum expectation value of the Φ field. The generic Φ vacuum
1109 state can be written as:

$$\langle \Phi \rangle = \frac{1}{\sqrt{2}} \begin{pmatrix} 0 \\ v + H(x) \end{pmatrix} \tag{1.15}$$

1110 The kinetic term of Eq. 1.12 can be expresses with respect to the Φ vacuum state of Eq.
1111 1.15 obtaining:

$$\mathcal{L}_{\Phi kin} = \frac{1}{2} \partial^\mu H \partial_\mu H + \left(1 + \frac{H}{v}\right)^2 \left[\frac{g^2 v^2}{4} W^{+\mu} W^-_\mu + \frac{1}{2} \frac{(g^2 + g'^2)2v^2}{4} Z^\mu Z^\mu \right] \quad \text{(A.25)} \tag{1.16}$$

1112 This result has two important consequences:

1113   • The non-zero vacuum expectation value of the Φ field introduces in the SM La-
1114   grangian the mass terms for the W$^\pm$ and Z bosons. The W$^\pm$ and Z bosons masses
1115   can be related to the v constant as:

$$m_{\mathrm{W}} = \frac{gv}{2} \quad \text{and} \quad m_{\mathrm{Z}} = \frac{\sqrt{g^2 + g'^2}v}{2} = \frac{m_{\mathrm{W}}}{\cos(\theta_w)} \tag{1.17}$$

In addition, the v value can be related to the Fermi constant G_F, experimentally measured with a very good precision:

$$v = \sqrt{\frac{1}{\sqrt{2}G_F}} = 246 \text{ GeV} \tag{1.18}$$

- In the Lagrangian, new interaction terms between one or two H fields and a vector boson pair arise. The corresponding vertices are proportional to the squared mass of the vector bosons.

In the same way, the potential term of Eq. 1.13 can be expresses with respect to the Φ vacuum state of Eq. 1.15 obtaining:

$$V(\langle\Phi\rangle) = \frac{1}{2}(2\lambda v^2)H^2 + \lambda v H^3 + \frac{\lambda}{4}H^4 - \frac{\lambda}{4}v^4 \tag{1.19}$$

This result has important consequences:

- A mass term for the H field arise in the Lagrangian. Therefore, the H scalar field describes a boson with spin 0, without electric charge, and with a mass $m_{\mathrm{H}} = \sqrt{2\lambda}v$. This particle takes the name of Higgs boson.

- Tri-linear and quadri-linear H self-coupling terms arise in the Lagrangian with a coupling constant proportional to λv and $\lambda/4$, respectively.

It is worth to notice that the functional form for the Higgs boson potential of Eq. 1.13 was chosen arbitrarily as the lowest order polynomial ensuring the SU(2)$\otimes$U(1) gauge symmetries and providing a vacuum expectation value different from zero. The actual functional form can differ. Therefore, in order to test the accuracy of the model predictions, it is fundamental to perform precision measurements of the m_H value and of the trilinear and the quadrilinear Higgs boson self-coupling constants.

1.3   Higgs Self Coupling

The Higgs boson discovery at the LHC in 2012 [1][2] and the subsequent campaign of measurements of its properties [23, 24], have provided a wonderful confirmation of our understanding of elementary particles and their interactions. So far, the predictions of the Standard Model (SM) for the Higgs boson couplings to the vector bosons and to third generation fermions are in spectacular agreement with observations. On the other hand, its interactions with lighter sectors, such as the first and second generation quarks and leptons, are still to be confirmed.

More precisely, the SM Higgs boson couplings to fundamental fermions are linearly proportional to the fermion masses, whereas the couplings to bosons are proportional to the square of the boson masses. The SM Higgs boson couplings to gauge bosons and fermions, as well as the Higgs boson self-coupling, are shown in the Fig.1.2. Because of charge-neutral and color-singlet property, the Higgs boson does not couple at tree level to the mass-less photons and gluons. Its coupling to gluons is induced at leading order by a one-loop process in which it couples to a virtual $t\bar{t}$ pair (with minor contributions from the other lighter quarks). Likewise, the Higgs boson coupling to photons is also generated via loops.

One key sector, which is currently very weakly constrained and could very easily hide or be connected to new physics, is the scalar potential. In the SM, the Higgs scalar potential is fixed by just two low energy parameters, the Higgs mass ($m_H \simeq 125$ GeV) and the Fermi constant G_F (or equivalently the vacuum expectation value $v \simeq 246$ GeV). The scalar potential can be written in terms of the Higgs trilinear (λ_3) and quartic (λ_4) self-couplings :

$$V(H) = \frac{1}{2}m_H^2 H^2 + \lambda_3 v H^3 + \frac{1}{4}\lambda_4 H^4 \qquad (1.20)$$

where in the SM, $\lambda_3 = \lambda_4 = m_H^2/2v^2 \equiv \lambda_{SM}$. In particular, higher-point Higgs boson self interactions are forbidden in SM. The measurement of the parameters that describe the shape of the Higgs potential are therefore a milestone in the quest of understanding the mechanism of the electroweak symmetry breaking and of exploration of new physics.

14

Gauge interaction $\propto (M_V^2/v^2)$

Yukawa interaction $\propto (M_f/v)$

Trilinear self interaction $\propto (M_H^2/v^2)$

Quartic self interaction $\propto (M_H^2/v^2)$
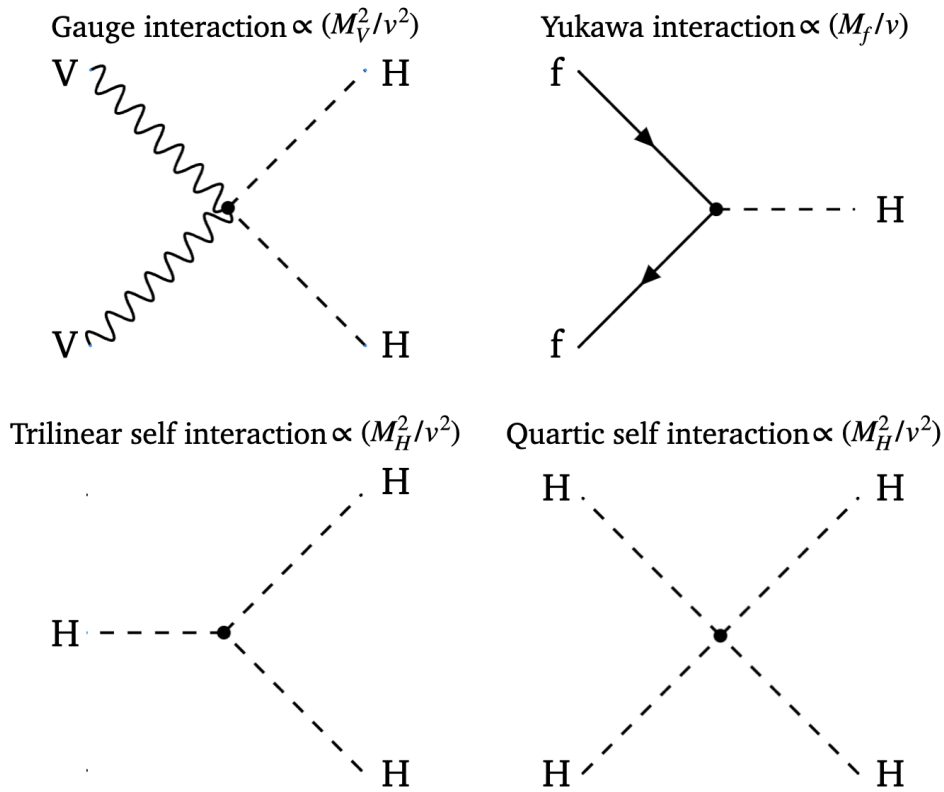
Figure 1.2: Higgs interactions.

The interpretation of possible scenario with new physics is shown in Fig.1.3. As from SM, $\lambda_3 = \lambda_4$ is theoretical prediction and not yet experimentally observed. Thus, there are chances that λ_4 can be different from λ_3 which can create second stable or meta-stable minima for Higgs field and can direct towards new physics, new solution for the mystery of 95% unknown universe.
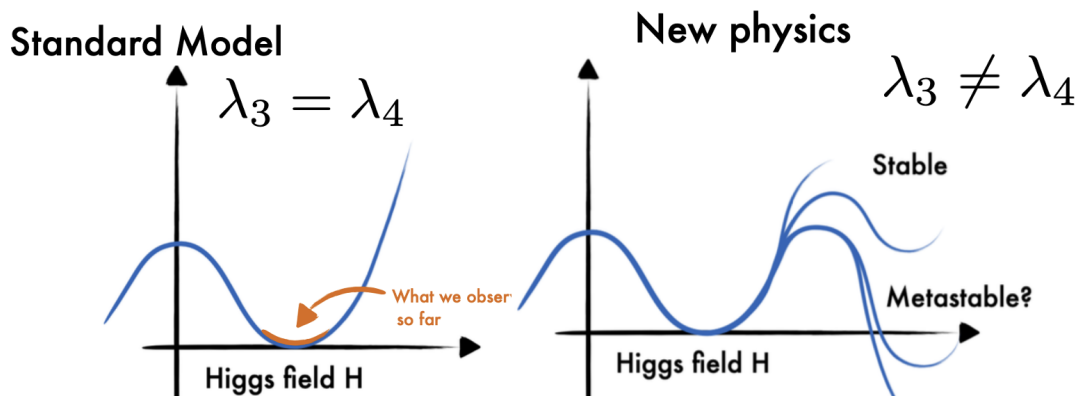
Figure 1.3: Possible interpretation of the Higgs field in SM and BSM.

Chapter 2

The Higgs Boson Phenomenology

2.1 Higgs Boson Searches in the pre-LHC Era

Various experiments in the 1970s and 1980s confirmed the general structure of the Standard Model and, broadly, the predictions concerning the gauge sector. However, the scalar sector, signifying the generation of mass via the Higgs mechanism, remained to be established experimentally. In other words, the existence of a new type of fundamental scalar particle, the Higgs boson remained questionable. This affirmation requiring discovery of the particle continued to be elusive in the next few decades making the SM to be an incomplete description. The mass of the Higgs boson, M_H, is not predicted from the theory, though the nature of the interaction and other relevant aspects are. Various considerations allowed a wide possible range of M_H, up to about 750 GeV. [25]

The Higgs boson was searched for extensively in the experiments at the large-electron-positron (LEP) collider at CERN, near Geneva, Switzerland using different production processes depending on the centre-of-mass energy ($\sqrt{s}$). In the LEP1 (1984-1994) era production of Z boson with subsequent decay through $e^- e^+ \rightarrow Z \rightarrow qq$ channel was the main target. In the LEP2 (1994-2004) era with higher $\sqrt{s}$ the Higgsstrahlung process - $e^- e^+ \rightarrow Z^* \rightarrow ZH$ opened up and the Higgs boson was searched for in the $b\bar{b}$ final state due to the largest decay branching ratio. This was combined with leptonic and hadronic decay modes of Z, providing good event statistics.

16

For the highest value of $\sqrt{s} = 206$ GeV at LEP2, the kinematic considerations allowed a maximum value for M_H to be about 115 GeV. In spite of some experimental hints of possible production of the Higgs boson, the final conclusion from LEP by the turn of the century (2000) was a lower limit on the mass: $M_H > 114.4$ GeV at 95% confidence level (CL). [26]

The Higgs boson search continued extensively at the Tevatron proton-antiproton collider at Fermilab. Despite being a hadron machine, it was more challenging to exploit the related Higgsstrahlung production. The experimentally sensitive mass region was limited essentially between 140 to 180 GeV for production modes initiated via quark-antiquark pair. Just before the physics analysis started at the LHC, the CDF and D0 experiments at the Tevatron excluded the mass range of the Higgs boson 162-166 GeV at the 95% CL. [27] By the time the Higgs boson was discovered at the LHC in 2012, Tevatorn data also hinted at an excess of 3 standard deviations in the mass range of 115-140 GeV.

2.2 Search for Higgs Boson at LHC

By early 1990s search capability for the Higgs boson became a major benchmark for the planned LHC experiments. A search had to be made across the entire allowed range of masses; from around a mass of approximately 50 GeV, the lower limit at the time, up to its largest possible value of approximately 1000 GeV. Since the LHC was capable of producing the Higgs boson of wide range of masses, the mandate was to hunt out the particle and resolve the issue of electroweak symmetry breaking. Accordingly, the search strategy and hence the detector design were focused on specific final states for different mass regions.

2.2.1 Higgs Boson at LHC

At the LHC, the Higgs boson can be produced by several mechanisms over the whole possible mass range, due to the availability of highly energetic partons. The major production modes are briefly discussed below:

1. **Gluon-Gluon Fusion (ggH)** - The Higgs boson production mechanism with the largest cross section is the gluon fusion. It contributes almost 88 (85)% of the total Higgs cross section at the LHC center-of-mass energy of $\sqrt{s}$=7(13) TeV. In the SM, the direct coupling between the Higgs boson and gluons are not allowed, so the production of the Higgs boson proceeds via virtual quark loops. The dominant contribution comes from the exchange of a virtual top quark while contributions from lighter quarks propagating in the loop are suppressed due to their lower masses. This process thus indirectly gives access to the top quark Yukawa coupling (y_t) from the virtual loop. A representative Feynman diagram of ggH process at the leading order (LO) is shown in Fig.2.1 (left).
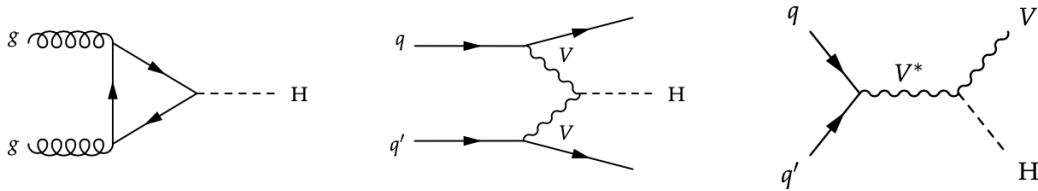
Figure 2.1: Left: Leading order Feynman diagram of ggH process, middle: VBF Higgs production and right: Higgsstrahlung (VH) process of Higgs boson in association with a vector boson.

2. **Vector Boson Fusion (VBF)** - The mechanism with the second-largest cross section is VBF with reduced cross section by about a factor of ten than the ggH production process. The colliding parton pair simultaneously radiates two vector bosons which are fused to produce the the Higgs boson in the central region as shown in Fig.2.1 (middle). The outgoing quarks continue almost along the original direction. The distinctive topology of the event and the kinematics of the final state makes this process very unique and can be exploited to distinguish them from overwhelming backgrounds and used as a clean environment not only for Higgs searches but also for the determination of the Higgs boson couplings. This process gives direct access to the $HVV = c_V$ coupling.

3. **Higgsstrahlung (VH)** - In this case the the Higgs boson is produced in association with a weak interaction gauge boson (V), ie., either W± or Z as shown in Fig.2.1 (right). As in case of VBF, the VH production mode also provides the access to c_V. As neither the Higgs boson nor the vector bosons are stable particles, their decay

18

channels have to be considered. Tagging the leptonic decay of V, the search for the hadronic decay of H, i.e. $H \rightarrow b\bar{b}$ is possible due to reduction of the QCD induced multijet backgrounds.

4. **In association with top pair** $(t\bar{t}H)$ - The Higgs boson production in association with $t\bar{t}$ provides a direct probe of the Higgs-top Yukawa coupling, y_t, in contrast with the y_t measurement from the virtual top quark loop. Since top quark mass is much more than $m_H/2$, kinematically the Higgs boson cannot decay to top quark pair, and hence this coupling cannot be measured from the decay of the Higgs boson to top pair. Representative Feynman diagrams of ttH process are shown in Fig.2.2
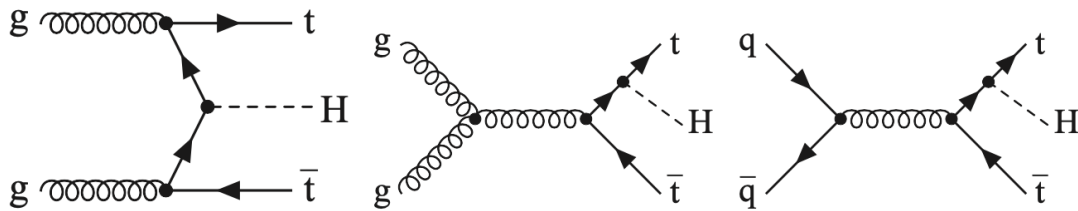
Figure 2.2: Representative tree-level Feynman diagrams of the $t\bar{t}H$ production.

5. **In association with single top (tH)** - Production in association with a single top quark, the Higgs boson can be radiated either from the exchanged W boson or from the top quark in the two dominant leading order processes as shown in Fig. 2.3. The relative sign between the two Higgs boson couplings, y_t and c_V, decides the sign of the interference terms of the two diagrams; thus can bring valuable information, in particular regarding the sign of the top Yukawa coupling. It is to be noted that this process has not yet been observed experimentally at the LHC. The current signal strength of the tH has been observed from the multilepton final state study by the CMS experiment to be 5.7±2.7(stat)±3.0(syst)[28] times the SM predicted value of 0.0724 pb with observed(expected) significance amounts to 1.4(0.3) for tH production.

The cross sections for the production of the Higgs boson with their theoretical uncertainties are shown in Fig.2.4.

After the production of H, it subsequently decays within a short lifetime of $\mathcal{O}(10^{-22})$s[30]. Driven mainly by the value of M_H and the coupling constants of the Higgs boson to vector
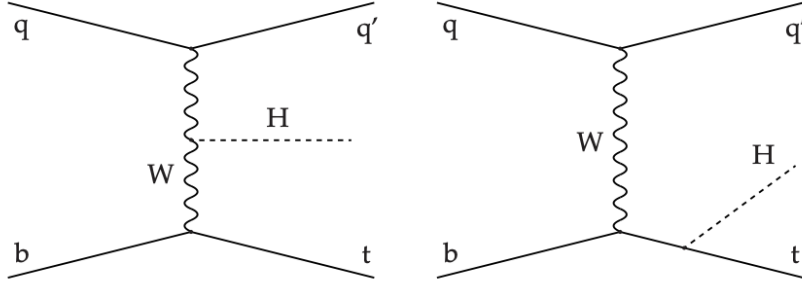
Figure 2.3: Representative tree-level Feynman diagrams of the tH process. Diagram on the left contains c_V and the right one has y_t.
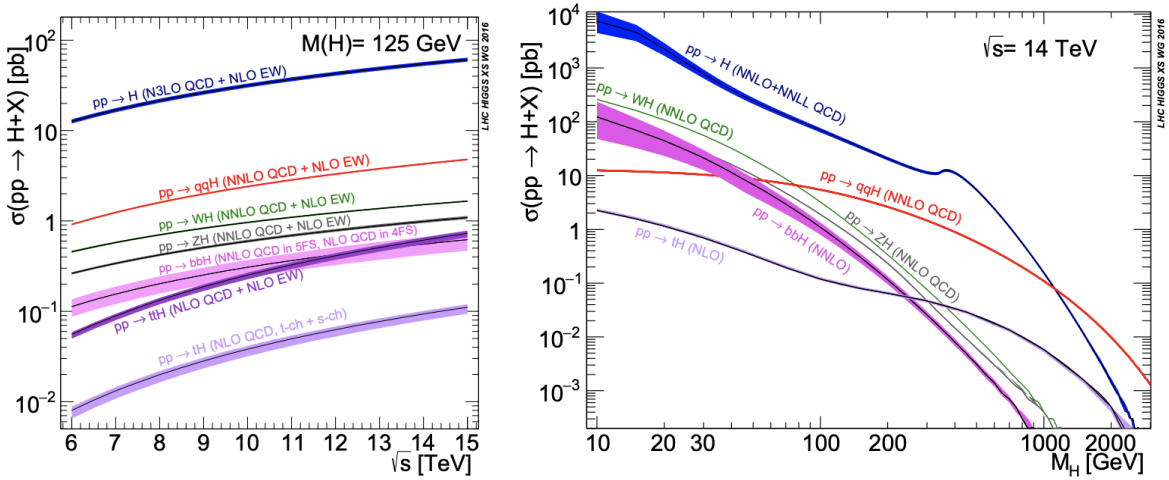
Figure 2.4: Left - Production cross section of a SM Higgs boson of mass $m_H = 125$ GeV as a function of center-of-mass energy $\sqrt{s}$. Right - Production cross section of a SM Higgs boson at $\sqrt{s} = 14$ TeV as a function of Higgs Mass. The lines with different colors correspond to the different production modes with a certain order of accuracy, while the band across each lines give the uncertainty of the calculation. Figure taken from [29].

bosons and fermions, various decay final states are possible. Interestingly, the measured mass of M_H allows, fortunately, a large variety of possible decay channels, most of which can be detected experimentally.

Of course, at a hadron collider like the LHC, the experimental challenges for measurements are greater for the hadronic final states. The general purpose detectors at the LHC are designed to be maximally sensitive to non-hadronic final states involving photons, electrons and muons, such that the discovery milestone could be reached even with limited data.

The branching ratio (Br) to a particular decay final state $(H \rightarrow xx)$ is defined as the ratio of decay width of the Higgs boson to that particular decay mode to the total decay

width.

$$Br(xx) = \frac{\Gamma_{xx}}{\Gamma_{total}} \qquad (2.1)$$

Fig. 2.5 shows the Br of the Higgs boson in different final states for M_H =125 GeV. The dominant decay modes of the Higgs boson with mass of 125 GeV are $H \to b\bar{b}$ and $H \to WW^+$, followed by $H \to gg$, $H \to \tau^+\tau^-$, $H \to cc$ and $H \to ZZ^*$. With much smaller rates follow the Higgs boson decays into $H \to \gamma\gamma$, $H \to \gamma Z$ and $H \to \mu^+\mu^-$. The importance of studying the the Higgs boson in different final states has been described in the later sections of this thesis.
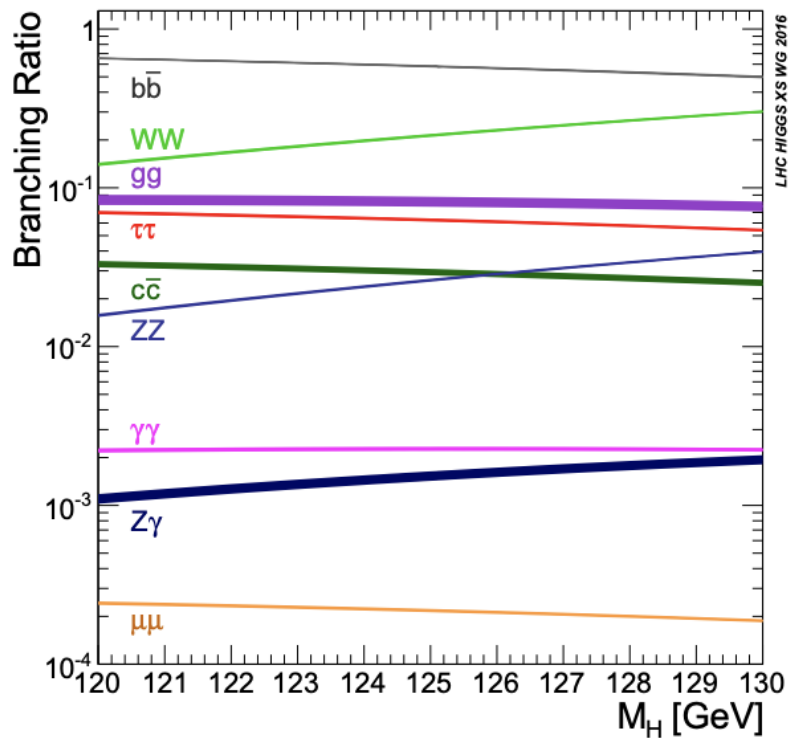
Figure 2.5: Branching ratios of the Higgs boson in the SM as a function of the mass. Figure taken from [29].

2.2.2 Higgs Boson Discovery

The LHC physics journey started in earnest in April 2010, when the first proton–proton collisions at an unprecedented centre-of-mass energy of $\sqrt{s}$=7 TeV, 3.5 times larger than at the previous most powerful hadron collider - the Tevatron. The collision energy was

1282 raised to $\sqrt{s}$=8 TeV in 2012. The first LHC data-taking period ('Run 1') covered about

1283 3 years, from April 2010 to February 2013.

1284 A large amount of data, about 5 billion events, from the examination of some 2000 trillion

1285 proton–proton interactions, was recorded in Run 1 by each of the two experiments, ATLAS

1286 and CMS. Owing to the excellent performance, ATLAS and CMS were able to 'reproduce'

1287 50 years of particle physics in less than 1 year of operation.

1288 Undoubtedly, the most striking result to emerge from the ATLAS[1] and CMS[2] experi-

1289 ments is the discovery of a new heavy boson with a mass of approximately 125 GeV. The

1290 Higgs boson discovery was announced on July 4, 2012. Humongous efforts from a large

1291 community consisting of accelerator engineers, theoretical and experimental physicists

1292 matched by computing experts made it possible; this discovery has been truly termed

1293 as *a big leap for human kind*. This hallmark result established the last part of the SM

1294 particle spectrum which was missing for several decades and resolved the mystery about

1295 the mass generation of the weak gauge bosons and the fermions.

1296 The ATLAS Collaboration reported the existence of a neutral scalar boson with a mass

1297 measured at $126.0 \pm 0.4(\text{stat}) \pm 0.4(\text{syst})$ GeV with a signal significance of 5.9 standard

1298 deviations corresponding to a background fluctuation probability of 1.7×10^{-9} [1]. The

1299 analysis was based on the accumulated data of 4.8 fb^{-1} collected at $\sqrt{s} = 7$ TeV in 2011

1300 and 5.8 fb^{-1} at $\sqrt{s} = 8$ TeV in 2012. In parallel, the CMS Collaboration also established

1301 an excess of events corresponding to a neutral resonance production at the mass of 125.3

1302 $\pm 0.4(\text{stat}) \pm 0.5(\text{syts})$ GeV with a signal significance of 5.9 standard deviations based on

1303 analysis of 5.1 fb^{-1} and 5.7 fb^{-1} of data collected at $\sqrt{s} = 7$ and 8 TeV, respectively [2].

1304 For both the experiments the analysis sensitivities were mostly driven by the di-photon

1305 $(H \rightarrow \gamma\gamma)$ and four-leptons $(H \rightarrow ZZ^* \rightarrow 4l)$ final states with excellent, high resolution

1306 $(\Delta m/m \sim 1 - 2\%)$ measurements. The discovery plots from CMS Collaboration are

1307 presented in Fig. 2.6. As the newly discovered particle decays to a pair of photons, it

1308 ensures that its intrinsic spin cannot be one unit and it belongs to the bosonic family.

1309 As mentioned already, the intrinsic mass of the Higgs boson is a free parameter and for

1310 the measured value of the m_H, SM can predict almost all the important properties of

1311 H. At the same time, for scenarios beyond the SM, the Higgs field structure is extended

1312 and thereby existence of multiple physical Higgs bosons are predicted. In some models,

22
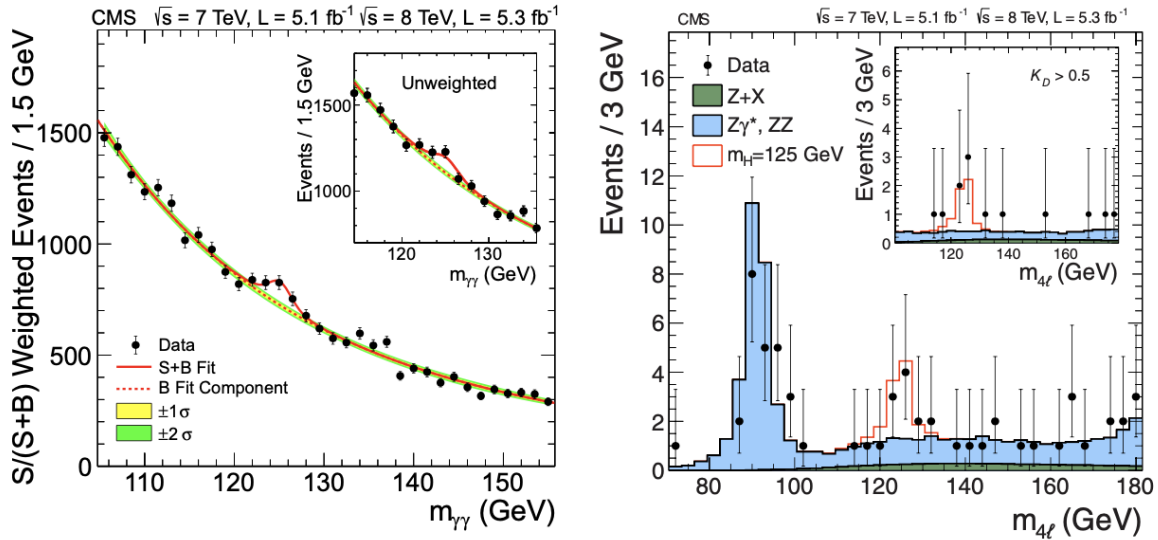
Figure 2.6: Left: The diphoton invariant mass distribution weighted by the $S/(S + B)$ value of its category, the peak around 125 GeV from the SM the Higgs boson contribution on top of the continuum diphoton background is shown with red solid line. Right: Distribution of the four-lepton invariant mass for the $ZZ \to 4l$ analysis, the Higgs boson with a mass of m_H 125 GeV has been shown in red solid line sitting on the background. The figure is taken from [2].

eg. minimal supersymmetric extension of SM (MSSM), the lightest member of the Higgs boson family resemble the SM particle, although with slight differences in some of the properties, like couplings to various particles. Hence, even after observing the existence of the Higgs boson at $m_H \sim 125$ GeV, the dilemma was whether the discovered resonance belongs to the SM or not. To resolve this, all the properties of the Higgs boson must be measured thoroughly and compared with the attributes in the SM. Both the ATLAS and the CMS experiments have been studying painstakingly various properties of the Higgs boson utilizing both the Run 1 and Run 2 data.

The wisdom gained during last one decade is extremely rich and unexpected to a good extent. The exemplary works of the collider physics community has made many interesting measurements possible. All the measurements are compatible with the predictions of SM so far. However the current level of uncertainties still allows the particle to belong to certain physics scenarios beyond SM, although the specific nature of them cannot be judged.

2.3 Interpretation of LHC Data

Before further moving on, it is important to know some basic notations or framework for interpretation of LHC data. It will help understand next chapters.

2.3.1 Signal Strength μ

This is the first and the most simplified theoretical framework developed to interpret the LHC data. To understand it with example, for a particular mass hypothesis of H, the expected number of signal events $(s(M_H))$ in a particular decay mode can be written as:

$$s(M_H) = \sigma_{SM}(M_H) \cdot Br \cdot L \cdot \epsilon \cdot A \qquad (2.2)$$

Here $\sigma_{SM}(M_H)$ is the production cross section, Br is the branching ratio of the particular the Higgs boson decay mode, L is the integrated luminosity of the data being used and ϵ and A are the efficiency and the geometrical acceptance of the experiment. In a total of n number of observed events with b number of background events predicted from SM, $\sigma_{SM}(M_H)$ can be fitted like:

$$n = \mu \cdot s(M_H) + b \qquad (2.3)$$

where μ is called signal strength which is defined as the ratio of the observed value of $\sigma \cdot Br$ to its expectation predicted from the SM.

$$\mu = \frac{(\sigma \cdot Br)_{obs}}{(\sigma \cdot Br)_{SM}} \qquad (2.4)$$

Normally, a measured value of $\mu = 1$ corresponds to the SM prediction, while a deviation indicates the effects of the beyond the SM physics (BSM). Nevertheless, there are uncertainties in the measurements which have both the statistical and the systematic components. A lot of effort goes into improving the precision.

24

2.3.2   kappa-Framework (κ)

In simple words, κ is the ratio of quantity to its SM prediction and mainly used to check agreement with SM ($\kappa = 1$); if not, there is scope for new physics.

The κ-framework introduced in Ref. [31] can be considered as a special case of the SMEFT [29] to consistently parametrize the Higgs boson production cross section and decay width in presence of anomalous Higgs coupling values. In the κ-framework, only the EFT operators whose effect is the modification of the SM couplings are considered, while the other EFT operators are assumed to be negligible. In addition, the new operators are assumed to impact only on the coupling strength, and not on the tensor structure of the coupling.

The couplings of the Higgs boson to the massive SM particles (neutrinos are ignored) are taken into account both at the production as well as at the decay vertices. The production cross section, the total width and the decay branching ratio to a particular mode are scaled separately by the relevant scale factors called κ. Considering a process $ii \to H \to ff$, where the Higgs boson is produced with a cross section of σ_{ii} followed by decay $H \to ff$ with total decay width of Γ_H and partial width of Γ_{ff}, under narrow-width approximation one can write :

$$
\begin{aligned}
(\sigma \cdot BR)(ii \to H \to ff) &= \sigma(ii \to H) \cdot BR(H \to ff) \\
&= \sigma(ii \to H) \cdot \frac{\Gamma_{ff}}{\Gamma_H} \\
&= \sigma^{SM}(ii \to H) \cdot \frac{\Gamma_{ff}^{SM}}{\Gamma_H^{SM}} \cdot \frac{\kappa_i^2 \cdot \kappa_f^2}{\kappa_H^2}
\end{aligned}
\tag{2.5}
$$

κ_i appears due to the couplings at the production side, while κ_f is the coupling modifier for the coupling between the the Higgs boson and its decay products and, finally, κ_H is the coupling modifier for the total decay width, since some of the couplings are yet to be established.

It is to be noted that experimentally we are only estimating the deviations of the couplings wrt SM via κ measurements; we are not directly measuring the individual couplings. In various measurements there is also an implicit assumptions that the couplings do not

"run" or vary across different datasets collected at different energies.

Under zero-width assumption, κ parameters are defined to parametrize the modification of the Higgs couplings strengths in such a way that $\kappa_i^2 = \sigma_i/\sigma_i^{SM}$, or $\kappa_i^2 = \Gamma_i/\Gamma_i^{SM}$. The κ_b, κ_t, κ_τ, κ_μ, κ_W and κ_Z define the coupling modifiers of the Higgs boson to the bottom quark, top quark, τ lepton, μ lepton, W boson, and Z boson, respectively. In addition the $H \rightarrow \gamma\gamma$ and the ggH vertices can be considered as effective vertices with coupling modifiers κ_γ and κ_g, respectively, or they can be expressed in term of the particles contributing inside the loops. Such loops are dominated by the top quark contribution, and for the $H \rightarrow \gamma\gamma$ also by the W boson contribution. The κ_γ and κ_g parameters are typically used to probe whether BSM particles contribute to the effective $H \rightarrow \gamma\gamma$ and ggH vertices.

2.4 HH Production

As mentioned above, experimentally, the trilinear coupling can be directly measured using the Higgs boson pair production mode $pp \rightarrow HH$, also known as di-Higgs production. Within the SM, non-resonant production is the only process for di-Higgs production, while the resonant di-Higgs production has its own importance to look for the new BSM particles.

At the LHC, the main production mode of the di-Higgs process is through gluon gluon fusion which produces almost 95% of the HH events. Similar to the single-H production, there are other subdominant modes of HH production which can also be probed at the LHC by utilizing special properties of the concerned processes.

- **Gluon Gluon Fusion (ggF HH)** - The dominant production mode of the HH is via gluon pair fusion with a cross section of about 31.05 fb at N2LO accuracy in QCD [32, 33] at a centre-of-mass energy of 13 TeV; it is about 1000 times smaller than the single-H production. Fig. 2.7 shows the leading order diagrams of the ggF HH process, where Higgs bosons are produced via a heavy quark loop and contain the t-quark Yukawa coupling (y_t). The first diagram called triangle diagram contains λ_{HHH} and y_t, while the second box diagram only contains y_t.
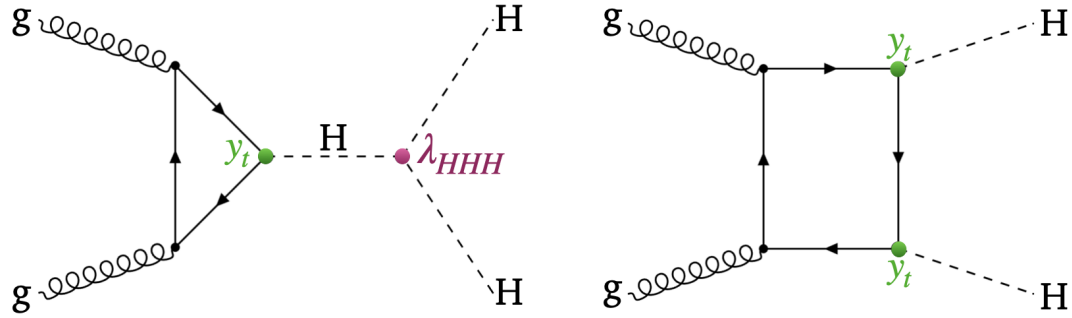
Figure 2.7: Feynman diagrams for the SM gluon-gluon fusion di-Higgs production (left) triangle diagram (right) box diagram.

The cross section and kinematics of the ggF HH process depends on the λ_{HHH} and y_t. The reason behind a smaller cross section value is not only the small λ_{HHH}^{SM} value (=0.13), but also box and triangle diagrams have opposite signs leading to destructive interference. The contribution of the individual diagrams and the interference term is shown in Fig. 2.8 as a function of HH invariant mass.
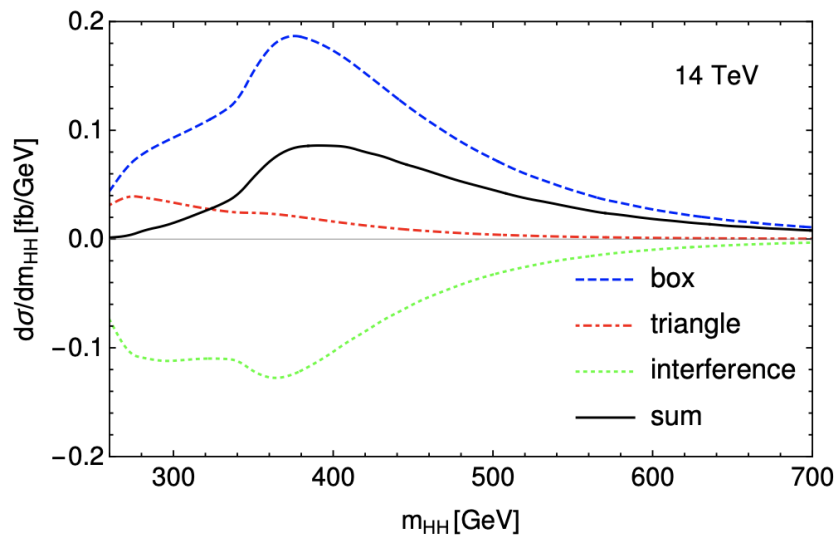
Figure 2.8: Higgs pair invariant mass distribution at LO for the different contributions (box and triangle) to the ggF HH production mechanism and their interference. Figure taken from [34]

Contributions from physics beyond the SM (BSM) can significantly enhance the HH production cross section, as well as change the kinematical properties of the produced Higgs boson pair, and consequently those of the decay products. The modification of the properties of non-resonant HH production via ggF from BSM effects can be parameterized through an effective Lagrangian that extends the SM

one with dimension-6 operators[29, 35]. This parameterization results in five cou-
plings: λ_{HHH}, the coupling between the Higgs boson and the top quark (y_t), and
three additional couplings not present in the SM. Those three couplings represent
contact interactions between two Higgs bosons and two gluons (c_{2g}), between one
Higgs boson and two gluons (c_g), and between two Higgs bosons and two top quarks
(c_2). The Feynman diagrams contributing to BSM ggF HH production at leading
order (LO) are shown in Fig. 2.9.
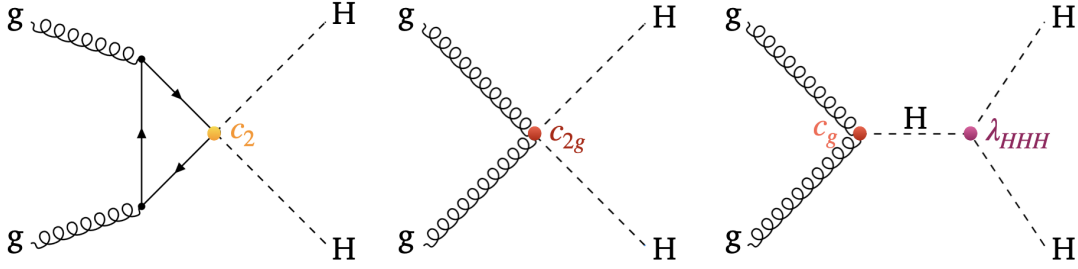
Figure 2.9: Feynman diagrams of the processes contributing to the production of Higgs
boson pairs via BSM ggF at LO. The diagram on the left involves the contact interaction
of two Higgs bosons with two top quarks (c_2), the middle diagram shows the contact
interaction between the Higgs bosons and two gluons (c_{2g}), and the diagram on the right
describes the contact interactions between the Higgs boson and gluons (c_g).

As mentioned before, λ_{HHH}^{SM} has small value but BSM model allows larger values of
λ_{HHH}. We can define $\kappa_\lambda = \lambda_{HHH}/\lambda_{HHH}^{SM}$ and for SM production modes, $\kappa_\lambda = 1$.

- **Vector Boson Fusion (VBF HH)** - HH production via VBF process is the sub-
  leading mode, where a soft emission of two massive vector bosons (V = W,Z) from
  the colliding partons (quarks) is followed by their fusion leading to the hard scat-
  tering $VV \to HH$. At $\sqrt{s} = 13$ TeV, the cross section of VBF HH process is 1.73
  fb at N3LO QCD accuracy [36, 37]. The representative Feynman diagrams for the
  VBF HH process at LO are shown in Fig. 2.10.

  The most interesting fact about VBF HH process is the unique and direct access to
  the coupling of Higgs bosons pair with vector bosons pair, c_{2V}, whereas the other
  two diagrams contains the self-coupling λ_{HHH} which is mainly constrained from
  measurements of HH production via ggF and the coupling of a single Higgs boson
  with a pair of vector bosons c_V is constrained by measurements of vector boson
  associated production of a single Higgs boson and the decay of the Higgs boson to
  a pair of bosons. Despite having a very small cross section, a very small change
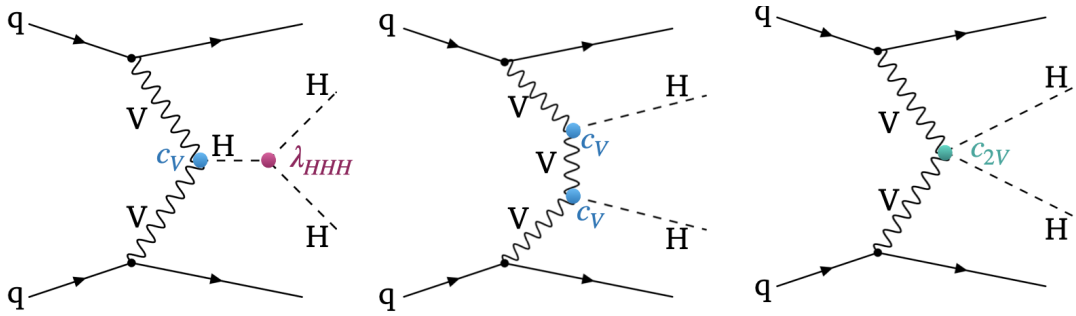
Figure 2.10: Feynman diagrams that contribute to the production of Higgs boson pairs via VBF at LO. On the left the diagram involving the HHH vertex (λ_{HHH}), in the middle the diagram with two HVV vertices (c_V), and on the right the diagram with the HHVV vertex (c_{2V}).

in the couplings can induce a striking increase of the cross section; this enhanced sensitivity potentially adds extra impact on the measurement and the constraints on λ_{HHH} and c_{2V}. Anomalous values of c_{2V} can be investigated to establish the presence of the HHVV-mediated process as a probe of BSM physics.

There are other possible production modes like VHH and $t\bar{t}HH$ that have very small cross-section at the LHC $\sqrt{s} = 13$ TeV. They can be included in future projects with higher centre-of-mass energy and luminosity.

In the search for di-Higgs boson production, the crucial step is to choose a decay channel. This choice depends on the purity, selection efficiency and branching ratio of the channel. Fig. 2.11 shows the possible decay channels, which are explored and analyzed by various experiments to understand di-Higgs physics.

In this thesis, we will focus on the decay channel $HH \to bb\gamma\gamma$ as $H \to bb$ has the largest branching ratio but high background rates and $H \to \gamma\gamma$ has excellent mass resolution with lower background but low branching ratio. In a way, these two channels complement each other and we are trying to get the best out of each.

Br(HH→XXYY)

$Br(H\to YY)$	$b\bar{b}$	WW	gg	$\tau\tau$	$c\bar{c}$	ZZ	$\gamma\gamma$	$Z\gamma$	$s\bar{s}$	$\mu\mu$
$\mu\mu$	2.53e-04	9.42e-05	3.75e-05	2.77e-05	1.27e-05	1.16e-05	9.99e-07	6.75e-07	1.08e-07	4.80e-08
$s\bar{s}$	2.84e-04	1.06e-04	4.22e-05	3.11e-05	1.43e-05	1.30e-05	1.12e-06	7.58e-07	6.05e-08	
$Z\gamma$	1.78e-03	6.62e-04	2.64e-04	1.95e-04	8.96e-05	8.13e-05	7.02e-06	2.37e-06		
$\gamma\gamma$	2.63e-03	9.80e-04	3.91e-04	2.88e-04	1.33e-04	1.20e-04	5.20e-06			
ZZ	3.05e-02	1.14e-02	4.52e-03	3.34e-03	1.54e-03	6.97e-04				
$c\bar{c}$	3.36e-02	1.25e-02	4.99e-03	3.68e-03	8.47e-04					
$\tau\tau$	7.29e-02	2.72e-02	1.08e-02	3.99e-03						
gg	9.89e-02	3.69e-02	7.34e-03							
WW	2.48e-01	4.62e-02								
$b\bar{b}$	3.33e-01									

Good mass resolution

High branching ratio

Rarer ⟶

Rarer ⟶ $Br(H\to XX)$

Figure 2.11: SM di-Higgs decay branching ratio (BR) for $m_H =$ 125 GeV

2.5 Higgs Boson Couplings

2.5.1 Higgs Boson Trilinear Self-Coupling

The parameter λ_{HHH} is the Higgs boson trilinear self-coupling. It arises in the SM from the expansion of the Higgs field potential around its vacuum expectation value $v/\sqrt{2}$. In the SM theory, the predicted λ_{HHH} value at the leading order is

$$\lambda_{HHH}^{SM} = \frac{m_H^2}{2v^2} = (1.291 \pm 0.003) \cdot 10^{-1} \tag{2.6}$$

where m_H is the Higgs boson mass with a measured value $m_H = 125.10 \pm 0.14$ GeV [38]. The value of v predicted by the SM is 246.22 GeV derived with an extremely good precision from the Fermi coupling constant. The direct measurement of the λ_{HHH} value provides a consistency test of the spontaneous symmetry breaking mechanism. On the other hand, several BSM theories predicts anomalous values of the λ_{HHH} value, such as the composite Higgs models [29, 39] and in general the Higgs-portal models [40]. It is practical to define κ_λ as the ratio of a BSM and the SM value.

As discussed before, SM cross section of HH production is very small. However, anomalous λ_{HHH} values could significantly increase the cross section, as visible in Fig. 2.12, and make the ggF HH process observable. As visible in the same figure, the cross sections of other HH production modes, i.e. the HH associated production with a $t\bar{t}$ quark pair $t\bar{t}HH$, and the HH associated production with a vector boson VHH, are also sensitive to the λ_{HHH} parameter. However, the cross section of these processes is much smaller than σ_{ggHH}, hence also the corresponding sensitivity to λ_{HHH} is reduced. In this work, only the qqHH (VBF HH) mechanism is considered along with the ggF HH mechanism, while the other HH production modes are neglected. In case of anomalous λ_{HHH} values, the HH invariant mass (m_{HH}) distribution could also be strongly modified, as shown in Fig. 2.12. This feature is properly exploited in the analysis to increase the sensitivity to the λ_{HHH} parameter.
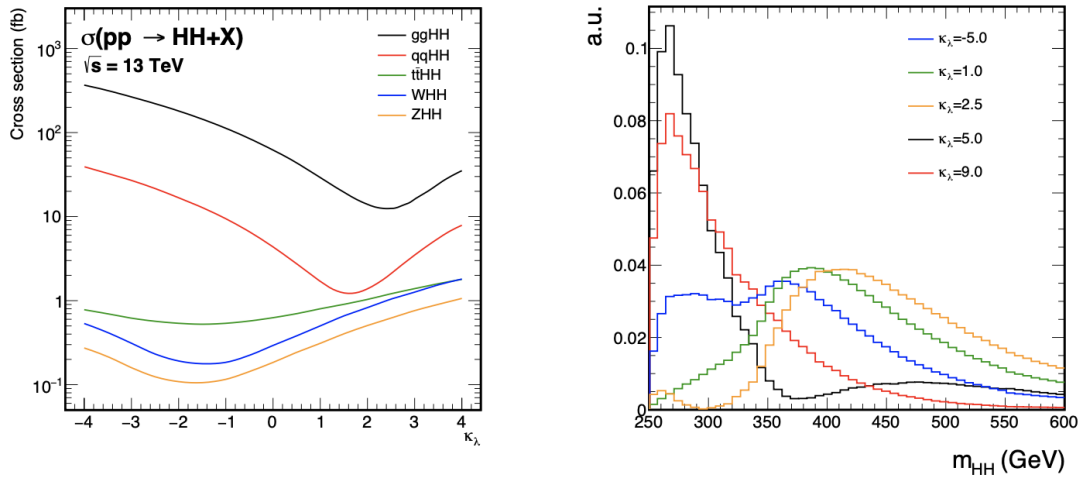
Figure 2.12: *Left*: cross sections of the main HH production modes as a function of κ_λ. *Right*: mHH distributions for the ggF HH process for different κ_λ hypotheses. The distributions are all normalized to unity.

2.5.2 Yukawa Coupling of the Higgs Boson to the top Quark

The Yukawa coupling of the Higgs boson to the top quark is predicted by the Standard Model with a strength:

$$y_t^{SM} = \frac{\sqrt{2}m_t}{v} = 0.992 \pm 0.002 \tag{2.7}$$

where m_t is the top quark mass with a value $m_t = 172.76 \pm 0.30$ [38]. As the Yukawa coupling of the Higgs boson with a fermion is proportional to the fermions mass, y_t is

the strongest coupling of the Higgs boson with a fermion. The fact that its predicted value is close to the unity suggests that the interaction of the Higgs boson with the top quark might have some special role not disclosed in the SM. The Higgs boson - top quark interaction induces also very large corrections to the SM Higgs boson potential which could produce additional minima in the Higgs field potential. The minima values are y_t-dependent and determine the SM vacuum (meta)stability [41]. On the other hand, some BSM theories predict deviations of y_t from the SM prediction up to 20 - 30% [42]. The measurement of the ggF HH and of the $H \rightarrow \gamma\gamma$ decay width provide access to the y_t parameter through loop-induced processes. In such processes other BSM phenomena, e.g. new particles in the loop, could modify the final observable, enhancing or compensating the effect of an anomalous y_t value. The variation of the HH cross sections for anomalous values of y_t is shown in Fig. 2.13, where for simplicity the κ_t parameter is defined as $\kappa_t \equiv y_t / y_t^{SM}$.

The ggF HH cross section σ_{ggHH} is very sensitive to $|\kappa_t| \gg 1$, because in that case the Feynman diagram with a box loop of top quarks is the dominating matrix element, thus σ_{ggHH} scales as κ_t^4 .
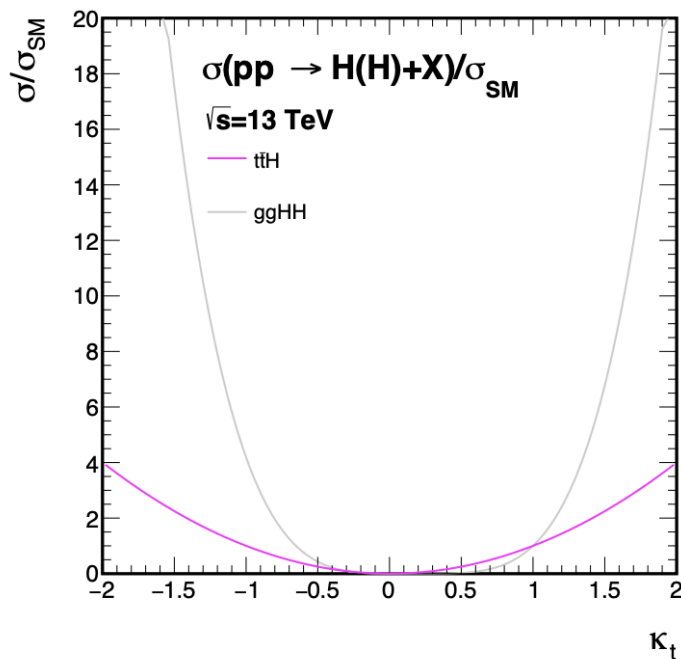
Figure 2.13: Variations of the ggF HH cross sections as a function of κ_t.

2.5.3 Higgs Boson Couplings to the Vector Bosons

The spontaneous symmetry breaking mechanism induces the couplings c_Z (c_W) between one Higgs boson and two Z (W) bosons, as well as the couplings c_{2Z} (c_{2W}) between two Higgs bosons and two Z (W) bosons. In the assumption that the BSM phenomena affect in the same way the c_Z and c_W couplings, it is practical to define c_V and c_{2V} as:

$$c_V = c_Z/c_Z^{SM} = c_W/c_W^{SM}$$
$$c_{2V} = c_{2Z}/c_{2Z}^{SM} = c_{2W}/c_{2W}^{SM}$$

$$(2.8)$$

The measured value of c_V is consistent with the SM prediction with an uncertainty of about 10% [43]. In the SM, considerations of perturbative unitarity of the VBF HH cross section [44] require that the c_{2V} and the c_V values are related through the relation:

$$c_{2V} = c_V^2 \qquad (2.9)$$

It is fundamental to test the relation in Eq. 2.9 because its violation, hence a violation of the perturbative unitarity, would be a clear signature of a BSM dynamics. In fact, a BSM dynamics would be required at a higher energy scale to re-establish the unitarity. Therefore, a direct observation of the c_{2V} coupling, and a measurement of its strength, is a very important step toward the full characterization of the Higgs boson properties. The observation of the c_{2V} coupling is challenging because the most sensitive physics process, accessible at the LHC, is the VBF HH whose SM cross section is expected to be only 1.73 fb. Thus, the collected data are expected to provide only an upper limit to it. However, anomalous values of c_{2V} could significantly increase the VBF HH cross section, as shown in Fig. 2.14, making the process observable.

2.5.4 BSM Higgs Boson Couplings

Theoretical considerations [45] indicate that the scale of the new physics Λ, e.g. the mass of new particles not predicted by the SM, could be at the TeV scale. From the experimental point of view, the direct searches performed so far using the LHC data
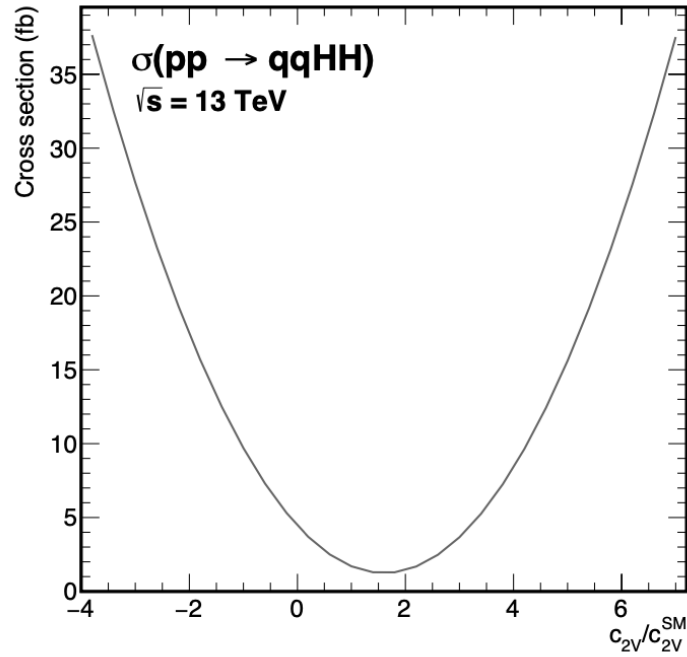
Figure 2.14: Variations of the VBF HH cross section as a function of c_{2V}.

exclude the presence of BSM resonances typically up to around 1 TeV. The possibility to probe masses beyond 1 TeV with direct searches is limited at LHC by the available center-of-mass energy and collected data. However, the indirect probe of high energy BSM phenomena at a smaller and accessible energy scale is possible thanks to radiative or perturbative effects. The SM effective field theory (SMEFT [29]) approach allows a quasi model-independent description of a phenomenon at an energy scale $E \ll \Lambda$. The only remnants of the high-energy dynamics are in the low-energy couplings and in the symmetries of the EFT. With the SMEFT approach new operators are added to the SM Lagrangian. Such operators are built using the SM particle fields and ensuring the SM Gauge and Lorentz invariance. As a consequence, new effective couplings between the SM particles and modifications of the SM coupling constants could arise.

As visible in Fig. 2.9, the HH production via gluon fusion, is sensitive to five Higgs EFT coupling constants κ_λ, κ_t, c_g, c_{2g}, and c_2 controlling the strength of the corresponding EFT operators. The c_{2g} and c_2 couplings are effective couplings that can be induced by loops dominated by new heavy BSM particles. The impact of the EFT couplings on the HH observables is double:

- They induce a variation, typically an increase, of the inclusive HH production cross

34

1528   section.

1529   • They significantly modify the differential HH cross section. In particular, the dis-
1530   tribution of the di-Higgs invariant mass m_{HH} can dramatically change in case of
1531   anomalous couplings.

1532 Therefore, the measured HH cross section together with the m_{HH} differential information
1533 can be used to constrain the EFT parameters.

BSM Benchmarks to Probe the Sensitivity

1535 Because of the small HH cross sections values, the HH processes are not sufficient to
1536 simultaneously constrain the κ_λ, κ_t, c_2, c_g and c_{2g} couplings. For this reason, twelve
1537 points in the five parameters space are selected to be representative of the HH kinematics
1538 for all the possible anomalous couplings scenarios [20,21]. Such points are called BSM
1539 benchmarks. Typically in the HH searches, the data compatibility with each specific BSM
1540 benchmark is tested. If no BSM evidences are found, upper limits on the benchmark cross
1541 sections are extracted. The coupling values for each benchmark is reported in Tab. 2.1,
1542 while the corresponding mHH distributions are visible in Fig. 2.15.

Benchmark	κ_λ	κ_t	c_2	c_g	c_{2g}
0	7.5	1.0	-1.0	0.0	0.0
1	1.0	1.0	0.5	-0.8	0.6
2	1.0	1.0	-1.5	0.0	-0.8
3	-3.5	1.5	-3.0	0.0	0.0
4	1.0	1.0	0.0	0.8	-1.0
5	2.4	1.0	0.0	0.2	-0.2
6	5.0	1.0	0.0	0.2	-0.2
7	15.0	1.0	0.0	-1.0	1.0
8	1.0	1.0	1.0	-0.6	0.6
9	10.0	1.5	-1.0	0.0	0.0
10	2.4	1.0	0.0	1.0	-1.0
11	15.0	1.0	1.0	0.0	0.0
SM	1.0	1.0	0.0	0.0	0.0

Table 2.1: Coupling values for the twelve defined BSM benchmarks.
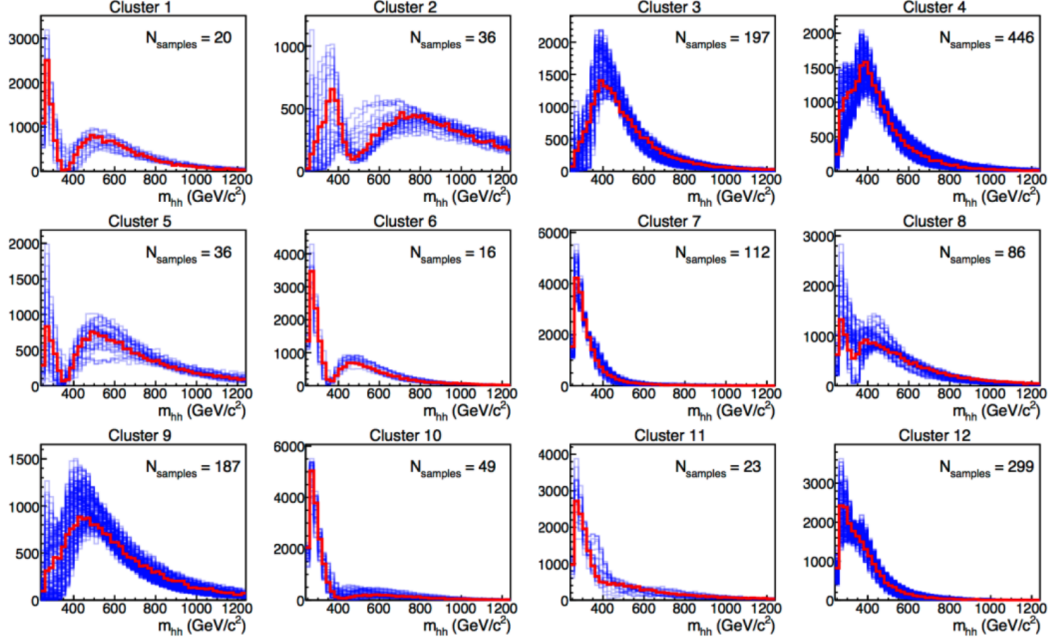
Figure 2.15: Generator-level distributions of di-Higgs boson mass for the clustered benchmarks from [46] are shown. The red distributions correspond to the chosen benchmark sample in each cluster, while the blue ones describe the other members of each cluster.

2.6 TRSM and HHH Production

The quartic self-coupling of the Higgs boson can be measured from the production of triplet Higgs bosons. However, due to the very small impact cross section ($\sim$80 ab at $\sqrt{s} = 13$ TeV) the search for triplet Higgs boson production in the context of the SM is beyond the reach of the LHC.

The two-real-scalar-singlet extension of the SM (TRSM) [13] extends the scalar sector of the SM by additional scalar fields that transform as singlets under the SM gauge group. In the TRSM, the gluon-fusion $pp \rightarrow HHH$ cross section is enhanced via the resonant production of X.

One of the simplest ways to realise this is through models that extend the SM scalar sector by two additional singlet fields. The most general extension of the SM by n real scalar singlet fields $\phi_i (i \in [1, ..., n])$ has a scalar potential of the form

$$V(\Phi, \phi_i) = V_{singlets}(\Phi, \phi_i) + V_{SM}(\Phi) \qquad (2.10)$$

Here, Φ describes the scalar $SU(2)_L$ doublet field of the SM and V_{SM} denotes the scalar potential of the SM. It is not possible to write down gauge invariant and renormalizable interactions between a scalar singlet and any of the SM fermions. The singlets will therefore only interact with the SM Higgs boson through the couplings of the scalar potential.

We consider here a specific version, TRSM [47], where in addition two $\mathbb{Z}_2$ symmetries are imposed, leading to a reduction of the available number of degrees of freedom. Depending on the masses, the heaviest scalar can decay to the two lighter scalars, which in turn decay to SM particles with the branching fractions depending on their masses. Here, however, we will focus on the scenario where the state H is identified with the SM-like Higgs boson, and Y and X are two new heavier scalars obeying the mass hierarchy,

$$2m_H < m_Y < (m_X - m_H) \tag{2.11}$$

This results in two real scalar singlets X and Y decaying to the SM Higgs boson H. The Feynman diagram for gluon-gluon production of said process is shown in Fig. 2.16
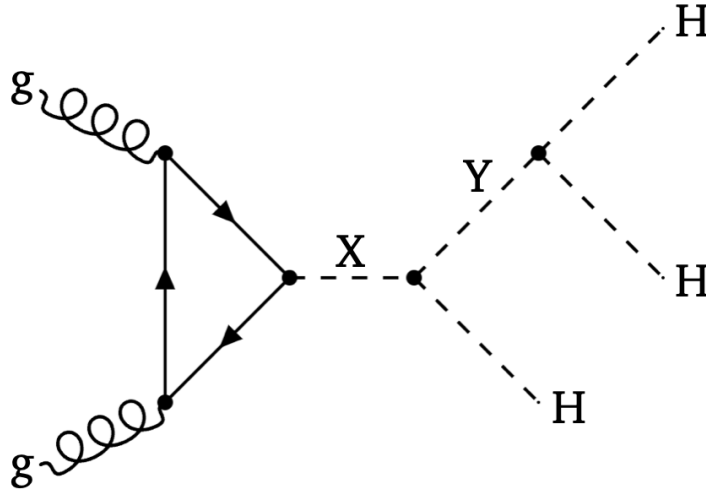
Figure 2.16: Feynman diagram showing the gluon-gluon production mode of a heavy scalar X followed by its decay process $X \rightarrow Y(HH)H$

As mentioned in earlier chapters, $H \rightarrow b\bar{b}$ has highest branching ratio and as triple-Higgs production has lower cross-section, we will focus on the case where all three Higgs bosonsare decaying to $b\bar{b}$ resulting in $X \rightarrow Y(HH)H \rightarrow b\bar{b}b\bar{b}b\bar{b}$.

Chapter 3

Experimental Setup

CERN, or the European Laboratory for Particle Physics, is an international research centre that operates the largest particle physics laboratory in the world. It sits astride the Franco-Swiss border west of Geneva and was founded in 1954 by twelve European countries. It was initially dedicated to the fields of nuclear and particle physics: its original name stands for Conseil Européen pour la Recherche Nucléaire, or European Council for Nuclear Research. Today, as our understanding of matter goes much deeper than the nucleus, the laboratory is oriented towards particle physics research. It has become an example of international scientific collaboration, with more than 13000 collaborators of over 100 nationalities representing more than 500 universities and institutes. As particle physics demands the ultimate in performance, CERN is at the forefront of technology development and knowledge transfer, and most notably served as the birthplace of the World Wide Web (WWW) in 1989.

CERN's current major facility is the Large Hadron Collider (LHC), the largest and most powerful particle accelerator ever built. It is a circular proton accelerator designed to reach a centre-of-mass energy of 14 TeV. Built between 1998 and 2008, the design of the LHC was largely driven to profit from the pre-existing CERN infrastructures: the LHC is installed in a 26.7 km long tunnel that was built to host its predecessor, the Large Electron Positron (LEP) collider, located between 45 m and 170 m below ground level. The LHC hosts two beam-pipes where protons circulate in opposite directions, and which are brought to collision at four interaction points, where four particle detectors

are installed. At one of this points sits the Compact Muon Solenoid (CMS) experiment, a general-purpose detector designed to explore a broad range of physics processes, from precision electroweak measurements to searches of supersymmetric particles. It is with the proton collision data collected by this detector that the analysis described in thesis was conducted

This chapter gives an overview of the LHC accelerator and the CMS detector. Section 3.1 reviews the design and parameters of the LHC. The CMS sub-detector structure with trigger system is presented in Section 3.2.

3.1 The Large Hadron Collider

The LHC was designed to deliver proton-proton (pp) collisions at an unprecedented maximum centre-of-mass energy of $\sqrt{s} = 14$ TeV with a very high instantaneous luminosity of 1×10^{34} cm^{-2}s^{-1}. It was conceived to investigate the nature of the spontaneous symmetry breaking through the search of the Higgs boson, which was observed by the ATLAS and CMS collaborations in 2012 [1, 2]. Additionally, it was intended to scan the accessible phase space in the search of new phenomena beyond the SM, aiming at favouring or ruling out the postulated scenarios. Complementary to the proton runs, a physics program of heavy ion collisions (Pb-Pb) is also carried out with the goal of studying the collective behaviour of quarks and gluons in plasma.

The realization of the LHC constituted a two decade-long international journey. Its frst proposal dates back to 1984 with the official recognition of the project, subsequently approved in 1994 and inaugurated in 2008. Two eras of physics operations have already been conducted: Run 1, which lasted from 2009 to 2013, and Run 2, from 2015 to 2018. The LHC is currently in the third data-taking era (Run 3) that will take place from 2022 to 2025. After that, the LHC and the accelerator complex will undergo a profound upgrade towards the High Luminosity LHC (HL-LHC), scheduled to start in 2029. A description of the accelerator complex and operations is given in the following.

3.1.1 Accelerator complex

The complete accelerator complex is illustrated in Fig. 3.1. The LHC is the last ring in a chain of particle accelerators, built well before the LHC and upgraded to meet its stringent requirements. The first step of the chain consists in the extraction of protons from a bottle of hydrogen gas making use of a strong electric field. The protons are then sent to a Radio Frequency Quadrupole (RFQ), where they are grouped into bunches and accelerated until they reach an energy of 750 keV. After that, the protons are supplied to the Linear Accelerator (LINAC 2), which brings the proton beam to an energy of about 50 MeV. The particles then arrive to the first circular collider, the Proton Synchrotron Booster (PSB), a 150 m ring that accelerates the beam up to an energy of 1.4 GeV and increases the intensity of the proton bunches. Next, the beam enters the Proton Synchrotron (PS) and then the Super Proton Synchrotron, two circular accelerators of 620 m and 6912 m in length which raise the energy of the beam to 26 GeV and 450 GeV, respectively.

The proton bunches are fed into the LHC with fast kicker magnets, which split the beam into two parallel beamlines that travel in opposite directions in the LHC tunnel. Once in the LHC, the beams are further accelerated to their maximal energy. The acceleration is performed in the high frequency accelerating cavities, placed in eight 545 m long straight sections along the ring. The trajectory of the beam is bent with 1232 superconducting dipole magnets placed throughout eight 2.45 km long arcs. These magnets generate a field of 8.3 T and need to be cooled down to a temperature of 1.9 K (-271.25°C) with superfluid helium-4. This structure is shown in Fig. 3.2, and the LHC contains 1232 such magnets for bending the beam. Aside from the dipole magnets, the LHC contains many other magnets, mainly quadrupole for correcting and stabilizing the beams to keep the particles focused in narrow beams.

Once the proton beam reaches the nominal energy and the beam is stabilized, protons are brought to collide at four different points along the LHC instrumented with particle detectors. ATLAS (A Toroidal LHC Apparatus) [50] and CMS (Compact Muon Solenoid) [51] are multipurpose detectors which can measure the products of both proton and heavy-ion collisions. They are installed in the diametrically opposite points of the LHC, where the highest instantaneous luminosity is achieved. The LHCb (LHC beauty) [52] experiment

40
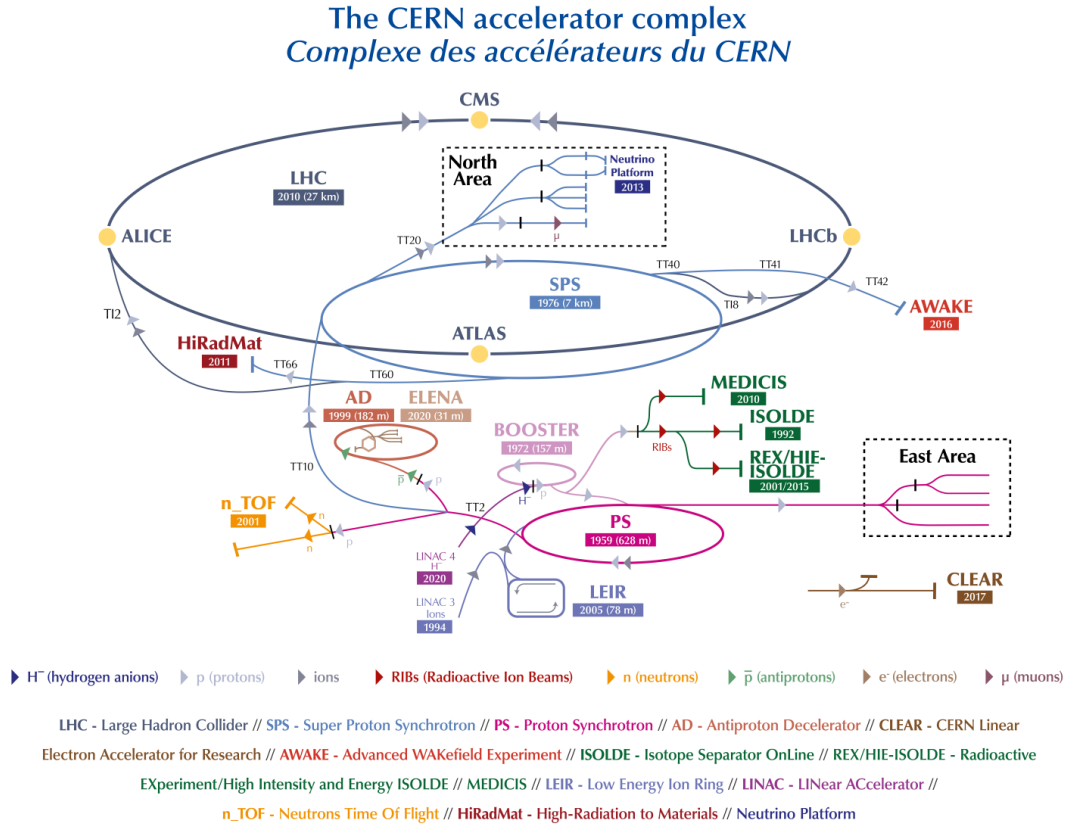
Figure 3.1: Illustration of the accelerator complex at CERN. Protons are accelerated to increasing energies at the LINAC 2 (in light pink), Booster (in light pink), PS (in dark pink), SPS (in light blue) and LHC (in grey) accelerators. The counter-circulating proton beams at the LHC collide in the centre of the CMS, ATLAS, LHCb and ALICE detectors [48].

consists of an asymmetric single-arm detector devoted to heavy flavour quarks physics; its primary goal is to search for evidence of new physics in charge-parity (CP) violation and rare decays. The last experiment, ALICE (A Large Ion Collider Experiment) [53], was designed to cope with very high particle multiplicities and is mainly devoted to the study of quark-gluon plasma in heavy-ion collisions.

3.1.2 Nominal Design Parameters

The LHC accelerates protons, which are charged, composite and stable particles. Being fundamental particles, electrons would be more appropriate for precision measurements, but protons have the advantage that they suffer much smaller synchrotron radiation losses due to their higher mass. This type of radiation is emitted when a charged particle is

LHC DIPOLE : STANDARD CROSS-SECTION

CERN AC/DI/MM - HE107 - 30 04 1999

ALIGNMENT TARGET

MAIN QUADRIPOLE BUS-BARS

HEAT EXCHANGER PIPE

SUPERINSULATION

SUPERCONDUCTING COILS

BEAM PIPE

VACUUM VESSEL

BEAM SCREEN

AUXILIARY BUS-BARS

SHRINKING CYLINDER / HE I-VESSEL

THERMAL SHIELD (55 to 75K)

NON-MAGNETIC COLLARS

IRON YOKE (COLD MASS, 1.9K)

DIPOLE BUS-BARS

SUPPORT POST
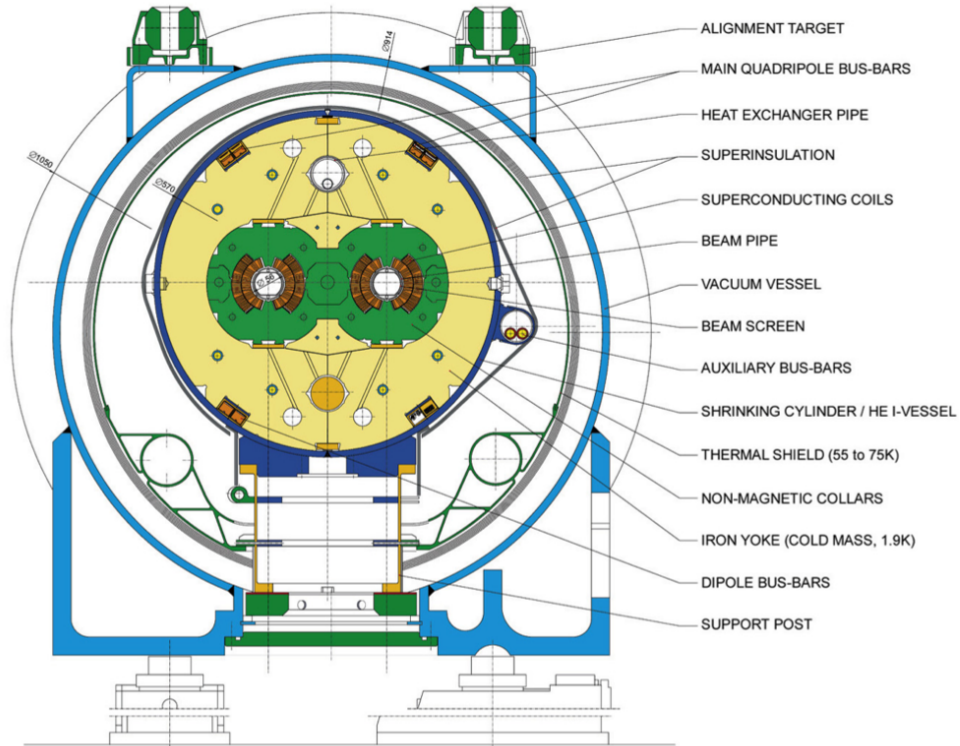
Figure 3.2: Cross section of an LHC dipole magnet [49].

accelerated radially; it produces energy losses which limit the maximum reachable energy in a circular collider. Thus a proton collider can achieve much higher energy than an electron collider, the maximum value being limited by the capacity of the magnets to maintain the protons in the circular trajectory. The design *centre-of-mass* energy of the proton-proton collisions at the LHC is $\sqrt{s} = 14$ TeV, meaning each beam has an energy of 7 TeV. An important fraction of the momentum of the proton is carried by the sea quarks and gluons that compose it; it is therefore possible to generate interesting physics without colliding protons with their antiparticles, which are much more difficult to produce.

Alongside the beam energy, a key parameter of the LHC machine is the *instantaneous luminosity* $\mathcal{L}$, which characterizes the collision rate and serves as an indicator of its performance. It relates the number of events per unit time $\partial N/\partial t$ produced for a given process with its cross section σ via

$$\frac{\partial N}{\partial t} = \mathcal{L} \times \sigma. \tag{3.1}$$

A large instantaneous luminosity is essential to produce low probability processes such as $t\bar{t}H$ and tH, but it also represents a challenge for the data acquisition system. Upon integration of $\mathcal{L}$ over time, one obtains the *integrated luminosity*, $L = \int \mathcal{L} dt$, which characterizes the amount of data produced. The instantaneous luminosity is usually expressed in units of $\text{cm}^{-2}\text{s}^{-1}$, while the integrated luminosity is expressed in units of inverse picobarns (pb^{-1}) or femtobarns (fb^{-1}).

Under the assumption that the two counter-rotating beams are identical, the instantaneous luminosity relates to the beam properties as

$$\mathcal{L} = \frac{N_p^2 n_b f \gamma_r}{4\pi \epsilon_n \beta^*} F,$$

(3.2)

where N_p is the number of protons per bunch and n_b is the number of bunches. The symbol f represents the revolution frequency of the bunches and γ_r is the relativistic factor. The transverse emittance ϵ_n characterizes the confinement of the beam in space and momentum, whereas the beta function β^* represents its focus at the interaction point. Finally, F is a geometric factor which accounts for the luminosity reduction due to the crossing-angle of the beams at the interaction point ($F \leq 1$). The values of the LHC design parameters are given in Tab. 3.1.

Symbol	Parameter	Nominal value
$\sqrt{s}$	Centre-of-mass energy	14 TeV
Λt	Bunch spacing	25 ns
$\mathcal{L}$	Instantaneous luminosity	1×10^{34} $\text{cm}^{-2}\text{s}^{-1}$
n_b	Number of bunches per beam	2808
N_p	Number of protons per bunch	1.15×10^{11}
f	Revolution frequency	11245 Hz
ϵ_n	Transverse emittance	3.75 μm rad
β^*	Beta function	0.55 m

Table 3.1: Design parameters of the LHC accelerator in proton-proton collisions [54].

In its nominal design, the LHC accelerates and collides as many as 2808 proton bunches per beam, each bunch containing about 115 billion protons. The bunches are grouped in trains of 48 bunches ("48b" scheme) spaced in intervals of 25 ns each, and circulate around the ring about 11000 times per second, only 3.1 m/s slower than the speed of light. Of these, 2544 bunches collide at the CMS interaction point at a bunch collision rate of 40 MHz. This configuration yields a luminosity of $\sim 1 \times 10^{34}$ $\text{cm}^{-2}\text{s}^{-1}$ at the beginning of

the fill, defined as the point when the proton injection is complete and the LHC cannot accommodate any more bunches.

Any collider with high instantaneous luminosity faces an important drawback: the *pileup* (PU), defined as the number of simultaneous interactions taking place in each bunch crossing. The average PU is directly proportional to the instantaneous luminosity and relates to the beam properties as

$$\langle PU \rangle = \frac{\mathcal{L}\, \sigma_{pp}^{inel}}{n_b\, f} \tag{3.3}$$

where σ_{pp}^{inel} is the inelastic *pp* cross section, which amounts to 69 mb at $\sqrt{s} = 13$ TeV [55], leading to a nominal average pileup of ~ 22 interactions per bunch crossing at the LHC, frequently exceeded during Run 2 operations. High pileup values result in a very high detector occupancy that degrades the efficiency and resolution of the particle reconstruction. The average number of simultaneous proton-proton (pp) interactions per bunch crossing (pileup) is shown on the left in Fig. 3.3.
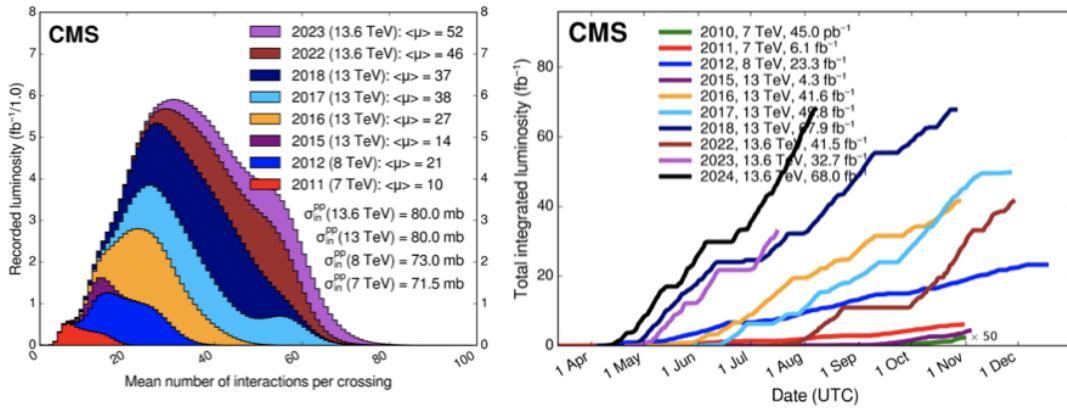
Figure 3.3: Average number of simultaneous pp interactions per bunch crossing (left) and integrated luminosity collected by the CMS experiment (right) by year of data taking [56].

So far, the LHC has completed two successful runs of data taking: Run 1 (2010-2012), at the centre-of-mass energies of 7 and 8 TeV , and Run 2 (2015-2018), at the centre-of-mass energy of 13 TeV. Run 3 (2022-2025) is ongoing with 13.6 TeV centre-of-mass energy. A total integrated luminosity of 340.6 fb^{-1} was delivered to CMS by the LHC by August 2024, 163.6 fb^{-1} of which at $\sqrt{s}$=13 TeV during Run 2. Furthermore, a peak luminosity of above 2×10^{34} cm^{-2}s^{-1} was achieved during Run 2, which amounts to twice the design value. The integrated luminosity delivered to the CMS experiment by year of data taking

is shown in Fig. 3.3.

The Long Shutdown 3 (LS3) is expected to start in 2026, concluding the *Phase 1* of the LHC. During this period, the LHC and the CMS detector will undergo a profound upgrade towards the High Luminosity LHC (HL-LHC), which will run in *Phase 2*. The goal of the upgraded machine is to reach a peak instantaneous luminosity of 5×10^{34} cm^{-2}s^{-1}, which yields to a total integrated luminosity of about 3000 fb^{-1} after a decade of operations, enhancing significantly the sensitivity to rare phenomena. The unprecedented collision rate will produce an average pileup of ~ 140. In its ultimate configuration, the machine could be pushed to an instantaneous luminosity of 7.5×10^{34} cm^{-2}s^{-1}, corresponding to an average pileup of ~ 200.

3.2   Compact Muon Solenoid

The CMS *(Compact Muon Solenoid)* [51] detector is a cylindrical detector with a length of 21.6 m and a diameter of 14.6 m. The term "compact" in its name refers to its weight of 14,500 tons, which is more than twice the weight of the ATLAS detector, which is roughly twice as large. It is situated at the LHC point 5, close to the French village of Cessy, 100 meters below the surface in a cavern. CMS is a general-purpose detector that was initially designed to precisely reconstruct the Higgs boson decay products. It is constructed with many concentric subdetectors that complement each other in the characterization of the different particles generated from the pp interactions. One of the key features of CMS is the intense magnetic field induced by the solenoid magnet (see Fig. 3.4). It is possible to precisely measure the momenta, trajectories, and interaction vertices of traversing charged particles using pixel and strip trackers in close proximity to the interaction point since these particles are bent under the effect of the field. The tracking system is surrounded by electromagnetic and hadronic calorimeters, which are meant to measure and absorb the energy of electrons, photons, and hadrons. Muons move through the calorimeters and are picked up by the muon tracking systems at the edge of CMS.

The LHC instantaneous luminosity sets a very difficult goal for the detector during the data collecting. With an instantaneous luminosity of about $2 \times 10^{34} cm^{-2} s^{-1}$, a peak pileup (PU) of almost 50 extra pp interactions is expected during collisions. This additional

CMS DETECTOR

Total weight   : 14,000 tonnes
Overall diameter : 15.0 m
Overall length   : 28.7 m
Magnetic field   : 3.8 T

STEEL RETURN YOKE
12,500 tonnes

SILICON TRACKERS
Pixel (100x150 µm²) ~1 m² ~66M channels
Microstrips (80–180 µm) ~200 m² ~9.6M channels

SUPERCONDUCTING SOLENOID
Niobium titanium coil carrying ~18,000 A

MUON CHAMBERS
Barrel: 250 Drift Tube, 480 Resistive Plate Chambers
Endcaps: 540 Cathode Strip, 576 Resistive Plate Chambers

PRESHOWER
Silicon strips ~16 m² ~137,000 channels

FORWARD CALORIMETER
Steel + Quartz fibres ~2,000 Channels

CRYSTAL ELECTROMAGNETIC CALORIMETER (ECAL)
~76,000 scintillating PbWO₄ crystals

HADRON CALORIMETER (HCAL)
Brass + Plastic scintillator ~7,000 channels

Figure 3.4: Schematic view of the CMS detector and its subcomponents [57]

activity raises detector occupancy while lowering detector performance. Every 25 ns, collisions occur at the CMS's center at the interaction point (IP). A bunch crossing (in-time pileup) can have multiple interactions occurring within it. The hadronic activity that is not derived from the hard scattering process, which are referred to as underlying events. The underlying events are usually softer and can be separated from the signals of interest provided the high granularity, fast reaction, and wide solid angle of CMS, equipped with radiation-hard detectors and electronics. Additionally, the experimental signatures overlap (out-of-time pileup) happens. This indicates that new proton bunches are colliding at the CMS core before the decay products from the previous collision have reached the active chambers of the detectors.

In achieving the wide range of physics goals, the main challenges for CMS are good electron and muon detection, high trigger efficiency and offline tagging of leptons and jets associated with b quarks, good electromagnetic energy resolution and good dijet, diphoton and dielectron mass resolution, and identification of missing transverse energy. Apart from efficient readout electronics performance, by construction the detector is prone to radiation damage, particularly in the forward regions.

1756 An overview of the CMS design and performance is given in the following subsections.

3.2.1 CMS coordinate system

1758 The CMS coordinate system is right-handed as given in Fig. 3.5. The origin of the
1759 CMS coordinate system is located within the detector, with the y-axis pointing vertically
1760 upward, the x-axis pointing radially inward to the middle of the LHC ring, and the z-axis
1761 pointing along the beam direction. The detector design can be understood using the
1762 spherical coordinate system where r is the distance from the z-axis, ϕ is the azimuthal
1763 angle (measured from the x-axis in the x-y plane), and θ is the polar angle (measured
1764 from the z-axis).
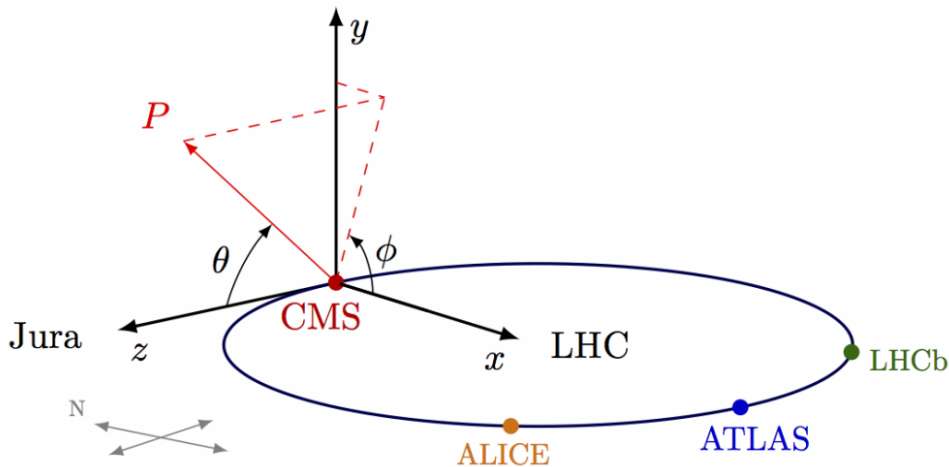
Figure 3.5: An illustration of the CMS detector with spherical co-ordinate system [58].

1765 A useful kinematic variable, which is often used in the LHC physics is rapidity (y), where
1766 the rapidity difference of two particles $(\Delta y = y_1 - y_2)$ is invariant under Lorentz boosts
1767 along the z axis, y is defined for a particle having momentum 4-vector (E, px, py, pz) as:

$$y = \frac{1}{2} \ln \frac{E + p_z}{E - p_z} \qquad (3.4)$$

1768 For a massless particle or for a particle with relatively small mass compared to its momen-
1769 tum ($E \approx |\vec{p}| \gg m$), the definition of the rapidity can be approximated by a quantity,
1770 called pseudorapidity (η), the pseudorapidity difference of two particles $(\Delta\eta = \eta_1 - \eta_2)$
1771 is also invariant under Lorentz boosts along the z axis. Pseudorapidity can be defined in
1772 terms of the polar angle θ as,

$$\eta = -\ln \tan \frac{\theta}{2} \tag{3.5}$$

The value of η is zero at the central part of the detector for polar angle $= 90°$, and $\eta = \pm\infty$ along the beam direction, $\theta = 0, \pi$. CMS detector covers a region up to $\eta \sim \pm 5$, which corresponds to an angle of $0.8°$ wrt beam line.

The transverse momentum is defined as the momentum projection on to the x-y plane and given as $p_T = \sqrt{p_x^2 + p_y^2}$. The usage of η and p_T at hadron colliders is motivated by the facts that the pseudorapidity difference and p_T are invariant under Lorentz boosts along the z axis. The beams enter along $\pm$z-axis within the detector; therefore, the transverse component for colliding particles is zero. Thus, after the collision, all outgoing particles should have the sum of transverse momenta equal to zero by following the momentum conservation law.

3.2.2 Tracker

The CMS tracker [59] sub-detector consists of a cylinder of 5.8 m in length and 2.6 m in diameter, placed at the inner most part at the detector. The main goal of the tracking system is to reconstruct the tracks of the charged particles as precise as possible and to reconstruct the position of the secondary vertices which is crucial for the study of the long lived particles (life time $\tau > 1$ ps) and to tag the quark-flavor of the jets. The tracking system was built under several basic requirements.

- In the p-p collision mode of the LHC, the number of pileup events are very high, so the tracking system needs to reconstruct the tracks from the high particle flux and then needs to associate them to the correct vertices at the origin.

- As the tracker system is closest to the detector interaction point, it experiences an enormously high radiation dose. So it is desirable that the tracking detectors are radiation hard.

- For tracking, the measurement should be non destructive. Hence, the material budget is expected to be minimal to avoid the energy losses and multiple scattering

₁₇₉₈   of particles inside the tracker material before reaching to the calorimeter sectors.

₁₇₉₉ CMS exploits two different types of tracking sub-system: pixel detector and silicon strip
₁₈₀₀ detectors. Fig. 3.6 shows the longitudinal view of one quarter of the CMS tracker system
₁₈₀₁ with both types of CMS tracker subsystems.
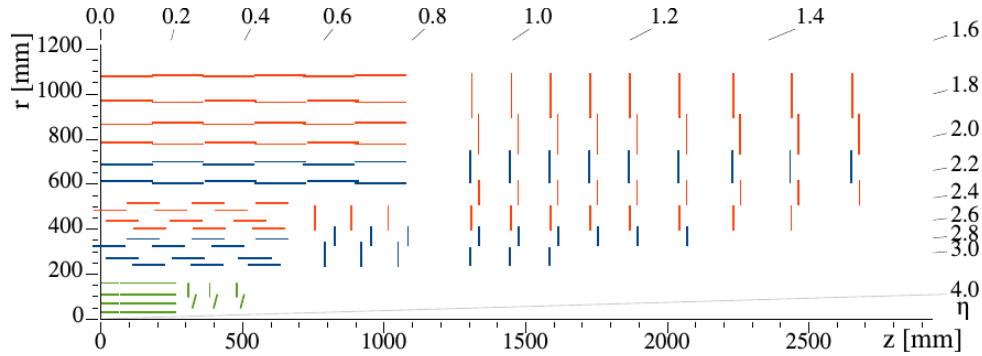
Figure 3.6: Sketch of one quarter of the Phase-1 CMS tracking system in r-z view. The
pixel detector is shown in green, while single-sided and double-sided strip modules are
depicted as red and blue segments, respectively. [60].

₁₈₀₂ Given the LHC collision conditions, the main challenges for the tracker system are gran-
₁₈₀₃ ularity, response time, and radiation hardness. It helps to detect the charged particles by
₁₈₀₄ constructing their trajectory and measuring their momentum. The design of the tracker is
₁₈₀₅ a result of a compromise between providing the best detector performance and keeping the
₁₈₀₆ amount of inactive material as low as possible. The latter is a critical feature of the tracker,
₁₈₀₇ as a higher amount of passive material generates multiple scattering, bremsstrahlung, pho-
₁₈₀₈ ton conversion and nuclear interactions. These distort the measurement of the trajectory
₁₈₀₉ in the tracker and the measurement of the energy in the calorimeters just after.

Silicon Pixel Detector
₁₈₁₀

₁₈₁₁ The pixel detector is the closest part of the tracker to the collision point and divided into
₁₈₁₂ 124 million pixels with size of 100μm by 150μm. The barrel region of the detector has
₁₈₁₃ four layers with radii of 3 cm, 7 cm, 11 cm, and 16 cm and three discs on either side
₁₈₁₄ of the barrel (endcap regions) with distance of 29 cm, 39.6 com, and 51.6 cm from the
₁₈₁₅ interaction point.

₁₈₁₆ Pixel detector provides three dimensional position measurement of the charged particles
₁₈₁₇ very close to the beam pipe. Due to radiation damage, the modules of the innermost layer

49

of BPIX were substituted with new ones during the long shutdown 2 in 2021 [61]. I was part of the installation and recommissioning of upgraded pixel detector.

Silicon Strip Detector

The silicon strip detector is the outer part of the tracking system with a coarse resolution in position measurements than the pixel detector. The particle flux decreases with increasing radial distance from the interaction point. The innermost part of the strip detector consists of 4 concentric cylindrical layers of tracker inner barrel (TIB) and 3 tracker inner disks (TID) on each side. Next layer is the outer silicon strip detector, divided into two parts (i) tracker outer barrel (TOB) consisting of six silicon strip layers and (ii) tracker end caps (TEC) consisting of 9 disks, each containing up to seven concentric rings of silicon strips. Additionally, in the modules of the first two layers (rings) of TIB (TID) and TOB and first, second and fifth rings of the TEC, a second micro-strip detector module is mounted back-to-back to the first with a stereo angle of 100 mrad, called the double sided or stereo module.

3.2.3 Calorimeters

Understanding what happened at the collision point depends on having information about the energy of the different particles created in each collision. Two different types of "calorimeters" in CMS are used to collect this data [62].

Electromagnetic Calorimeter (ECAL)

The CMS has a homogeneous electromagnetic calorimeter (ECAL) [63] made of fine-grained 75,848 lead tungstate ($PbWO_4$) crystals, just outside of the tracker system. The homogeneous medium minimizes the sampling fluctuations and provides a better energy resolution for photons and electrons. It is highly transparent and scintillates as electrons and photons pass through it. In other words, it generates light in proportion to the particle's energy. The crystals emit 80% of their light in less than 25 nanoseconds which is the nominal time between successive bunch crossings at the LHC; this satisfies the

50

requirement for quick detector response under LHC conditions. Since the light yield of PbWO$_4$ is temperature-dependent, a cooling system is needed to keep the crystals at $\sim$ 18 degree Celsius. The photo-detectors are used to detect this scintillated light and covert it into an amplified electric signal.

The crystals are arranged in barrel region (EB), covering pseudorapidity up to $|\eta| = 1.48$, and in two endcap regions (EE), covering up to $|\eta| = 3.0$. EB has a crystal length of 230 mm (220 mm in EE) corresponding to 26 (25) radiation lengths. The crystals on the front face have a transverse dimension of 2.2×2.2 cm^2 in EB (2.86×2.86 cm^2 in EE). The total volume of the crystal is 11 m^3, and its weight is 92 t. The barrel calorimeter is divided into 36 supermodules, each with 1,700 crystals. The endcaps are divided into two dees, each with 3,662 crystals as shown in Fig. 3.7.
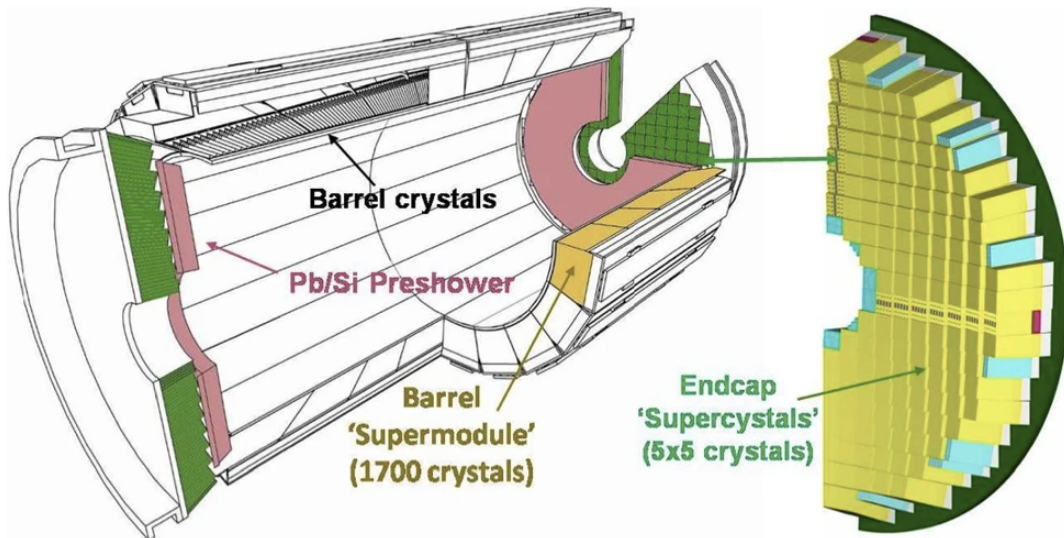
Figure 3.7: Schematic view of the ECAL showing the cylindrical barrel closed by the two endcap regions with one half endcap displayed [64].

The photon separation is improved by a preshower detector (ES) based on lead absorber and silicon strips sensors (4,288 sensors, 137,216 strips, 1.9061 mm^2 with x-y view) mounted in front of the endcaps at $1.65 < |\eta| < 2.6$. The ES has a cumulative thickness of around three radiation lengths. It resolves the highly collimated photon pairs coming from the light and short-lived π^0- meson decay, which are not possible to resolve using only ECAL.

The ECAL energy reconstruction is crucial for the rare physics searches with final states having charged leptons and photons, such as, $H \to \gamma\gamma$, $H \to ZZ \to 4l$ and many others.

Hadron Calorimeter (HCAL)

Hadron calorimeter [65] completes the CMS calorimetric systems. The sampling calorimeter is made up of the active material (4 mm thick plastic scintillator tiles) placed between copper absorber plates. HCAL determines a particle's location, energy, and arrival time as the particle passes through calorimeter. The active elements are read out using wavelength-shifting (WLS) plastic fibres. The scintillating light is collected by fibres and fed into readout boxes, where photo-detectors amplify the signal. The total amount of light in a given area, known as tower, is a measure of a particle's energy which is summed up over several layers of scintillator tiles in depth.
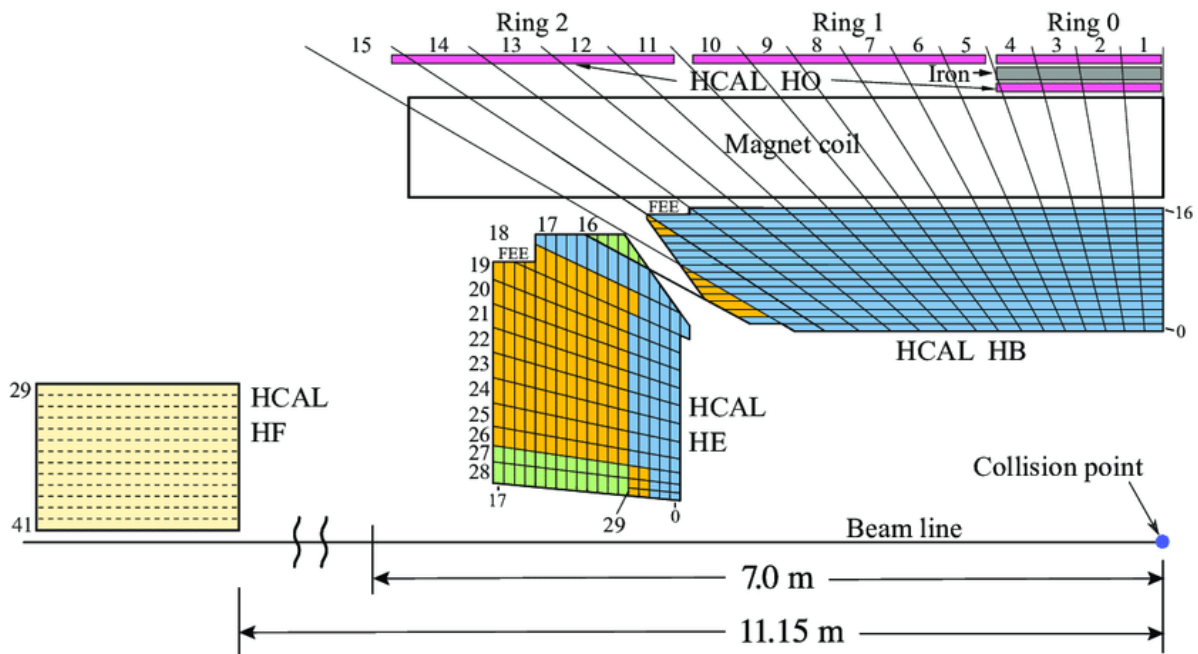
Figure 3.8: A schematic view of one quarter of the CMS HCAL, showing the positions of its four major components: the hadron barrel (HB), the hadron endcap (HE), the hadron outer (HO), and the hadron forward (HF) calorimeters [66].

HCAL also consists of two parts: the barrel region (HB) and the endcap region (HE) as shown in Fig. 3.8. The absorber plates are 5 cm thick in the HB region and 8 cm thick in the HE region. The depth of the barrel HB is around 79 cm or 5.15 nuclear interaction length. Nuclear interaction length is the mean distance travelled by a hadronic particle before undergoing an inelastic nuclear interaction.

As the material of the electromagnetic and hadronic calorimeters in the barrel may not provide enough stopping power for highly energetic particles in the central region ($|\eta| <$

1.4), the detector is complemented by an outer hadronic calorimeter (HO) located outside the solenoid, composed solely of scintillating material. The CMS also uses a separate forward calorimeter (HF) 6 m downstream of the HE endcaps. It extends the hermeticity of the central HCAL system to a pseudorapidity of 5.0 (as needed for an excellent missing transverse energy measurement). Quartz fibres are used as the active medium, and they are contained in a copper absorber matrix. It is specifically sensitive to Cherenkov light from neutral pions due to the quartz fibre active element. As a result, it has the unique and attractive property of providing a highly localized response to hadronic showers.

Along with measuring the energy of hadrons, HCAL also allows the detection of non-interacting and uncharged particles as missing transverse energy (MET). Measuring these particles is crucial because the measurement can reveal whether new particles have formed, such as the supersymmetric particles (much heavier versions of the standard particles). Some decay products of these new particles leave no trace of their existence in any part of the CMS detector. To detect them, the HCAL must be hermetic, which means it must catch any particle that emerges from the collisions to the greatest extent possible. We can deduce the existence of the invisible particles if we see particles fly out on one side of the detector but not on the other side, with an imbalance in momentum and energy.

3.2.4 Superconducting Solenoid Magnet

A complex arrangement of niobium-titanium (Nb-Ti) coils, capable of carrying a current of 19.5 kA and cooled by liquid helium, works as a superconducting solenoid magnet and generates a 3.8 T magnetic field. It consists of four layers NbTi coils with 542 turns in each of the layers. It is kept inside a liquid Helium cryostat at an operational temperature of -268.65° to reach the state of superconductivity. This magnet has an inner diameter of 6 m and a length of 12.5 m. The tracker and calorimeters are entirely contained inside it. It is the main feature of the CMS detector, which bends the path of charged particles while passing through the magnetic field.

The magnetic field $\vec{B}$ provokes the bending of the paths of the particles of non-zero charge q and speed $\vec{v}$ in the transverse plane via the Lorentz force $\vec{F}_L = q(\vec{v} \times \vec{B})$; the charge and momentum of a particle can be inferred from this bending, alongside the measurement

performed by the tracker. To achieve the highest precision, the magnetic field must be accurately characterized over the entire volume of the experiment. The curvature of the path within the tracker depends on the energy and mass of the charged particle. It helps in particle identification and provides good momentum resolution. A 14 m iron return yoke surrounds the magnet coils and returns the magnetic flux through the muon chambers.

3.2.5   Muon Chambers

As the name of the detector "Compact Muon Solenoid" indicates, muon physics is a vital task for CMS. Muons are the charged leptons similar to electrons but 200 times heavier. Despite being a charged particle, it can penetrate the detector for several meters as it interacts weakly and deposits little energy within calorimetric systems. Therefore, the outer part of the detector is entirely covered by muon chambers [67] to detect muons, almost the only surviving particles reaching the muon chambers. There are four muon stations outside the solenoid and interleaved with iron return yoke plates. They are used to reconstruct the hits made by muons while passing through them. Muons also leave hits within the tracker. The strong solenoidal magnetic field bends the muon track which helps in measuring muon's momentum. The hits within the tracker are combined with hits within the muon chambers for energetic muons.

The muon system contains gas ionization chambers. There are 1400 chambers in total. The 250 drift tubes (DTs) and 540 cathode strip chambers (CSCs) monitor the particles' positions and provide a trigger, and 610 resistive plate chambers (RPCs) form a redundant trigger network that quickly determines whether or not to hold the acquired muon event. All these components are robust and capable of suppressing background noise. The muon barrel (MB) region contains RPCs and DTs, while the endcap contains RPCs and CSCs. The arrangements depend on the muon rate in MB (muon barrel) and ME (muon endcap) region. A cross-sectional view of the muon system is shown in Fig. 3.9.

The DTs cover the pseudorapidity region $|\eta| < 1.2$. They can reconstruct the muon track from its hits within the stations with excellent time resolution and efficiency. A gas mixture of 85% Ar+15% CO_2 is surrounded by a gold-plated stainless-steel anode wire in each cell, resulting in a drift time of 380 ns.
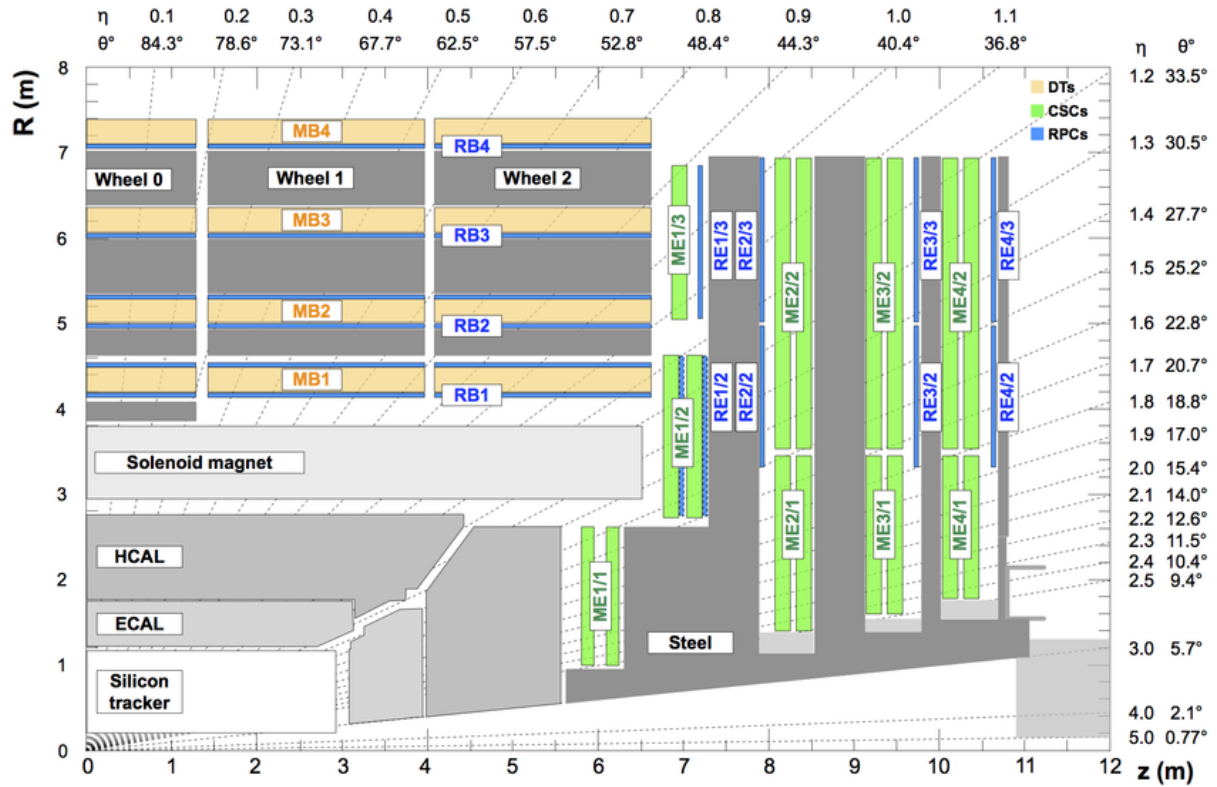
Figure 3.9: Schematic view, in the r-z plane, of one quadrant of the CMS detector, with the axis parallel to the beam (z) running horizontally and the radius (r) increasing upward. The interaction region is at the lower left corner. The position of the present RPC chambers is shown in blue. The RPCs are both in the barrel and in the endcaps of CMS. The DT chambers are labeled MB and the CSC chambers are labeled ME. The steel disks are displayed as dark gray areas. [67].

The CSCs cover a pseudorapidity region $0.9 < |\eta| < 2.4$. In each endcap, the 468 trapezoidal CSCs are arranged into four stations. Six anode planes are interleaved among seven cathode panels in each chamber, with wires running azimuthally. The ME chambers use a gas admixture of 50% CO_2 + 40% Ar and 10% CF_4.

The RPCs are interspersed in both the MB and ME covering $|\eta| < 1.9$ region. The RPCs are made of two resistive Bakelite plates separated by a gas volume. They provide an independent triggering system and a fast response with good time resolution (less than 25 ns) for muons.

3.2.6 Trigger System

At the LHC, the proton-proton collision occurs at very high luminosity, which leads to the production of rare physics signals at an appreciable rate. However, most of the collisions

are soft (low energy), so they do not produce any interesting physics events. Also, the size of each event is around 1 MB, and the frequency of collisions is 40 MHz, i.e., 40 TB of data per second get generated during the collisions. Considering the fact that in this huge data collection only a few events are of physics interest, a trigger system is used to select potentially interesting events. Only this fraction of data is stored on a computer disk for subsequent analysis. The full trigger system decreases the rate of interesting events to about 1 thousand per second. A series of trigger levels are used to achieve this. The detector stores all of the data from each crossing in buffers. A small amount of key data is used to perform a fast, approximate calculation to identify features of interest such as high-energy jets, muons, or missing energy. The levels are known as "L1-trigger" or level-1 trigger and "HLT" or high level trigger as given in Fig. 3.10.
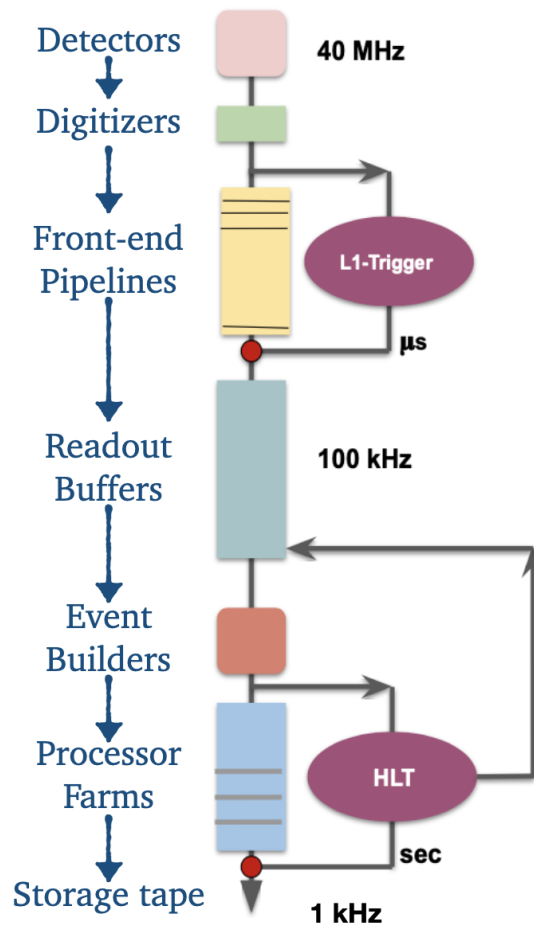
Figure 3.10: Flowchart of CMS trigger system. Image reproduced from Ref. [68].

L1-trigger

The L1-trigger is based on hardware. It uses a rapid and completely automated method that scans the basic signs of interesting physics, such as particles with high energy or rare combinations. From the 40 million events, 100k events are selected at this level with a latency of few microseconds using a simplified readout of the calorimeters and muon subdetectors.

A simple schematic of the CMS L1-trigger is given in Fig. 3.11. The trigger primitives (TP) from ECAL and HCAL as well as muon detectors (drift tubes (DT), cathode strip chambers (CSC), and resistive-plate chambers (RPC)) are processed in several steps until the combined event information is evaluated. After this, a decision is made to accept the event. The information from regional calorimeter triggers (RCTs) is combined to make up the L1 global calorimeter trigger (GCT). The RCT receives the transverse energies of e/γ objects from ECAL and of jets from HCAL. The L1 jet reconstruction algorithm is based on a square approach: it considers the energy deposit in a $9{\times}9$ trigger tower area centered on a local maximum. The RCT processes this data in parallel and sends objects and their energy information as outputs. The GCT sorts the objects using their energy information and classifies them as isolated, non-isolated, central, forward jets, and several global quantities.

To ensure good coverage and redundancy, each of the three muon detector systems participates in the L1 muon trigger. The front-end trigger electronics of DTs and CSCs identify tracks (hits) and transmit them to regional track finders. They further identify muons based on pattern recognition algorithms and measure their energy. In the overlap region of the DT track finder and CSC track finder, the information is shared for efficient coverage. For RPC hits, the information is sent to pattern comparator trigger logic boards via front-end electronics that identify muon candidates. The three regional track finders sort the muon candidates that have been detected and send them to the global muon trigger (GMT) with their pT and position information. The GMT then combines muon candidates identified by multiple systems to exclude candidates that pass multiple muon triggers. The GMT also conducts a consistency assignment so that candidates can be rejected at the final trigger stage if their quality is poor and they can only be reconstructed by one muon track finder.
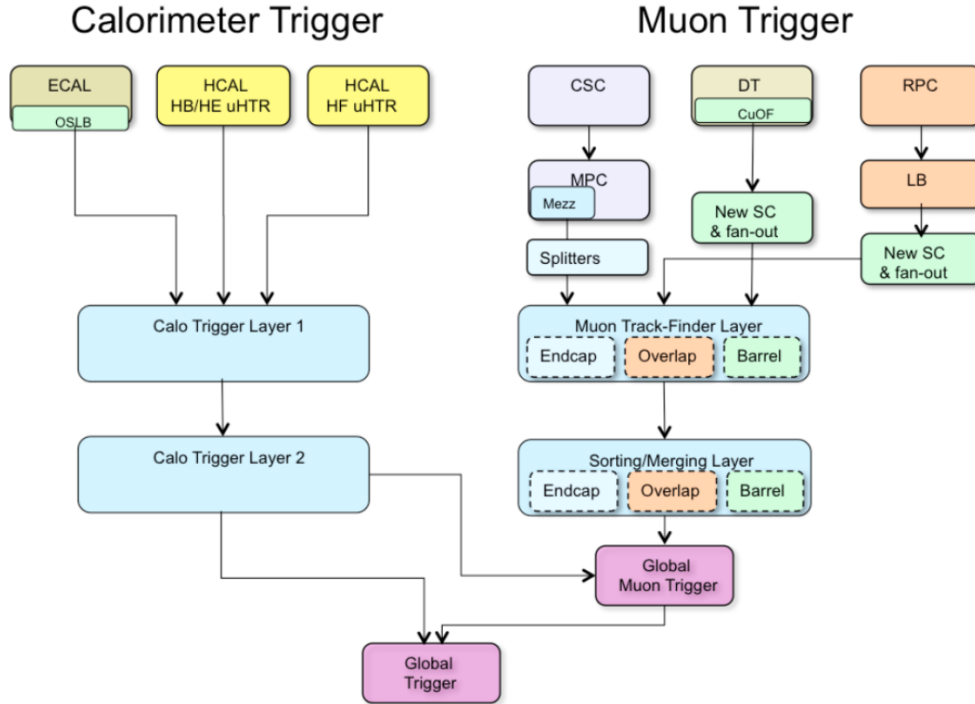
Figure 3.11: Schematic layout of L1 trigger system of the CMS experiment [69].

The global trigger (GT) completes the CMS L1 trigger scheme by implementing a menu of triggers. The decision from GT is sent to the tracker, ECAL, HCAL or muon system via the trigger, timing and control (TTC) system. Finally, a set of selections are imposed on these reconstructed objects at the L1 level to pick good events.

High-level Trigger (HLT)

The HLT consists of a farm of processors running a version of the full event reconstruction software optimized for fast processing. It reduces the event rate down to 1 kHz from 100kHz. Objects such as electrons, muons, and jets are reconstructed for each event, and identification criteria are used to select only interesting events for data analysis. After the HLT level selection, the data is stored on tape for further analyses.

In the HLT operation, the data from the readout buffers are sent to a processor farm. This trigger level is made up of a series of increasingly complex filters. The filtering process uses the complete detector information from all the subdetectors, starting from reconstruction to selection. In simple words, the HLT considers full data events to decide if the event should be kept or not. In order to create datasets with different physics signatures, the

final stage of HLT processing involves the reconstruction and event filtering. The time duration it takes to process an event varies depending on the algorithms used. The average time between events is about 60 ms, but some events can take up to a second.

The data acquisition system (DAQ) reads data from various subsystems for offline storage after the HLT decision. A complete sequence of L1 and HLT selection criteria, including any prescale, is referred to as a trigger path. Unlike in the case of offline analysis, the trigger selection is a non-reversible process, and discarded events cannot be recovered.

3.3   CMS simulation tools

The simulation plays a fundamental role in data analysis to perform any measurement or extract any relevant physics parameter. It consists of complete information on the physics process used for event generation and corresponding particle content. For event generation, Monte Carlo (MC) based event generators are used. They use numerical MC based techniques to produce collisions at the high energy as they occur in the LHC. The MC event generators provide a complete picture of the collision process from initial to final stages, including the strongly inelastic interaction, the radiation process, parton-hadronization, and the underlying event description. After the physical events are produced using information from theoretical models incorporated into the generator, the effects that a detector introduces into the basic theory must be considered. The choice of event generator depends on the physics process.

In simulation, each event has different probability that corresponds to its differential cross section. While generating events at next-to-leading order (NLO) in perturbation calculation, the infra-red (IR) divergences in the real-emission corrections and virtual corrections are taken into account using IR subtraction method. The contribution of the soft singularities makes the matrix element of real-emission finite. Therefore, the method adds a subtraction term to make virtual corrections finite. The events are generated separately for Born and real-emission phase space. For the events simulating real-emission, event weights become negative if simulation over-estimates real-emission matrix element. The negative weights contributes as the negative differential cross section term for real-emission. This results in reduction of effective simulation statistics. Generally the fraction

of events with negative weights is small, but still problematic while doing higher order calculation that requires more computational resources per event. Therefore, the event generators that take care of the negative weights issue are used for NLO event generation [70, 71]. CMS physics simulations are mostly based on the following event generators:

MADGRAPH: MADGRAPH [72] generates the matrix element for the multi-particle final state process. The updated version allows for matrix element calculations at NLO accuracy (controls theoretical uncertainty) and provides a technique for parton shower matching. Depending upon the Lagrangian of any renormalizable or effective theory, it can generate events for any physics process predicted by that theory.

POWHEG: POWHEG [73, 74] also produces NLO-accurate calculations of the hard scattering sub-processes. PowHeg has the characteristic of being free from negative event weights. The Refs. [71, 73, 75] have detailed description of PowHeg NLO calculations.

PYTHIA: The PYTHIA [76] is a standard tool for the generation of events in high-energy collisions, which works for various SM and BSM processes. It contains the models of hard processes and initial- and final-state parton showers, matching and merging methods between hard processes and parton showers, multiparton interactions, beam remnants, string fragmentation, and particle decays.

The last step of the simulation process is to pass the generated events through the detector response simulation. In CMS, it is done using GEANT4 [77] toolkit. The detector simulation includes the detector geometry, particle interactions with detector's materials, magnetic field effects, and real conditions during detector operation. The additional pp interactions (pileup) during collisions are also superimposed to the event at hit level using pileup mixing module. The module deals with a sequence of bunch crossings to properly simulate the contributions affecting the in-time bunch crossing. The next step in the event is modeling the response of the detector readout electronics, which is also known as digitization. The digitized signals are further processed in reconstruction of higher level physics objects, such as charged particle tracks, photons, etc. used in physics analyses.

Most of the aspects of simulations are integrated with the standard analysis software known as CMSSW [78]. The MC events are reconstructed using the same methods used for real data, allowing for a consistent comparison between the data and the simulation.

2064 We will briefly study these reconstruction algorithms in the next chapter.

Chapter 4

Physics Object Reconstruction and Identification

The reconstruction of an event implies the identification of all stable and visible particles produced in a proton-proton interaction. Particles are identified based on their specific signatures in the CMS detector, as illustrated in Fig. 4.1 and their kinematic properties are measured by combining the information from the various subdetectors. The event reconstruction within CMS is performed by reconstructing each final state particles with a particle flow algorithm, whether they are leptons, hadrons or photons.

After the collision, particles enter the tracker after leaving the beam interaction point, where signals (hits) in the sensitive tracker layers are used to reconstruct charged-particle trajectories (tracks) and their origins (vertices). The tracker is embedded in a magnetic field, which bends the trajectories and allows for measuring charged particle electric charge and momentum. ECAL absorbs electrons and photons as they pass through it. The corresponding electromagnetic showers are observed as energy clusters in neighbouring cells, which are used to calculate the particle's energy and direction. Hadrons, both charged and neutral, may induce a hadronic shower in the ECAL, which is then fully absorbed in the hadron calorimeter (HCAL). The energies and directions are calculated using corresponding clusters. Muons pass through the calorimeters with very few interactions. Muons generate hits in the muon detectors, located outside the calorimeters. Neutrinos do not interact with the CMS detector and escape undetected.
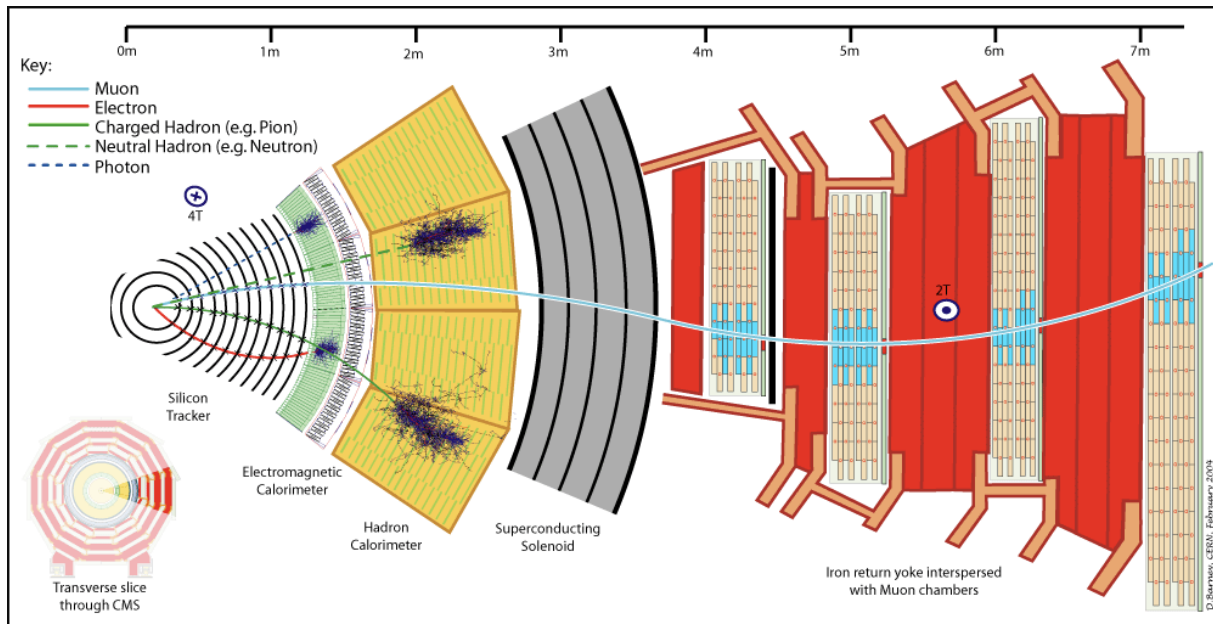
Figure 4.1: Transverse slice of the CMS detector, showing the experimental signatures of the different final-state particles [79].

All the above information from subdetectors are the basis of CMS reconstruction algorithms.

4.1   Track and Primary Vertex Reconstruction

For any data analysis, it is essential to understand how the tracks and origin of the charged particle tracks (also known as primary vertex) can be identified when dealing with the large number of PU interactions. At every bunch crossing, the collisions between protons give rise to interaction vertices which spread along the beam axis around the nominal interaction point, which can be reconstructed by combining information from reconstructed tracks, as illustrated in Fig. 4.2. Tracks are then associated to vertices, and the primary vertex (PV) is defined as the one with the largest value of summed physics-object p_T^2. The other vertices are referred to as pileup vertices. A detailed procedure of CMS track and vertex reconstruction is given in Ref. [80].

Tracks are essential for determining the production vertex of charged particles and measuring their momenta. For their reconstruction, firstly, the hits within the pixel and strip detectors are determined. They estimate the momentum and position parameters (longitudinal and transverse parameters) of the particles. For this estimation, tracking
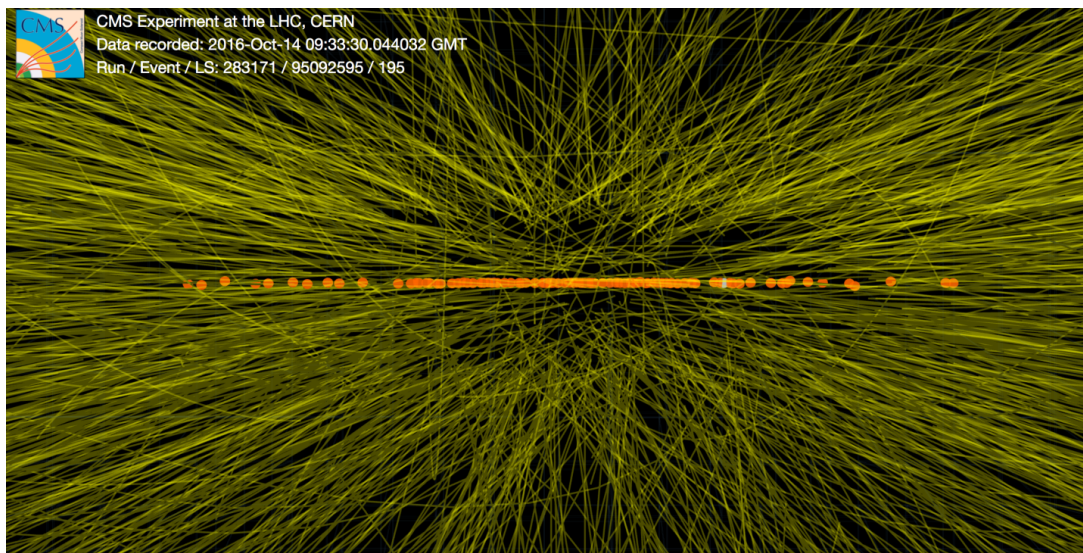
Figure 4.2: A collision recorded by the CMS detector during the 2016 data taking [81]. The lines correspond to the reconstructed tracks, while the dots represent the reconstructed interaction vertices.

algorithm called combinatorial track finder (CTF) is used.

The CTF is based on the concept of iterative tracking. At each iteration, track seeds are formed using a limited number of pixel hits, and an initial estimate of the track parameters is derived. A track-finding algorithm follows, based on the method of Kalman filter [82]. The filter uses track seeds to extrapolate the trajectory of the track to subsequent detector layers, taking into account the effect of multiple Coulomb scattering. At each layer, compatible hits are added to the trajectory, the track parameters are recalculated, and the resulting trajectory is extrapolated to the next layer. Finally, tracks that do not satisfy goodness-of-fit criteria are discarded. Tracks that are easier to reconstruct, e.g. those with large p_T (and therefore less pronounced curvature) and produced close to the interaction point, are reconstructed first. Hits associated to these tracks are then removed, reducing the complexity of subsequent iterations. Multiple iterations are performed, each time with decreasingly stringent requirements on the track seeds. In particular, the last iterations are optimized to reconstruct tracks with lower p_T or with larger displacement from the interaction vertex. The efficiency of reconstructing tracks with $p_T > 1$ GeV is found to be larger than 99% for isolated muons over the entire coverage of the tracker, while efficiencies for electrons and pions range between 80 and 99%, depending on the track pseudorapidity. Fake rates are at the level of 5% in the barrel and of up to 15% in the endcap and transition regions. The resolution on the track p_T significantly depends

64

on the p_T and η of the tracks, and is below 1% for central muons with p_T between 1 and 10 GeV [80].

Primary vertex reconstruction depends on the selected tracks where it finds a common meeting point (vertex) among a set of tracks. It aims to determine the position and associated uncertainty of all proton-proton interaction vertices, including the signal vertex and any vertices from pileup collisions. It consists of three steps:

1. Tracks selection

2. Clustering of tracks originated from the same interaction vertex

3. Track fitting for each vertex's location using its corresponding tracks

The inclusive vertex finder (IVF) algorithm is used for reconstructing secondary vertices (SV). Based on their separation in three dimensions, it clusters tracks around seeds with high impact parameter significance. Then, an outlier-resistant fit of a common vertex of all the tracks in a cluster yields the SV position. Tracks are then re-associated to either the primary or the secondary vertex based on their compatibility and the SV position is fitted again using only the remaining tracks if there are at least two tracks remaining. SVs aren't employed directly in this study, but in the event that they can be reconstructed, they offer significant jet flavor differentiation and are thus used in b-tagging discriminant like DeepCSV.

4.2 Particle Flow

The Particle Flow (PF) algorithm aims to reconstruct and classify all of the particles from a collision by integrating the information from the various subdetectors in the most optimal way. For each collision, the set of the reconstructed and identified particles by the algorithm (PF candidates) provides a global event description that leads to phenomenal CMS performance for jet and τ hadronic decay reconstruction, MET determination, and e and μ identification. This method also identifies particles from PU interactions; therefore, it is used to build efficient PU mitigation techniques. The output of the PF consists of a list of candidates classified as electrons, photons, muons, charged hadrons, or neutral

2148 hadrons, as illustrated in Fig. 4.3. The algorithm consists of two separate steps: the
2149 reconstruction of the PF elements, and the link between the reconstructed elements.
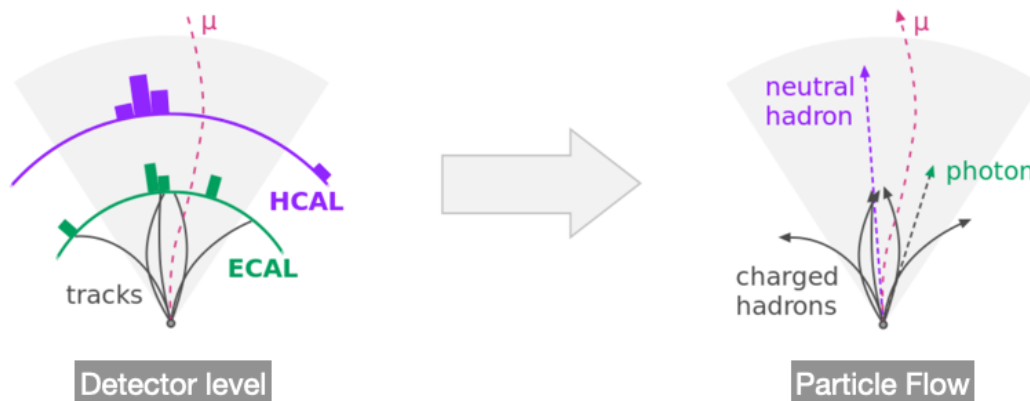
Figure 4.3: The particle-flow algorithm combines information from various subdetectors to provide a global description of the event in terms of electrons, photons, muons, charged hadrons, and neutral hadrons.

2150 Any physics study is conducted purely based on final decay products, including the fea-
2151 tures of the physics process. In this part, we study how the PF algorithm works for the
2152 final observable states that leave signals in the detector.

2153 • **Electrons (e) and Photons (γ):** Nearly all of the energy of electrons and photons
2154   is deposited in the ECAL, where electrons also create hits in the tracker layers.
2155   Extrapolation from the last measured hit in the tracker to any cluster in the ECAL is
2156   used to link them. The signals in the ECAL crystals are reconstructed by subtracting
2157   the PU contributions. This technique has been used for both the HLT and offline
2158   event reconstruction during the entire LHC Run-2 data-taking period.

2159   While travelling through the tracker material in front of the ECAL, almost 60%
2160   of the photons start to convert into a pair of electron-positron through the pair-
2161   production mechanism. Furthermore, the produced electron or positron experiences
2162   bremsstrahlung photon radiation. So the energy measurement of a photon from
2163   a particular single crystal deposition is not possible. Hence, the photon-electron
2164   reconstruction algorithm starts by grouping the crystals into 3×3 cluster in $\eta - \phi$
2165   space around the most energetic one (called seed crystal). In the presence of the
2166   CMS magnetic field the trajectories of the electrons and positrons are bent leading
2167   to photon radiations spread radially over ϕ direction. To catch the corresponding

energy deposits, multiple ECAL clusters are needed to be combined to produce a super cluster (SC). In CMS this step is done by two different algorithms (i) mustache algorithm, which is particularly useful to properly measure the low energy deposits, and (ii) refined algorithm, it uses the tracking information of the extrapolated bremsstrahlung tangents and the conversion tracks of the electron-positron pair to match with the SC position to combine into a single candidate.

All these ECAL clusters, superclusters, electrons tracks, and tracks from photon conversion are used as input to link this element into a block of particles. Starting from electron tracks or superclusters, respectively, the blocks are divided into electron and photon. At this point the supercluster is called a refined supercluster. A further track selection criteria are applied to these object to reconstruct "PF electron". Without passing track selection, the particle is labelled as "PF photons".

- **Muons (μ):** Muons are reconstructed using information from the tracker and the muon systems in CMS [67]. The reconstruction is performed with three following methods:

  – The local reconstruction is the first step in the muon reconstruction chain. First, digitized electronic signals are used to recreate hits in DTs, CSCs, and RPCs. Hits are then matched within each DT and CSC chamber to form segments (track stubs) using the Kalman filter method. The reconstructed muons are labelled as "standalone muons".

  – A search is performed for tracks that fit each standalone muon track among those reconstructed in the inner tracking system, with the best-matching tracker track being chosen. The track fitting, using all hits in both tracks, is performed for each tracker track-standalone muon pair, again using the Kalman filter technique. The result is a collection of objects referred to as "global muons".

  – Tracker muon tracks are built from the inner tracker trajectory reconstruction. The tracker-muon algorithm is beneficial for identifying low-pT muons that may not leave enough hits in the muon stations to be reconstructed as a standalone muon. Tracker muons should not be used without additional specifications because the default conditions for tagging a tracker track as "tracker

67

muon" are pretty loose.

The resulting muon candidate collections are used as input for PF muon identification. The PF muon reconstruction has been fine-tuned to distinguish muons within jets with high accuracy, resulting in a low rate of false positives due to misidentified charged hadrons.

- **Charged and neutral hadrons:** As the collisions occur at a high energy, the process may end up with having partons in the final state carrying colour charge. Since they can not exist in a free state, they hadronize to produce stable colourless hadrons as a result of QCD confinement. The produced hadrons appear to move in the same direction as the parton they originate from, creating collimated bunches of particles known as jets. After the identification of muons, electrons, and isolated photons and their extraction from the PF blocks, the remaining particles to be detected are hadrons originating from jet fragmentation and hadronization.

- **Missing Transverse Energy (MET):** The MET is identified as momentum imbalance in the transverse direction and defined as the negative vector sum of the transverse momentum of the reconstructed PF candidates in the event [83, 84]. It originates from weakly interacting neutrinos or any BSM particles that hardly leave any signals within the detector. Since W bosons, top quarks, and tau leptons may decay into neutrinos, CMS uses MET to reconstruct them. Furthermore, several BSM physics models, such as dark matter models, supersymmetric models, and models with warped extra dimensions, predict the presence of particles that might be invisible and can carry momentum. Accurate MET reconstruction is complex because it requires the precise reconstruction of all visible particles in an event. The CMS detector meets these requirements with its highly granular electromagnetic calorimeters, hermetic hadronic calorimeters, redundant muon systems, and silicon trackers in a strong magnetic field.

The next Sections provide a detailed description of the object reconstruction of photons and jet formed by b quark, which are majorly used for the physics analysis explored in this thesis.

68

4.3 Photon Reconstruction and Identification

The photon candidates are reconstructed from the energy deposition in the ECAL crystals, that are not linked with the charged tracks coming from the tracker as discussed in Sec. 4.2.

4.3.1 Photon Identification

After the reconstruction of the photons, there is always a finite probability that a photon can be faked by a jet. To distinguish a prompt photon from a fake photon CMS has developed two different methods. One is the cut-based method, where some threshold values on different shower shape and isolation variables are applied. The second one is the multivariate technique, where using the similar identification variables, BDT is trained to discriminate the prompt photons against the fake ones. For precision measurements, the latter one is more optimal. The identification variables used as input for the multivariate photon identification technique [85] can be described as follows:

- **Isolation variables** (Iso_{ph}, Iso_{ch}): These two are the isolation variables obtained by sum of the transverse momenta of the electromagnetic candidates and charged hadrons within a $\Delta R = 0.3$ isolation cone in $\eta - \phi$ plane around photon object. The isolation thresholds depend on the energy of the photon objects.

- **Shower shape variables:** Another strategy for rejecting high-electromagnetic-content jets is to take advantage of the ECAL electromagnetic shower shape. The energetic jets with photons from hadronic decay make a wider shower within ECAL in comparison to an isolated single photon. The following are two of the most relevant variables used for photon identification depending upon the geometric shower shape from prompt and background photons:

  H/E Ratio: The ratio of energy stored in the HCAL in a cone of radius $\Delta R = 0.15$ around the supercluster direction compared to the energy of the photon candidates is known as the H/E ratio. For low energy photons, HCAL contribution comes due to HCAL noise and pileup, while for high energy photons, it is due to leakage of photons through the inter-module gaps.

$\boldsymbol{\sigma_{i\eta i\eta}}$ **:** This variable gives crystals with energy deposits of at least 0.9% of $E_{5\times5}$ (the energy deposited in a 5×5 crystal matrix around the most energetic crystal) contribute to $\sigma_{i\eta i\eta}$ defined as:

$$\sigma_{i\eta i\eta} = \sqrt{\frac{\sum_i^{5\times5} \omega_i(\eta_i - \bar{\eta}_{5\times5})^2}{\sum_i^{5\times5} \omega_i}} \qquad (4.1)$$

where η_i is the pseudorapidity of the ith crystal, $\bar{\eta}_{5\times5}$ is mean pseudorapidity of crystal matrix, and ω_i is weight factor defined as $\max(0, 4.7 + ln(E_i/E_{5\times5}))$, and is nonzero if $ln(E_i/E_{5\times5}) > -4.7$, which corresponds to the $E_i > 0.9\%$ of the total energy of 5×5 cluster. This ensures that only the crystals above a noise thresholds are included in this variables. The distributions of $\sigma_{i\eta i\eta}$ of a prompt photon or electrons are narrow compared to the fake photons coming from jets.

- $\boldsymbol{R_9}$**:** The sum of the energy deposition of the 3×3 crystals centered on the most energetic seed crystal in the supercluster divided by the total energy deposition on that supercluster. The shape of R_9 distribution for the unconverted photons has high value close to unity whereas photons that convert before reaching ECAL have a lower R_9 value.

A BDT is trained using very loose selections on photon identification variables with the median energy per unit area (ρ), η and uncorrected energy of photon supercluster as input. A comparison of the performance between cut-based identification and BDT identification for photons is shown in Fig. 4.4 which clearly shows for a fix background misidentification rate, MVA-based photon identification performs better. The clustering algorithms allow to achieve reconstruction of about 95% of photon energy deposits.

4.3.2 Photon Energy Regression

Due to shower leakage, detector gaps, and dead crystals, the ECAL is not suitable for collecting all of the energy deposited by photons. The noise causes systematic varia-tions in measured ECAL energy and reduce photon energy resolution. A multivariate technique-based correction is used to minimize the impact of these losses. The target of this regression is the ratio between particle-level and reconstructed level photon energy,
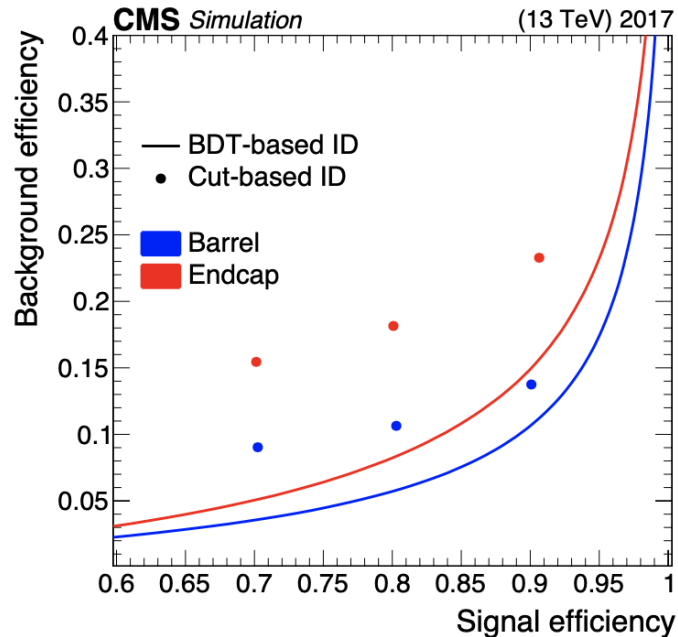
Figure 4.4: Performance of the photon identification based on cut-based and MVA based approach. The three points for the cut-based method refer to the three different working points: loose, medium, and tight [85].

and its output correction factors are applied to reconstructed energy of data and simulated events to obtain the best estimate of the true energy.

There remains a slight variation in energy scales and resolutions for data and simulation after applying the energy regression, which is fixed by scaling and smearing correction factors. The studies are performed using simulated $Z \to e^+e^-$ events. For photons, only ECAL reconstructed information of the events is used.

The photon energy scales are adjusted by changing the scale observed in simulated events to match the data scale. The results of fitting the invariant mass m_{ee} distributions in different eta regions, obtained from data and simulated events separately, are compared to derive a scale offset. This method extracts corrections to both the energy resolution in the simulation and the scale for the data in bins of $|\eta|$ and R_9 in the second stage. It fixes the residual discrepancy between data and simulation in m_{ee} distributions by applying an energy Gaussian spreading function to simulated events.

Depending on the pseudorapidity region and energy loss in the detector material, the ultimate energy resolution after all corrections (regression and scale corrections) ranges

from 2 to 5%. The performance of the regression is shown in Fig. 4.5 for barrel and endcaps.
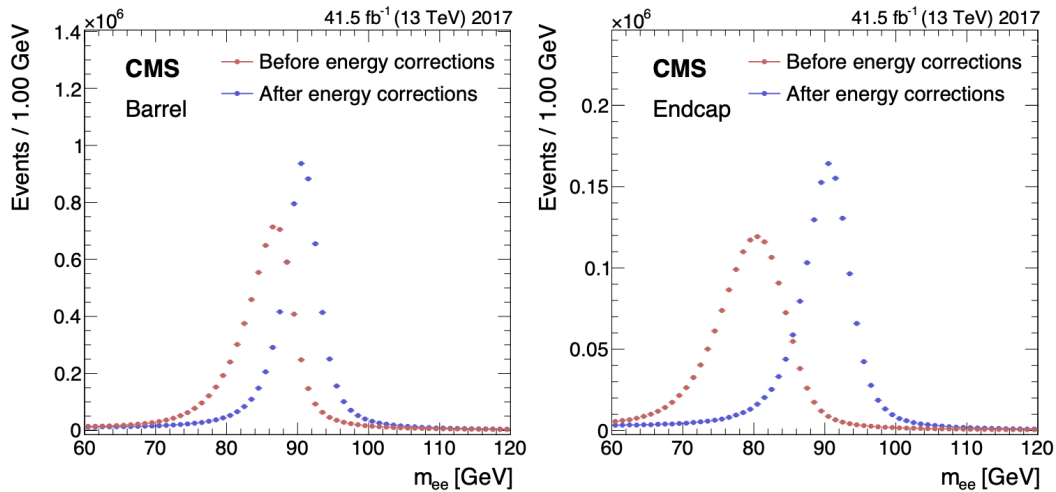
Figure 4.5: Reconstructed $Z \rightarrow e^+ e^-$ invariant mass distribution before and after the energy regression correction for the barrel (left) and endcap (right). [85].

4.4 Jet Reconstruction

In CMS, jets are reconstructed using a sequential recombination algorithm known as anti-k_T [86]. The algorithm is designed to be safe against infrared and collinear singularities, i.e. insensitive to soft and collinear gluon emission, and collinear gluon splitting. The jets are reconstructed by clustering their constituents together using various algorithms that follows collinear and infrared safety principles [87]. A final state parton from hard-scattering and hadrons can have multiple collinear splitting or soft emissions which create infrared collinear (IRC) divergences. In theory, these divergences get cancel out with one order loop correction. But this cancellation does not happen within jet algorithm. If algorithm is not IRC safe, it will result in unrealistic infinite cross-section. Also, jet defined by any algorithm should be invariant of choice of algorithm. Particle-flow candidates are sequentially recombined following the procedure described below. A distance d_{ij} between entities (i.e. particles or combinations of particles) i and j is introduced together with a distance d_{iB} between entity i and the beam. These two quantities are defined, respectively, as:

72

$$d_{ij} = \min(\mathrm{p}_{\mathrm{T}i}^{-2}, \mathrm{p}_{\mathrm{T}j}^{-2})\frac{\Delta R_{ij}^2}{R^2},$$

$$d_{iB} = \mathrm{p}_{\mathrm{T}i}^{-2},$$

$$(4.2)$$

where $\Delta R_{ij}^2 = (\Delta y_{ij})^2 + (\Delta \phi_{ij})^2$, and p_{Ti} is the transverse momentum of entity i. The distance parameter R controls the size of the jet and can be chosen arbitrarily. The quantities d_{ij} and d_{iB} are calculated for all possible combinations of entities in the event. If the smallest d_{ij} is smaller than the smallest d_{iB}, entities i and j are combined to form a new entity. Otherwise, entity i is removed and called a jet. The procedure is iterated until no particles are left. The jet momentum is then defined as the vectorial sum of the momenta of all particles in the jet.

The algorithm allows clustering of the hard particles. The algorithm involves a combination of energy and angle in its distance measure. The achievement of anti-k_T is that it gives circular-shaped jets without using a cone-based jet algorithm. The anti-k_T algorithm is widely used to define a set of collimated particles as a PF jet. The spread area of the jet is given in terms of jet distance parameter R. The value of R can be different for different collision energies. For the boosted scenario where hadrons get produced at very high energy, it is hard to separate the particles from two different hadronic jets. Therefore, the bunches of particles are merged and reconstructed using a large R in the algorithm. They are called fat or large-area jets.

CMS generally uses AK4 PF jets, i.e., anti-k_T jets clustered with distance parameter R = 0.4. For large-area jets, the value of R is taken 0.8, and they are called AK8 PF jets. Despite the excellent functionality of the jet clustering algorithm, we get discrepancies between the energy of partons and the reconstructed energy of jets due to the efficiency and acceptance of the detector. That is why jet energy corrections (JEC) and jet energy resolution correction (JER) are applied on the reconstructed jets including uncertainty associated with them. In order to mitigate the effect of pileup interactions, charged particles associated to pileup vertices are removed prior to the jet clustering. This procedure is knows as charged hadron subtraction [88]. The energy of the jets is calibrated using a factorized approach where subsequent corrections that account for different effects are applied.

There are two types of PF Jets used in CMS analyses. For PF CHS (Charged Hadron Subtraction) jets, charged particles from non-primary vertices (pileup) are removed before clustering. Another one is PF PUPPI (Pile-Up Per Particle Identification) jets which use the PUPPI [89] algorithm. Apart from PF jets and PF MET, Calo jets/MET and TRK jets/met is also used for various studies. Calo objects are reconstructed using the energies in calorimeter towers, and their direction and TRK objects are reconstructed using hits information from the inner tracker.

For LHC studies, pileup is a big challenge. PUPPI [89] is one of the new ideas proposed for pileup mitigation. The algorithm uses global information (like PV) of an event and local information (like tracks) at particle level to identify pileup. Within this algorithm, a weight is calculated, using this global and local information, for each particle in the event. It is calculated by a shape parameter α, which distinguishes parton shower-like radiation from pileup-like radiation for every particle in the event. Apart from the shape parameter, p_T also helps for pileup mitigation as p_T distribution for pileup falls much faster. The tracking information also helps to differentiate between charged tracks that originate from the primary vertex (PV) and the charged tracks that originate from the pileup. The PF algorithm can be used to relate these tracks to particles. Using PF, particles can be sorted into three class: charged hadrons from PV, charged hadrons from pileup and neutral hadrons from both pileup and PV. For all neutral particles, the algorithm assumes them to be originated from PV and assign weights depending upon their p_T. As a result, it gives low weights to soft pileup contributions, which lowers the event's neutral pileup contribution. Hence, PUPPI even works for the region where tracking is not available.

The PUPPI weights are further used to rescale the four momenta of the particles. Ideally, this weight is one for particles from hard scattering, and zero for pileup originated particles. However, in the real picture, the weights can be in fractional form, depending upon the particles' properties. Particles with a very small weight are discarded. Using PUPPI weighted particles, one can perform jet clustering without any other treatment for pileup. This algorithm has proven very efficient to correct jet p_T , jet mass and missing transverse energy in a high pileup collision conditions.

4.4.1 Jet Energy Corrections (JEC)

The jet energy corrections (JEC) are used to calibrate the energy of the jet and correct the value as much as possible to match the corresponding particle-level jets. In-time pileup from charged particles can be subtracted in regions where tracking is available, by removing tracks compatible with a pileup vertex. This procedure keeps only the tracks associated to the primary vertex and tracks which can't be associated to any vertex. The corrected jets are now called charged hadron subtracted (CHS) PF jets and this step is limited only upto $|\eta| < 2.5$ due to the tracker acceptance.

Even after the CHS correction, a significant contribution from the pileup remains in the jets. The first step of it is called L1 Pileup correction to remove the energy coming from the pileup particles clustered inside the jet. The pileup offset correction is determined from the simulation of a QCD dijet event sample with and without the pileup contribution, parameterized as a function of jet p_T and η of the jet, the energy density (ρ) of the event and jet area. The residual difference between the data and the MC is corrected using a random cone method applied in zero bias data, which is collected by the CMS experiment without using any external trigger. In the random cone method, many jets are reconstructed by clustering particles in randomly placed cone, the average energy of these jets are mostly due to the detector response and the pileup effects. An uncertainty of 5% on the jet response is applied based on data-simulation comparison in the random cone method.

The second step is called L2L3 MC-truth corrections, which are obtained from the simulation as a function of the p_T and η of the jet, by comparing the average energy of the reconstructed jet with a geometrically matched particle-level jet energy. The correction factors are then applied on the jets both in the simulation and the data. After application of the simulation-based L2L3 correction factors, the residual differences between the data and the simulation is accounted for in terms of jet energy scale (JES). JES is determined in two steps. If the jets are in the central region of $|\eta| < 1.3$, the JES is determined from the photon+jet and $Z(\to e^+e^-/\mu^+\mu^-)$+jet events where p_T of the photons and the Z boson can be well measured. The JES in the forward regions are obtained from a QCD dijet event where two jets are expected to be balanced by each other and the leading jet is required to be in the central region. The JES is estimated for the forward jet with

respect to the well calibrated central jet. The residual discrepancy of JES between data and simulation is appeared as data-to-simulation correction factor.

4.4.2   Jet Energy Resolution (JER)

The jet energy resolution (JER) is derived using the principle of p_T balance in dijet, photon+jet and Z+jet events, where the jet energy response has been derived with respect to a reference object i.e. central jet, photon and Z boson, respectively. For each jet, the response in a given p_T and η range is modelled with a double-sided Crystal Ball function (DSCB); the width of the DSCB gives the measurement of JER. The JER in data is found to be worse than in simulation. To match the JER in simulation with data, a correction factor is added to the resolution. The data-to-simulation correction factors are extracted using data-based methods and are used to smear the simulated jet resolution. These correction factors are derived for a jet in different η regions and shown in Fig. 4.6.
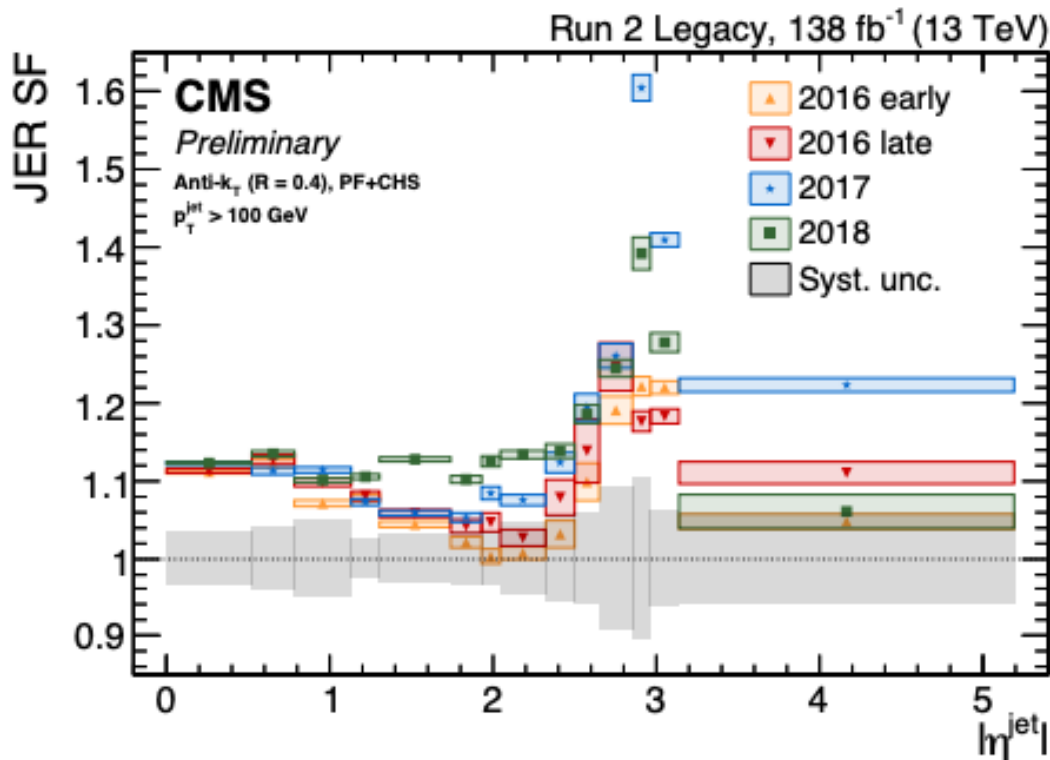
Figure 4.6: JER scale factor as a function of absolute value of pseudorapidity ($|\eta|$) [90].

76

4.4.3   Jet b tagging

As the name reflects, b tagging aims to identify a heavy quark jet from a light flavour jet. Identification of the origin of jets is critical for studying and characterizing different channels, such as top quark/Higgs boson events and a variety of new physics scenarios. The long lifetime, high mass, and hard fragmentation function of b quarks and the existence of soft leptons from semileptonic b hadron decays are used to develop CMS b tagging algorithms.

Semileptonic decays of b hadrons give rise to b jets that contain a muon. A cascade decay of $b \rightarrow c \rightarrow l$ also gives muon in the final state. Since the CMS muon systems identify the origin of a muons with high efficiency and resolution, this information helps to tag the b jets. Due to long lifetime, b hadron travels some distance until it decays at a point called the secondary vertex (SV) shown in Fig. 4.7. With the high resolution of the CMS tracking system, it is possible to reconstruct the SV. The distance between the PV and the SV is called the flight distance. In the SV vertex finding process, the tracks associated with PV are not considered.
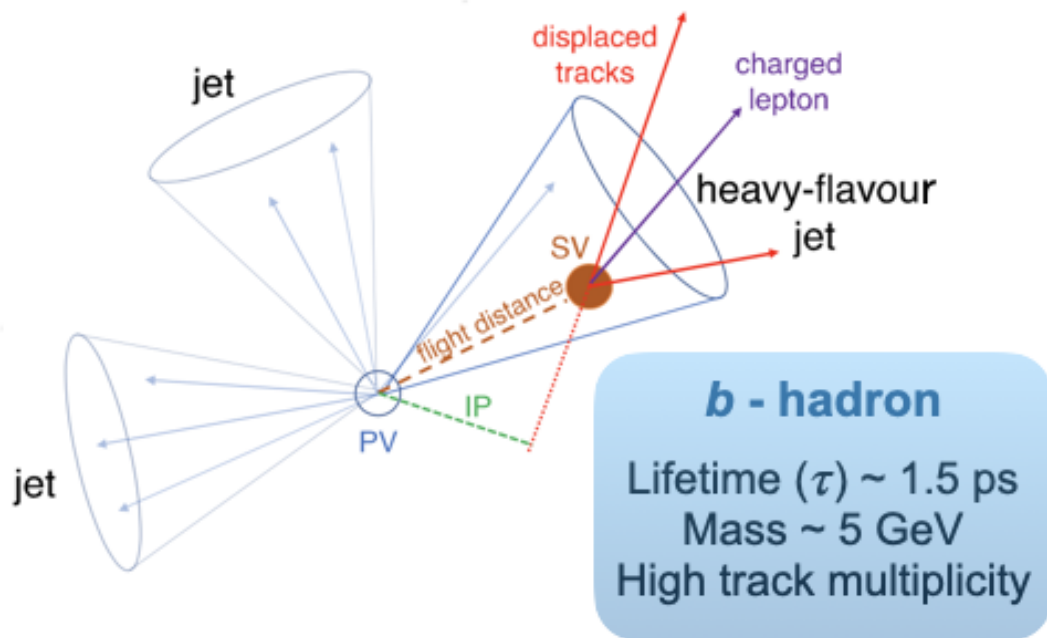
Figure 4.7: An illustration of b-hadron decay and corresponding impact parameter (IP) [91].

The distance of closest approach of a track to the primary vertex is known as the impact parameter (IP) given in Fig. 4.7. IP's sign is positive/negative if the track passes closest to

its associated jet direction down/upstream of the PV. It is calculated in three-dimensions, which benefits from a good x-y-z resolution from the pixel detector. Due to the long lifetime, the IP from b jets is mostly positive, while for light jets, the impact parameter remains symmetric around zero. A tight selection on impact parameter helps to reject the tracks associated with the background process.

The important variables for b tagging algorithms are the IP significance of the tracks, the position of the secondary vertex and transverse momentum of muon with respect to jet direction. CMS used jet-probability (JP) (uses impact parameter significance of the tracks) and combined secondary vertex (CSVv2) (combines the information of displaced tracks with the information of secondary vertices associated with the jet using a multi-variate technique) taggers during Run-1 [92]. For Run-2, the new versions of the b tagging algorithms known as DEEPCSV and DEEPJET have been developed using deep neural network (DNN) [93] training.

DEEPCSV and DEEPJET: DEEPCSV uses input tracks and secondary vertex information similar to JP and CSVv2 taggers including track-variables for up to six tracks, p_T, η information of jets to learn the correlation between jet kinematics and other input variables. The DNN training is performed using jets with p_T up to 1 TeV and within the tracker acceptance. A mixture of $t\bar{t}$ and multijet events is used so that the training could learn about heavy flavour and light flavour jets and discriminate them. The neural network uses four hidden layers that are fully connected. A normalized exponential function is used to activate the nodes in the last layer so that the output value can be interpreted as a likelihood/probability P(f) for a specific jet flavour category. There are five such categories known as jet having one b hadron P(b), at least two b hadrons P(bb), one c hadron without any b hadron P(c), at least two c hadrons without any b-hadron P(cc) and without any b/c hadron P(udsg). A b discriminator P(b)+P(bb) is combined to tag b jets in physics analyses. The performance of DEEPCSV improves with the 2017 and 2018 data-taking years.

Apart from DEEPCSV, CMS has developed one more DNN-based b tagger DEEPJET [94], which uses a large number (approximately 650) of jet variables as input. The inputs used here contain the information about all PF candidates clustered inside the jet and they can be classified into four different types:

1. The global variables related to the jet level information: jet 4-momentum, number of constituent particles, primary and secondary vertices,

2. Charge particle information: charged track p_T, η, 2D and 3D impact parameters etc.,

3. Neutral hadron information,

4. The variables related to the secondary vertex: tracks associated with SV, etc.

It is a multiclass discriminator which can differentiate b, c, uds and gluon jets by utilizing the same set of input variables used in DEEPCSV which results in better performance for 2016, 2017 and 2018 data-taking years. Unlike DEEPCSV, it has seven output categories. Four are similar to DEEPCSV and the rest of the three P(lepb), P(g) and P(uds) discriminate against b jet having lepton or jet originating from gluon or light quark. The difference between both DNN-based b taggers is explained in Tab. 4.1 and performance curves are shown in Fig. 4.8.

	DEEPCSV	DEEPJET
Input	Information about displaced tracks and SV	Particle flow candidates
Additional feature	Use more charge particle tracks	Use soft lepton information
	—	Discriminate uds jets from gluon jets
	—	Recovers degradation at high momentum
	Performance degrades for phase-0 pixel configuration (2016)	Similar performance for phase-0 and phase-1 pixel configurations
Category	5 P(b/bb/c/cc/udsg)	7 P(b/bb/c/cc/uds/g/lepb)
***b*-discriminator**	P(b + bb)	P(b + bb + lepb)

Table 4.1: Difference between DEEPCSV and DEEPJET.

Within an analysis, we can use either a selection on b discriminant or full shape of b discriminant. The selection is applied depending upon the Loose, Medium or Tight working point corresponding to 10%, 1% or 0.1% misidentification probability. While using
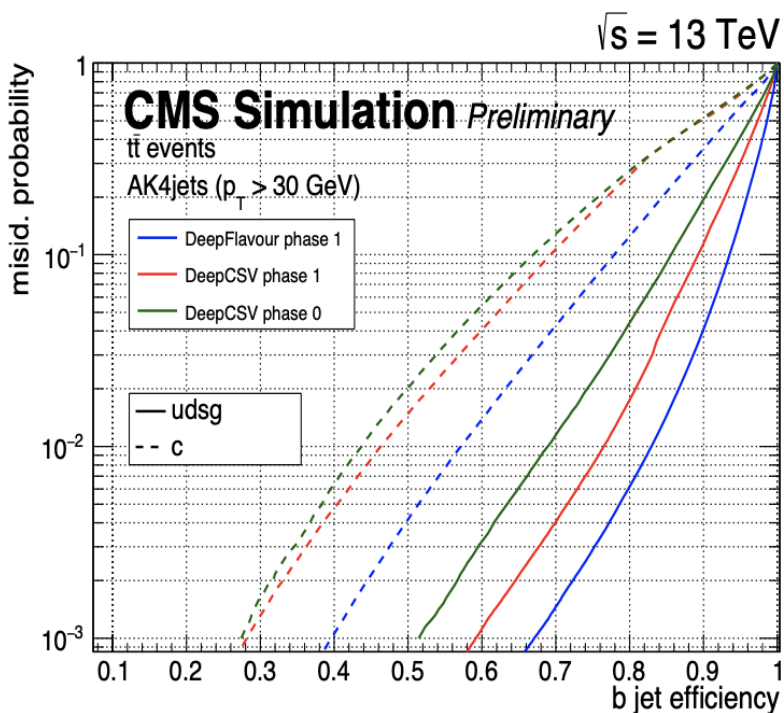
Figure 4.8: DeepCSV and DeepJet performance curves for AK4 jets [95].

b tagging algorithms, we need to consider how differently the algorithms behave for jets reconstructed in simulations and data. For this purpose, CMS provides the scale factors (SF) to

(a) correct separately for the final yield of jets tagged as heavy or light flavour (working point based calibration), or

(b) correct for the whole shape of the discriminator (shape calibration or reshaping), if the analysis needs it (for example, as an input to MVA training).

The SFs of a jet depends on its flavour, p_T and η (and jet discriminator value for reshaping). Depending upon the properties of the jet, SFs are calculated and applied to simulations to minimize discrepancy with data. In my work, DeepJet was used in the $HH \to b\bar{b}\gamma\gamma$ analysis and for resolved jets in the $HHH \to 6b$ analysis, whereas DeepCSV was used in the VHbb analysis.

4.4.4 Boosted Higgs boson jet tagging

In Chapter 6, BSM triple-Higgs boson searches are solely explored in the boosted regime. Therefore, understanding of the boosted Higgs jet identification is essential. As the SM predicts the highest branching ratio for $b\bar{b}$ as the final state for Higgs boson decay, boosted $H \to b\bar{b}$ tagging might be crucial for new physics searches. The approach of tagging a b jet in a boosted regime is different from general AK4 b jet tagging. In boosted regime, jet mass is the first jets' property that distinguishes signal jet from background one. The jet mass of the signal should peak around resonance mass (Higgs boson in our case). However, this happens only in an ideal picture. In reality, the jet mass distribution gets worse, and its peak gets shifted due to soft emissions, pileup and underlying events. For $H \to b\bar{b}$ decay, QCD multi-jet processes (mainly gluon splitting in $b\bar{b}$) are dominant backgrounds. The background jets acquire mass through showering, which grows as a function of transverse momentum. Boosted hadronic objects keep a different energy pattern than QCD jets of comparable invariant mass. This is a motivation to go beyond jet mass and exploit jet substructure [96]. It removes soft radiation contamination and identifies and selects features related to hard decay.

The main idea of H boson tagging is to reconstruct a large-area jet with jet substructure (grooming and tagging) algorithms that remove soft contribution and try to understand the subjet structure and shape of the jet, which discriminate signal jets from background jets. At this stage, selected jet is called the Higgs jet. In the end, using boosted b tagging algorithms, subjets are identified as b jets, and the Higgs jet is identified as a jet with two b-hadrons. Let's understand all these steps one by one.

- **Jet grooming:** When a boosted large-area jet originates from a Higgs boson, its mass should peak near Higgs boson mass. Jet grooming removes background contamination and related component from the jet mass calculation. Soft drop declustering is one of the grooming technique. It suppresses wide-angle soft radiation from a jet in order to mitigate the effects of contamination from initial state radiation, underlying event, and multiple hadron scattering (pileup).

  Starting from AK8 reclustered jet with radius R_0, it does declustering of the last

step and drop the soft contributions with following condition:

$$\text{softdrop condition} = \frac{min(p_{T1}, p_{T2})}{p_{T1} + p_{T2}} > z_{cut} \left(\frac{\Delta R_{12}}{R_0}\right)^{\beta} \tag{4.3}$$

where, p_{Ti} is transverse momenta of constituents, ΔR_{12} is distance in $\eta - \phi$ plane, z_{cut} is the soft drop threshold, and β is angular exponent. The efficiency and performance of grooming depends on z_{cut} and β ($\beta \to \infty$ for ungroomed jet). For $\beta < 0$, it works as tagger vetoing jets that do not have two well-separated hard prongs. While for $\beta > 0$, it works as groomer changing the constituents of a jet. This technique is IRC safe and removes all soft contributions. CMS uses this technique with β set to 0 as the standard choice for jet grooming.

- **Jet shapes:** QCD jets have a fundamentally different pattern of energy deposits in the detector when compared to a boosted Higgs jet. To identify an N sub-jet structure within a jet, we define a variable called the N-subjettiness τ_N [97] as:

$$\tau_N = \frac{1}{d_0} \sum_k p_{\mathrm{T}}^k min\{\Delta R_{1,k}, \Delta R_{2,k}, ..., \Delta R_{N,k}\} \tag{4.4}$$

$$d_0 = \sum_k p_{\mathrm{T}}^k R_0. \tag{4.5}$$

Here, k runs over the constituent particles in a given jet, p_{T}^k are their transverse momenta, $\Delta R_{J,k}$ is the distance in the $\eta - \phi$ plane between a candidate subjet-J and a constituent particle k and R_0 is the jet radius. For $\tau_N \approx 0$, all the radiation is along the candidate subjet, and the jet has N (or fewer) subjets. For $\tau_N \gg 0$, a large fraction of the jet energy is scattered away from the candidate subjet, which implies the jet has at least N+1 subjets. τ_2 is expected to be small for Higgs jets. However, QCD jets can randomly have small values of τ_2 too, and to increase the discrimination power, $\tau_{21} = \tau_2/\tau_1$ is used as an identifier for Higgs jets. Smaller the value of τ_{21}, more likely it is that the jet is a Higgs jet.

- **boosted b tagging:** For boosted jets, b tagging can be applied either on the AK8 jet or its subjets. Double-b tagger algorithm includes the probability of each subjet being a b jet. This is achieved by applying the DeepJet b-tagging algorithm, which returns the probability of the subjet having come from a b quark, $b\bar{b}$ pair, leptonic

2543 b decay, c quark, light-flavour quark, or gluon. These probabilities along with the

2544   soft-drop mass of the subjet are also included in classification of the large-area jet.

2545   In order to classify a hadronically decaying particle through a single large-area jet,

2546   the DeepAK8 [98] algorithm defines five main categories: W, Z, H, t, and other. The

2547   algorithm's goal is multi-classification of jets by exploiting particle-level information

2548   directly. The DeepAK8 algorithm uses a large number of variables, both low- and

2549   high-level, but not all variables are treated in the same way. The architecture of

2550   the algorithm consists of two steps: In the first step, the input variables are split in

2551   two lists and processed separately with two classifiers. In the second step, the two

2552   previous outputs are combined through a third classifier.

2553   An alternative DeepAK8 algorithm, DeepAK8-MD, has been developed to be largely

2554   decorrelated from the mass of jets while providing an efficiency similar to that of

2555   the mass-correlated version. The ROC curves in Fig. 4.9 show the performances of

2556   double-b, DeepAK8 and DeepAK8-MD on the same simulated dataset.
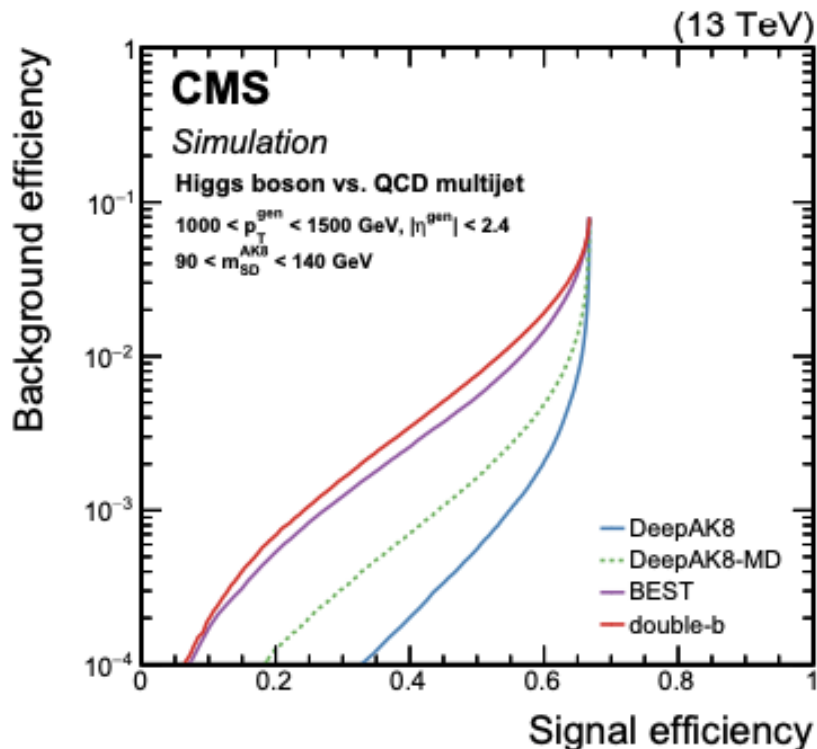
Figure 4.9: Performance comparison in terms of ROC curves on the Higgs boson taggers [98].

2557   The ParticleNet algorithm [99] is a Dynamic Graph Convolutional Neural Network

2558   (DGCNN) trained to classify jets according to their flavour type. Compared to the

83

previous state-of-the-art jet tagging algorithms, like DeepAK8 tagger, ParticleNet relies on a highly sophisticated jet representation and network architecture. The ParticleNet algorithm treats a jet as an unordered set (permutation-invariant) of its constituents ("particle cloud"). This technique provides a natural representation of the jet, unlike other algorithms that treat jets as images or particles ordered by their p_T. The graph network architecture allows the algorithm to efficiently explore the correlations between the various jet constituents. Particle-flow candidates and secondary vertices within the jet cone are used as inputs to the algorithm.

The ParticleNet algorithm has two versions:

 - the "nominal" version is designed for maximum performance but may introduce sculpting in the mass spectrum of the background jets,

 - the "mass decorrelated" (MD) version which is designed to be largely decorrelated with respect to the mass of a jet, at the cost of slight degradation in the discrimination power.

The tagger assigns a set of output classifier scores for each jet, corresponding to the probability of the jet originating from a resonance that decays into a pair of quarks ($X \rightarrow b\bar{b}$, $X \rightarrow c\bar{c}$, $X \rightarrow q\bar{q}$, i.e., X decaying to light quarks), or non-resonant quark-and-gluon jet (QCD_{bb}, QCD_b, QCD_{cc}, QCD_c and QCD_{others}). To focus on the discrimination power between $X \rightarrow b\bar{b}$ and QCD jets, the $b\bar{b}$-tagging discriminant T_{Xbb} that we use for this analysis is defined to be:

$$T_{Xbb} = \frac{S}{S + B} = \frac{P_{Xbb}}{P_{Xbb} + P_{QCD}} \qquad (4.6)$$

In this work, ParticleNet tagger is used to tag boosted Higgs jets for triple-Higgs production searches and DeepAK8 tagger was used in the VHbb boosted region.

Chapter 5

Search for Non-resonant Higgs Pair Production in $b\bar{b}\gamma\gamma$ Final State

5.1 Introduction

With the increasingly large dataset of proton-proton collisions events delivered at the LHC, rare physics processes become experimentally accessible.

This chapter presents the search for the non-resonant production of Higgs boson pairs in the $b\bar{b}\gamma\gamma$ final state. The work exploits the data collected by the CMS detector in proton-proton collisions with a center-of-mass energy of 13 TeV, for data collected during Run2 (2016-2018) with a total integrated luminosity of 137 fb^{-1}. The analysis targets the main HH production modes: the gluon-gluon fusion (ggF HH) production mode and the vector boson fusion mode (VBF HH) as described in Section 2.4. Both modes are analyzed following similar strategies. After reducing the nonresonant $\gamma\gamma b\bar{b}$ background and the background coming from single Higgs boson production in association with a top quark-antiquark pair ($t\bar{t}H$), the events are categorized into ggF HH and VBF HH enriched signal regions using a multivariate technique. The signal is extracted from a fit to the invariant masses of the Higgs boson candidates in the $b\bar{b}$ and $\gamma\gamma$ final states. An orthogonality in the event selection criteria for the two processes has been maintained properly between the ggF HH and VBF HH analysis and described in the following sections whenever needed.

The $b\bar{b}\gamma\gamma$ final state has a combined branching ratio of $2.63\pm0.06\times10^{-3}$ [29] for $m_H = 125$ GeV, which can be derived from the individual branching ratio of the $H \to b\bar{b}$ and $H \to \gamma\gamma$ decay, $2 \times Br(H \to b\bar{b}) \times Br(H \to \gamma\gamma) = 2 \times 0.58 \times 0.00223$. This channel is one of the most sensitive to HH production because of the large SM branching fraction of $H \to b\bar{b}$, the good mass resolution of the $H \to \gamma\gamma$ candidate, and relatively low background rates.

5.2 Search Strategy

For signal events, the distributions of the invariant mass of diphoton $M(\gamma\gamma)$ and dijet $M(jj)$ peak around the mass of the Higgs boson (125 GeV). Photon energy, and consequently $M(\gamma\gamma)$, can be reconstructed with high precision thanks to the CMS electromagnetic calorimeter, while worse resolution (roughly one order of magnitude worse) is expected for $M(jj)$.

The analysis strategy is therefore based on extracting the number of signal and background events using a parametric fit to the invariant mass of the diphoton system $M(\gamma\gamma)$, fitting simultaneously $M(jj)$. In addition, 1D-analysis strategy was implemented : using a parametric fit to the invariant mass of the diphoton system $M(\gamma\gamma)$ and using the $M(jj)$ information in the multivariate discriminant used to separate signal or background. Both strategies were studied, finally the 2D simultaneous fit to $M(\gamma\gamma)$ and $M(jj)$ was chosen as the analysis strategy due to its better sensitivity.

For $M(\gamma\gamma)$ and $M(jj)$ different distributions are expected for two types of backgrounds:

- For the non-resonant background, mainly $\gamma\gamma$+jets and γ+jets and top events, $M(\gamma\gamma)$, and $M(jj)$ have a falling spectrum. This is a dominant background after the preselection is applied.

- For resonant background (SM Single Higgs production), $M(\gamma\gamma)$ is peaking at the Higgs mass, since the two photons are the decay products of the Higgs boson. Among the different production modes for SM single Higgs production, the two most relevant for this analysis are gluon-gluon fusion (ggH) and associated production with top quarks ($t\bar{t}H$), where the Higgs bosons decaying into a pair of photons. For

ggH production, additional jets originate from gluon splitting into a pair of b-quarks and additional light jets from radiation mistagged as b-jets. For $t\bar{t}H$ production, the two b-jets originate directly from the decay of the top pair. The $M(jj)$ distribution for resonant backgrounds is a falling spectrum. Even if the background rejection, in this case, is high, the cross-section of the process is several orders of magnitude larger than the signal one, causing a non-negligible contribution of this background.

The distribution of $M(\gamma\gamma)$ and $M(jj)$ for simulated signal and background events can be seen in Fig. 5.1, where all contributions are normalized to a unit area.
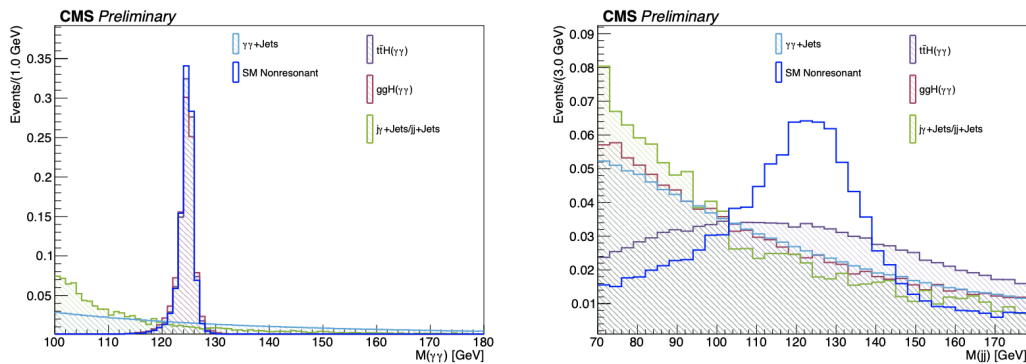
Figure 5.1: The distribution of $M(\gamma\gamma)$ (left) and $M(jj)$ (right) for signal and background events. All contributions are normalized to a unitary area.

To improve the sensitivity of the search, MVA techniques are used to distinguish the ggF and VBF HH signal from the dominant nonresonant background. The output of the MVA classifiers is then used to define mutually exclusive analysis categories targeting VBF and ggF HH production. The HH signal is extracted from a fit to the invariant masses of the two Higgs boson candidates in the $(M(\gamma\gamma), M(jj))$ plane simultaneously in all categories.

The $H \to b\bar{b}$ and $H \to \gamma\gamma$ candidates can be used to reconstruct the double Higgs system (HH). In this analysis, the following variable is used as a proxy to a 4-body mass:

$$\widetilde{M}_x = M(jj\gamma\gamma) - M(jj) - M(\gamma\gamma) + 2m_H \tag{5.1}$$

where $m_H = 125$ GeV is the mass of the Higgs boson and $M(jj\gamma\gamma)$ is the invariant mass of the two Higgs boson candidates, is particularly sensitive to different values of the Higgs couplings. This definition of $\widetilde{M}_x$ is less dependent on the dijet and diphoton

energy resolution than $M(jj\gamma\gamma)$ under the assumption that the dijet and diphoton pairs originates from a Higgs boson [100].

The distribution of $\widetilde{M_x}$ for SM and some representative BSM benchmark points is shown in Fig.5.2 (left). It can be seen that different values of the couplings can introduce large variations in the shape of the four-body mass. Fig. 5.2 (right) shows the $\widetilde{M_x}$ distribution for the individual background components and the SM signal.
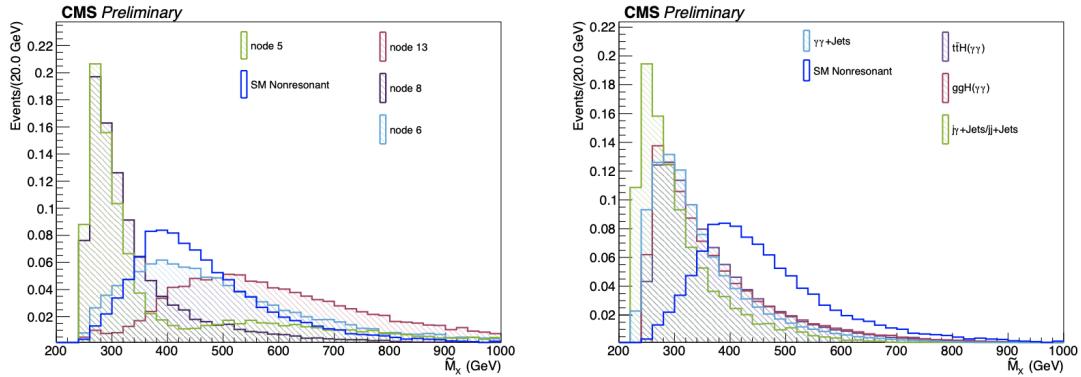
Figure 5.2: (left) Distribution of $\widetilde{M_x}$ for some benchmark signal datasets, and for the resonant and non-resonant backgrounds. (right) Distribution of $\widetilde{M_x}$ for SM-like HH production and for the different background components. All contributions are normalized to a unit area.

As can be seen from the distributions, a lower cut on this variable would noticeably reduce the background contribution without losing efficiency on the SM sample; on the other hand, for some benchmarks points, this would result in a considerable loss in the efficiency. Instead of having a single cut, this variable is therefore used to categorize events, with the goal of maximizing the sensitivity to all considered signal hypotheses: SM and BSM.

The analysis will follow the flowchart shown in Fig. 5.3

5.3   Data Samples and Simulated Events

5.3.1   Trigger Requirements

At the L1 trigger level, the events are selected requiring one or two electromagnetic (e/γ) candidates. In case of a single (e/γ) candidate, the minimum p_T is required to be
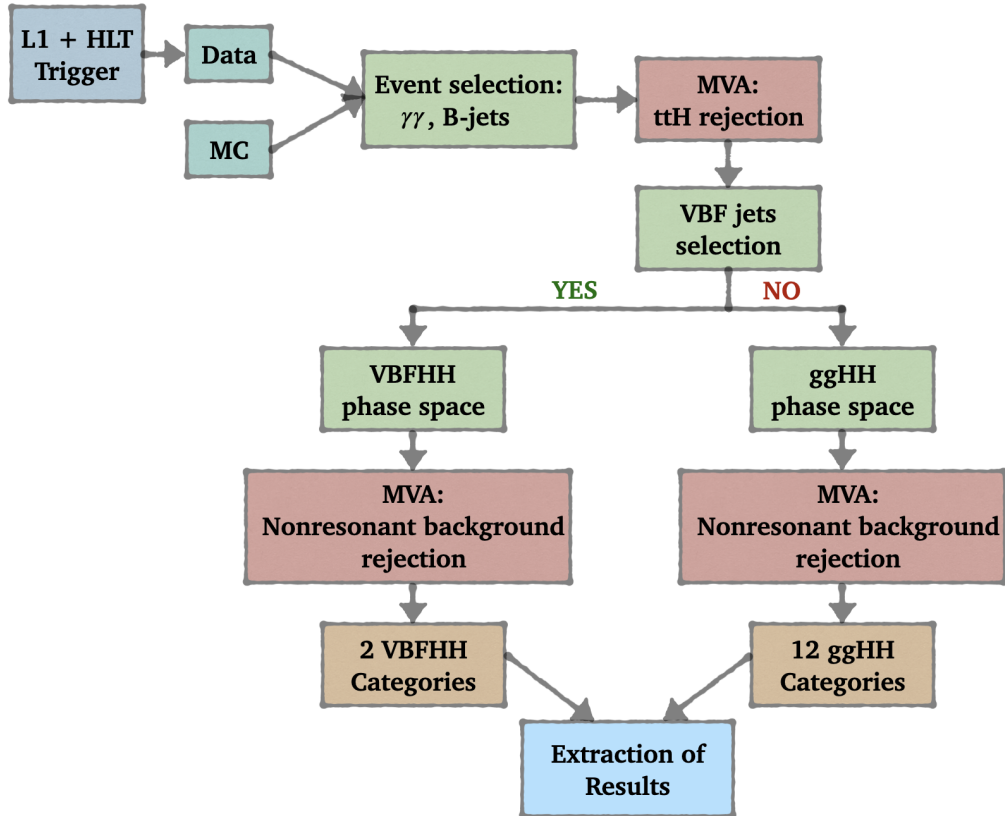
Figure 5.3: Scheme of the analysis workflow.

40 GeV (30-32 GeV in case of an isolated candidate) to maintain the trigger rate at a sustainable level. For the events with a double (e/γ) candidate, the p_T thresholds for the leading(subleading) candidates are set to 23(10) GeV in the 2016 data-taking period. In the following years(2017-2018), featuring a higher luminosity, the p_T thresholds are raised to 25(14) GeV to limit the trigger rate.

Relying on a refined reconstruction of the events, the HLT trigger requirements are tighter than the L1 trigger. Furthermore, the inclusion of the tracker information allows the separation of diphoton from dielectron candidates in dedicated trigger paths. In the HLT diphoton trigger, used for this analysis, the p_T variable is required to be higher than 30(18) GeV for the leading(subleading) photon in 2016, and than 30(22) GeV in 2017 and 2018.

In order to reduce the contamination from misidentified jet, additional selections are applied on the Hadronic over electromagnetic energy ratio (H/E ratio), on the photons isolation, and on the photons shower shapes. For good quality of photons the value of H/E is expected to be small. R_9 is the sum of the energy deposition of the 3×3 crystals

centered on the most energetic seed crystal in the supercluster divided by the total energy deposition on that supercluster.

The efficiency of the trigger selections is estimated from the data and then used to scale the MC simulations which do not include the trigger effects. In particular, a Tag and Probe (T&P) method with $Z \to e^+e^-$ events is used [101]. The "probe" electron is treated as a photon candidate, i.e., ignoring the track information. The efficiency is estimated in intervals of p_T, η and R_9. The different kinematics of the $Z \to e^+e^-$ and $H \to \gamma\gamma$ events, and the different interaction of electrons and photons with the material upstream the ECAL, resulting in a different shower shape, are properly taken into account. A rescaling of the "probe" electrons weights in intervals of η and R_9, denser than the ones considered to compute the efficiencies, is performed to match the corresponding distributions of the $H \to \gamma\gamma$ photons. The scale factors are derived from MC simulations and are shown in Fig. 5.4. The main effect of the scale factors consists in a shift of the R_9 distribution to values close to unity. The shifting is more pronounced in the region $1 < |\eta| < 1.5$ where the upstream material (beampipe, tracker and support structures) is maximum.
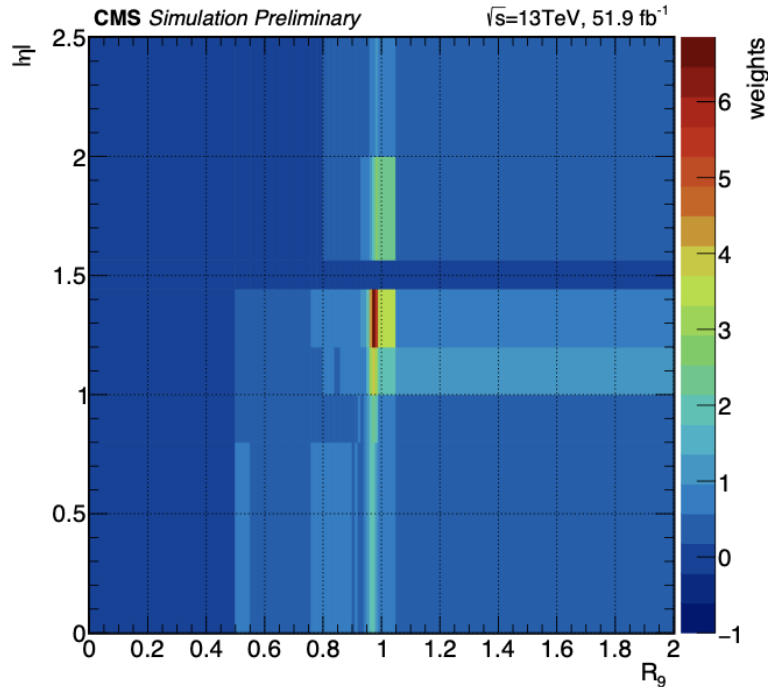
Figure 5.4: Re-weighting factors in (R_9, η) for $Z \to e^+e^-$ selected events with respect to $H \to \gamma\gamma$ events.

The HLT efficiencies have been derived for both leading and subleading photons with

respect to different p_T, R_9 regions separately in two η regions ECAL barrel (EB) and ECAL endcap (EE) directly from data. The efficiencies for 2018 leading and subleading photons are shown in Fig. 5.5.
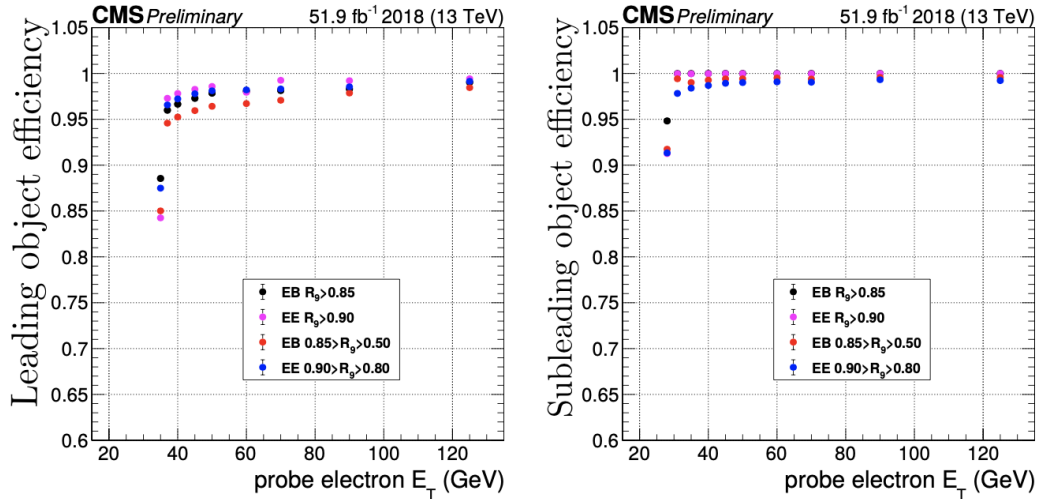
Figure 5.5: Diphoton trigger efficiency measured on 2018 data for $Z \rightarrow e^+ e^-$ events using tag-and-probe method.

5.3.2 Simulated Samples

The sample are simulated using the MADGRAPH5 generator for LO accuracy in QCD, and MADGRAPH5 AMCNLO [102] or POWHEG BOX2 [73] generators for up to NLO accuracy in QCD. The generators are interfaced with PYTHYA8 [76] that performs the parton showering and the hadronization. The PYTHIA tuning CUETP8M1 and CP5 [103, 104] is used for the underlying events modeling of 2016 and 2017-2018 samples, respectively. The PDFs are taken from the NNPDF3.0 [105] (2016) and NNPDF3.1 [106] (2017 and 2018) sets. The particles interaction with the detector and the subsequent readout is simulated using the Geant4 package [77].

Higgs Boson Production Samples

The ggF HH samples are generated using POWHEG BOX2 at the NLO accuracy in QCD and including the full top quark mass dependence [107]. The VBF HH samples are generated using MADGRAPH5 AMCNLO at the LO accuracy. While the two extra light

quark jets at LO cause the VBF HH event topology to diverge from ggF HH, at NNLO the extra gluon radiations cause ggF HH to imitate the VBF HH signals, and nearly 30% of ggF HH events migrate to VBF HH selection.

The SM ggF HH and VBF HH samples are generated along with BSM samples with anomalous (κ_λ, κ_t, c_V, c_{2V}) coupling values, as shown in Tab. 5.1.

Mechanism	Coupling values	Cross section (fb) (including k-factor)
ggF HH(SM)	$\kappa_\lambda = 1$, $\kappa_t = 1$	$3.105\cdot10^1$
ggF HH	$\kappa_\lambda = 0$, $\kappa_t = 1$	$6.973\cdot10^1$
ggF HH	$\kappa_\lambda = 2.45$, $\kappa_t = 1$	$1.312\cdot10^1$
VBF HH(SM)	$\kappa_\lambda = 1$, $c_V = 0$, $c_{2V} = 0$	$1.73\cdot10^0$
VBF HH	$\kappa_\lambda = 1$, $c_V = 1$, $c_{2V} = 2$	$1.42\cdot10^1$
VBF HH	$\kappa_\lambda = 2$, $c_V = 1$, $c_{2V} = 2$	$1.42\cdot10^0$
VBF HH	$\kappa_\lambda = 0$, $c_V = 1$, $c_{2V} = 1$	$4.61\cdot10^0$
VBF HH	$\kappa_\lambda = 1$, $c_V = 1.5$, $c_{2V} = 1$	$6.60\cdot10^1$
VBF HH	$\kappa_\lambda = 1$, $c_V = 1$, $c_{2V} = 0$	$2.71\cdot10^1$

Table 5.1: List of the simulated ggF HH and VBF HH BSM samples for anomalous coupling values. The same setup of the corresponding SM sample is used for the simulation.

In addition, ggF HH samples are generated at LO for the BSM benchmarks described in Section 2.5.4 using MADGRAPH5 AMC@NLO. The twelve BSM benchmarks are added together to increase the statistical precision, and then reweighed to any coupling configuration (κ_λ, κ_t, c_V, c_{2V}) using the generator-level information.

We apply a global k-factor to the generated ggF HH and VBF HH signal samples to scale the cross section to NNLO and next-to-NNLO accuracy respectively. The k-factor is obtained for the cross section prediction in the SM and applied to all considered scenarios. The k-factor for the ggF HH cross section depends on the invariant mass of the two Higgs bosons, however, within the region of sensitivity of this analysis, this effect is covered by the total scale uncertainty.

Background Samples

The dominant backgrounds in this search are irreducible prompt diphoton production ($\gamma\gamma$+jets) and the reducible background from γ+jets events, where the jets are misidentified as isolated photons and b jets. Although these backgrounds are estimated using data-driven methods, simulated samples are used for the training of multivariate discriminants and the optimization of the analysis categories. Single Higgs boson production, where the Higgs boson decays to a pair of photons, is considered as a resonant background. These production processes are simulated at NLO in QCD precision. The cross sections and decay branching fractions are taken from ref. [29]. The contribution from the other single H decay modes is negligible.

The list of the samples used is shown in Tab. 5.2 and 5.3. Further selections are applied at the generator level to enrich the sample with signal-like events. In particular, for the γ+jets at least one jet is required to have a high fraction of electromagnetic energy to mimic a e/γ object.

Mechanism	Generator	Cross section (fb) (including k-factor)
ggH	POWHEG BOX2	$4.41 \cdot 10^4$
qqH	POWHEG BOX2	$3.78 \cdot 10^3$
VH	MADGRAPH5 AMCNLO	$2.25 \cdot 10^3$
tHq	POWHEG BOX2	$7.4 \cdot 10^2$
$b\bar{b}$H	MADGRAPH5 AMCNLO	$5.3 \cdot 10^2$
$t\bar{t}$H	MADGRAPH5 AMCNLO	$5.1 \cdot 10^2$

Table 5.2: List of the simulated SM Higgs boson production samples.

Mechanism	Generator	Cross section(pb)
$\gamma\gamma$+jets ($m_{\gamma\gamma} > 80$ GeV)	Sherpa	88.36
$\gamma\gamma$+jets ($m_{\gamma\gamma} > 80$ GeV, 1 b-jet)	Sherpa	0.8185
$\gamma\gamma$+jets ($m_{\gamma\gamma} > 80$ GeV, 2 b-jets)	Sherpa	0.4874
γ+jets ($m_{\gamma\gamma} > 80$ GeV, $p_T^\gamma > 40$ GeV, EM-enriched)	Sherpa	874.2

Table 5.3: List of the simulated background samples.

5.4   Event Selection

5.4.1   Photon Reconstruction

Photon candidates are reconstructed as part of the global event reconstruction with particle flow as described in Sec. 4.3, using the algorithms provided centrally from the CMS E/gamma group. A preselection is applied. This loose selection requires cuts on shower shapes, kinematics and isolation variables slightly tighter than the trigger ones to improve Data/MC comparison. A multivariate identification method, based on photon shower-shape and kinematic variables, is used to separate the signal from background photons. A very loose cut on photon ID is also applied. Tab. 5.4 summarizes the preselection cuts. Scale factors are used to cover Data/MC discrepancies related to the identification criteria.

Requirements	Leading Photon	Subleading Photon
P_T	30 GeV	20 GeV
$|\eta|$	$|\eta| < 1.44$ or $1.55 < |\eta| < 2.5$	
Shower shape and Isolation	$R_9 > 0.8$ or $Iso_{ch} < 20$ GeV or $Iso_{ch}/p_T < 0.3$	
Identification	H/E < 0.08 and MVA ID > -0.9	

Table 5.4: Caption

5.4.2   Jet Reconstruction

Jets are reconstructed using the anti-kt algorithm with a distance parameter $R = 0.4$. The jet candidates in the event, after passing the ID requirements (Loose ID : 2016, Tight ID : 2017 and 2018 - both ID correspond to efficiency $> 99\%$), must have $p_T > 25$ GeV, $|\eta| < 2.4$ (2.5) for 2016 (2017-2018), so that they are within the tracker of CMS and can be tagged as coming from b quarks. The jets must also be outside the photon cone with a $\Delta R(j, \gamma) > 0.4$.

94

DeepJet b-Tagger

Within CMS, a deep neural network (DNN) classifier (DeepJet [91]) is used. The algorithm exploits the distance between the production and the decay position of the b-hadrons, of the order of 1 mm, resulting in a secondary vertex resolvable from the primary interaction vertex. The algorithm exploits also the fact that the b hadron decay can produce leptons (and undetected neutrinos) with high p_T. Finally, because of the high bottom quark mass, the b-jet have a wider $\eta - \phi$ extension than a light flavor jet. The DeepJet score is used for the b-jets candidates selection and as input for the MVA classifiers.

5.4.3 Energy Regression for b-Jets

Level 1: DNN b-jet Energy Regression

A b-jet energy regression is developed to improve b-jets resolution and, therefore, the invariant mass of the two jets coming from the $H \rightarrow b\bar{b}$ decay. The energy correction, for each jet, is computed through a regression-based on a deep neural network, trained on jet properties and jet composition information. The b-jet energy correction and b-jet resolution estimator are output simultaneously by the neural network (NN). This allows to correct the measured jet p_T and to use the resolution estimator to improve the analysis sensitivity, as described later. This regression was developed for the CMS Collaboration [108] and is analysis independent. The b-jet energy regression improves single jet energy resolution by about 15%, and dijet invariant mass resolution by about 20-25% depending on the phase-space. The regression technique was validated on data for the CMS $H \rightarrow b\bar{b}$ discovery.

Level 2: m_{jj} Oriented Energy Regression for b-j=Jets

A regression to improve the mass resolution of the reconstructed $M_{H \rightarrow b\bar{b}}$ was developed (Level 2 or L2 regression). The approach is to improve the resolution beyond what was achieved using the b jet p_T regression (Level 1 or L1 regression), which used as inputs jet-related variables. However, the $M_{H \rightarrow b\bar{b}}$ resolution can be further improved by using event

variables, particularly the missing transverse energy E_T^{miss} and the kinematic variables of the reconstructed physics objects.

The comparison of the mass resolution in this analysis, obtained including L2 and L1 regression, to mass resolutions without these corrections are shown in Fig. 5.6. The L1 regression affects both the resolution (σ) and the position of the peak (μ), while the L2 leaves the latter unchanged. The L1 regression moves the m_{jj} peak position by 5.5 GeV (5%) closer to the expected Higgs mass. Overall the b-jet energy corrections improve the m_{jj} resolution of about 25%.
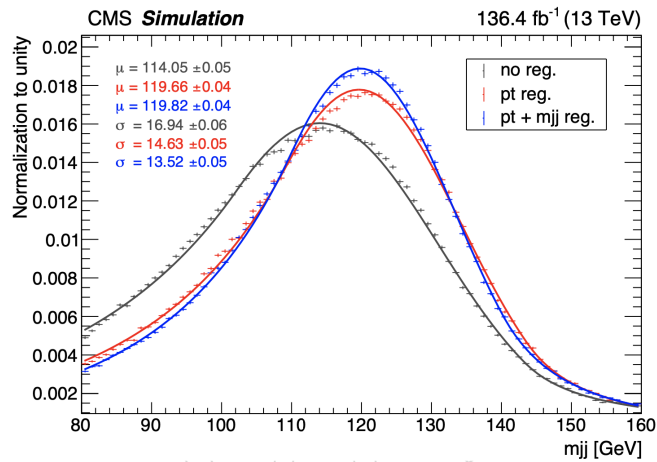
Figure 5.6: Mass resolution in this analysis for SM ggF HH samples merging all years weighted by the luminosity: without regression (grey), with L1 regression (red), and with L1+L2 regression (blue).

Validation of $M_{H\to b\bar{b}}$ Regression

To validate the L2 regression on $HH \to \gamma\gamma b\bar{b}$, similar $ZZ \to l^+l^- b\bar{b}$ was considered. where l is e or μ leptons. ZZ events were obtained by applying the following selection criteria. The samples were obtained using the framework of the $VH \to b\bar{b}$ analysis.

- Trigger in the e^+e^- channel: `HLT_Ele23_Ele12_CaloIdL_TrackIdL_IsoVL_DZ`

- Triggers in the $\mu^+\mu^-$ channel: `HLT_Mu17_TrkIsoVVL_Mu8_TrkIsoVVL`
  `HLT_Mu17_TrkIsoVVL_TkMu8_TrkIsoVVL`
  `HLT_Mu17_TrkIsoVVL_Mu8_TrkIsoVVL_DZ`
  `HLT_Mu17_TrkIsoVVL_Mu8_TrkIsoVVL_DZ`

₂₈₀₀ • Lepton $p_T > 25$ GeV and $|\eta| < 2.5$

₂₈₀₁ • $85 < \mathrm{M}(e^+e^-) \leq 97$ GeV

₂₈₀₂ • $p_T(ll) > 50$ GeV

₂₈₀₃ • Jet $p_T > 25$ GeV and $|\eta| < 2.5$

₂₈₀₄ • Primary jet with DeepCSV score > 0.4941 (medium) and secondary jet with
₂₈₀₅   DeepCSV score > 0.1522 (loose) working points.
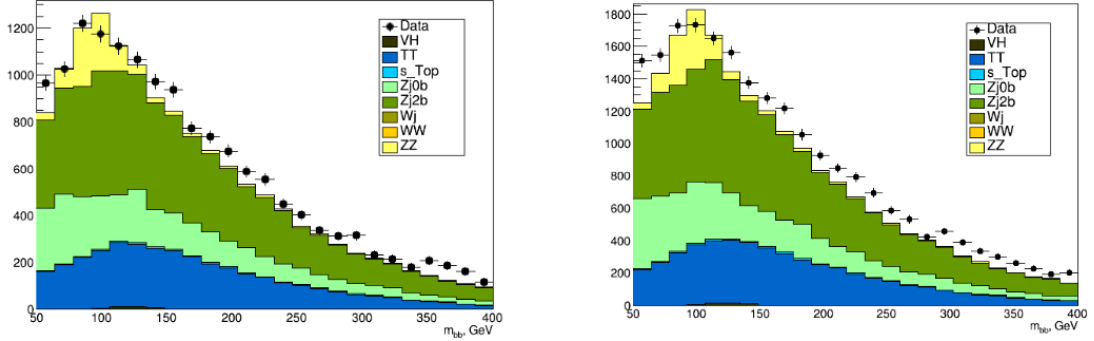
Figure 5.7: The m_{jj} distributions in the data, the ZZ signal, and the DY and $t\bar{t}$+jets backgrounds before BDT selection for the e^+e^- (left) and the $\mu^+\mu^-$ (right) channels.

₂₈₀₆ The m_{jj} distributions after these selections are shown in Fig. . DY with b jets and $t\bar{t}$+jets
₂₈₀₇ make up the majority of events. The signal ZZ also has a sizeable component. The S/B
₂₈₀₈ ratio (the S here being ZZ) is 0.21. To improve this, a BDT was trained to reject the DY
₂₈₀₉ and tt+jets background. The following variables were used:

$$-\Delta\eta(j,j),\ \Delta\eta(l,l),\ \Delta\eta(jj,ll),$$
$$-m_{jj}/p_T(jj),\ m_{ll}/p_T(ll),$$
$$-p_T(l_1)/m_{ll},\ p_T(l_2)/m_{ll},\ p_T(j_1)/m_{jj},\ p_T(j_2)/m_{jj},$$
$$-\text{b-}jet_1\text{ DeepCSV},\ \text{b-}jet_2\text{ DeepCSV},$$
$$-\Delta R(j,j),$$
$$-p_T\text{-sum of all jets}$$
$$-m_{ll}$$

97

The signal and background efficiencies as a function of the BDT score, the ROC curve, and the overtraining checks are shown in Fig. 5.8. Based on the ROC curve, one working points is explored: BDT > 0.2 corresponding to a signal efficiency of about 60% and background efficiency of about 20%. The m_{jj} distribution after this cut is shown in Fig. 5.9. The S/B ratio after BDT cut is 0.35 for e^+e^- channel and 0.30 for the $\mu^+\mu^-$ channel.
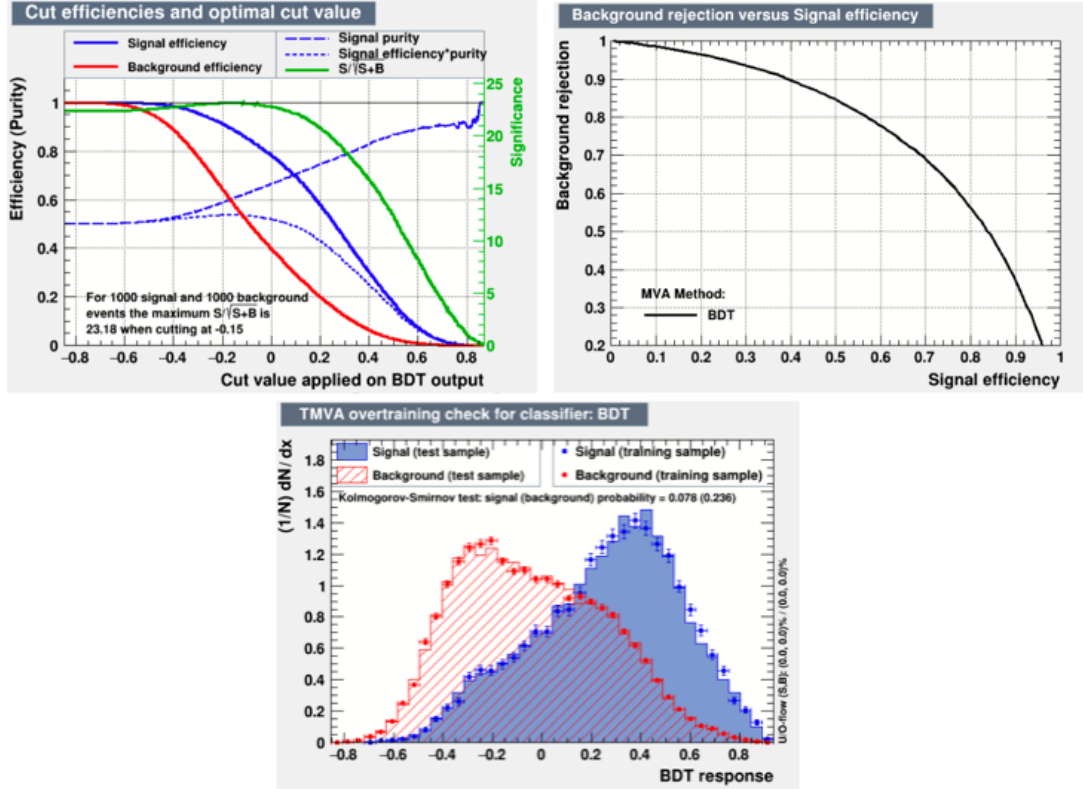
Figure 5.8: The signal and background efficiencies as a function of the BDT score (upper left), ROC curve (upper right) and the overtraining check (lower).
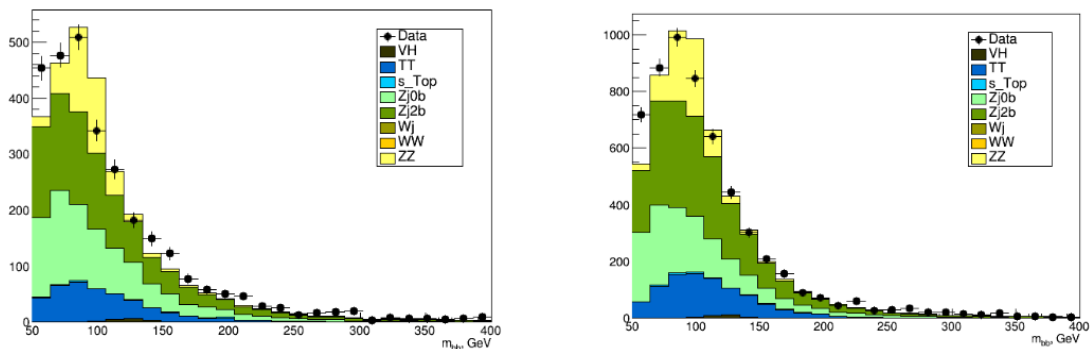
Figure 5.9: The m_{jj} distributions in the data, the ZZ signal, and the DY and $t\bar{t}$+jets backgrounds with BDT > 0.2 selection for the e^+e^- (left) and the $\mu^+\mu^-$ (right) channels.

The validation is performed, looking at the p_T balance properties. For jets, the invariant mass of the dijet system can be connected to the transverse momentum of the dijet system.

98

Therefore a regression that improves m_{jj} resolution also improves to some extent the momentum balance in the event, that may be distorted due to the presence of neutrinos. Traditionally the RMS value of two distributions: $p_{T_{b\bar{b}}} \cdot C_{p_T}^{reg}/p_{T_{\gamma\gamma}}$ and $p_{T_{b\bar{b}}}/p_{T_{\gamma\gamma}}$, provides the confirmation of E_T^{miss} effect on the p_T balance. Here, we propose a slightly modified method of "p_T-balance" using $\frac{p_T(ll)-p_T(b\bar{b})}{p_T(ll)+p_T(b\bar{b})}$. This distribution is by construction more symmetric, and easier to used to measure the effect of the L2 regression.

In Fig. 5.10 the distribution of $\frac{p_T(ll)-p_T(b\bar{b})}{p_T(ll)+p_T(b\bar{b})}$ is shown for $E_T^{miss} > 40$ GeV and $E_T^{miss} < 40$ GeV. The improvement is studied separately for data and for MC. A visible effect in the reduction of the resolution of $\frac{p_T(ll)-p_T(b\bar{b})}{p_T(ll)+p_T(b\bar{b})}$ is observed in events with large E_T^{miss}. This improvement in data is compatible with the one observed in MC. We can conclude out of it that the L2 regression is working as expected.
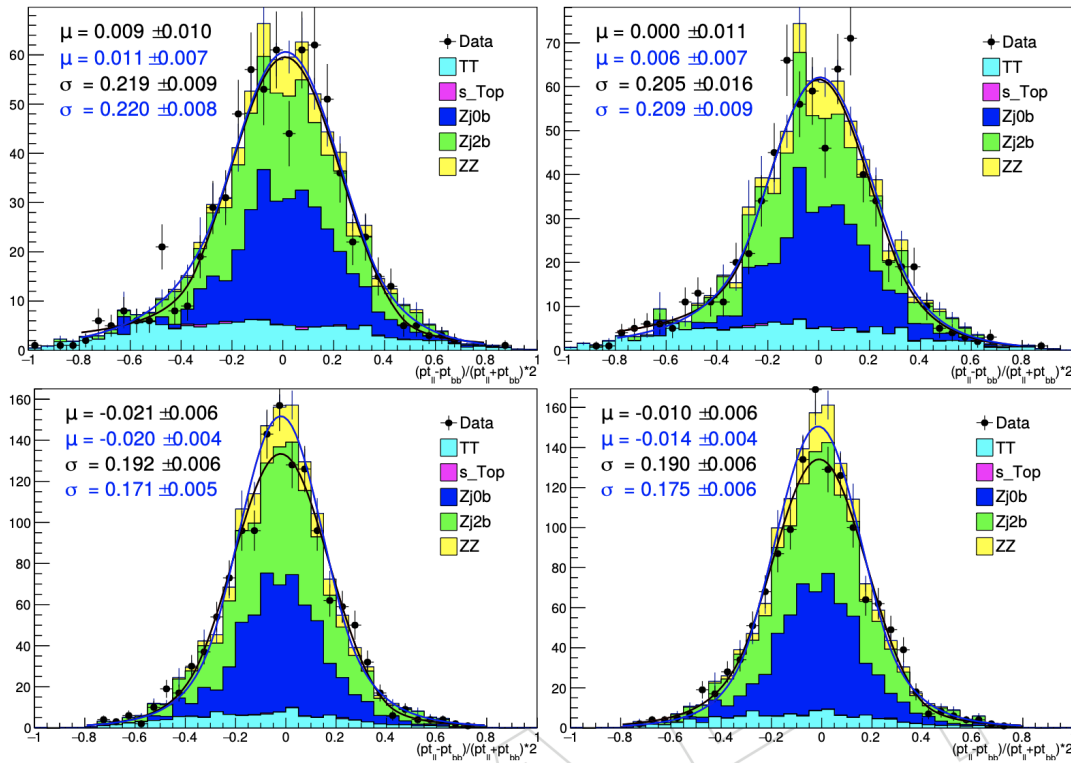
Figure 5.10: Data and MC events with a Crystal-Ball. TOP - $E_T^{miss} > 40$ (effect observed and expected), BOTTOM - $E_T^{miss} < 40$ (no effect observed and expected). Left - with L1 regression, right - with L1+L2 regression. Results for 2017 data sample.

5.4.4 Selection of the $H \to \gamma\gamma$ Candidate

The $H \to \gamma\gamma$ candidate is built using the photons passing the identification criteria described in Section 5.4.1. If more than two photons are present, the two photons with the highest p_T are selected. The leading and subleading photons are required to have $p_T^\gamma/m_{\gamma\gamma} > 1/3$ and $p_T^\gamma/m_{\gamma\gamma} > 1/4$, respectively. In addition, the diphoton invariant mass is required to be in the window 100 GeV $< m_{\gamma\gamma} < 180$ GeV. The selections on the photon $p_T^\gamma/m_{\gamma\gamma}$ ratio was proven to prevent distortions of the $m_{\gamma\gamma}$ spectrum on the low mass side with a negligible loss of efficiency on the $H \to \gamma\gamma$ signal.

5.4.5 Selection of the $H \to b\bar{b}$ Candidate

The jets passing the identification selections are also required to have $|\eta| < 2.4$ and $|\eta| < 2.5$ for 2016 and 2017-2018 datasets, respectively, and $p_T > 25$ GeV for both jets. An angular distance from the two selected photons to the jet must be at least 0.4. The two b-jets with the highest b-tag score are selected to build the $H \to b\bar{b}$ candidate in the HH categories while minimum cut on Deep Jet b-tag discriminator is > 0. Finally, the m_{jj} value is required to be in the window 70 GeV$< m_{jj} < 190$ GeV.

A summary of the preselection criteria for jets and photons can be found in Tab. 5.5.

Photons		b-jets	
Variable	Selection	Variable	Selection
$p_T^{\gamma 1}$ [GeV]	$> m_{\gamma\gamma}/3$	p_T [GeV]	> 25
$p_T^{\gamma 2}$ [GeV]	$> m_{\gamma\gamma}/4$	$\Delta R_{\gamma j}$	> 0.4
$|\eta|$	< 2.5	$|\eta|$	< 2.4
$m_{\gamma\gamma}$ [GeV]	[100,180]	$m_{b\bar{b}}$ [GeV]	[70,190]
		DeepJet Score	> 0

Table 5.5: Summary of the baseline selection criteria.

5.4.6 Requirements for the VBF HH Topology

The events with a $H \to \gamma\gamma$ and a $H \to b\bar{b}$ candidate (HH candidates) are required to have at least two additional jets passing the tight PU ID selection. The jets are required to have $p_T > 40\ (30)$ GeV for leading (subleading), $|\eta| < 4.7$, and an angular distance $\Delta R >$

2848 0.4 from each of the two selected photons and b-jets. The two jets with the highest dijet

2849 invariant mass are selected as VBF jets candidates.

5.5   Background Rejection

2851 The distribution of the $m_{\gamma\gamma}$ and m_{jj} distributions after requiring the presence of a $H \rightarrow \gamma\gamma$

2852 and a $H \rightarrow b\bar{b}$ candidate in the events are visible in Fig. 5.11. The signal appears as

2853 a peak at 125 GeV in the two distributions smeared by the experimental resolution. A

2854 continuum background mainly from $\gamma\gamma$+jets and γ+jets events dominates the HH signal

2855 region. The single Higgs production processes represent another important source of

2856 background because it is resonant in the $m_{\gamma\gamma}$ distribution as the HH signal.

2857 In order to maximize the separation of the signals from the background contaminations,

2858 specific MVA-based strategies were developed. MVA classifiers based on different archi-

2859 tectures are trained using the simulated events. The classifier outputs are used to define

2860 the signal regions and also to classify the events in exclusive categories. The MC simula-

2861 tion events are divided in two subsets. One subset of events is used for the MVA trainings,

2862 the other subset is used for the MVA outputs validation, the category optimization, and

2863 the signal modeling.
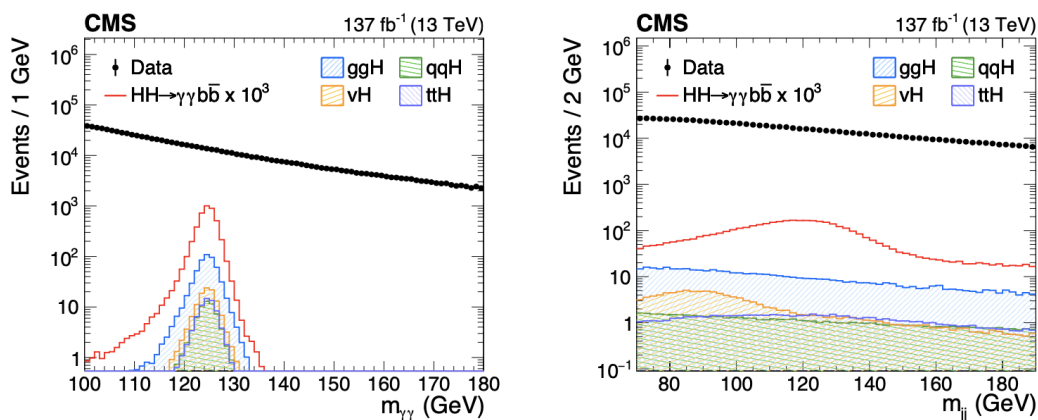
Figure 5.11: Distributions of $m_{\gamma\gamma}$ (left) and m_{jj} (right) for the selected HH candidates for data and for the simulated single and double Higgs processes.

5.5.1 $t\bar{t}H(\gamma\gamma)$ Background Rejection

With two photons resonant on m_H and two b-jets in the final state, the $t\bar{t}H(\gamma\gamma)$ process was found to be one of the main backgrounds in the most sensitive HH categories. Therefore, a specific strategy was developed to discriminate the $t\bar{t}H(\gamma\gamma)$ from the $HH \to b\bar{b}\gamma\gamma$ mechanisms. In particular, a DNN classifier is trained using the simulated $t\bar{t}H$ events as background and the combination of all the twelve simulated ggF HH benchmarks samples (including the SM) as signal. The twelve benchmarks are combined with the same weight. It was verified that this strategy improves the BSM ggF HH selection efficiency with a negligible impact on the SM ggF HH efficiency. This strategy makes also the classifier suitable to separate the $t\bar{t}H$ from the VBF HH events, not included in the training because the corresponding MC simulation became available only at an advanced stage of the analysis. The classifier exploits the angular variables related to the different topologies of the two processes as well as the presence of a W boson, decaying hadronically or leptonically, originated by the top quark decay.

The discriminant uses a combination of low-level information from the individual PF candidates and high-level features describing kinematic properties of the event. The kinematic variables used in the DNN training can be classified in three groups: angular variables, variables to distinguish semileptonic decays of W bosons produced in the top quark decay, and variables to distinguish hadronic decays of W bosons.

Angular Variables

- The minimum angular distance between one of the two selected photons and one of the two selected jets $\Delta R_{min}(\gamma, b-jet)$.

- Helicity angle: $|cos\theta_{HH}^{CS}|$. It is the Collins-Soper angle [109] between the direction of the $H \to \gamma\gamma$ candidate and the average beam direction in the HH center-of-mass frame.

- The cosine of the angle in the dijet rest-frame between the leading jet and the beam axis $|cos\theta_{jj}|$.

The distributions of these angular variables are shown in Fig. 5.12.
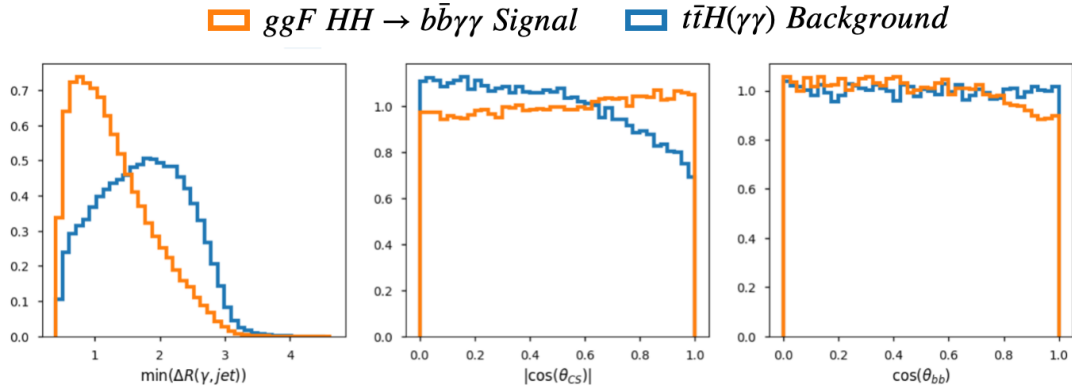
Figure 5.12: Angular variables used in the training, from left to right: $\Delta R_{min}(\gamma, b-jet)$, $|cos\theta_{HH}^{CS}|$ and $|cos\theta_{jj}|$. These variables are used for the training of the $t\bar{t}H$ discriminant.

Variables to Reject Events with a Semileptonic Decay of the W Boson

- The E_T^{miss} absolute value and its azimuthal angles with the selected b-jets $\Delta\phi(p_T^{miss}, b-jet)$.

- The pT of the leading and subleading electrons and muons of the event, if any,

Events with a leptonic decay W boson are expected to have significant MET due to the presence of neutrinos. Leptonic decay W boson event also could have leptons reconstructed in the final state. Thus the four vectors of reconstructed leptons with $p_T > 10$ GeV are also included in the training. The distributions of most of these variables are shown in Fig. 5.13.

Variables to Reject Events with a Hadronic Decay of the W Boson

- A top quark sensitive variable χ_{top}^2 defined for the events with at least two additional jets as:

$$\chi_{top}^2 = \min_{j1j2jb}\left[\left(\frac{m_W - m_{j1j2}}{0.1 \cdot m_W}\right)^2 + \left(\frac{m_t - m_{jbj1j2}}{0.1 \cdot m_t}\right)^2\right] \quad (5.2)$$

Where j1 and j2 are two among the additional jets and jb is one of the two selected b-jets. m_W and m_t are the true mass values of the W boson and the top quark, taken to be 80.3 GeV and 173.5 GeV, respectively. Among all the possible jet combinations, the one minimizing the quantity is chosen. In case of four or more additional jets, an additional χ_{top}^2 variable is built in the same way with the remaining jets.
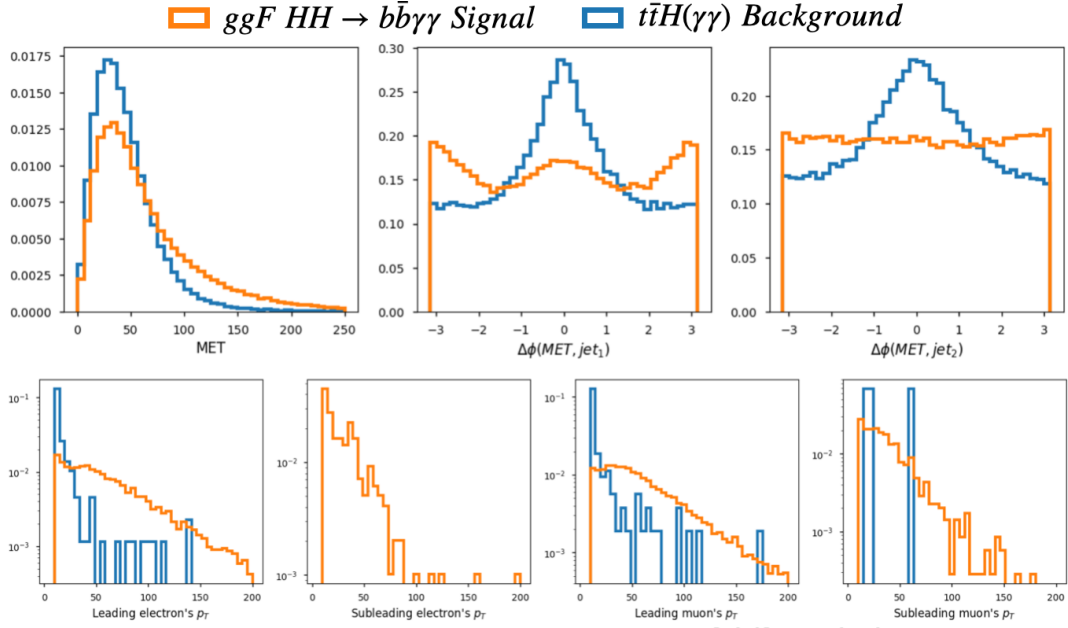
Figure 5.13: Major variables used in the training to reject events with a leptonic-decay W boson, from left to right top to bottem: E_T^{miss} , $\Delta\phi(p_T^{miss}, b-jet1)$, $\Delta\phi(p_T^{miss}, b-jet2)$ and the transverse momentum of the leading and subleading electrons and muons.

This variable is calculated for events with at least 2 additional jets and 4 additional jets besides the two b-tagged jets, and the distributions in these two cases are shown in Fig. 5.14.
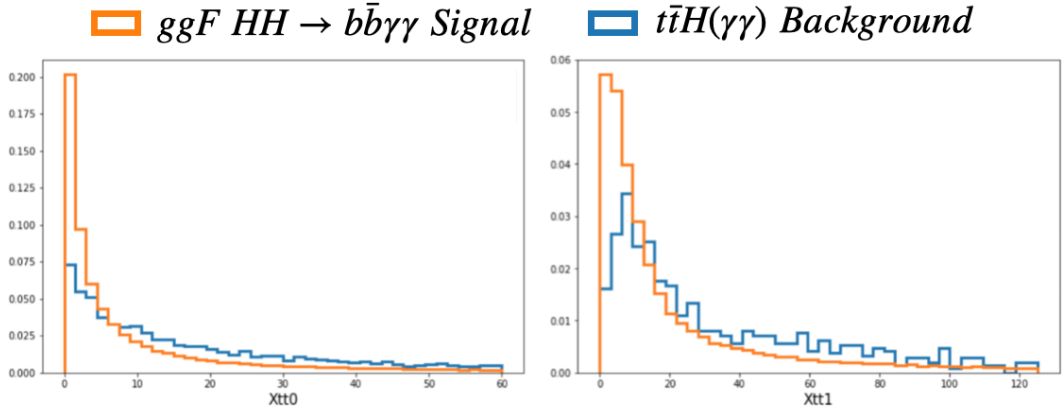
Figure 5.14: χ_{top}^2 variables in training to reject events with a hadronic decay W boson, for events with at least 2 additional jets (left plot) and 4 additional jets (right plot) besides the two b-tagged jets.

A selection on the output score of this DNN ($t\bar{t}H$-score) is applied to reject the $t\bar{t}H$ events from the HH enriched categories. The selection on the $t\bar{t}H$-score is optimized together with the ggF HH category boundaries definition, and separately with the VBF HH one, to provide the best sensitivity. The chosen working point ensures a $t\bar{t}H$ rejection of about

80% with an efficiency of about 95% on the ggF HH signal. A good performance is also achieved with respect to the VBF HH signal. In particular, after the VBF HH additional requirements presented in Section 5.4.6, the chosen working point provides a $t\bar{t}H$ rejection of about 85% with 90% efficiency on the VBF HH signal.

Validation of the Method

In order to validate the training variables for the $t\bar{t}H$ discriminant, their distributions in data and MC simulation were compared. The comparison included the preselected events with a $H \rightarrow \gamma\gamma$ and a $H \rightarrow b\bar{b}$ candidate (HH candidates) outside the diphoton invariant mass region 115 GeV$< m_{\gamma\gamma} <$ 135 GeV containing the expected signal. The distributions from simulation were found compatible with the distributions observed in data. The distribution of the $t\bar{t}H$-score for the different background sources was also studied by means of MC simulations considering for simplicity the 2016 and 2017 datasets, as shown in Fig. 5.15 (left). The peak at $t\bar{t}H$-score = 0, corresponding to $t\bar{t}H$-like events, is populated by all the $t\bar{t}$ + (X) processes, while the peak at $t\bar{t}H$-score = +1 is populated by the HH-signal and all the other backgrounds, hence dominated by the $\gamma\gamma$+jets events. Considering the full Run 2 dataset, the $t\bar{t}H$-score distributions for the selected data events, and for the ggF HH and single Higgs simulated events, are found compatible as shown in Fig. 5.15.
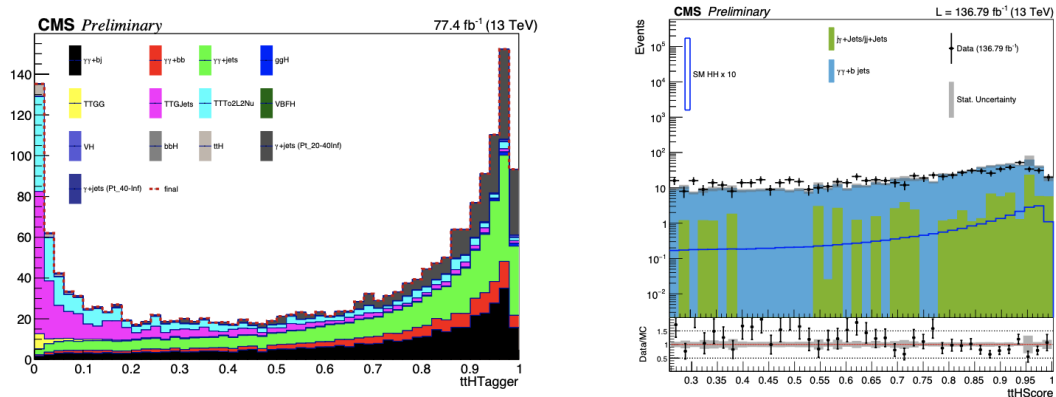
Figure 5.15: *Left*: $t\bar{t}H$-score distribution for all the main background components from the MC simulations of the 2016 and 2017 events. *Right*: Comparison between data and MC simulation of the $t\bar{t}H$-score distribution for the HH candidates with $t\bar{t}H$-score > 0.26.

5.5.2 Non-resonant Background Rejection

Background Reduction in the ggF HH Signal Region

The dominating background for the ggF HH signal region consists in the $\gamma(\gamma)$+jets processes. The optimal background rejection is achieved through an MVA approach using a BDT classifier trained using MC simulated events. The variables optimized for this training exploit the HH system kinematic, the identification variables to reject background processes with jets misidentified as photons or b-jets, and the resolution variables to account for the resonant nature of the signal. In particular, the variables chosen are:

- The $H \to \gamma\gamma$ and $H \to b\bar{b}$ candidates kinematics described by $p_T^\gamma/m_{\gamma\gamma}$ for each of the two selected photons, and p_T^j/m_{jj} for each of the two selected jets;

- The transverse balance of the HH system consisting in $p_T^{\gamma\gamma}/m_{\gamma\gamma jj}$ and $p_T^{jj}/m_{\gamma\gamma jj}$ where $p_T^{\gamma\gamma}$ and p_T^{jj} are the diphoton and dijet transverse momentum respectively, and $m_{\gamma\gamma jj}$ is the four-objects invariant mass;

- The $|cos\theta_{HH}^{CS}|$ and $|cos\theta_{jj}|$ helicity angles as defined for the $t\bar{t}H$ discriminant, and in addition, the cosine of the angle in the diphoton rest-frame between the leading photon and the beam axis $|cos\theta_{\gamma\gamma}|$;

- The angular separation of the objects, i.e., $\Delta R_{min}(\gamma, b-jet)$ as defined for $t\bar{t}H$ discriminant, and additionally, the ΔR between the other selected photon and jet;

- The b-tag score provided by the DeepJet algorithm for the two selected jets;

- The photon ID output for the two selected photons;

- The energy resolution for the two selected photons, and the diphoton energy resolution estimated by the photon energy regression algorithm;

- The energy resolution for the two selected jets, and the dijet energy resolution estimated by the b-jet energy regression algorithms;

- The global event energy density ρ to account for the different pileup conditions.

106

The distributions of some of the most discriminating variables for data and simulated events are shown in Fig. 5.16. As for the $t\bar{t}H$ discriminant, this BDT is trained using a combination of the twelve ggF HH BSM benchmarks samples as signal, and the $\gamma(\gamma)$+jets as background. Each event used for the training is weighed by the inverse of the estimated diphoton and dijet energy resolutions because the events with good resolutions are expected to provide the highest sensitivity to the HH signal.

In order to prevent for any sculpting of the $m_{\gamma\gamma}$ and m_{jj} distributions, the p_T^{γ} and p_T^{j} variables are provided as input for the BDT training scaled by $m_{\gamma\gamma}$ and m_{jj}, respectively. This is fundamental for a correct estimation of the signal and background. The training is performed separately for the three years of data taking because the different detector conditions have modified the variables distributions and correlations. This strategy offsets the differences across the years, providing very similar BDTs output distributions for the three years, both for signal and backgrounds. Therefore, it is possible to merge the three distributions and then uniformly optimize the BDT selections. The distributions of the BDT output for signal and background are very well separated. In order to avoid problems of numerical precision when defining optimal signal-enriched regions, the BDT output is transformed such that the signal distribution is uniform. This transformation is applied to all events, both in simulation and data. The distribution of the MVA output for data and simulated events is shown in Fig. 5.17.
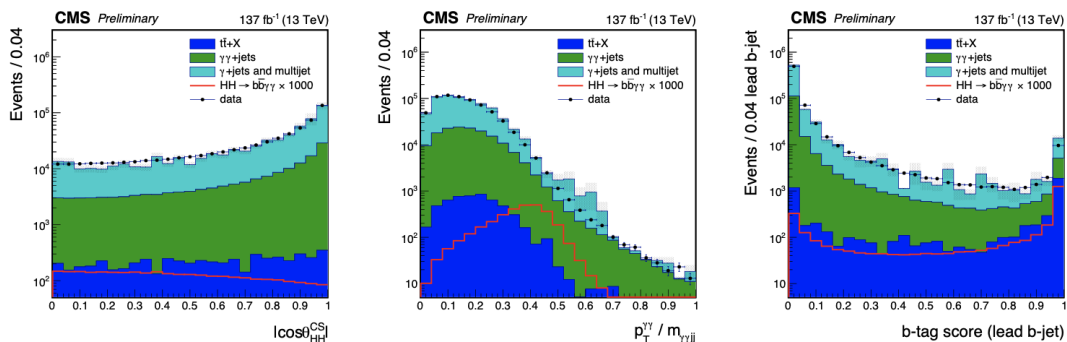
Figure 5.16: Distribution of $|cos\theta_{HH}^{CS}|$ (left), $p_T^{\gamma\gamma}/m_{\gamma\gamma jj}$ (center), and the b-tag score for the leading jet (right) of the selected HH candidates for the data as well as the simulated $t\bar{t}$+X, $\gamma\gamma$+jets, γ+jets, and multijet events excluding the signal region $120 < m_{\gamma\gamma} < 130$ GeV. The distribution of the simulated $HH \rightarrow b\bar{b}\gamma\gamma$ events is also shown with a red line.
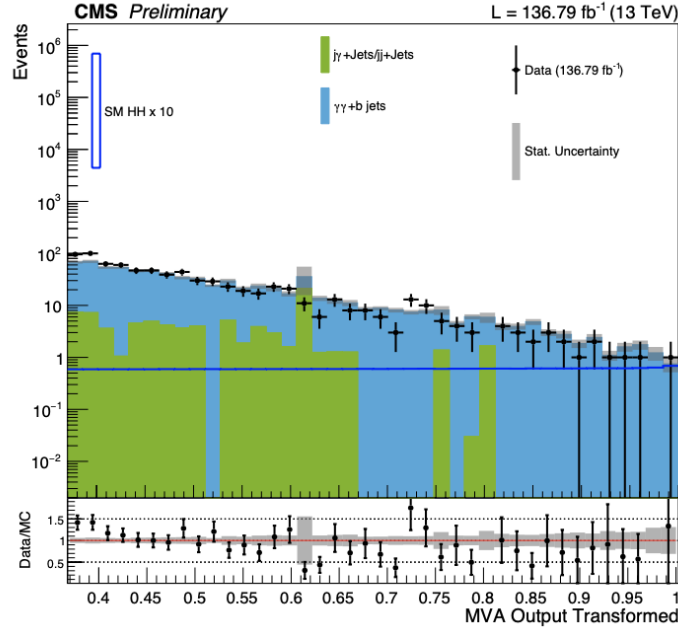
Figure 5.17: The distribution of the MVA output to discriminate the ggF HH signal from the continuum background for the selected data and simulated events in the ggF HH signal region (including the selection MVA score > 0.37).

Background Reduction from the VBF HH Signal Region

Analogously to the ggF HH process, the background for the VBF HH is dominated by $\gamma(\gamma)$+jets processes. In addition, the ggF HH (+jets) process represents a contamination in the VBF HH signal region limiting the sensitivity to the vector boson fusion production mode. Therefore, an MVA approach is used to optimize the separation of the VBF HH events from the continuum background and from the ggF HH events. In particular, a BDT multi-classifier is trained using the simulated events to discriminate between three classes of processes: VBF HH, ggF HH, and $\gamma(\gamma)$+jets. Beside the variables already optimized for the background rejection from the ggF HH signal region, additional variables exploiting the VBF HH kinematic are included in the training. Such variables improve the separation of the two HH production modes and also the continuum background rejection. In particular, the VBF jets are produced in opposite directions at large pseudorapidities recoiling against the diHiggs object. The VBF jets feature also a p_T typically larger than the background jets as well as a large dijet invariant mass. The additional variables are:

- The dijet invariant mass m_{jj}^{VBF};

- The VBF jets kinematic described by their p_T/m_{jj}^{VBF} and pseudorapidities η_1^{VBF}

and η_2^{VBF};

- Product and difference of pseudorapidity of the two VBF jets;

- Quark-gluon likelihood [110] of the two VBF jets to discriminate between jets originating from quarks and from gluons;

- Minimum angular distance between the VBF jets and the selected photons $\Delta R_{min}(j^{VBF}, \gamma)$, or the selected b-jets $\Delta R_{min}(j^{VBF}, b-jet)$;

- The diHiggs kinematics described by the HH transverse momentum p_T^{HH} and the $\widetilde{M}_x$ variable.

- Centrality variable for the $H \to \gamma\gamma$ and a $H \to b\bar{b}$ candidates defined as:

$$C_{xx} = exp\left[-\frac{4}{\left(\eta_1^{VBF} - \eta_2^{VBF}\right)^2} \left(\eta_{xx} - \frac{\eta_1^{VBF} + \eta_2^{VBF}}{2}\right)^2 \right] \quad \text{with } xx = \gamma\gamma, bb \tag{5.3}$$

because the two Higgs boson candidates are typically produced centrally with respect to the VBF jets. where H is the Higgs boson candidate reconstructed either from diphoton or dijet pairs, and η_1^{VBF} and η_2^{VBF} are the pseudorapidities of the two VBF-tagged jets.

The distributions of some of the most discriminating additional variables for data and simulated events are shown in Fig. 5.18. The training is performed separately in two four-body mass categories because of the different VBF HH kinematics (see Section 5.6.1). The four-body mass variable $\widetilde{M}_x$ is defined as Eq. 5.1. This definition reduces the impact of the jet and photon energy resolutions on the reconstructed four-body mass.

Two $\widetilde{M}_x$ categories are defined by the selections $\widetilde{M}_x < 500$ GeV and $\widetilde{M}_x > 500$ GeV. In both categories the training is performed using as signal a combination of the SM VBF HH sample and the BSM VBF HH sample with $c_{2V} = 0$. This strategy ensures a good sensitivity both to the SM and to the BSM hypotheses, especially to the $c_{2V} = 0$ case. The distribution of the BDT multiclassifier output relative to the VBF HH class for the data events (VBF HH-BDT score) as well as for the VBF HH and single Higgs simulated events is shown in Fig. 3.12 for the two $\widetilde{M}_x$ categories.
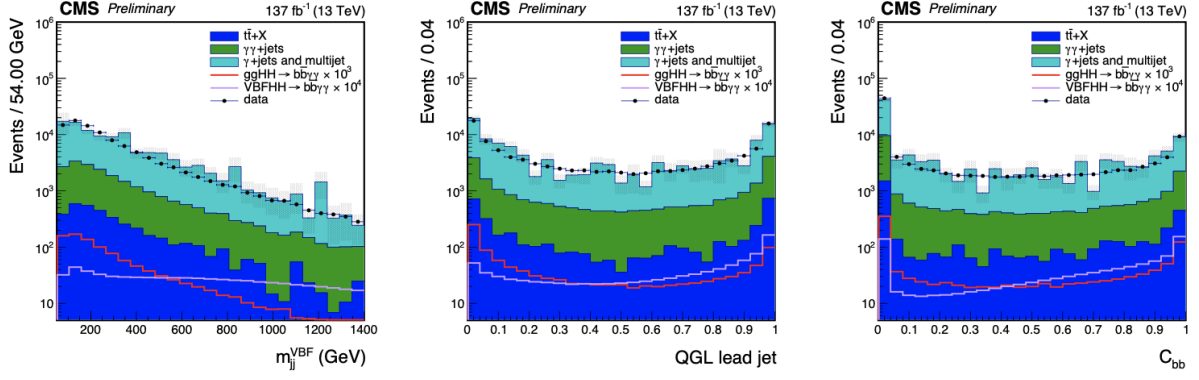
Figure 5.18: Distribution of m_{jj}^{VBF} (left), the quark-gluon likelihood (center), and the C_{bb} centrality variable for the selected VBF HH candidates for the data as well as the simulated $t\bar{t}$+X, $\gamma\gamma$+jets, γ+jets, and multijet events, excluding the signal region $120 < m_{\gamma\gamma} < 130$ GeV. The distributions of the simulated ggF HH and VBF HH events are also shown with red and purple lines, respectively.
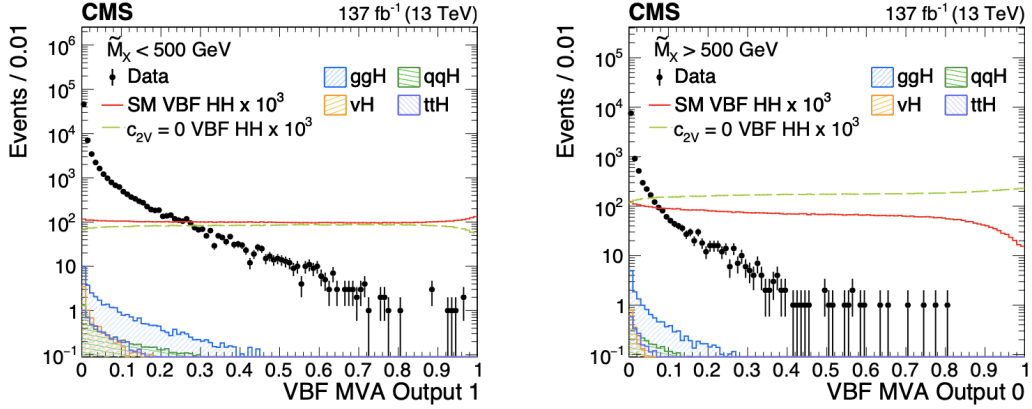
Figure 5.19: MVA multiclassifier output relative to the VBF HH class for the data events as well as for the VBF HH and single Higgs simulated events, for the $\widetilde{M_x} < 500$ GeV and $\widetilde{M_x} > 500$ GeV on the left and right, respectively.

5.6 Event Categorization

In order to maximize the sensitivity of the search, events are split into different categories according to the output of the MVA classifier and the mass of the Higgs boson pair system $\widetilde{M_x}$. The $\widetilde{M_x}$ distribution changes significantly for different BSM hypotheses, as shown in Fig. 5.2. Therefore, a categorization of HH events in $\widetilde{M_x}$ creates signal regions sensitive to multiple theoretical scenarios. In the search for VBF HH production, the categories in $\widetilde{M_x}$ are defined before the MVA is trained, as described in section 5.5.2. For the categories that target ggF HH production, categories in $\widetilde{M_x}$ are defined after the MVA is trained.

5.6.1 VBF HH-enriched Categories

In the first place, the HH candidates are tested for the VBF HH-enriched categories. The VBF HH categories are given highest priority because the VBF HH production has the smallest cross section among the signals considered, about 15 times smaller than the ggF HH cross section. Therefore, a high selection efficiency on this signal is fundamental. At the same time, a selection on the VBF HH-BDT score mitigates the ggF HH (+jets) events migration to the VBF HH-enriched categories.

The HH candidates passing the additional VBF HH requirements are classified in two $\widetilde{M_x}$ categories to improve the sensitivity both to the SM signal and to the anomalous c_{2V} hyphothesis. The VBF HH analysis is optimized to maximize the sensitivity to the SM VBF HH signal and, at the same time, to the VBF HH signal for anomalous c_{2V} values. In particular, the result of the ATLAS experiment for the $HH \rightarrow b\bar{b}b\bar{b}$ channel [111] indicates that the experimental sensitivity is close to the exclusion of $c_{2V} = 0$ at 95% confidence level. Therefore, the analysis is optimized to achieve the best sensitivity both for $c_{2V} = 0$ and $c_{2V} = 1$ (SM). For this reason, the value chosen as boundary of the two categories is $\widetilde{M_x} = 500$ GeV. As visible in Fig. 5.20, the $\widetilde{M_x} < 500$ GeV category is especially sensitive to the SM signal, while the $\widetilde{M_x} > 500$ GeV category is more populated by events produced with $c_{2V} = 0$.
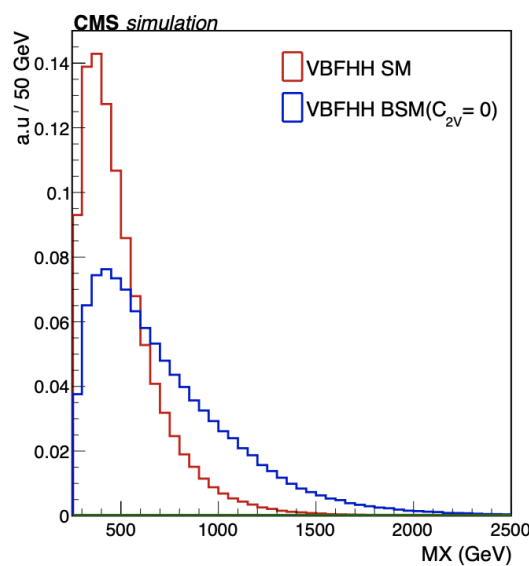
Figure 5.20: $\widetilde{M_x}$ distribution for the VBF HH simulated events for $c_{2V} = 1$ and $c_{2V} = 0$ in red and blue, respectively.

The selections on the $t\bar{t}H$-score and on VBF HH-BDT score are simultaneously optimized to maximize the expected significance on the VBF HH signal. The expected significance is estimated as the sum in quadrature over the two categories of $S/\sqrt{B}$, where S and B are the expected VBF HH signal and background yields in each category, respectively. Both S and B are estimated using MC events in the $122 < m_{\gamma\gamma} < 128$ GeV region. The signal considered for the optimization consist in the same mixture of the SM VBF HH sample and the $c_{2V} = 0$ VBF HH sample used for the BDT training. The signal times the branching ratio is normalized to the expected excludable cross section estimated of 0.5 fb. The number of expected events in the sidebands (outside $115 < m_{\gamma\gamma} < 135$ GeV) of each category is required to be higher than 6. This number is found to be the minimum for a data-driven background modeling with a sufficient accuracy (see Section 5.7.3). This constraint is found to be the factor mostly controlling the optimization of the VBF HH-BDT score boundaries. The significance is around its maximum for $t\bar{t}H$-score values in the range [0.2-0.3]. Therefore, for simplicity the $t\bar{t}H$-score > 0.26 selection is chosen, identically to the selection applied for the ggF HH categories. The VBF HH-BDT score boundaries for the categories definition are summarized in Tab. 5.6. The visualized version of categories and constraints is shown in Fig. 5.22 (Left).

5.6.2 ggF HH-enriched Categories

The HH candidate events that do not pass the VBF HH category selections are tested for the ggF HH-enriched categories. The ggF HH-BDT score is used to reject the background-like events and to classify the remaining events in three exclusive categories. The boundaries of the categories, along with the $t\bar{t}H$-score selection, are simultaneously optimized with the same procedure used for the VBF HH categories (Section 5.6.1). It was verified that the same $t\bar{t}H$-score selection for all the three categories makes the optimization more robust without a significant worsening of the expected significance.

Within each of the three defined BDT score categories, four $\widetilde{M}_x$ exclusive categories are defined to improve the sensitivity to several BSM scenarios. As discussed in Section 2.5.1, the four-body mass is highly sensitive to the BSM benchmarks as well as to the anomalous κ_λ hypothesis. The distribution for the SM ggF HH and the main backgrounds MC events is shown in Fig. 5.21. The optimization of the 3×4 $\widetilde{M}_x$ boundaries is performed

simultaneously with the same procedure adopted for the MVA boundaries optimization.

Unlike the VBF HH categories optimization, this optimization is performed with respect to the SM (ggF HH) signal. It was verified that this does not penalize the BSM sensitivity thanks to the dense $\widetilde{M}_x$ categorization. The number of categories was also optimized repeating the procedure with a different number of BDT-score and $\widetilde{M}_x$ categories between one and four. The BDT-score and $\widetilde{M}_x$ selections for the categories is summarized in Tab. 5.6. As for the VBF HH categories, the optimization of the boundaries for the high-purity categories is controlled by the constraint on the minimum number of expected background events in the sidebands. The visualized version of categories and constraints is shown in Fig. 5.22 (Right).

The expected composition of the categories, estimated through simulation is shown in Fig. 5.23
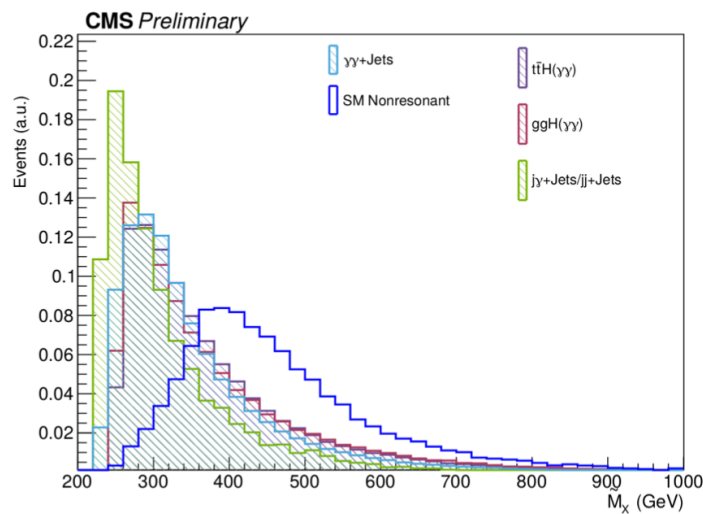
Figure 5.21: $\widetilde{M}_x$ distribution for the SM ggF HH and the main background MC events. All the distributions are normalized to one.

5.7 Statistical Analysis

The data analysis aims to determine the compatibility of the experimental observation with the "signal + background" hypothesis against the "background only" hypothesis, or viceversa. In case a signal is observed, the data are used to measure the corresponding

Category	MVA	$\widetilde{M}_x$ (GeV)
VBF HH CAT 0	0.52-1.00	>500
VBF HH CAT 1	0.86-1.00	250-500
ggF HH CAT 0	0.78-1.0	>600
ggF HH CAT 1		510-600
ggF HH CAT 2		385-510
ggF HH CAT 3		250-385
ggF HH CAT 4	0.62-0.78	>540
ggF HH CAT 5		360-540
ggF HH CAT 6		330-360
ggF HH CAT 7		250-315
ggF HH CAT 8	0.37-0.62	>585
ggF HH CAT 9		375-585
ggF HH CAT 10		330-375
ggF HH CAT 11		250-330

Table 5.6: Optimized BDT-score and $\widetilde{M}_x$ selections for the HH categories. In all the categories the selection $t\bar{t}H$-score > 0.26 is also applied.
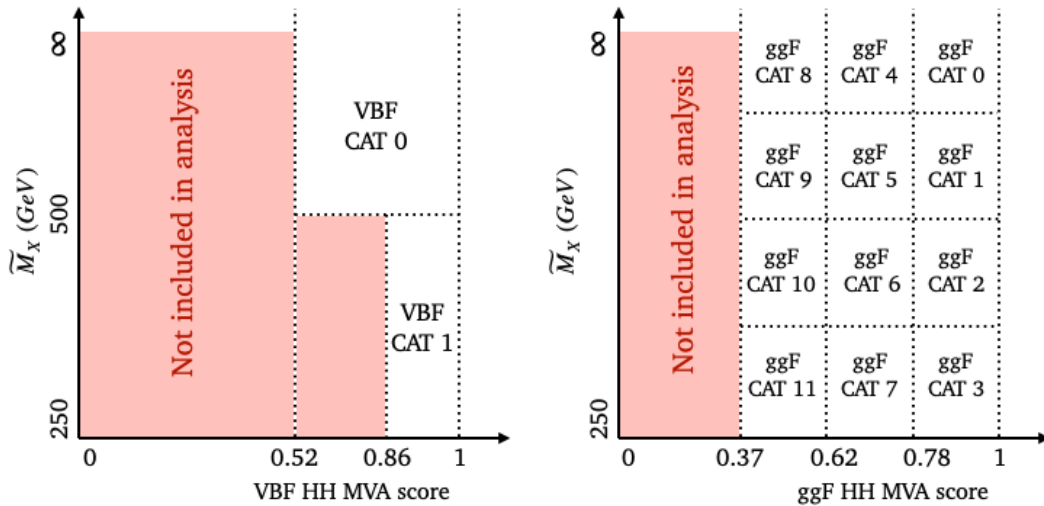
Figure 5.22: Visualized categorization scheme for the VBF HH (left) and ggF HH (right) analysis.
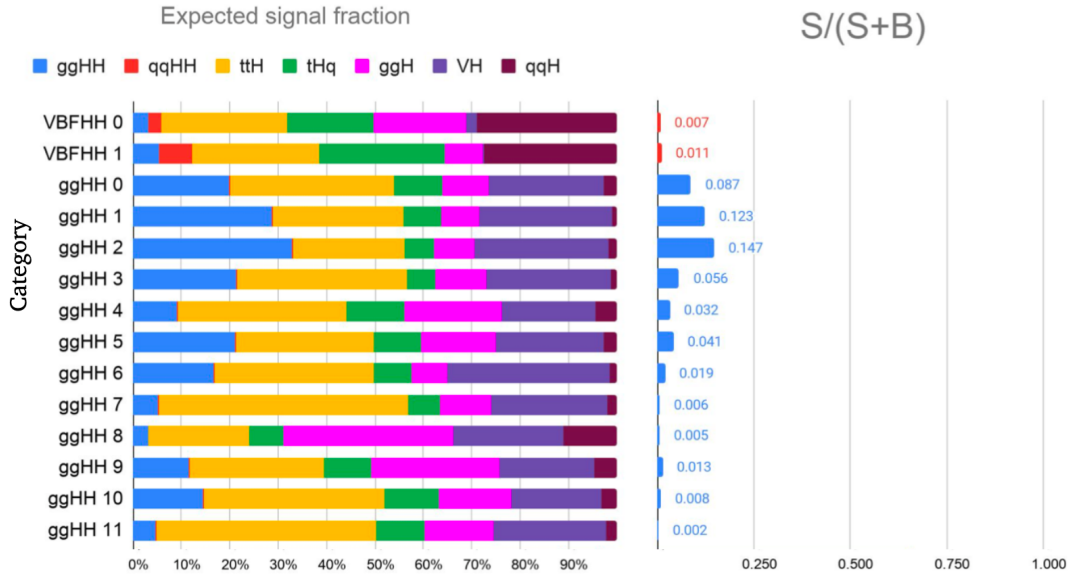
Figure 5.23: *Left*: Expected categories composition in terms Higgs boson processes. *Right*: Expected $S/(S+B)$ in $\pm 1\sigma_{eff}$ for each category. S is referred to the Higgs boson process target of each category, and B is the sum of the expected Higgs boson background processes and of the expected continuum background.

signal strength μ defined as:

$$\mu = \frac{\sigma_{obs}}{\sigma_{SM}} \tag{5.4}$$

Setting $\mu = 0$ corresponds to the background-only model where as $\mu = 1$ is the Standard Model expectation. The measured cross section's compatibility with the SM prediction is demonstrated by a μ value being consistent, within the uncertainties, with one. In case the signal is not observed, the data are used to set an upper limit on its cross section. In this analysis, multiple signals are tested: the ggF HH signal ($\mu_{ggF\ HH}$), the VBF HH signal ($\mu_{VBF\ HH}$), and the inclusive HH production (ggF HH + VBF HH) signal (μ_{HH}).

Alternatively, the data can be interpreted in terms of Higgs boson coupling modifiers (κ_λ, κ_t, c_V, c_{2V}). Due to the limited number of considered Higgs production and decay channels, at most two coupling constants are measured simultaneously, fixing the other couplings to the SM prediction. The measurement can be performed under the assumption of a SM HH signal, or no HH signals. The statistical analysis adopts a maximum likelihood method described in Section 5.7.1 while the signal and background modeling are described in Section 5.7.2 and Section 5.7.3, respectively.

5.7.1   Likelihood Definition

A likelihood function is used as test statistics. The likelihood is split into two terms:

$$\mathcal{L} = \mathcal{L}_{HH} \cdot p(\theta|\tilde{\theta}) \tag{5.5}$$

where $\mathcal{L}_{HH}$ is the likelihood functions corresponding to the HH enriched categories. Defined θ as the vector of all the nuisance parameters, $p(\theta|\tilde{\theta}$ is the distribution of θ given the true values (Bayesian interpretation) $\tilde{\theta}$. For the nuisance description, the frequentist approach common to the CMS and ATLAS experiment is used [112].

The $\mathcal{L}_{HH}$ factor is built exploiting the resonant nature of the HH signal in the m_{jj} and $m_{\gamma\gamma}$ distributions. Given the low statistic regime, the $\mathcal{L}_{HH}$ function is built as an unbinned likelihood. Therefore, $\mathcal{L}_{HH}$ is defined for each analysis category as:

$$\begin{aligned}
\mathcal{L} =& k^{-1} \prod_{i \in events} \left[\sum_{\substack{j=ggF\ HH, \\ VBF\ HH}} \mu_j S_j f_j(m_{\gamma\gamma}^i, m_{jj}^i) + \sum_{\substack{j=t\bar{t}H,\ tHq \\ ggH,\ VH, \\ qqH}} S_j f_j(m_{\gamma\gamma}^i, m_{jj}^i) \right. \\
&\left. + B f_B(m_{\gamma\gamma}^i, m_{jj}^i|\theta) \right] \cdot exp\left(\sum_{\substack{j=ggF\ HH, \\ VBF\ HH}} \mu_j S_j + \sum_{\substack{j=t\bar{t}H,\ tHq \\ ggH,\ VH, \\ qqH}} S_j + B \right)
\end{aligned} \tag{5.6}$$

where k is the total number of observed events, S_j is the number of events predicted by the SM for the j-th Higgs process, and f_j is the corresponding two dimensional ($m_{\gamma\gamma}$, m_{jj}) parametric pdf. B is the expected number of continuum background events and f_B is the corresponding parametric pdf. For simplicity, the dependence of the S_j, f_j, and f_B quantities from the nuisance parameters θ is omitted from Eq. 5.6. The correlation between the $m_{\gamma\gamma}$ and m_{jj} variables is found to be negligible both for the signals and the backgrounds. Therefore, the two dimensional models can be factorized as:

$$f_j(m_{\gamma\gamma}, m_{jj}) = f_j^{\gamma\gamma}(m_{\gamma\gamma} f_j^{jj}(m_{jj}) \tag{5.7}$$

where $f_j^{\gamma\gamma}$ and f_j^{jj} are the one dimensional $m_{\gamma\gamma}$ and m_{jj} models for the j-th Higgs process.

3122 For the measurement of the coupling modifiers, the signal strengths are fixed to one while

3123 the number of expected events for the single and double Higgs processes S_j is expressed

3124 as a function of the $(\kappa_\lambda, \kappa_t, c_V, c_{2V})$ parameters. In particular, the SM and BSM ggF HH

3125 and VBF HH samples are properly combined to provide a per-category description of the

3126 signals rate variations. For the single Higgs processes a parametric description of the total

3127 cross section variation as a function of the coupling modifiers is used for all the categories.

3128 Although modifications of the p_T spectrum of the single Higgs processes, especially for

3129 $t\bar{t}H$, are expected in case of anomalous κ_λ values, an explicit p_T categorization is not

3130 performed. Since the p_T distribution is found to be similar in all the categories, the

3131 inclusive cross section variation provides sufficient accuracy for the description of the

3132 anomalous coupling effects. A future extension of this work can be a p_T classification of

3133 the single Higgs events to improve the sensitivity to anomalous couplings. The $H \to \gamma\gamma$

3134 and $H \to b\bar{b}$ branching ratios variations for anomalous couplings are also considered.

3135 **Estimation of the Parameters of Interest**

3136 Let a generic μ be the parameter of interest. The likelihood estimators of μ and θ, namely

3137 $\hat{\mu}$ and $\hat{\theta}$, are the values simultaneously maximizing the likelihood function, or equivalently

3138 the values minimizing the negative logarithm of the likelihood function (log-likelihood L).

3139 The latter is much easier to compute from the algorithmic point of view. In order to

3140 estimate the uncertainty on $\hat{\mu}$, a "profile likelihood" is defined as:

$$\mathcal{L}_{prof}(\mu) = -2log\frac{\mathcal{L}(\mu, \hat{\hat{\theta}})}{\mathcal{L}(\hat{\mu}, \hat{\theta})} \tag{5.8}$$

3141 Where $\mathcal{L}$ is the likelihood defined in Eq. 5.5, $\hat{\hat{\theta}}$ represents the set of nuisance values

3142 maximizing $\mathcal{L}$ for a given μ and the denominator is maximized over the full parameter

3143 space. The 68% and 95% confidence intervals on μ correspond to the μ values satisfying

3144 the condition $\mathcal{L}_{prof}(\mu) < 1$ and $\mathcal{L}_{prof}(\mu) < 3.84$, respectively.

Hypothesis Testing to Set an Upper Limit

In case no evidence of the double Higgs production is found with data, an upper limit can be set on the ggF HH, VBF HH, and HH cross sections. To do that, the following test statistic is defined:

$$q_\mu = -log \frac{\mathcal{L}(\mu, \hat{\hat{\theta}})}{\mathcal{L}(\hat{\mu}, \hat{\theta})} \text{ with } 0 \leq \hat{\mu} \leq \mu \tag{5.9}$$

where $\mathcal{L}$ is the likelihood, $\hat{\mu}$ and $\hat{\theta}$ are the signal strength and the nuisances values maximizing $\mathcal{L}$, while $\hat{\hat{\theta}}$ is the set of nuisance values maximizing $\mathcal{L}$ for a given value of μ.

Depending on the cross section of interest, the μ variable is referred either to the ggF HH, or VBF HH, or the inclusive HH signal. The constraint $\hat{\mu} \leq 0$ is to avoid the unphysical situation of negative signals, while the constraint $\mu \leq \hat{\mu}$ is required to avoid to use upward fluctuations of the data against the signal hypothesis. The modified frequentist criterion [113] is adopted for the limit extraction. The level of disagreement of the observed data with a given hypothesis is quantified through a "p-value" which is the probability to obtain results worse than or equal to the one observed under the given hypothesis.

In particular, given the observed value of the test statistic q_μ^{obs}, two p-values p_μ and p_b can be derived for the signal plus background and background only hypotheses respectively:

$$p_\mu = Prob(q_\mu > q_\mu^{obs}|signal + background) 1 - p_b = Prob(q_\mu > q_\mu^{obs}|background only) \tag{5.10}$$

Such p-values are computed using the asymptotic properties of the test statistics [114]. This avoids the computationally expensive procedure of the MC toy generation to explicitly derive the q_μ distributions. The p_μ value is not used directly for the limit extraction because it is not sufficiently robust against background under-fluctuations. Such under-fluctuations could lead to exclude small values of μ even if the sensitivity to the signal would not be sufficient. In order to prevent for that effect, the $CL_s(\mu)$ quantity is defined as:

$$CL_s(\mu) = \frac{p_\mu}{1 - p_b} \tag{5.11}$$

A signal strength μ is said to be excluded at a confidence level (CL) α if $CL_s(\mu) < 1 - \alpha$. The value commonly chosen for α is 95%. The limit on μ is in fact a limit on the cross

section normalized to the corresponding SM prediction.

Hypothesis Testing to Quantify an Excess

The following test statistics is defined to quantify the excess of events:

$$q_0 = -log\frac{\mathcal{L}(\mu, \hat{\hat{\theta}})|_{\mu=0}}{\mathcal{L}(\hat{\mu}, \hat{\theta})} \text{ with } \hat{\mu} > 0 \qquad (5.12)$$

This is in fact the likelihood computed for the background-only hypothesis normalized by the likelihood value for the best fit point. Given the observed value of the test statistic q_0^{obs}, the p-value is then defined as:

$$p_0 = Prob(q_0 \geq q_0^{obs}|backgroundonly) \qquad (5.13)$$

This is the probability that a background fluctuation gives an excess larger than or equal to the observed one. For a more direct interpretation, the p_0 probability is converted to a Z significance by expressing it as a one-sided Gaussian integral:

$$p_0 = \int_Z^{+\infty} \frac{1}{2\pi} e^{-x^2/2} dx \qquad (5.14)$$

It is customary to consider a significance larger than 3σ as an evidence, and a significance larger than 5σ as an observation of a signal above the background.

5.7.2 Modeling of HH Processes

For each analysis category and each Higgs production mechanism, the MC simulations are used to derive the expected number of events (S_j) and to model the $m_{\gamma\gamma}$ distribution ($f_j^{\gamma\gamma}$), and, the m_{jj} distribution (f_j^{jj}).

The $m_{\gamma\gamma}$ peak is modeled as a sum of up to five gaussian functions. Examples of the $m_{\gamma\gamma}$ models for the HH processes are visible in Fig. 5.24.
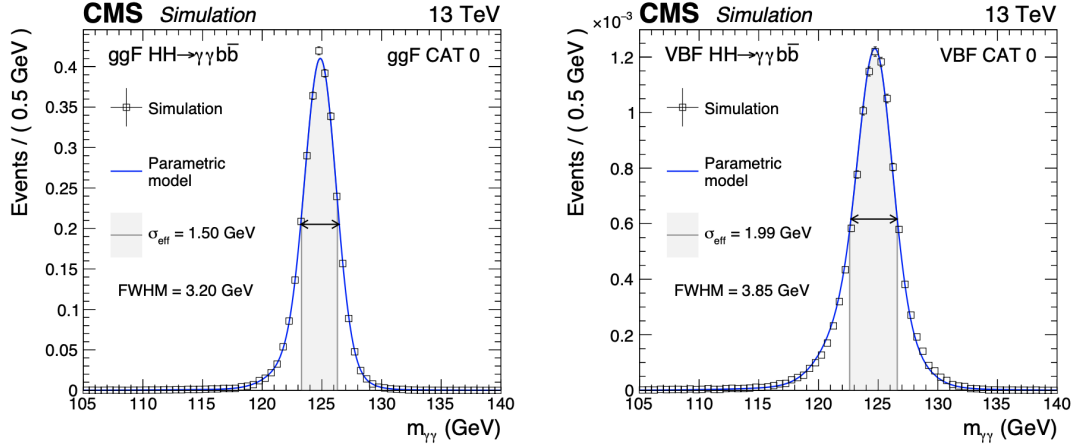
Figure 5.24: $m_{\gamma\gamma}$ modeling for the ggF HH and VBF HH process on the left and right, respectively, for the best resolution (high $\widetilde{M_x}$ and high BDT score) category in the 2018 dataset. The open squares represent simulated events and the blue lines are the corresponding models. Also shown are the σ_{eff} value (half the width of the narrowest interval containing 68.3% of the invariant mass distribution) and the corresponding interval as a gray band, and the full width at half the maximum (FWHM) and the corresponding interval as a double arrow.

The m_{jj} distribution for the VBF HH and ggF HH processes is modeled with a double-sided Crystal Ball (CB) function which is a CB function with two independent exponential tails instead of one, as shown in Fig. 5.25. This function is found to provide an adequate description of the m_{jj} peak with its left and right tails related to the jet energy resolution.

The functions parameters are determined for each category through a fit to the selected simulated events. The final signal model is built as the product of the obtained $m_{\gamma\gamma}$ and m_{jj} distributions.

The assumption of no-correlation between the $m_{\gamma\gamma}$ and m_{jj} variables hypothesis is verified comparing the two dimensional $(m_{\gamma\gamma}, m_{jj})$ distribution of the simulated events, visible in Fig. 5.26 for the simulated ggF HH events from the 2018 dataset, to the product of the derived m_{jj} and $m_{\gamma\gamma}$ models. The difference of the two distributions is found to be negligible within the statistical uncertainties related to the expected number of signal events.

120
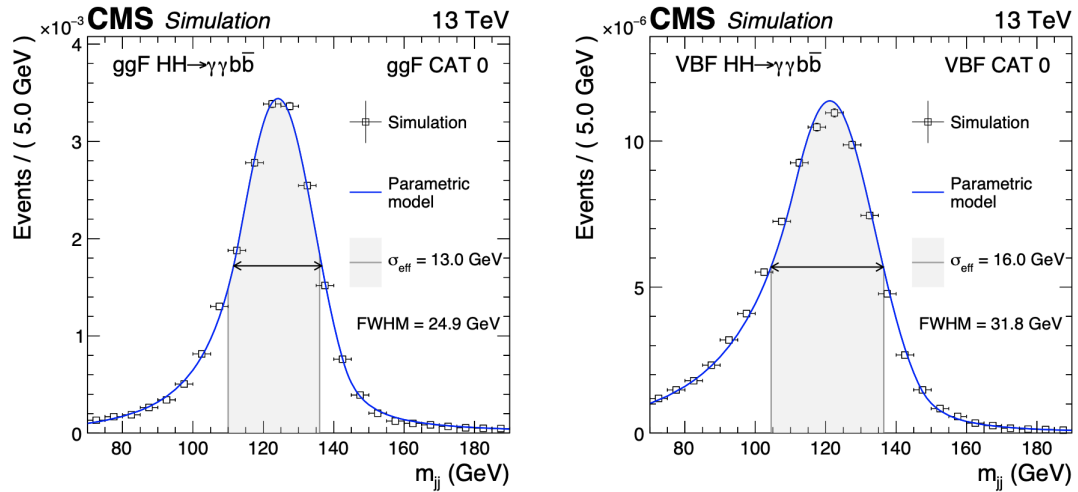
Figure 5.25: m_{jj} modeling for the ggF HH and VBF HH process on the left and right, respectively, for the best resolution (high $\widetilde{M_x}$ and high BDT score) category in the 2018 dataset.
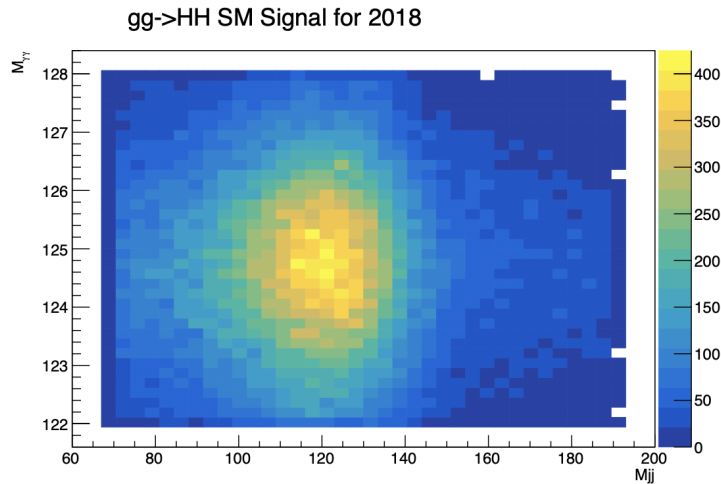
Figure 5.26: Two dimensional $(m_{jj}, m_{\gamma\gamma})$ distribution for the selected HH candidates of the simulated ggF HH events using the 2018 dataset.

5.7.3 Background Modeling

Single Higgs Background

For the Single Higgs categories, the m_{jj} pdf parametrization depends on the specific production mechanism:

- The m_{jj} distribution for the VH process, consisting in a peak in correspondence of the vector bosons masses, is modeled through a standard CB function. This function, with a lower number of free parameter than a double-sided CB, provides

121

the required robustness and accuracy for the VH modeling. The simulated VH events are in fact affected by higher statistical uncertainties because of the limited number of selected events.

- The m_{jj} distributions for the ggH and qqH processes have a smooth falling shape, thus they are parametrized by Bernstein polynomials.

- The $t\bar{t}H$ and tHq events kinematics feature a m_{jj} distribution peaking at about 110-120 GeV. Thus, a gaussian function is used to model their m_{jj} distributions.

The number of simulated events for the single-Higgs production mechanisms in the HH signal regions is limited, especially for the ggH, VH, and qqH processes. Therefore, the simulated events of the three data-taking years within the same BDT-score category are merged together, and a common m_{jj} model is extracted to improve the model accuracy. It was verified that the m_{jj} models across different $\widetilde{M}_x$ categories and different years are compatible within the uncertainties. Examples of the m_{jj} models for the high BDT score category are visible in Fig. 5.27. In order to improve the accuracy of the $m_{\gamma\gamma}$ modeling of the ggH, VH, and qqH processes in the HH signal regions, in case the number of MC entries is less than 500, the used $m_{\gamma\gamma}$ model is the same one used for the $t\bar{t}H$ process in that category. Then the normalization is set according to the expected yield for that specific process.

Continuum Background

The continuum background is modeled in each category through a fit of the $m_{\gamma\gamma}$ (and m_{jj}) distribution of the selected data events. Since the parametrization of the underlying model is not known, a specific method called "envelope method" [115] is used to choose the background parametrization estimating also the related uncertainty.

The envelope method considers the choice of the background functional form as an additional (discrete) nuisance parameter to be included in the likelihood definition. In particular, an integer number called "envelope index" is used to select a specific functional form among the set of given parametrizations. Therefore, the negative log-likelihood is minimized with respect to all the nuisance parameters including the envelope index. The
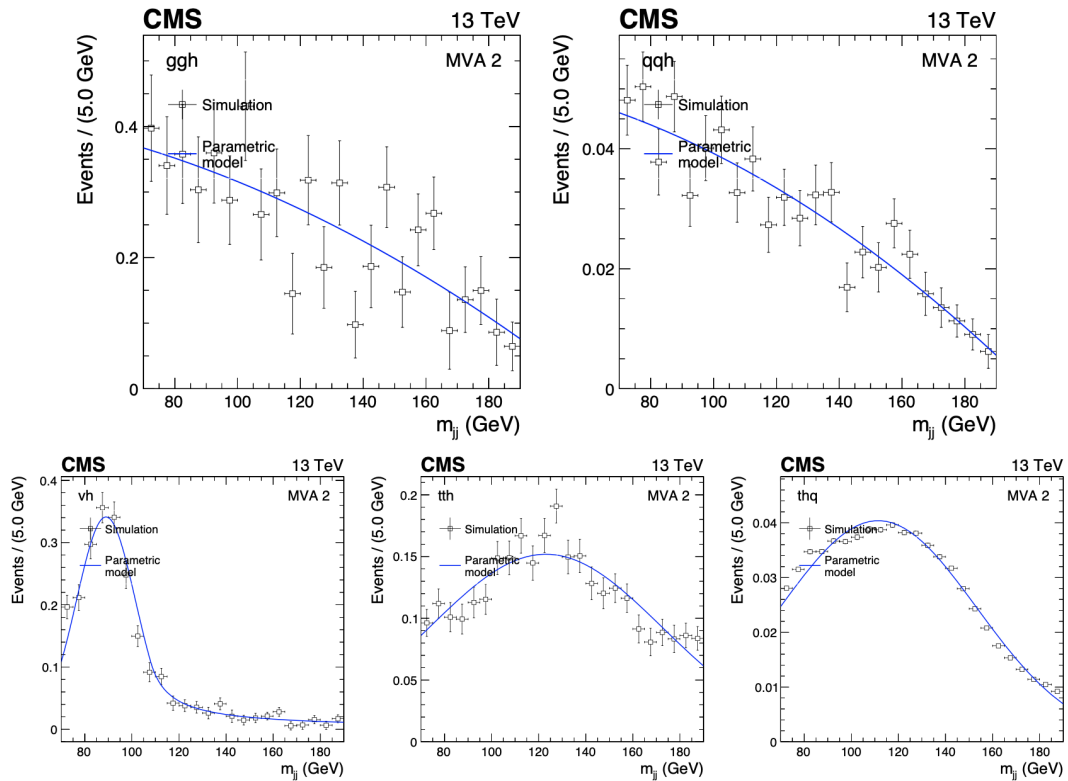
Figure 5.27: m_{jj} modeling for the ggH (top-left), qqH (top-right), VH (bottom-left), $t\bar{t}H$ (bottom-center), and tHq (bottom-right) processes, in the ggF HH-enriched category with the highest BDT score value.

impact of this additional nuisance parameter is a broadening of the profile likelihood of Eq. 5.8 corresponding to an increase of the uncertainty in the parameter estimation. This is expected because a nuisance parameter corresponds to a loss of information in the measurement.

For a correct usage of the envelope method, a proper choice of the set of functions is crucial. The set of functions has to provide a negligible bias in the estimation of the parameter of interest and a consistent estimation of the corresponding uncertainty (coverage). The studies presented in Ref. [115] show that for an exponentially falling background such as the $m_{\gamma\gamma}$ background distribution in the $H \rightarrow \gamma\gamma$ analysis, a good coverage is provided by the following set of function families:

$$\text{Power law sum:} f(x) = p_0 x^{p_1} + p_2 x^{p_3} + p_4 x^{p_5} + ...$$

$$\text{Exponential sum:} f(x) = p_0 e^{p_1 x} + p_2 e^{p_3 x} + p_4 e^{p_5 x} + ...$$

$$\text{Laurent series:} f(x) = \sum_{i=0}^{N} p_i / x^i$$

$$\text{Polynomial:} f(x) = \sum_{i=0}^{N} p_i x^i$$

A second important aspect is how to compare functions with different degrees of freedom in terms of data agreement. By construction, a function with a higher number of free parameters within the same family is able to better describe the data, thus the likelihood minimization will select it. However, it is more sensitive to the data fluctuations. Therefore, a correction to the likelihood penalizing the higher order functions is defined to make the method robust against the background fluctuations. In Ref. [115], a good correction for the $H \to \gamma\gamma$ case is found to be:

$$L_{corr} = L + N_{par} \tag{5.15}$$

where L is the negative log-likelihood and N_{par} is the number of free parameters of the function considered.

For the HH categories, the envelope method is used for the description both of the $m_{\gamma\gamma}$ and the m_{jj} backgrounds. In the assumption of no-correlations between the $m_{\gamma\gamma}$ and m_{jj} variables, the generalization of the envelope method for the 2D fit is straightforward. The same function families defined for the $m_{\gamma\gamma}$ description can be used also for the m_{jj} variable because the background shape is analogous. The correction defined in Eq. 5.15 accounts for the sum of free parameters of the m_{jj} and $m_{\gamma\gamma}$ distributions.

From the practical point of view, the numerical minimization with discrete parameters is not reliable. Therefore, for each 2D combination of $(m_{\gamma\gamma}, m_{jj})$ envelope indexes, a minimization is performed and the envelope is built afterwards. In order to reduce the computing time required for the minimization, a preliminary procedure determines the optimal order of each function family in each category. All the functions with up to six

124

free parameters are considered. The functions with order higher than the optimal one are then not considered for the envelope construction.

The range for the $m_{\gamma\gamma}$ and m_{jj} fits are 100 GeV$< m_{\gamma\gamma} < 180$ GeV, and 70 GeV$< m_{\gamma\gamma} <$ 190 GeV. However, for the two ggF HH enriched categories with the lowest $\widetilde{M}_x$ at low BDT score, the fit region is reduced to 90 GeV$< m_{\gamma\gamma} < 190$ GeV because the background shape is not well described. It was verified that with the reduced m_{jj} range the background modeling remains robust and that the bias induced on the expected signal strength is negligible. The changes of the expected upper limits on the HH cross section and of the constraints on anomalous couplings are found to be below 1%.

5.8 Systematic Uncertainties

The analysis is statistically limited, therefore the impact of the systematics uncertainties on the result is small. In particular, as we will see, the upper limit on μ_{HH} including the systematics uncertainties is only 2% worse than the limit computed considering only the statistical uncertainties. The impact of the systematics uncertainties consists in a modification of the single and double Higgs yields in the categories, due to the event loss or migration across categories. The only systematic uncertainty associated with the continuum background, estimated from data, is the choice of its parametric modeling within the envelope method. The impact of the systematics uncertainties, quoted for simplicity on μ_{HH}, is shown in Tab. 5.7, while their description is listed below:

- QCD scale: it accounts for the uncertainty on the renormalization and factorization scale. They are set accordingly to Ref. [29], [32], and [116] for the single Higgs, ggF HH, and VBF HH processes, respectively. In particular, the uncertainties associated with the ggF HH and $t\bar{t}H$ QCD scales, whose 1σ variations change the total cross sections of up to 5 and 9%, respectively, represent the dominant uncertainties for this analysis.

- Parton distribution functions (PDF) modeling: it is computed according to the PDF4LHC15 prescriptions [117]. The PDF modeling affects the total number of events and also the event categorization since it modifies the number of jets produced

Systematic uncertainty	$\Delta\mu_{HH}$ (%)
QCD scale	+7/-2
PDF modeling + α_s	3
Branching ratio	3
Parton shower modeling	<1
Luminosity	3
Photon preselection	2
Per-photon σ_E/E	1
Photon ID	<1
Trigger	<1
Photon energy & res.	<1
Jet energy & res.	<1
b-tag efficiency	<1
Pileup jet ID	<1

Table 5.7: Impact of the systematic uncertainties on the signal strengths in percentage.

in association with the Higgs boson signals. The event migration is computed using the NNPDF30 set with the MC2hessian method [118].

- α_s value: the uncertainty on the QCD coupling constant is computed along with the PDF modeling uncertainty using the PDF4LHC15 prescriptions. The α_s value affects in fact also the PDF modeling, thus the impact of the two uncertainties is estimated together.

- Parton shower modeling: this uncertainty is considered for the VBF HH process because different showering schemes can significantly change some of the VBF observables [119], hence the total number of events and their classification. This uncertainty is conservatively estimated as the full symmetrized difference in yields in each category obtained from VBF HH MC samples generated with different parton shower ISR and FSR configurations.

- Uncertainty in the $H \to \gamma\gamma$ and $H \to b\bar{b}$ branching fractions which amounts to about 3 and 0.5%, respectively, according to Ref. [29].

The dominant experimental systematic uncertainties are:

- Photon identification BDT score: it accounts for the residual data-simulation discrepancy of the photon ID BDT score distribution. Such a discrepancy is ascribed to the limited accuracy of the regression used to correct the BDT input variables

to cover the residual discrepancies between data and simulation. It is estimated through the procedure described in Section 5.4.1.

- Photon energy scale and resolution: it accounts for the residual discrepancy between the data and MC simulation after the corrections. It accounts for effects such as non-linearities of the light collection, the different shower-shape of electrons, used to derive the correction, and photons, as well as different trainings in the energy regression and variation of the binning used to derive the correction.

- Per-photon energy resolution estimate: this variable is computed by the photon energy regression. Its impact on the event selection and classification is estimated by varying the resolution of $\pm 5\%$ around its nominal value.

- Jet energy scale and resolution corrections: the energy scale and resolution of jets is measured using the p_T balance in Z(ee)+jets, Z($\mu\mu$)+jets, γ+jets, and multijet events [110]. The uncertainty on the calibration is a few percent and depends on p_T and η. The impact of jet energy scale uncertainties in event yields is estimated by varying the jet energy corrections within their uncertainties, ranging between 1 and 3% in central barrel, and propagating the effect to the final result. Some sources of the jet energy scale uncertainty are fully (anti-)correlated, while others are considered uncorrelated.

- Jet b-tagging: such uncertainties are computed comparing the distribution of the b tagging efficiency between data and simulation. The efficiency on light flavour jets is measured using a inclusive multijet sample, while the efficiency on heavy-flavour jets is measured using muon-enriched jet samples, and $t\bar{t}$ plus one or two leptons samples [91]. The uncertainties include the statistical component on the estimate of the fraction of heavy and light flavour jets in data and simulation.

- Trigger efficiency: as discussed in Section 5.3.1, the efficiency of the trigger selection and the corresponding uncertainty is measured with $Z \to e^+ e^-$ events using a T&P technique. An additional uncertainty is introduced to account for a gradual shift in the timing of the inputs of the ECAL L1 trigger in the region $|\eta| > 2$, causing a specific trigger inefficiency during the 2016 and 2017 data taking periods. Photons and also jets are affected by this inefficiency, which has a small impact.

- Photon preselection: as discussed in Section 5.4.1, the photon preselection efficiency (including the electron veto efficiency) is estimated using $Z \to e^+e^-$ and $Z \to \mu^+\mu^-\gamma$ events with a T&P method. The uncertainty on the scale factors derived to match the efficiency of the simulation to the one measured with data is propagated throughout the analysis.

- Integrated luminosity: the related uncertainties are determined through auxiliary measurements by the CMS luminosity monitoring for the 2016–2018 data-taking years [120, 121, 122]. The uncertainties across the different years of data-taking are partially correlated to account for common sources of uncertainty in the luminosity measurement schemes. The total 2016–2018 integrated luminosity has an uncertainty of 1.8%.

- Pileup jet ID output score: it accounts for the differences between data and simulation in the distribution of the pileup jet ID variable. Only the VBF jets are affected. This uncertainty is estimated by comparing the score of jets in Z+jets events in data and simulation in intervals of p_T and η.

Other systematics uncertainties impact the signal strength by less than 1% and are thus negligible with regard to the ones described above. They include uncertainties on lepton identification and isolation efficiencies, on the correct vertex assignment efficiency, and on the missing transverse momentum.

5.9 Results

This work led to two results: the search for the double Higgs production presented in Section 5.9.1, and the measurement of the Higgs boson couplings presented in Section 5.9.3. All the results were found compatible with the SM predictions. In particular, no significant excesses over the background of double Higgs production events were found, thus upper limits on the HH cross sections were extracted.

A simultaneous fit of the HH and the $t\bar{t}H$ cross sections is also performed to improve the sensitivity on the $\lambda)HHH$ and the y_t parameters, and to simultaneously measure the

two parameters. The $t\bar{t}H$ and HH processes are intrinsically correlated because they both depend on the $\lambda)HHH$ and y_t constants.

5.9.1   Search for HH Process

The HH categories (twelve ggF HH and two VBF HH categories) are included in the extraction of the HH production yield. A likelihood fit is performed using the likelihood defined in Eq. 3.5 to measure the μ_{HH} signal modifier. The fit to the $m_{\gamma\gamma}$ and m_{jj} distributions for two categories of VBF HH is shown in Fig. 5.28 and for twelve categories of ggF HH is shown in Fig. 5.29 and 5.30 respectively. The weighted distribution of events while merging all categories according to the factor $S/(S+B)$ is shown in Fig. 5.31. Analogous fits are performed to measure either the $\mu_{ggF\ HH}$ or the $\mu_{VBF\ HH}$ parameter fixing the other parameter to one. The observed and expected signal strengths are reported in Tab. 5.8.

Parameter	Expected	Observed
μ_{HH}	$1.0^{+2.7}_{-1.9}$	$2.7^{+2.6}_{-2.0}$
$\mu_{ggF\ HH}$ fixing $\mu_{VBF\ HH} = 1$	$1.0^{+2.7}_{-1.9}$	$2.8^{+2.7}_{-2.0}$
$\mu_{VBF\ HH}$ fixing $\mu_{ggF\ HH} = 1$	$1.0^{+91.3}_{-65.1}$	$10.2^{+97.21}_{-61.6}$

Table 5.8: Expected and observed signal strength for inclusive HH(ggF HH + VBF HH), ggF HH and VBF HH

Due to a small excess observed in data, the observed signal strengths are larger than one, but still compatible with the SM within the uncertainties. The inclusive μ_{HH} signal strength is dominated by the ggF HH process because of the larger cross section, as visible by the large uncertainty on $\mu_{VBF\ HH}$ compared to the uncertainty on $\mu_{ggF\ HH}$. Alternatively, $\mu_{ggF\ HH}$ and $\mu_{VBF\ HH}$ are measured simultaneously, as shown in Fig. 5.32.

Since no evidences of double Higgs production were found, upper limits on the corresponding cross sections are extracted using the procedure described in Section 5.7.1. The observed and expected upper limits are presented in Tab. 5.9.

The upper limit on $\sigma_{ggF\ HH}$ of 7.8×SM is the best result from the CMS experiment to date, and it is comparable to the constraint set by the ATLAS experiment combining the

	Upper limit at 95% C.L.		
	Expected	Observed	Best published result (Observed)
σ_{HH}	5.2×SM	7.7×SM	-
$\sigma_{ggF\ HH}$ fixing $\mu_{VBF\ HH} = 1$	5.3×SM	7.8×SM	6.9×SM (HH comb. with 36 fb^{-1} [123])
$\sigma_{VBF\ HH}$ fixing $\mu_{ggF\ HH} = 1$	208×SM	225×SM	840×SM ($HH \rightarrow b\bar{b}b\bar{b}$ with 126 fb^{-1} [111])

Table 5.9: The observed and expected upper limits.

most sensitive HH decay channels with the 2016 dataset. This is also the first upper limit on $\sigma_{VBF\ HH}$ set by the CMS experiment, which improves the best constraint set by the ATLAS experiment.

5.9.2   Constraints on the BSM Benchmark Hypotheses

Upper limits are also set on the twelve BSM benchmark hypotheses. The ggF HH events simulated at the LO for each benchmark hypothesis are used to derive the expected number of events as well as the signal model. Only the ggF HH categories are considered, and the VBF HH process is neglected in the statistical interpretation of the data. The observed and expected upper limits at 95% C.L. on the BSM benchmark hypotheses are shown in Fig. 5.33. The observed limits are slightly larger than the expected limits because of the small excess of events found in the ggF HH-enriched categories. The expected limits span from about 0.1 to 1 fb. The different sensitivity is due to the kinematics of each specific BSM benchmark hypothesis, which change the population of the expected signal events in the four-body mass categories.

5.9.3   Constraints on the Higgs Boson Couplings

Since no evidence of the HH signal are found, the 95% C.L. upper limits on $\sigma_{ggF\ HH} \times$ BR($HH \rightarrow \gamma\gamma b\bar{b}$) are derived as a function of the κ_λ parameter, as shown in the left panel of Fig. 5.34. The upper limit dependence on κ_λ is determined by the variation of the $\widetilde{M_x}$ distribution of the ggF HH signal that modifies the categories population,
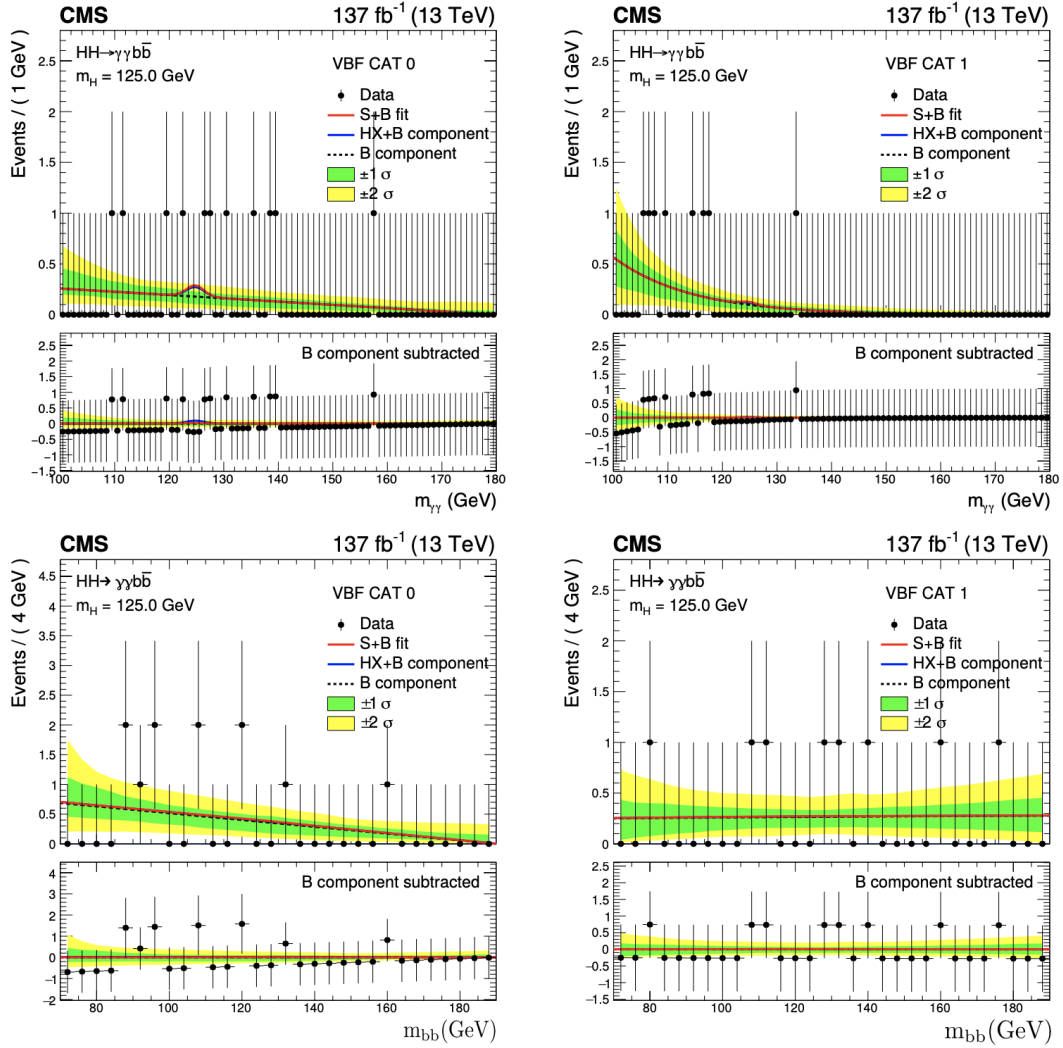
Figure 5.28: The $m_{\gamma\gamma}$ (upper row) and m_{jj} (bottom row) distribution for the selected events in data (black points) is shown for the two VBF HH categories with the curves corresponding to the signal + background fit (solid red),the single Higgs boson and the non-resonant processes H+B (solid blue) and the background only (dashed black), with bands covering the $\pm 1\sigma$ and $\pm 2\sigma$ uncertainties in the fitted background.
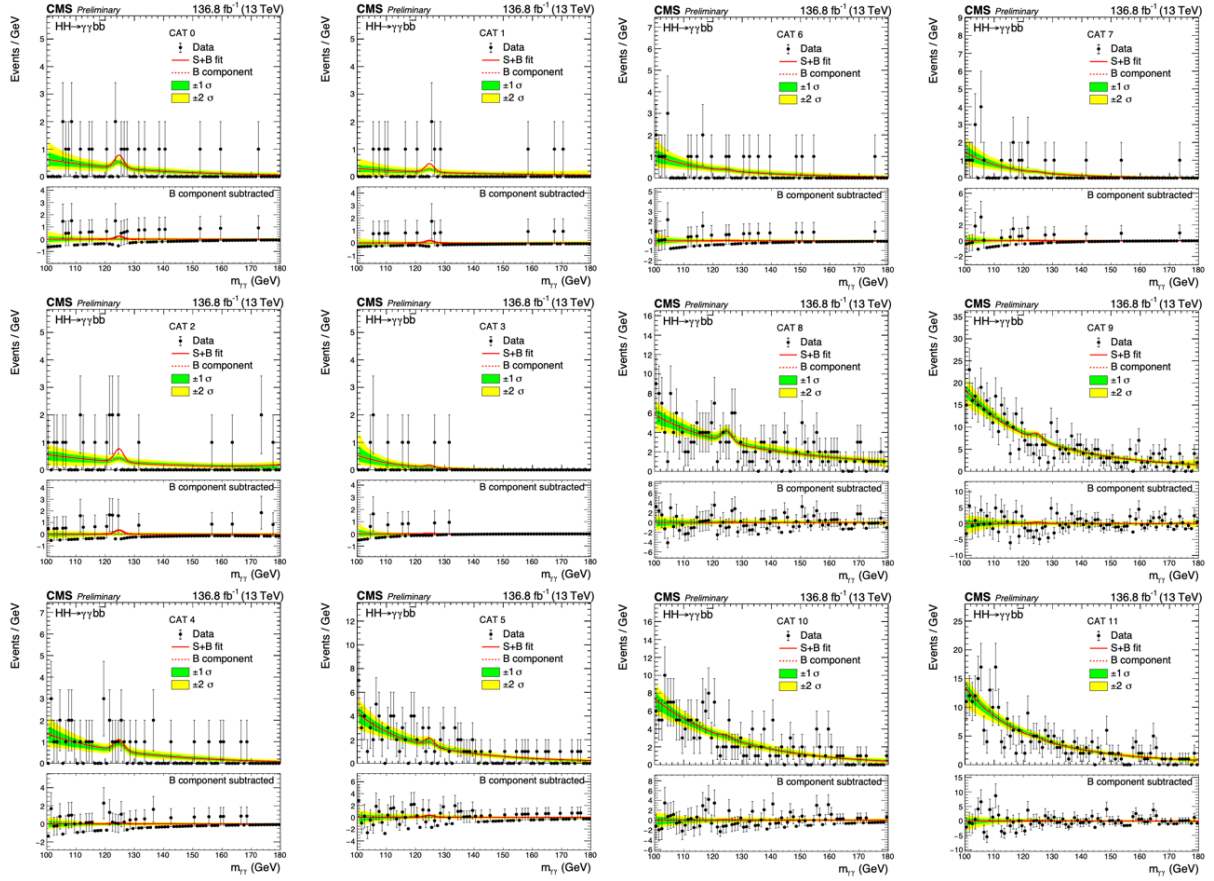
Figure 5.29: The $m_{\gamma\gamma}$ distribution for the selected events in data (black points) is shown for the twelve ggF HH categories with the curves corresponding to the signal + background fit (solid red) and the background only (dashed red), with bands covering the $\pm 1\sigma$ and $\pm 2\sigma$ uncertainties in the fitted background.
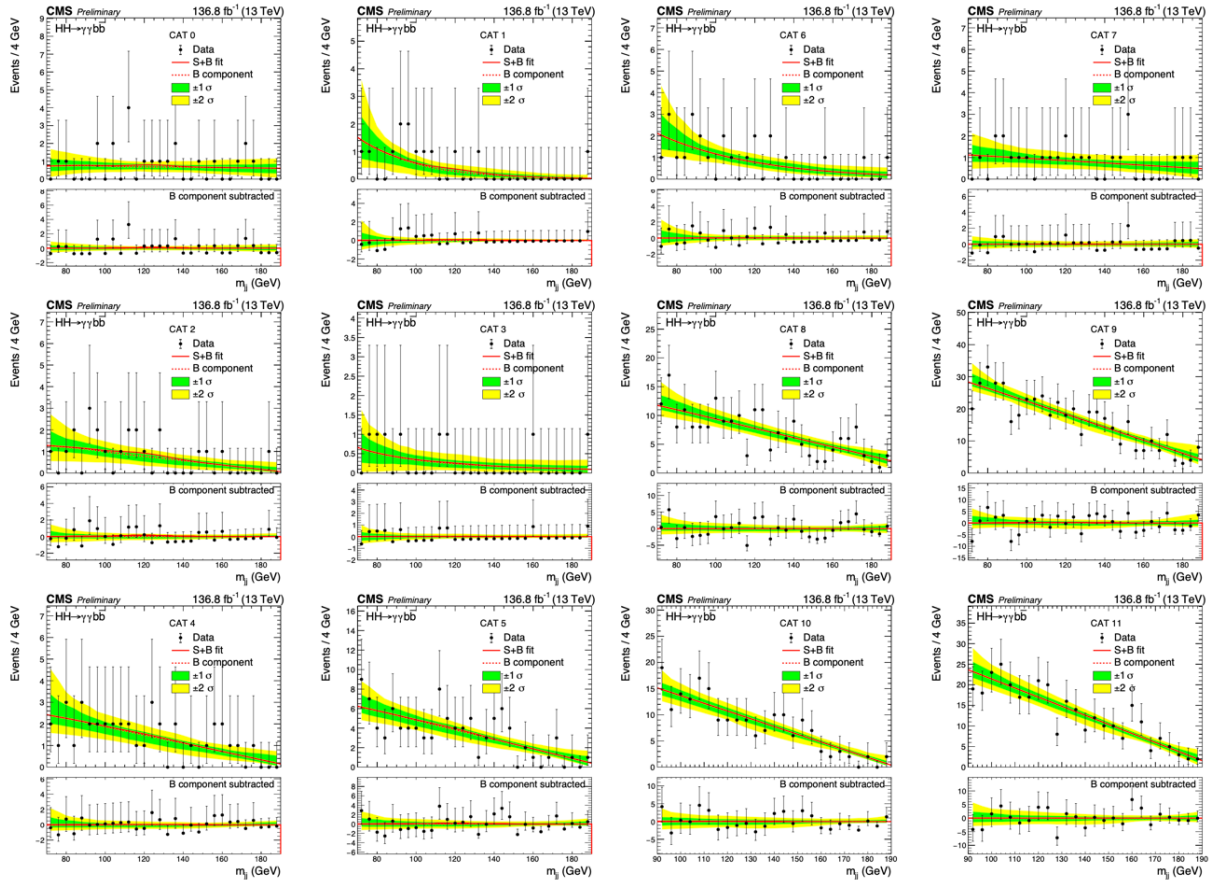
Figure 5.30: The m_{jj} distribution for the selected events in data (black points) is shown for the twelve ggF HH categories with the curves corresponding to the signal + background fit (solid red) and the background only (dashed red), with bands covering the $\pm 1\sigma$ and $\pm 2\sigma$ uncertainties in the fitted background.
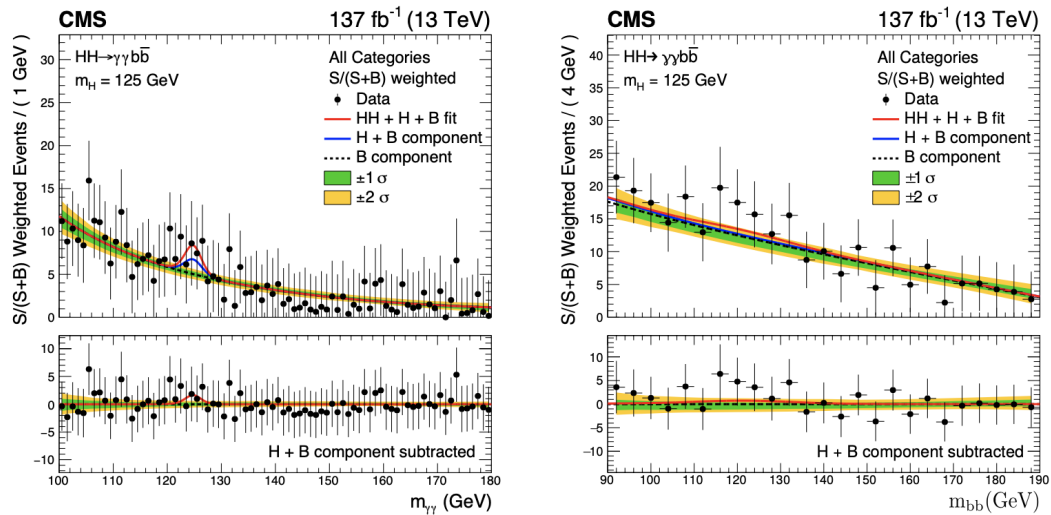

Figure 5.31: The $m_{\gamma\gamma}$ and m_{jj} distribution for the selected events in data (black points) weighted by $S/(S + B)$ with the curves corresponding to the signal + background fit (solid red),the single Higgs boson and the non-resonant processes H+B (solid blue) and the background only (dashed black), with bands covering the $\pm 1\sigma$ and $\pm 2\sigma$ uncertainties in the fitted background.
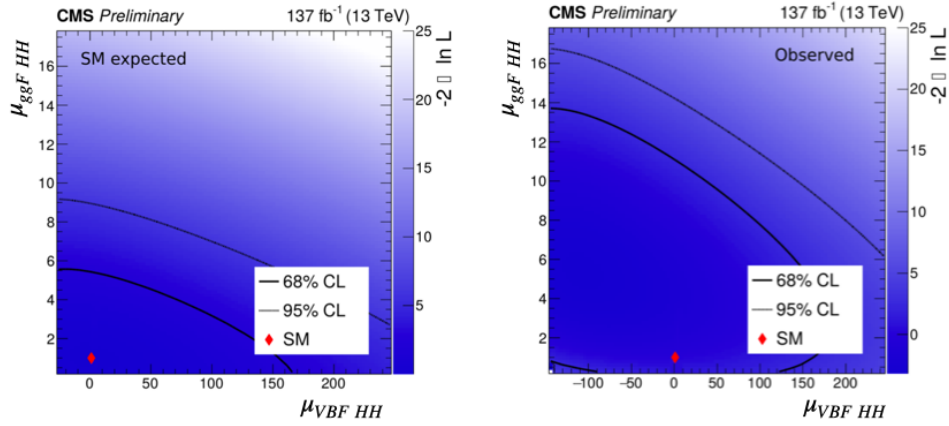
Figure 5.32: Expected and observed two dimensional likelihood scan of the $\mu_{ggF\ HH}$ (y-axis) and $\mu_{VBF\ HH}$ (x-axis) parameters, on the left and on the right side, respectively. The exclusion contours are also shown for the 68% (solid black line) and 95% (dashed black line) confidence levels.
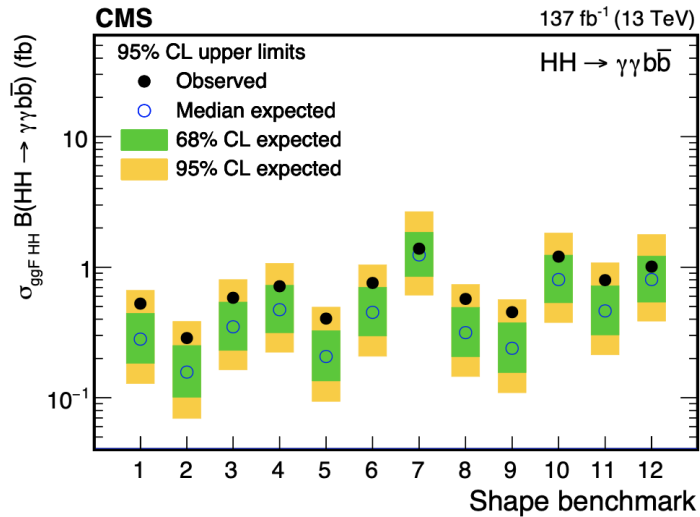

Figure 5.33: Expected and observed 95% CL upper limits on the $\sigma_{ggF\ HH} \times$ BR($HH \rightarrow \gamma\gamma b\bar{b}$) for the BSM benchmark models, shown with transparent and solid circles, respectively. The green and yellow bands represent the one and two standard deviation extensions beyond the expected limit, respectively.

thus the sensitivity to that signal. In particular, the high-$\widetilde{M}_x$ categories provides a higher sensitivity than the low-$\widetilde{M}_x$ categories because they have a smaller continuum background contamination. For κ_λ values in the [0,6] interval, the destructive interference between the ggF HH production diagram with a box loop of top quarks and the one with the triHiggs vertex is maximum. This causes a strong variation of the $\widetilde{M}_x$ distribution which migrates from the highest energy spectrum at about $\kappa_\lambda = 2$ to the softest spectrum at about $\kappa_\lambda = 5$. Comparing with the theoretical prediction, the resulting constraint on the κ_λ parameter is found to be:

$$\begin{aligned} &\text{Observed: -3.26} < \kappa_\lambda < 8.48 \text{ at 95\% C.L.} \\ &\text{Expected: -2.61} < \kappa_\lambda < 8.28 \text{ at 95\% C.L.} \end{aligned} \tag{5.16}$$

This result improves the existing most stringent constraint using the HH signal (-5 < κ_λ < 12 at 95% CL), from the ATLAS HH combination with the 2016 dataset [123] (36 fb^{-1}).

The same procedure is performed to extract a constraint on the c_{2V} parameter, as visible in the right panel of Fig. 5.34. In this case the upper limit is derived on $\sigma_{VBF\ HH} \times$ BR($HH \to \gamma\gamma b\bar{b}$) because the c_{2V} sensitivity is totally retained by the VBF HH process. As for the κ_λ parameter, the variation of the upper limit as a function of the c_{2V} value is determined by the corresponding $\widetilde{M}_x$ distribution variation. In this case, the interference between the three VBF HH production diagrams makes the $\widetilde{M}_x$ distribution spectrum migrate to high energies as soon as c_{2V} deviates from its SM prediction, enhancing the sensitivity to the VBF HH signal. The resulting constraint on the c_{2V} parameter is found to be :

$$\begin{aligned} &\text{Observed: -1.31} < c_{2V} < 3.45 \text{ at 95\% C.L.} \\ &\text{Expected: -0.96} < c_{2V} < 3.07 \text{ at 95\% C.L.} \end{aligned} \tag{5.17}$$

This is the first upper limit on the c_{2V} parameter set by the CMS experiment. The $HH \to \gamma\gamma b\bar{b}$ channel provides a good sensitivity also to the c_V parameter.

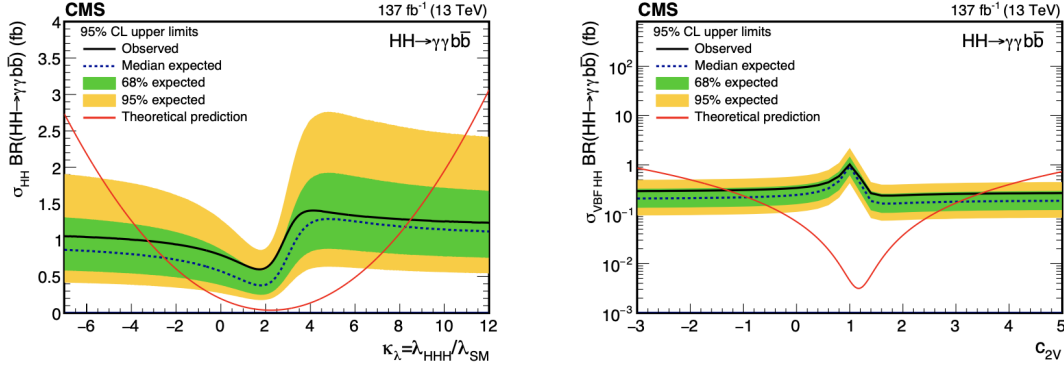Figure 5.34: Expected and observed 95% CL upper limits on the SM-like VBF HH production cross section times BR$(HH \to \gamma\gamma b\bar{b})$ obtained for different values of κ_λ and c_{2V} on the left and right side, respectively. The green and yellow bands represent the one and two standard deviation extensions beyond the expected limit, respectively. The red lines show the theoretical predictions.

Likelihood Scan for the Coupling Measurements

In order to measure the $(\kappa_\lambda,\ \kappa_t,\ c_V,\ c_{2V})$ parameters a profile likelihood is defined as:

$$\mathcal{L}_{prof}(\kappa_\lambda, \kappa_t, c_V, c_{2V}) = -2log\frac{\mathcal{L}(\kappa_\lambda, \kappa_t, c_V, c_{2V}, \hat{\hat{\theta}})}{\mathcal{L}(\hat{\kappa_\lambda}, \hat{\kappa_t}, \hat{c_V}, \hat{c_{2V}}, \hat{\theta})} \tag{5.18}$$

Where $\mathcal{L}$ is the likelihood defined in Eq. 5.5 expressed as a function of the Higgs couplings. The $\hat{\kappa_\lambda}$, $\hat{\kappa_t}$, $\hat{c_V}$, $\hat{c_{2V}}$, and $\hat{\theta}$ are the parameters values maximizing $\mathcal{L}$, i.e. their best estimate. Instead, $\hat{\hat{\theta}}$ is the set of nuisance values maximizing $\mathcal{L}$ for a given set of $(\kappa_\lambda,\ \kappa_t,\ c_V,\ c_{2V})$ values.

Since the Higgs boson production and decay channels considered are insufficient to constrain the full set of couplings, only one or two parameters are measured at a time while the other ones are fixed to the SM prediction. The profile likelihood is used to extract also the exclusion regions at 68% and 95% confidence level.

The $\mathcal{L}_{prof}$ value as a function of the parameter of interest (likelihood scan) is reported in Fig. 5.35 and 5.36 for the κ_λ and κ_t parameters, respectively. Each figure compares the likelihood scan with and without the inclusion of the $t\bar{t}H$ categories.

For the κ_λ-scan, when considering only the HH categories a difference is observed between the expected and the observed result because the small excess of events observed especially
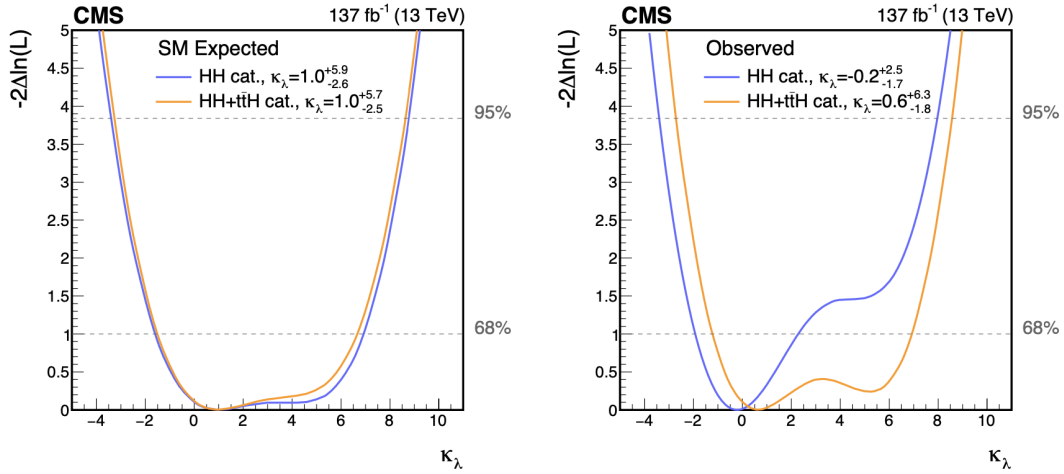
Figure 5.35: Expected and observed likelihood-scan of the κ_λ parameter, on the left and right sides, respectively. The likelihood scan is shown including the $t\bar{t}H$ categories (orange line) or using only the HH categories (blue line). The likelihood values corresponding to the 68% and 95% confidence levels are represented by the lower and upper horizontal dashed grey lines, respectively.
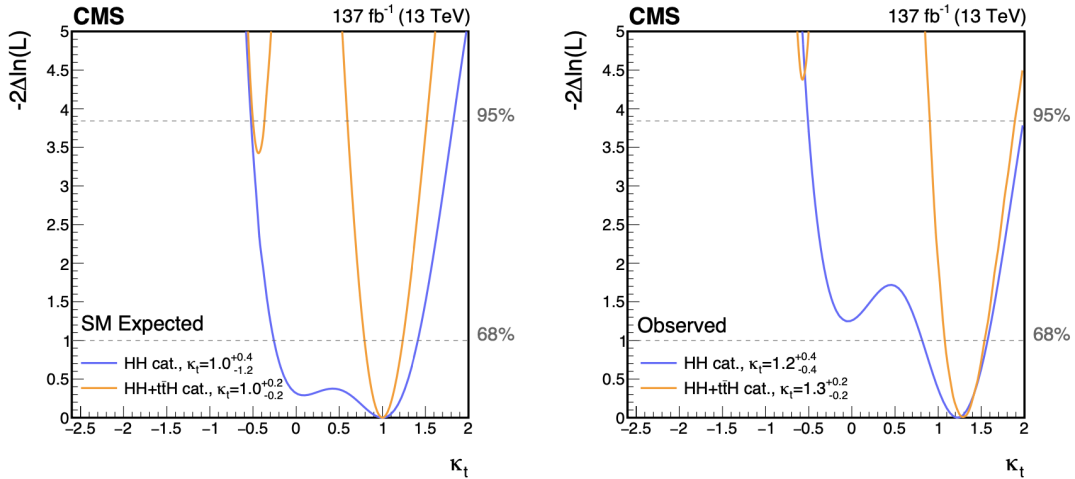

Figure 5.36: Expected and observed likelihood-scan of the κ_t parameter, on the left and right sides, respectively. The likelihood scan is shown including the $t\bar{t}H$ categories (orange line) or using only the HH categories (blue line). The likelihood values corresponding to the 68% and 95% confidence levels are represented by the lower and upper horizontal dashed grey lines, respectively.

in the ggF HH categories at medium $\widetilde{M_x}$, tends to exclude κ_λ values moderately larger than one. The inclusion of the $t\bar{t}H$ categories brings the observed likelihood close to the expectation of the SM. In fact, the $t\bar{t}H$ categories help constrain the $t\bar{t}H$ contamination in the HH categories. In particular, an excess of events is observed also in the $t\bar{t}H$ categories according to Ref. [124] that measured a signal strength of $\mu_{t\bar{t}H} = 1.4$ with an uncertainty of about $\pm 30\%$. As a consequence, the small excess of events observed in the HH categories is partially attributed to the excess of $t\bar{t}H$ signal that tends instead to favour a κ_λ value larger than one.

Due to the sensitivity of both the $t\bar{t}H$ cross section and the $H \to \gamma\gamma$ branching ratio to κ_t, the addition of the $t\bar{t}H$ categories greatly improves the sensitivity to the coupling for the κ_t-scan. Specifically, for $\kappa_t = \pm 1$, the $t\bar{t}H$ cross section and roughly the HH production cross section are symmetric. On the other hand, the sensitivity to a negative κ_t value is enhanced by the highly asymmetric $H \to \gamma\gamma$ branching ratio dependency on κ_t. This allows the exclusion of a negative value of κ_t at 95% confidence level.

The c_{2V} scan is shown in Fig. 5.37. For this parameter the sensitivity comes entirely from the VBF HH cross section, thus the contribution from the $t\bar{t}H$ categories is completely negligible. A c_V likelihood scan is out of the scope for this analysis because there are not experimental categories targeting the VH and qqH events that dominates the c_V sensitivity.
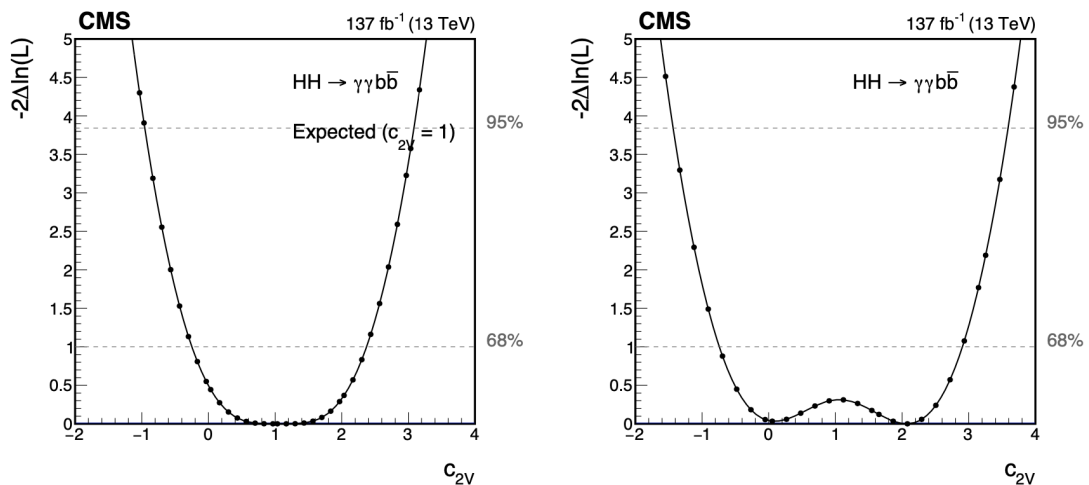

Figure 5.37: Expected and observed likelihood-scan of the c_{2V} parameter, on the left and right sides, respectively. The likelihood values corresponding to the 68% and 95% confidence levels are represented by the lower and upper horizontal dashed grey lines, respectively.

3464 The two dimensional likelihood scan of the $(\kappa_\lambda, \kappa_t)$ parameters is reported in Fig. 5.38.

3465 In the figure, the regions where the parametrization of $\sigma_{t\bar{t}H}$ $(\kappa_\lambda, \kappa_t)$ is not reliable are

3466 shown with a gray band. As expected, the improvement from the $t\bar{t}H$ categories is large.

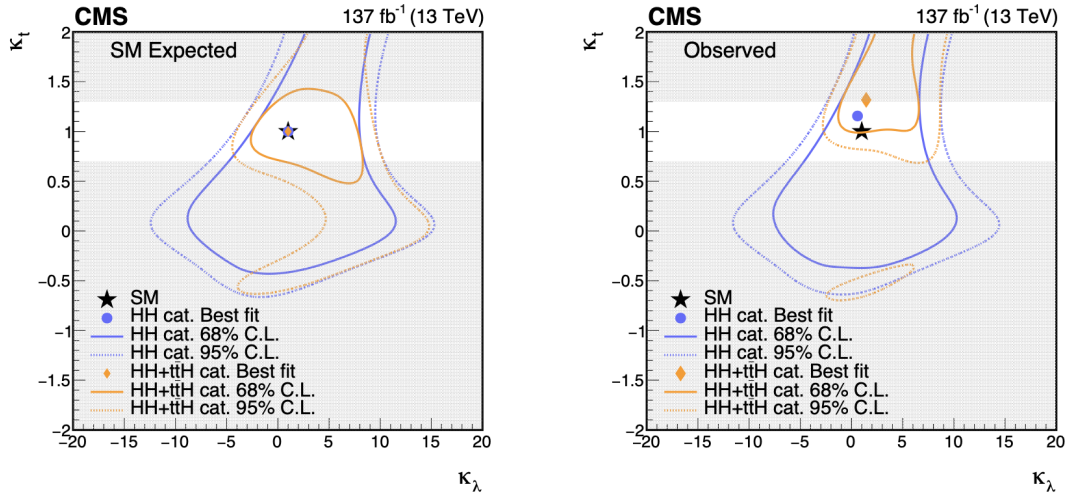3467 The result is found compatible with the SM.

Figure 5.38: Expected (left) and observed (right) two dimensional likelihood-scans of the $(\kappa_\lambda, \kappa_t)$ parameters including the $t\bar{t}H$ categories (orange) and using only the HH categories (blue). The exclusion regions at 68% and 95% confidence level are represented with the solid and the dashed lines, respectively. The region where the $\sigma_{t\bar{t}H}$ $(\kappa_\lambda, \kappa_t)$ parametrization is not reliable is highlighted in gray.

3468 The (κ_λ, c_{2V}) likelihood scan is shown in Fig. 5.39. The sensitivity on those two pa-

3469 rameters is dominated by the two considered HH production mechanisms. The coupling

3470 measurements are summarized in Tab. 5.10.

Parameters		Best fit $\pm 1\sigma$	Interval at 95% C.L.
κ_λ	obs	$0.6^{+6.3}_{-1.8}$	[-2.7, 8.6]
	exp	$1.0^{+5.7}_{-2.5}$	[-3.3, 8.6]
κ_t	obs	$1.3^{+0.2}_{-0.2}$	[0.90, 1.90]
	exp	$1.0^{+0.2}_{-0.2}$	[-0.50, -0.37] $\cup$ [0.59, 1.52]
c_{2V}	obs	$2.1^{+0.8}_{-2.8}$	[-1.4, 3.6]
	exp	$1.0^{+1.2}_{-1.2}$	[-2.0, 3.1]
$(\kappa_\lambda, \kappa_t)$	obs	(1.4, 1.3)	-
	exp	(1, 1)	-
(κ_λ, c_{2V})	obs	(0.0, 0.3)	-
	exp	(1, 1)	-

Table 5.10: Best fit values for the 1D and 2D likelihood scans of the Higgs coupling parameters. For the 1D scans the 1σ uncertainties and the 95% confidence intervals are also quoted.
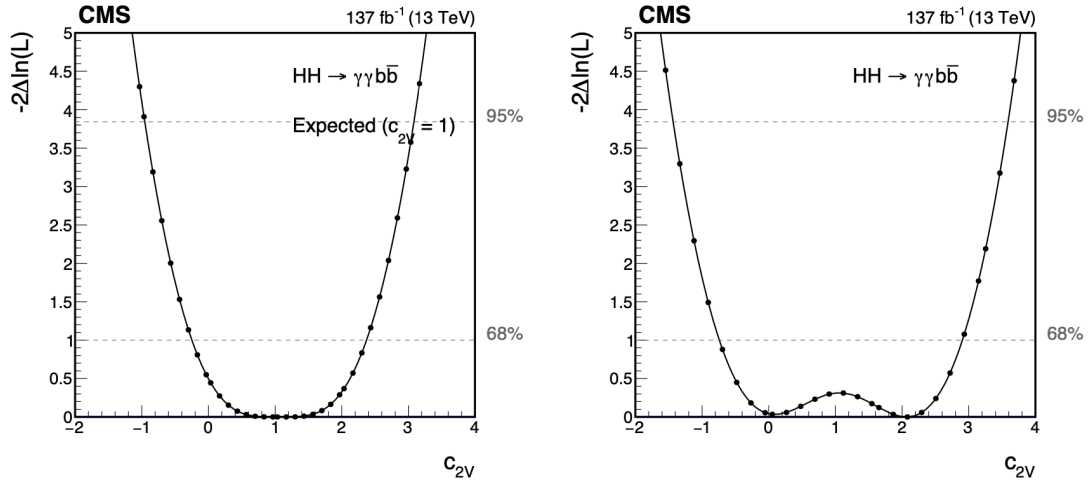
Figure 5.39: Expected (left) and observed (right) two dimensional likelihood-scans of the (κ_λ, c_{2V}) parameters. The exclusion regions at 68% and 95% confidence level are represented with the solid and the dashed lines, respectively.

5.10 Conclusion

In summary, all the results were found compatible with the SM predictions. No evidence of the HH process is found, thus, an upper limit was set to its cross section. The observed upper limit on the inclusive HH production cross section is 7.7×SM and corresponds to the most stringent result achieved by the CMS experiment to date. In the assumption of no HH signals, constraints on anomalous κ_λ values, and, for the first time with the data collected by the CMS experiment, on c_{2V} values are set. The observed constraints at 95% C.L. are -3.26 < κ_λ < 8.48, which is the most stringent constraint among the published results [123, 125], and -1.31 < c_{2V} < 3.45.

In the assumption of a HH signal, measurements of the κ_λ and κ_t parameters are performed through a combination of HH and $t\bar{t}H$ enriched categories. The measured values with one standard deviation uncertainty are $\kappa_\lambda = 0.6^{+6.3}_{-1.8}$ and $\kappa_t = 1.3\pm0.2$. A simultaneous measurement of the κ_λ and κ_t parameters is performed and the result is shown in Fig. 5.38

Further data will be collected by the CMS experiment during the Run 3, equivalent to an integrated luminosity of about 300 fb^{-1}. This dataset will improve the sensitivity to the HH signal and to the coupling parameters. Preliminary studies provide a projected limit (expected SM) on the inclusive ggF HH cross section of about 3.6×SM for the end

140

of Run 3. Run 3 will not provide the required amount of data for an evidence of the HH process. An evidence of a (SM) HH process is expected during the high-luminosity phase of the LHC.

Chapter 6

Resonant Triple Higgs Production and Decay to Six b-Quarks

6.1 Introduction

The Higgs boson is the simplest manifestation of the Brout-Englert-Higgs mechanism featuring a complex scalar field that generates mass through its interaction with other particles. Extensions to the scalar sector of the standard model (SM) provide prospective methods for observing physics beyond the standard model (BSM). Many theoretical models postulate extensions featuring additional scalar fields, yielding a rich phenomenology comprising additional scalar bosons, such as in the next-to-minimal supersymmetric standard model (NMSSM) [126], the two real scalar singlet model (TRSM) [47], and models with warped extra dimensions [127].

This analysis explores one of many possible extensions and investigates the production of a BSM resonance that decays into a Higgs boson and a BSM scalar, motivated by the TRSM, which proposes three scalar bosons, the lightest of which is the familiar SM Higgs boson. In this framework, the heaviest BSM resonance, denoted by X, decays into the BSM scalar, denoted Y, and the SM Higgs boson, following the mass hierarchy $m_X > m_Y > m_H$ where m_Y is large enough that the decay of $Y \to HH$ is kinematically available.

The search will consider solely the scenario in which the Higgs bosons decay into pairs of

142

b quarks.

6.2 Search Strategy

The objective of this analysis is to search for the asymmetric multi-scalar production process in which a new resonance (X) decays into a Higgs boson (H) and an extra scalar (Y), where Y decays into two Higgs bosons and the three Higgs bosons decay into pairs of b quarks, resulting in the six b final state. The search is performed in mass ranges of X (1–4 TeV) and Y (300–2800 GeV) where the H is highly Lorentz-boosted. In this kinematic regime, decayed b-quark pairs are collimated enough to allow the reconstruction of H using single large-area jets (fatjets). Combination of three Higgs bosons with different energies gives different topologies for different mixes as shown in Fig. 6.1 where fraction of generated boosted Higgs bosons are displayed. The fraction is ratio of $f_{gen} = N^{boostedH}/N^{Higgs}$ where, $N^{boostedH}$ is number of generated boosted Higgs bosons and N^{Higgs} is total number of Higgs bosons. The generated boosted Higgs bosons are selected using $|\eta| < 2$ and distance between two generated b-quark $\Delta R(b, b) < 0.8$ cuts. The Fig. 6.1 shows different topologies are concentrated in different phase space depending on the m_X and m_Y. Out of which, two topologies are considered: one topology where all three Higgs bosons are boosted and another where two of the three Higgs bosons are boosted.

The analyzed mass range is for m_X from 1 TeV to 4 TeV and m_Y from 250 GeV 2.8 TeV. Events are selected by implementing a cut-based approach and the identified jets are paired to reconstruct the H candidates or in boosted case, fatjets are identified to reconstruct the H candidate.

One of the most significant challenges presented in this analysis arises from the prediction of background events, of which the predominant expected processes are quantum chromodynamic (QCD) multijet production and top quark pair ($t\bar{t}$) production. Monte Carlo (MC) simulations of QCD multijet events are precise only to leading order (LO) and are therefore typically inaccurate, motivating the development of a data-driven method designed to accurately model the background shape and event yields. 2D-alphabet method is used to model background explained in Sec. 6.5.1
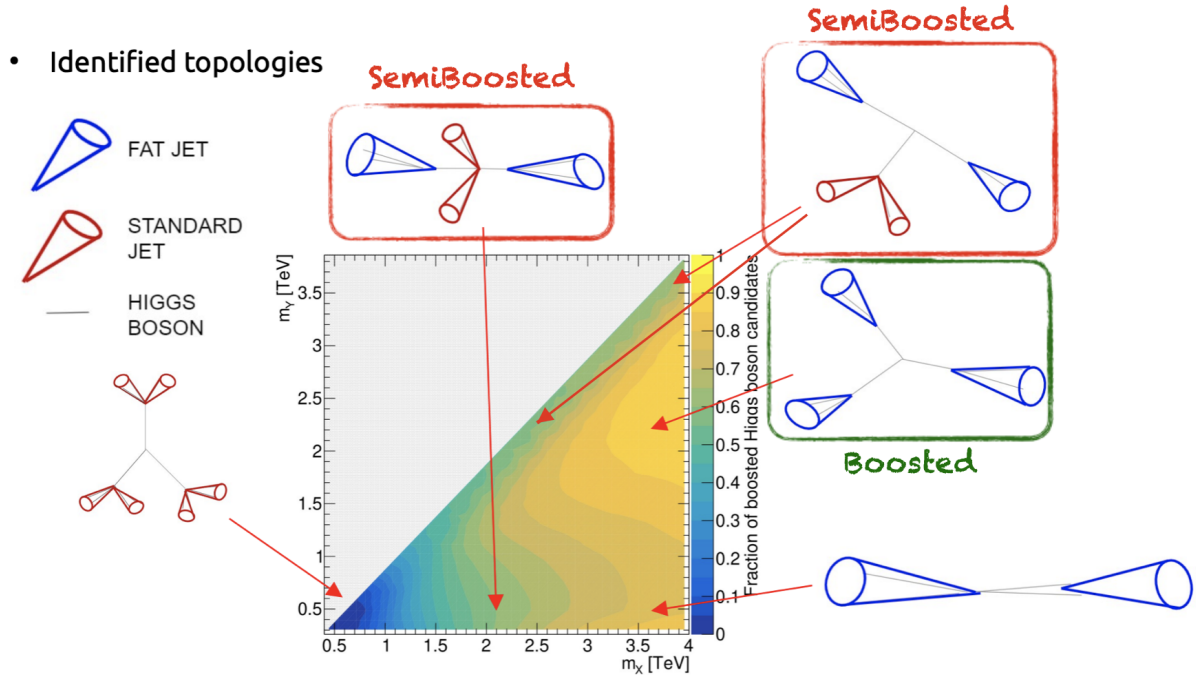
143

Figure 6.1: Fraction of generated boosted Higgs boson candidates in (m_X, m_Y) plane.

Signal and background event distributions are plotted as a function of M_{jjj} corresponding to reconstructed mass of X and M_{jj} - reconstructed mass of Y with consideration of applicable systematic variations in order to extract the expected upper limit on the production cross section for the array (m_X, m_Y). The data analysis will be carried out independently but in a similar fashion for the 2016, 2017, and 2018 datasets and the full Run 2 result will be a statistical combination of the independent results. The final results are still to be determined and published.

6.3   Data Samples and Simulated Events

6.3.1   Data Samples and Trigger Requirements

The analysis is performed on the full Run 2 dataset, corresponding to an integrated luminosity of 137.6 fb^{-1} collected at $\sqrt{s} = 13$ TeV in 2016, 2017, and 2018. Datasets produced in Ultra Legacy Campaign NanoAODv9 are used as listed below:

`/JetHT/Run2017B-UL2017_MiniAODv2_NanoAODv9-v1/NANOAOD`

`/JetHT/Run2017C-UL2017_MiniAODv2_NanoAODv9-v1/NANOAOD`

```
3553  /JetHT/Run2017D-UL2017_MiniAODv2_NanoAODv9-v1/NANOAOD
3554  /JetHT/Run2017E-UL2017_MiniAODv2_NanoAODv9-v1/NANOAOD
3555  /JetHT/Run2017F-UL2017_MiniAODv2_NanoAODv9-v1/NANOAOD
```

The events are characterized by highly energetic fatjets arising from collimated b-quark pairs of boosted Higgs bosons. Multijet event selection at the trigger level is achieved by choosing High Level Trigger (HLT) paths featuring large transverse momentum jets. Tab. 6.1 lists the trigger paths used in this analysis.

Year	HLT Trigger Paths
2016	HLT_PFHT900_v* OR HLT_PFJet450_v*
2017	HLT_PFHT1050_v* OR HLT_AK8PFJet500_v* OR HLT_PFJet500_v*
2018	HLT_PFHT1050_v* OR HLT_AK8PFJet500_v* OR HLT_PFJet500_v*

Table 6.1: HLT Trigger Paths applied

6.3.2 Simulated Signal Samples

$X \to Y(HH)H$ Monte Carlo samples have been produced following the recommendation from the LHC Higgs Cross Section working group using MADGRAPH5_AMC@NLO 2.6.5 to simulate event generation and PYTHIA8 to simulate the hadronization process. The X and Y resonances are assumed to be narrow and the generated width is set to 1 MeV. The generated samples are produced in context of an NMSSM model implemented.

The individual dataset samples were centrally produced with the standard CMS full simulation procedure. List of m_Y points considered for each m_X hypothisis considered for the analysis is listed in Tab. 6.2. Fig. 6.2 gives idea about covered phase-space of used and generated samples for 2017 where empty region denotes kinematically forbidden region $(2m_H < m_Y < (m_X - m_H))$

6.3.3 Simulated Background Samples

Monte Carlo background samples are generated to determine the background composition 98 but are not used to estimate the expected background shapes or yield. A full list of the MC background samples is provided in Tab. 6.3 for year 2016 and Tab. 6.4 for years 2017 and 2018.

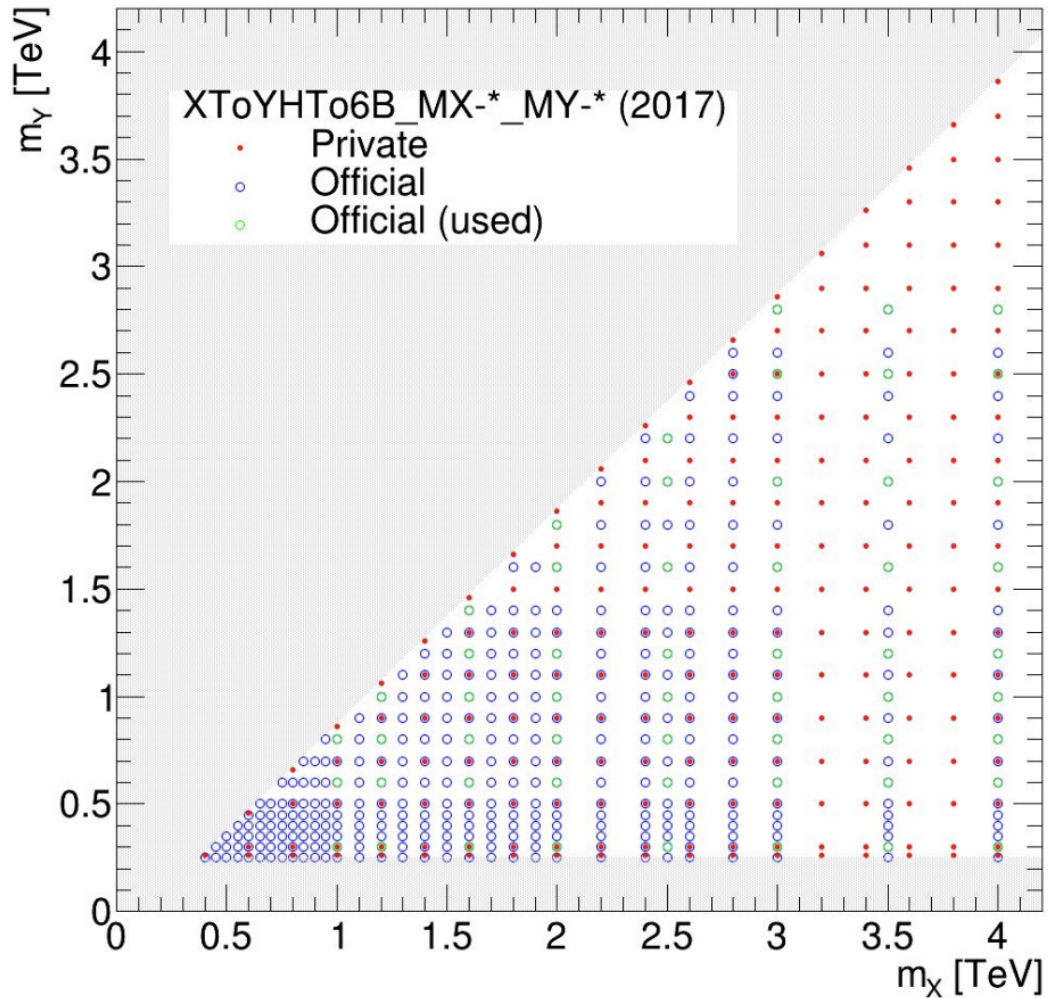| m_X	m_Y
1000	300, 600, 800
1200	300, 600, 800, 1000
1600	300, 600, 800, 1000, 1200, 1400
2000	300, 600, 800, 1000, 1200, 1600, 1800
2500	300, 600, 800, 1000, 1200, 1600, 2000, 2200
3000	300, 600, 800, 1000, 1200, 1600, 2000, 2500, 2800
3500	300, 600, 800, 1000, 1200, 1600, 2000, 2500, 2800
4000	300, 600, 800, 1000, 1200, 1600, 2000, 2500, 2800

Table 6.2: List of m_Y points for each m_X hypothesis considered in the analysis.

Figure 6.2: Simulated Signal samples for 2017. Blue circles are centrally produced samples at CMS from which green circled ones are used for this analysis.

Year	Process	Dataset Name
2016	TTbarHadronic	/TTToHadronic_TuneCP5_13TeV-powheg-pythia8/RunIISummer20UL16NanoAODv9-106X_mcRun2_asymptotic_v17-v1/NANOAODSIM
	TTbarSemileptonic	/TTToSemiLeptonic_TuneCP5_13TeV-powheg-pythia8/RunIISummer20UL16NanoAODv9-106X_mcRun2_asymptotic_v17-v1/NANOAODSIM
	QCD, $700 < H_T < 1000$ GeV	/QCD_HT700to1000_TuneCP5_PSWeights_13TeV-madgraph-pythia8/RunIISummer20UL16NanoAODv9-106X_mcRun2_asymptotic_v17-v1/NANOAODSIM
	QCD, $1000 < H_T < 1500$ GeV	/QCD_HT1000to1500_TuneCP5_PSWeights_13TeV-madgraph-pythia8/RunIISummer20UL16NanoAODv9-106X_mcRun2_asymptotic_v17-v1/NANOAODSIM
	QCD, $1500 < H_T < 2000$ GeV	/QCD_HT1500to2000_TuneCP5_PSWeights_13TeV-madgraph-pythia8/RunIISummer20UL16NanoAODv9-106X_mcRun2_asymptotic_v17-v1/NANOAODSIM
	QCD, $H_T > 2000$ GeV	/QCD_HT2000toInf_TuneCP5_PSWeights_13TeV-madgraph-pythia8/RunIISummer20UL16NanoAODv9-106X_mcRun2_asymptotic_v17-v1/NANOAODSIM
2016-APV	TTbarHadronic	/TTToHadronic_TuneCP5_13TeV-powheg-pythia8/RunIISummer20UL16NanoAODAPVv9-106X_mcRun2_asymptotic_preVFP_v11-v1/NANOAODSIM
	TTbarSemileptonic	/TTToSemiLeptonic_TuneCP5_13TeV-powheg-pythia8/RunIISummer20UL16NanoAODAPVv9-106X_mcRun2_asymptotic_preVFP_v11-v1/NANOAODSIM
	QCD, $700 < H_T < 1000$ GeV	/QCD_HT700to1000_TuneCP5_PSWeights_13TeV-madgraph-pythia8/RunIISummer20UL16NanoAODAPVv9-106X_mcRun2_asymptotic_preVFP_v11-v1/NANOAODSIM
	QCD, $1000 < H_T < 1500$ GeV	/QCD_HT1000to1500_TuneCP5_PSWeights_13TeV-madgraph-pythia8/RunIISummer20UL16NanoAODAPVv9-106X_mcRun2_asymptotic_preVFP_v11-v1/NANOAODSIM
	QCD, $1500 < H_T < 2000$ GeV	/QCD_HT1500to2000_TuneCP5_PSWeights_13TeV-madgraph-pythia8/RunIISummer20UL16NanoAODAPVv9-106X_mcRun2_asymptotic_preVFP_v11-v1/NANOAODSIM
	QCD, $H_T > 2000$ GeV	/QCD_HT2000toInf_TuneCP5_PSWeights_13TeV-madgraph-pythia8/RunIISummer20UL16NanoAODAPVv9-106X_mcRun2_asymptotic_preVFP_v11-v1/NANOAODSIM

Table 6.3: Summary of the Monte Carlo background samples used for 2016.

Year	Process	Dataset Name
2017	TTbarHadronic	/TTToHadronic_TuneCP5_13TeV-powheg-pythia8/RunIISummer20UL17NanoAODv9-106X_mc2017_realistic_v9-v1/NANOAODSIM
	TTbarSemileptonic	/TTToSemiLeptonic_TuneCP5_13TeV-powheg-pythia8/RunIISummer20UL17NanoAODv9-106X_mc2017_realistic_v9-v1/NANOAODSIM
	QCD, $700 < H_T < 1000$ GeV	/QCD_HT700to1000_TuneCP5_PSWeights_13TeV-madgraph-pythia8/RunIISummer20UL17NanoAODv9-106X_mc2017_realistic_v9-v1/NANOAODSIM
	QCD, $1000 < H_T < 1500$ GeV	/QCD_HT1000to1500_TuneCP5_PSWeights_13TeV-madgraph-pythia8/RunIISummer20UL17NanoAODv9-106X_mc2017_realistic_v9-v1/NANOAODSIM
	QCD, $1500 < H_T < 2000$ GeV	/QCD_HT1500to2000_TuneCP5_PSWeights_13TeV-madgraph-pythia8/RunIISummer20UL17NanoAODv9-106X_mc2017_realistic_v9-v1/NANOAODSIM
	QCD, $H_T > 2000$ GeV	/QCD_HT2000toInf_TuneCP5_PSWeights_13TeV-madgraph-pythia8/RunIISummer20UL17NanoAODv9-106X_mc2017_realistic_v9-v1/NANOAODSIM
2018	TTbarHadronic	/TTToHadronic_TuneCP5_13TeV-powheg-pythia8/RunIISummer20UL18NanoAODv9-106X_upgrade2018_realistic_v16_L1v1-v1/NANOAODSIM
	TTbarSemileptonic	/TTToSemiLeptonic_TuneCP5_13TeV-powheg-pythia8/RunIISummer20UL18NanoAODv9-106X_upgrade2018_realistic_v16_L1v1-v1/NANOAODSIM
	QCD, $700 < H_T < 1000$ GeV	/QCD_HT700to1000_TuneCP5_PSWeights_13TeV-madgraph-pythia8/RunIISummer20UL18NanoAODv9-106X_upgrade2018_realistic_v16_L1v1-v2/NANOAODSIM
	QCD, $1000 < H_T < 1500$ GeV	/QCD_HT1000to1500_TuneCP5_PSWeights_13TeV-madgraph-pythia8/RunIISummer20UL18NanoAODv9-106X_upgrade2018_realistic_v16_L1v1-v1/NANOAODSIM
	QCD, $1500 < H_T < 2000$ GeV	/QCD_HT1500to2000_TuneCP5_PSWeights_13TeV-madgraph-pythia8/RunIISummer20UL18NanoAODv9-106X_upgrade2018_realistic_v16_L1v1-v1/NANOAODSIM
	QCD, $H_T > 2000$ GeV	/QCD_HT2000toInf_TuneCP5_PSWeights_13TeV-madgraph-pythia8/RunIISummer20UL18NanoAODv9-106X_upgrade2018_realistic_v16_L1v1-v1/NANOAODSIM

Table 6.4: Summary of the Monte Carlo background samples used for 2017 and 2018.

6.4 Event Selection

This analysis focuses on two main topology as mentioned before. The first, boosted topology is where all three Higgs bosons are lorentz boosted and each Higgs boson decays into AK8jet consisting of two b-quarks which gives three AK8jets. Thus, for signal region, at least three AK8jets are required with $p_T > 250$ GeV, $|\eta| < 2.5$, and $m_{SD} \in [100, 150]$. To select validation region close to signal region phase space, it has same selection criteria as signal region except two AK8jets with highest p_T are required to be outside the Higgs mass window with $m_{SD} > 50$.

The second topology considered is semi-boosted topology. It has two out of three Higgs bosons lorentz boosted, each decaying to one AK8jet consisting two b-quarks and one Higgs boson decays into two separate b-quark jets gives two AK8jets and pair of AK4 b-jets. To avoid double counts, semi-boosted topology requires exactly two AK8jets present in the event. For signal region, events with exactly two AK8jets with $p_T > 250$ GeV, $|\eta| < 2.5$, and $m_{SD} \in [100, 150]$ are required. Two AK4jets are required with $p_T^{jet} > 30$ GeV, $|\eta^{jet}| < 2.5$, DeepJet score > 0.0532 (loose WP), to separate them from already selected two AK8jets, $\Delta R(AK4, AK8) > 0.8$ and invariant mass of jet pair, $m_{dijet} \in [90, 150]$. For the validation region, exactly same cuts except two AK8jets are required to be outside the Higgs mass window with $m_{SD} > 50$.

For background estimation, explained in Section 6.5.1, events are divided into pass and fail category based on ParticleNet XbbvsQCD score. If one of more AK8jet passes the loose working point (WP) cut (ParticleNet XbbvsQCD score > 0.9105), the event falls into the pass category. For the cases where no jet passes the cut, the event is in fail category. For both boosted and semi-boosted topology, it is applied in the same manner. Fig. 6.3 gives overview of selection cuts for boosted and semi-boosted topologies respectively.

Fig. 6.4 shows cut-flow for boosted and semi-boosted signal region with pass and fail categories is given. Fig. 6.5 gives efficiency map of boosted topology (left) with maximum efficiency around 20% and semi-boosted topology (right) with maximum efficiency around 15%. In large parts of the mass plane boosted and semi-boosted selections complement one another.

149

Boosted signal region (SR_b)	
≥3 AK8 jets with	
p_T > 250 GeV $|\eta|$ < 2.5 100 < $m_{softdrop}$ < 150 GeV	
Categories: based on ParticleNet score > 0.9105 (loose WP)	
Fail	**Pass**
0 jets passing the cut	≥1 jets passing the cut

Semiboosted signal region (SR_sb)	
==2 AK8 jets as in the boosted selection	
≥1 AK4 jet pair with	
p_T^{jet} > 30 GeV $|\eta^{jet}|$ < 2.5 DeepB^{jet} > 0.0532 (loose WP) ΔR(AK4, AK8) > 0.8 90 < m_{dijet} < 150 GeV	
Categories: as in the boosted selection	
Fail	**Pass**
0 AK8 jets passing the cut	≥1 AK8 jets passing the cut

Boosted validation region (VR_b)
Same as the signal region but with the 2 leading jets (in p_T) outside the Higgs mass window and having $m_{softdrop}$ > 50 GeV

Semiboosted validation region (VR_sb)
Same as the signal region but with the 2 AK8 jets outside the Higgs mass window and having $m_{softdrop}$ > 50 GeV

Figure 6.3: Event selection criteria for boosted and semi-boosted topologies.
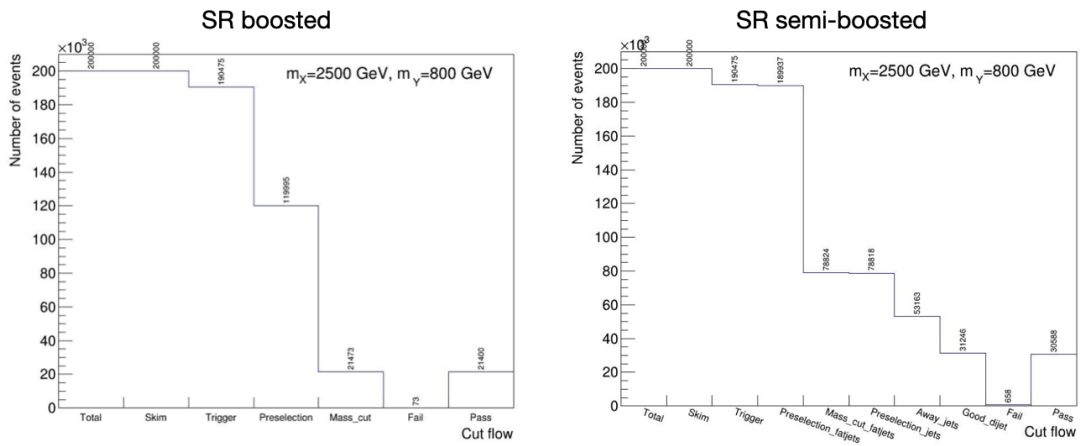
Figure 6.4: Cut-flow for boosted and semi-boosted signal region with pass and fail categories.
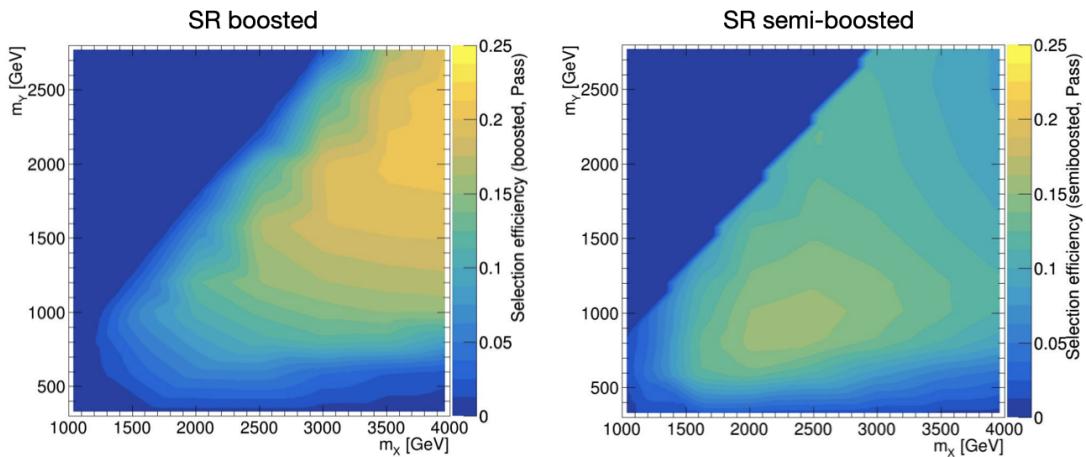
Figure 6.5: Efficiency map for boosted and semi-boosted signal region pass category.

6.4.1   Dijet mass vs Trijet mass

As mentioned in Section 6.2, presence of two heavy resonances X and Y in m_{jj} vs m_{jjj} distribution indicates the signal. The analysis is to search for 2D bump corresponding to X and Y resonances. This 2D plane consists of dijet mass (m_{jj}) and trijet mass (m_{jjj}). After the event selection, we get three Higgs boson candidates and invariant mass of all three Higgs boson gives reconstructed mass of X resonance - trijet mass.

The Y resonance decays into two Higgs bosons. From three reconstructed Higgs boson candidates, there can be three possible pairs. There is no general way to find the right combination of Higgs boson candidate pair from the Y resonance. To overcome this issue, all three pair combinations are considered and for dijet mass distribution, there are three entries per event. It is still expected to see mass peak at m_Y.

Fig. 6.6 shows the distribution of trijet mass and dijet mass for mass points $m_X = 2500$, $m_Y = 600, 800, 1200, 2000$ for boosted and semi-boosted topologies.

6.5   Background Estimation

Since background events are not accurately modeled by Monte Carlo simulations, a data driven background estimation procedure is developed and used to model the background in the signal region. Background modeling is performed using 2D Alphabet method.

6.5.1   2D Alphabet

2D Alphabet is a framework to construct the workspace for a specific type of background estimate, provide input to the Combine statistical tool, plot the 2D distributions from the fit result, and provide the infrastructure to test this result.

The name of the framework is derived from its data-driven background estimate of combinatorial backgrounds that are otherwise poorly modeled by Monte Carlo simulation. In many cases, the background being modeled is QCD multijet production and as a default.
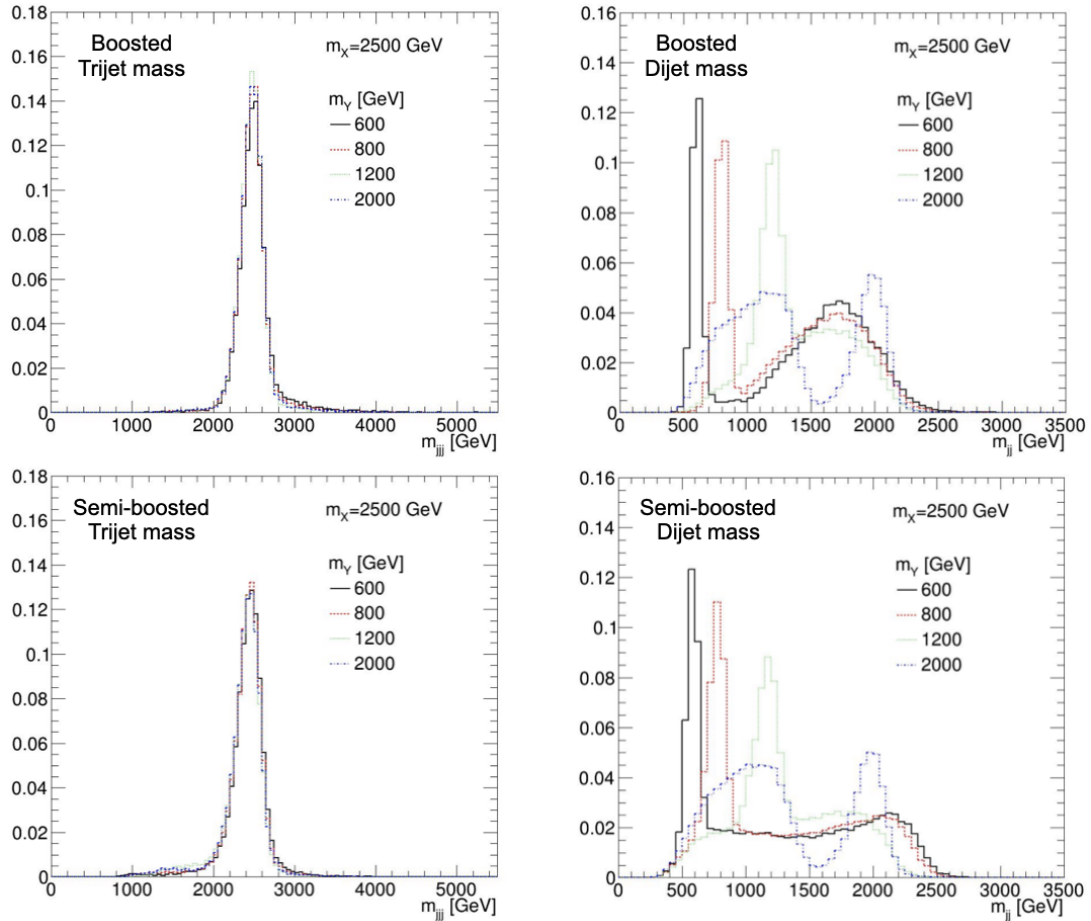
Figure 6.6: Trijet mass (left) and dijet mass (right) distribution for boosted (upper) and semi-boosted (lower) topologies.

However, depending on the selection, there may be other backgrounds accounted for as well such as $t\bar{t}$ in our case.

The data driven background estimation method is a two dimensional version. It uses an analytic *transfer function* to *transfer* the background contribution in a control region to the contribution in the signal region. If the shapes of the background distributions in the control region and signal region are identical, then the transfer function is just a constant factor which only changes the normalization from one region to the other.

The events are divided in two categories: pass - signal rich and fail - signal depleted category. These categories are further divided in signal region (SR) and validation region (VR). Validation region is used to validate the background estimation method. This gives four separate phase-space which consists of three signal depleted and one signal rich region shown in Fig. 6.7.

The ABCD method measures data distributions in selection regions A, B, and D (Fig. 6.7) which are enriched in background and depleted of signal. In the figure, var1 and var2 are the selection variables and the C region is the signal region of the analysis. Binned distributions are created in some third variable (var3) for each of the four regions. The ratio of A/B and C/D are assumed to be equal and therefore, $A/B * D = C$. Here, A/B is the transfer function.
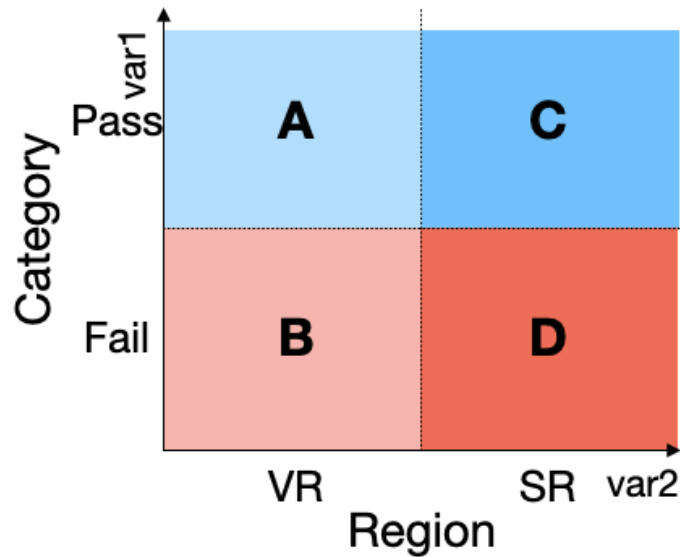
Figure 6.7: Illustration of 2D alphabet method.

To create QCD estimate, measure the binned transfer function from A and B and then weight events in region D to get the estimate along your var3 axis of the QCD. a smooth $R_{P/F}$ transfer function relates event yields of the data-driven background components in the pass (P) and fail (F) categories. For QCD background, event yields in i^{th} bin for fail category can be given as:

$$n_F^{QCD}(i) = n_F^{data}(i) - n_F^{bkg,MC}(i) \tag{6.1}$$

Here, last term is well modeled background component other than QCD taken from MC simulation. For fully data-driven background estimation for all backgrounds combined, one can set $n_F^{bkg,MC}(i) = 0$. Transfer function is derived from the ratio of background components in pass and fail category.

$$n_P^{QCD}(i) = n_F^{QCD}(i) \cdot R_{P/F}(i) \tag{6.2}$$

where $R_{P/F}$ transfer function is modeled as a simple low-order 2D polynomial.

6.5.2 2DAlphabet fits

From event selection, we have signal and validation regions with pass and fail categories. The first step for background estimation is to derive transfer function from validation regions. Fig. 6.8 and 6.9 show 2D Alphabet background only fit for pass and fail categories in validation region for boosted and semi-boosted topology respectively using 2017 samples.
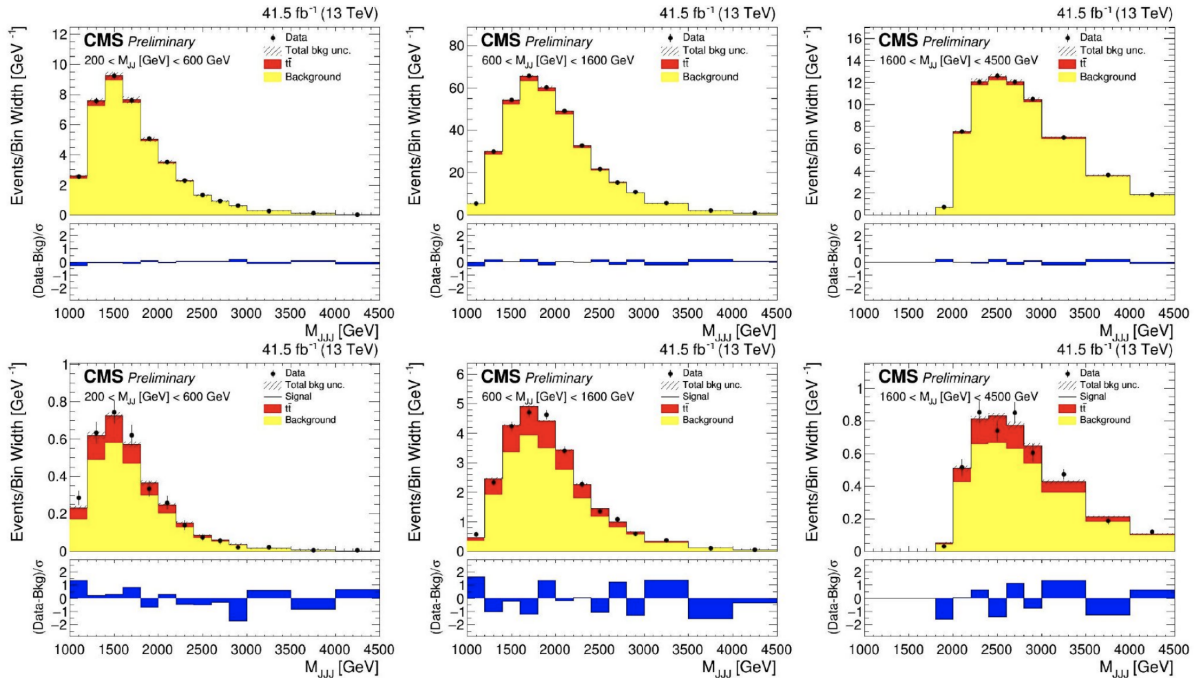
Figure 6.8: 2D Alphabet background only fit for fail (upper) and pass (lower) categories in validation region for boosted topology.

After deriving transfer function from validation region, the 2DAlphabet method would formally require unblinding the signal region (SR) for in-situ $R_{P/F}$ transfer function measurement. It is only possible after unblinding the analysis. Before that, signal-depleted SR fail category can be unblinded and use the data together with the validation region (VR) $R_{P/F}$ transfer function to obtain toy data in the SR pass category assuming that $R_{P/F}$ transfer function is same for validation region and signal region.
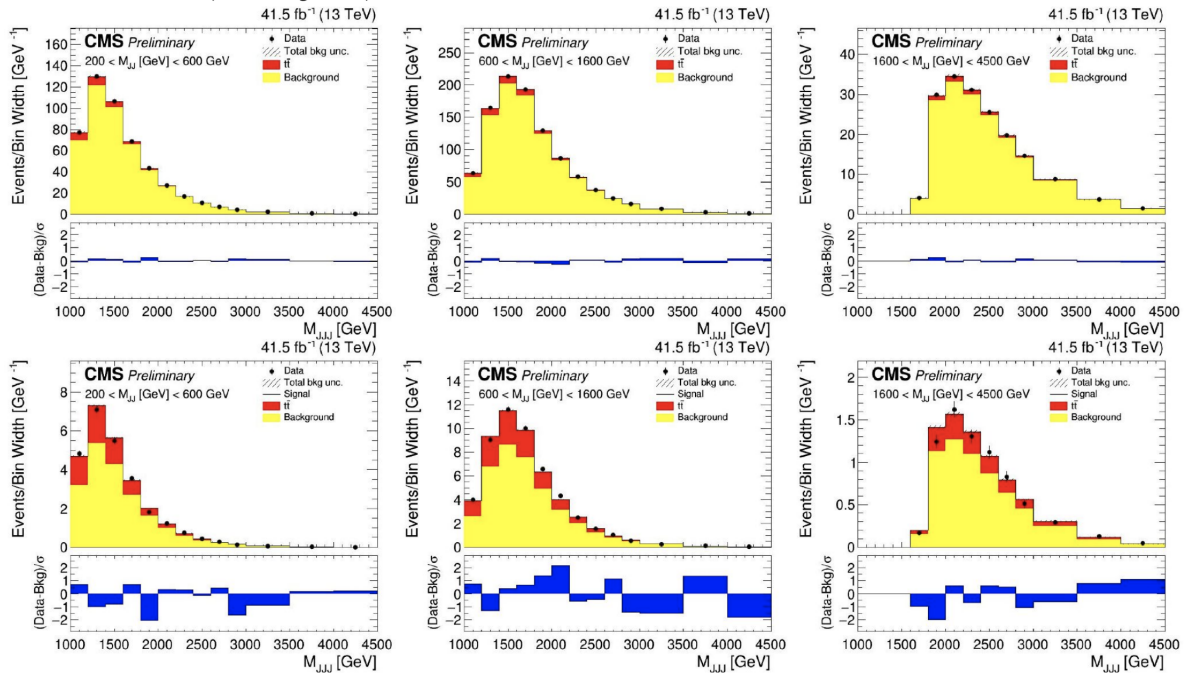
Figure 6.9: 2DAlphabet background only fit for fail (upper) and pass (lower) categories in validation region for semi-boosted topology.

Fig. 6.10 and 6.11 show 2DAlphabet background only fit for pass and fail categories in signal region (using generated toy data in pass category) for boosted and semi-boosted topology respectively using 2017 samples.
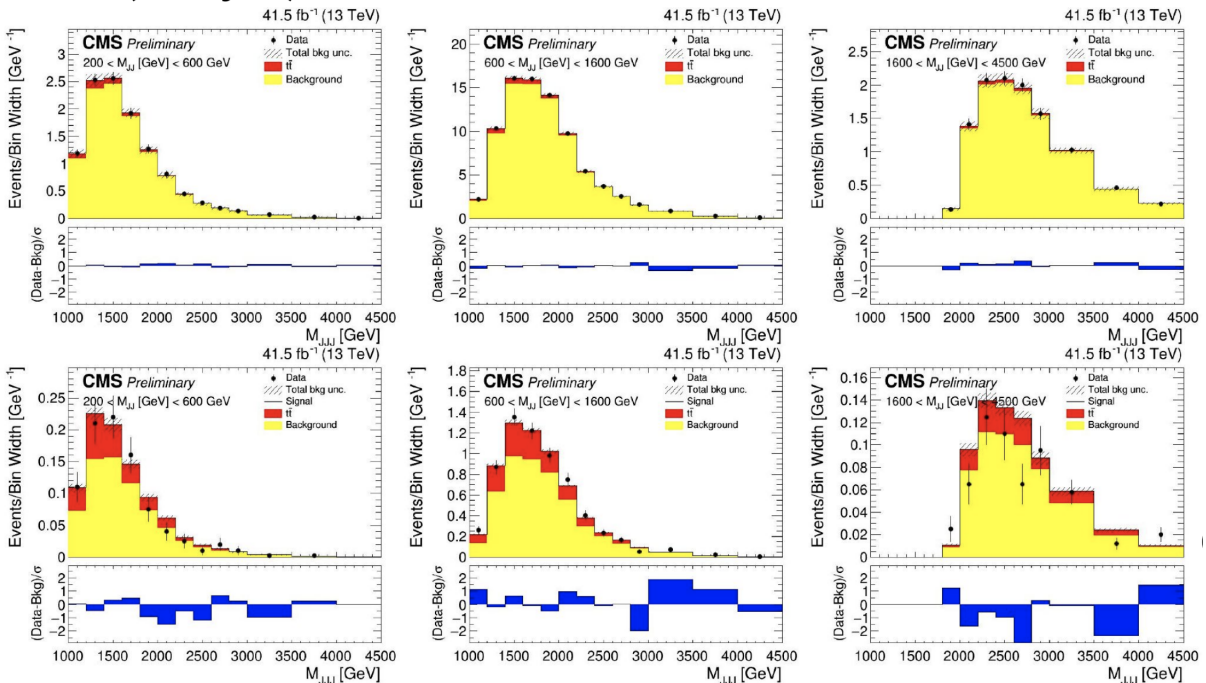
Figure 6.10: 2D Alphabet background only fit for fail (upper) and pass (lower, using toy data) categories in validation region for boosted topology.
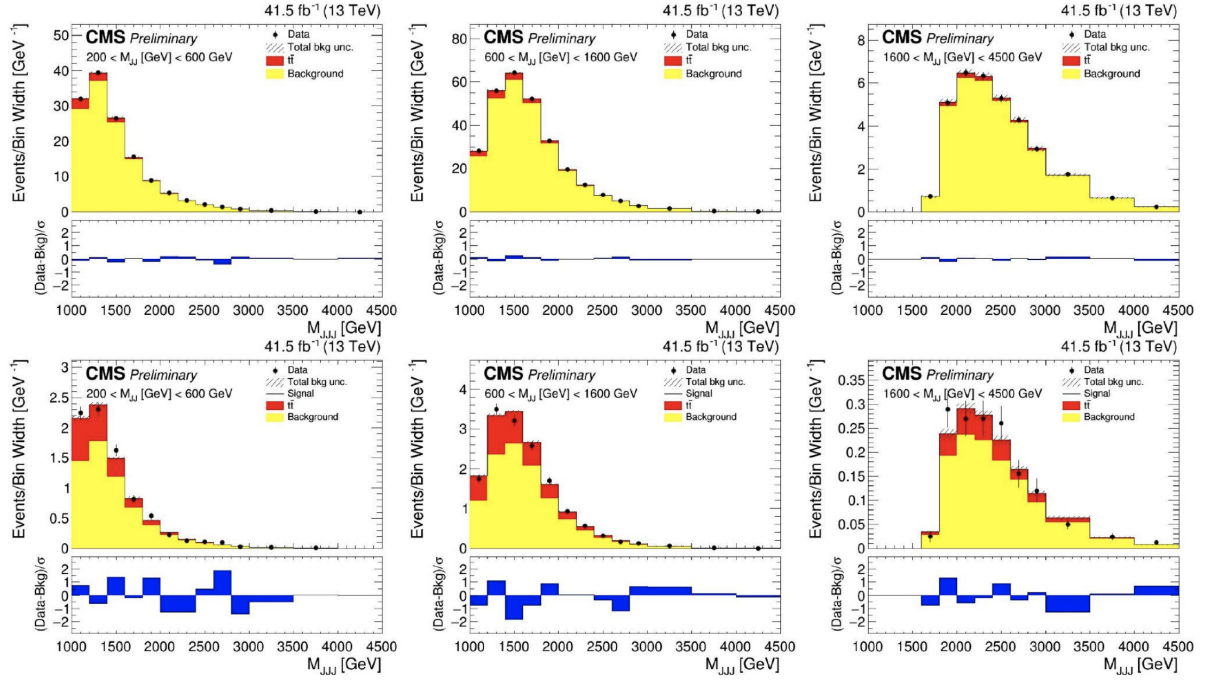
Figure 6.11: 2DAlphabet background only fit for fail (upper) and pass (lower, using toy data) categories in validation region for semi-boosted topology.

6.6   Future Goals

Several sources of systematic uncertainties are to be considered in the analysis. Next steps are to implement systematic uncertainties and check for different ways to increase signal sensitivity. The end goal is to extract the expected upper limit on the production cross section for the array (m_X, m_Y).

Chapter 7

Conclusion

The search for the non-resonant production of Higgs boson pairs in the $HH \to b\bar{b}\gamma\gamma$ final state is presented. The data analyzed were collected by the CMS detector in proton-proton collisions with a center-of-mass energy of 13 TeV, for a total integrated luminosity of 137 fb^{-1}. The considered di-Higgs production processes are the ggF HH, which is the main production process, and the VBF HH.

A b-jet energy regression is developed to improve b-jets resolution and, therefore, the invariant mass of the two jets coming from the $H \to b\bar{b}$ decay. It is a key element to achieve the best sensitivity because it determines the width of the $H \to b\bar{b}$ peak in the dijet mass distribution, which is used for the signal measurement. Overall the b-jet energy corrections improve the m_{jj} resolution of about 25%. This regression technique was validated using CMS $H \to b\bar{b}$ discovery data.

No significant deviations from the SM predictions are found for the $HH \to b\bar{b}\gamma\gamma$ process in the two production mechanisms considered. In particular, no evidence of the HH signal is found, thus an upper limit on its cross section is set. The observed (expected) upper limit on the inclusive $HH \to b\bar{b}\gamma\gamma$ cross section is 7.7 (5.2) times the Standard Model. This result is the most stringent upper limit on the HH cross section set by the CMS experiment to date. Constraints on anomalous values of the Higgs coupling parameters κ_λ, κ_t, and c_{2V} are also extracted. In the hypothesis of no HH signal and all the other Higgs couplings equal to their SM value, the κ_λ parameter is constrained in the range [-3.3, 8.5] at 95% confidence level. This is the most stringent constraint to the κ_λ parameter

from a HH search, to date. Under the same assumptions, the c_{2V} parameter is constrained in the range [-1.3, 3.5] at 95% confidence level.

The search for resonant production of triple Higgs boson considering TRSM model is presented. As an extension of SM, TRSM introduces two new real scalars X and Y to enhance the SM cross-section of triple Higgs boson production. The process of two real scalar singlets X and Y decaying to the SM Higgs boson H is considered. Since $H \rightarrow b\bar{b}$ has the highest branching ratio, to maximize the statistics, we are considering all three Higgs bosons decay to b-quark pairs. This gives, $X \rightarrow Y(HH)H \rightarrow b\bar{b}b\bar{b}b\bar{b}$. The search is performed in mass ranges of X (1–4 TeV) and Y (300–2800 GeV) where the H is highly Lorentz-boosted. In this kinematic regime, decayed b-quark pairs are collimated enough to allow the reconstruction of H using single fat jet. Here, combination of three Higgs bosons will give different topology, out of which we have considered topology where all three Higgs bosons are boosted, and two of the three Higgs bosons are boosted.

The major background for this process is QCD multijets and top quark production. We have used 2D-alphabet method to estimate the background shape in the Signal region. This analysis is still ongoing. A scan will be performed in a two dimensional plane spanned by the mass of the two large-area jets associated to Y, and the invariant mass of three large-area jets used to reconstruct X.

Bibliography

[1] The ATLAS Collaboration. "Observation of a new particle in the search for the Standard Model Higgs boson with the ATLAS detector at the LHC". In: (2012). DOI: 10.1016/j.physletb.2012.08.020. eprint: arXiv:1207.7214 (cit. on pp. 1, 5, 14, 22, 39).

[2] The CMS Collaboration. "Observation of a new boson at a mass of 125 GeV with the CMS experiment at the LHC". In: (2012). DOI: 10.1016/j.physletb.2012.08.021. eprint: arXiv:1207.7235 (cit. on pp. 1, 5, 14, 22, 23, 39).

[3] CMS Collaboration. "Observation of a new boson with mass near 125 GeV in pp collisions at $\sqrt{s}$ = 7 and 8 TeV". In: (2013). DOI: 10.1007/JHEP06(2013)081. eprint: arXiv:1303.4571 (cit. on p. 1).

[4] Ilaria Brivio and Michael Trott. "The Standard Model as an Effective Field Theory". In: (2017). DOI: 10.1016/j.physrep.2018.11.002. eprint: arXiv:1706.08945 (cit. on p. 1).

[5] Steven W. Allen, August E. Evrard, and Adam B. Mantz. "Cosmological Parameters from Observations of Galaxy Clusters". In: (2011). DOI: 10.1146/annurev-astro-081710-102514. eprint: arXiv:1103.4829 (cit. on p. 1).

[6] Edvige Corbelli and Paolo Salucci. "The Extended Rotation Curve and the Dark Matter Halo of M33". In: (1999). DOI: 10.1046/j.1365-8711.2000.03075.x. eprint: arXiv:astro-ph/9909252 (cit. on p. 1).

[7] Ze-Long Yi and Tong-Jie Zhang. "Constraints on holographic dark energy models using the differential ages of passively evolving galaxies". In: (2006). DOI: 10.1142/S0217732307020889. eprint: arXiv:astro-ph/0605596 (cit. on p. 1).

[8]   Fred Jegerlehner. *The hierarchy problem of the electroweak Standard Model revisited*. 2013. eprint: arXiv:1305.6652 (cit. on p. 1).

[9]   Raymond Davis, Don S. Harmer, and Kenneth C. Hoffman. "Search for Neutrinos from the Sun". In: *Physical Review Letters* 20.21 (May 1968), pp. 1205–1209. ISSN: 0031-9007. DOI: 10.1103/physrevlett.20.1205. URL: http://dx.doi.org/10.1103/PhysRevLett.20.1205 (cit. on p. 1).

[10] J. Wess and B. Zumino. "Supergauge transformations in four dimensions". In: *Nuclear Physics B* 70.1 (Feb. 1974), pp. 39–50. ISSN: 0550-3213. DOI: 10.1016/0550-3213(74)90355-1. URL: http://dx.doi.org/10.1016/0550-3213(74)90355-1 (cit. on p. 1).

[11] Lisa Randall and Raman Sundrum. "A Large Mass Hierarchy from a Small Extra Dimension". In: (1999). DOI: 10.1103/PhysRevLett.83.3370. eprint: arXiv:hep-ph/9905221 (cit. on p. 2).

[12] Lyndon Evans and Philip Bryant. "LHC Machine". In: *Journal of Instrumentation* 3.08 (Aug. 2008), S08001–S08001. ISSN: 1748-0221. DOI: 10.1088/1748-0221/3/08/s08001. URL: http://dx.doi.org/10.1088/1748-0221/3/08/S08001 (cit. on p. 2).

[13] Tania Robens, Tim Stefaniak, and Jonas Wittbrodt. "Two-real-scalar-singlet extension of the SM: LHC phenomenology and benchmark scenarios". In: (2019). DOI: 10.1140/epjc/s10052-020-7655-x. eprint: arXiv:1908.08554 (cit. on pp. 3, 36).

[14] CMS Collaboration. "Search for nonresonant Higgs boson pair production in final states with two bottom quarks and two photons in proton-proton collisions at $\sqrt{s} = $ 13 TeV". In: (2021). DOI: 10.1007/JHEP03(2021)257. eprint: arXiv:2011.12373 (cit. on p. 4).

[15] L. Corcodilos. *2DAlphabet - Background modeling framework*. URL: https://github.com/CMS-H3PO/2DAlphabet/blob/285680706c2f0bc92c9199803655ed0274831a1e/2DAlphabet.md (cit. on p. 4).

[16] L. Corcodilos. *The 2D Alphabet background modeling method and its use in the search for an excited bottom quark*. 2021. URL: https://j10p-stage.library.jhu.edu/server/api/core/bitstreams/74b17791-7ef7-4451-a077-dff7818f82bb/content (cit. on p. 4).

[17] M. J. Herrero. *The Standard Model*. 1998. eprint: arXiv:hep-ph/9812242 (cit. on p. 5).

[18] F. Englert and R. Brout. "Broken Symmetry and the Mass of Gauge Vector Mesons". In: *Physical Review Letters* 13.9 (Aug. 1964), pp. 321–323. ISSN: 0031-9007. DOI: 10.1103/physrevlett.13.321. URL: http://dx.doi.org/10.1103/PhysRevLett.13.321 (cit. on p. 11).

[19] Peter W. Higgs. "Broken Symmetries and the Masses of Gauge Bosons". In: *Physical Review Letters* 13.16 (Oct. 1964), pp. 508–509. ISSN: 0031-9007. DOI: 10.1103/physrevlett.13.508. URL: http://dx.doi.org/10.1103/PhysRevLett.13.508 (cit. on p. 11).

[20] G. S. Guralnik, C. R. Hagen, and T. W. B. Kibble. "Global Conservation Laws and Massless Particles". In: *Physical Review Letters* 13.20 (Nov. 1964), pp. 585–587. ISSN: 0031-9007. DOI: 10.1103/physrevlett.13.585. URL: http://dx.doi.org/10.1103/PhysRevLett.13.585 (cit. on p. 11).

[21] Gerald S. Guralnik. "The History of the Guralnik, Hagen and Kibble development of the Theory of Spontaneous Symmetry Breaking and Gauge Particles". In: (2009). DOI: 10.1142/S0217751X09045431. eprint: arXiv:0907.3466 (cit. on p. 11).

[22] Tom Kibble. "Englert-Brout-Higgs-Guralnik-Hagen-Kibble mechanism". In: *Scholarpedia* 4.1 (2009), p. 6441. ISSN: 1941-6016. DOI: 10.4249/scholarpedia.6441. URL: http://dx.doi.org/10.4249/scholarpedia.6441 (cit. on p. 11).

[23] CMS Collaboration. "Combined measurements of Higgs boson couplings in proton-proton collisions at $\sqrt{s} = 13$ TeV". In: (2018). DOI: 10.1140/epjc/s10052-019-6909-y. eprint: arXiv:1809.10733 (cit. on p. 14).

[24] ATLAS Collaboration. "Combined measurements of Higgs boson production and decay using up to 80 fb^{-1} of proton-proton collision data at $\sqrt{s} = 13$ TeV collected with the ATLAS experiment". In: (2019). DOI: 10.1103/PhysRevD.101.012002. eprint: arXiv:1909.02845 (cit. on p. 14).

[25] G. Ridolfi. *Search for the Higgs boson: theoretical perspectives.* https://cds.cern.ch/record/506136. [Frascati Phys. Ser. 22 (2001) 291–304.] (cit. on p. 16).

[26] G. Abbiendi. "Search for the Standard Model Higgs Boson at LEP". In: (2003). DOI: 10.1016/S0370-2693(03)00614-2. eprint: arXiv:hep-ex/0306033 (cit. on p. 17).

[27] The CDF Collaboration et al. *Combined CDF and D0 Upper Limits on Standard Model Higgs-Boson Production with 2.1-5.4 fb^{-1} of Data.* 2009. eprint: arXiv:0911.3930 (cit. on p. 17).

[28] CMS Collaboration. "Measurement of the Higgs boson production rate in association with top quarks in final states with electrons, muons, and hadronically decaying tau leptons at $\sqrt{s} = 13$ TeV". In: (2020). DOI: 10.1140/epjc/s10052-021-09014-x. eprint: arXiv:2011.03652 (cit. on p. 19).

[29] D. de Florian et al. "Handbook of LHC Higgs Cross Sections: 4. Deciphering the Nature of the Higgs Sector". In: (2016). DOI: 10.23731/CYRM-2017-002. eprint: arXiv:1610.07922 (cit. on pp. 20, 21, 25, 28, 30, 34, 86, 93, 125, 126, 178).

[30] CMS Collaboration. "Measurement of the Higgs boson width and evidence of its off-shell contributions to ZZ production". In: (2022). DOI: 10.1038/s41567-022-01682-0. eprint: arXiv:2202.06923 (cit. on p. 19).

[31] The LHC Higgs Cross Section Working Group. "Handbook of LHC Higgs Cross Sections: 3. Higgs Properties". In: (2013). DOI: 10.5170/CERN-2013-004. eprint: arXiv:1307.1347 (cit. on p. 25).

[32] Massimiliano Grazzini et al. "Higgs boson pair production at NNLO with top quark mass effects". In: (2018). DOI: 10.1007/JHEP05(2018)059. eprint: arXiv:1803.02463 (cit. on pp. 26, 125).

[33] J. Baglio et al. "$gg \to HH$: Combined Uncertainties". In: (2020). DOI: 10.1103/PhysRevD.103.056002. eprint: arXiv:2008.11626 (cit. on p. 26).

[34] B. Di Micco et al. "Higgs boson potential at colliders: status and perspectives". In: (2019). DOI: 10.1016/j.revip.2020.100045. eprint: arXiv:1910.00012 (cit. on p. 27).

162

[35] Florian Goertz et al. "Higgs boson pair production in the D=6 extension of the SM". In: (2014). DOI: `10.1007/JHEP04(2015)167`. eprint: `arXiv:1410.3471` (cit. on p. 28).

[36] Ling Liu-Sheng et al. "NNLO QCD corrections to Higgs pair production via vector boson fusion at hadron colliders". In: (2014). DOI: `10.1103/PhysRevD.89.073001`. eprint: `arXiv:1401.7754` (cit. on p. 28).

[37] Frédéric A. Dreyer and Alexander Karlberg. "Fully differential Vector-Boson Fusion Higgs Pair Production at Next-to-Next-to-Leading Order". In: (2018). DOI: `10.1103/PhysRevD.99.074028`. eprint: `arXiv:1811.07918` (cit. on p. 28).

[38] P A Zyla et al. "Review of Particle Physics". In: *Progress of Theoretical and Experimental Physics* 2020.8 (Aug. 2020). ISSN: 2050-3911. DOI: `10.1093/ptep/ptaa104`. URL: `http://dx.doi.org/10.1093/ptep/ptaa104` (cit. on pp. 30, 31).

[39] Johannes Braathen and Shinya Kanemura. "Leading two-loop corrections to the Higgs boson self-couplings in models with extended scalar sectors". In: (2019). DOI: `10.1140/epjc/s10052-020-7723-2`. eprint: `arXiv:1911.11507` (cit. on p. 30).

[40] Stefano Di Vita et al. "A global view on the Higgs self-coupling". In: (2017). DOI: `10.1007/JHEP09(2017)069`. eprint: `arXiv:1704.01953` (cit. on p. 30).

[41] Fedor Bezrukov and Mikhail Shaposhnikov. "Why should we care about the top quark Yukawa coupling?" In: (2014). DOI: `10.1134/S1063776115030152`. eprint: `arXiv:1411.1923` (cit. on p. 32).

[42] Da Liu, Ian Low, and Carlos E. M. Wagner. "Modification of Higgs Couplings in Minimal Composite Models". In: (2017). DOI: `10.1103/PhysRevD.96.035013`. eprint: `arXiv:1703.07791` (cit. on p. 32).

[43] A. M. Sirunyan et al. "Combined measurements of Higgs boson couplings in proton–proton collisions at $\sqrt{s} = 13$ TeV". In: *The European Physical Journal C* 79.5 (May 2019). ISSN: 1434-6052. DOI: `10.1140/epjc/s10052-019-6909-y`. URL: `http://dx.doi.org/10.1140/epjc/s10052-019-6909-y` (cit. on p. 33).

[44] Fady Bishara, Roberto Contino, and Juan Rojo. "Higgs pair production in vector-boson fusion at the LHC and beyond". In: (2016). DOI: `10.1140/epjc/s10052-017-5037-9`. eprint: `arXiv:1611.03860` (cit. on p. 33).

[45] S. Dawson and H. Haber. *Electroweak Symmetry Breaking and Physics Beyond the Standard Model*. 1996. eprint: arXiv:hep-ph/9604354 (cit. on p. 33).

[46] Alexandra Carvalho et al. "Higgs Pair Production: Choosing Benchmarks With Cluster Analysis". In: (2015). DOI: 10.1007/JHEP04(2016)126. eprint: arXiv:1507.02245 (cit. on p. 36).

[47] Andreas Papaefstathiou, Tania Robens, and Gilberto Tetlalmatzi-Xolocotzi. "Triple Higgs Boson Production at the Large Hadron Collider with Two Real Singlet Scalars". In: (2020). DOI: 10.1007/JHEP05(2021)193. eprint: arXiv:2101.00037 (cit. on pp. 37, 142).

[48] E. Mobs. *The CERN accelerator complex*. 2018. eprint: https://cds.cern.ch/record/2636343 (cit. on p. 41).

[49] AC Team. *Diagram of an LHC dipole magnet*. 1999. URL: https://cds.cern.ch/record/40524 (cit. on p. 42).

[50] The ATLAS Collaboration. "The ATLAS Experiment at the CERN Large Hadron Collider". In: *Journal of Instrumentation* 3.08 (Aug. 2008), S08003–S08003. ISSN: 1748-0221. DOI: 10.1088/1748-0221/3/08/s08003. URL: http://dx.doi.org/10.1088/1748-0221/3/08/S08003 (cit. on p. 40).

[51] The CMS Collaboration. "The CMS experiment at the CERN LHC". In: *Journal of Instrumentation* 3.08 (Aug. 2008), S08004–S08004. ISSN: 1748-0221. DOI: 10.1088/1748-0221/3/08/s08004. URL: http://dx.doi.org/10.1088/1748-0221/3/08/S08004 (cit. on pp. 40, 45).

[52] The LHCb Collaboration. "The LHCb Detector at the LHC". In: *Journal of Instrumentation* 3.08 (Aug. 2008), S08005–S08005. ISSN: 1748-0221. DOI: 10.1088/1748-0221/3/08/s08005. URL: http://dx.doi.org/10.1088/1748-0221/3/08/S08005 (cit. on p. 40).

[53] The ALICE Collaboration. "The ALICE experiment at the CERN LHC". In: *Journal of Instrumentation* 3.08 (Aug. 2008), S08002–S08002. ISSN: 1748-0221. DOI: 10.1088/1748-0221/3/08/s08002. URL: http://dx.doi.org/10.1088/1748-0221/3/08/S08002 (cit. on p. 41).

[54] Oliver Sim Brüning et al. *LHC Design Report*. en. 2004. DOI: 10.5170/CERN-2004-003-V-1. URL: http://cds.cern.ch/record/782076 (cit. on p. 43).

[55] CMS Collaboration. "Measurement of the inelastic proton-proton cross section at $\sqrt{s} = 13$ TeV". In: (2018). DOI: `10.1007/JHEP07(2018)161`. eprint: `arXiv:1802.02613` (cit. on p. 44).

[56] CMS Collaboration. *Public luminosity results*. 2024 (last visited August 2024). URL: `https://twiki.cern.ch/twiki/bin/view/CMSPublic/LumiPublicResults` (cit. on p. 44).

[57] T. Sakuma. *Cutaway diagrams of CMS detector*. 2019. URL: `https://cds.cern.ch/record/2665537` (cit. on p. 46).

[58] I. Neutelings. *CMS Wiki Pages, How to draw diagrams in LaTeX with TikZ*. 2022. URL: `https://wiki.physik.uzh.ch/cms/latex:tikz` (cit. on p. 47).

[59] CMS Collaboration et al. *The CMS tracker system project: Technical Design Report*. 1997. URL: `https://cds.cern.ch/record/368412` (cit. on p. 48).

[60] CMS Collaboration. *CMS Tracker Detector Performance Results*. 2024 (last visited August 2024). URL: `https://twiki.cern.ch/twiki/bin/view/CMSPublic/DPGResultsTRK` (cit. on p. 49).

[61] Dinko Ferenček, Matej Roguljić, and Andrey Starodumov. "Production, Calibration, and Performance of the Layer 1 Replacement Modules for the CMS Pixel Detector". In: *Proceedings of the 29th International Workshop on Vertex Detectors (VERTEX2020)*. Journal of the Physical Society of Japan, 2021. DOI: `10.7566/jpscp.34.010023`. URL: `http://dx.doi.org/10.7566/JPSCP.34.010023` (cit. on p. 50).

[62] CMS Collaboration. *CMS workflow*. URL: `https://cms.cern/detector` (cit. on p. 50).

[63] D. J. A. Cockerill. *The CMS Electromagnetic Calorimeter at the LHC*. 2008. eprint: `arXiv:0810.0381` (cit. on p. 50).

[64] D. Abadjiev et al. "Autoencoder-Based Anomaly Detection System for Online Data Quality Monitoring of the CMS Electromagnetic Calorimeter". In: *Computing and Software for Big Science* 8.1 (2024). ISSN: 2510-2044. DOI: `10.1007/s41781-024-00118-z`. URL: `http://dx.doi.org/10.1007/s41781-024-00118-z` (cit. on p. 51).

[65] CMS Collaboration. *The CMS hadron calorimeter project: Technical Design Report*. 1997. URL: https://cds.cern.ch/record/357153 (cit. on p. 52).

[66] CMS Collaboration. "Calibration of the CMS hadron calorimeters using proton-proton collision data at $\sqrt{s} = 13$ TeV". In: (2019). DOI: 10.1088/1748-0221/15/05/P05002. eprint: arXiv:1910.00079 (cit. on p. 52).

[67] CMS Collaboration. "Performance of the CMS muon detector and muon reconstruction with proton-proton collisions at $\sqrt{s} = 13$ TeV". In: (2018). DOI: 10.1088/1748-0221/13/06/P06015. eprint: arXiv:1804.04528 (cit. on pp. 54, 55, 67).

[68] CMS Collaboration and C. Seez. *The CMS trigger system*. 2003. URL: https://cds.cern.ch/record/687840/files/cr03_008.pdf (cit. on p. 56).

[69] CMS Collaboration, Darin Acosta, and Austin Ball. *CMS Technical Design Report for the Level-1 Trigger Upgrade*. 2013. URL: https://cds.cern.ch/record/1556311 (cit. on p. 58).

[70] Katharina Danziger, Stefan Höche, and Frank Siegert. *Reducing negative weights in Monte Carlo event generation with Sherpa*. 2021. eprint: arXiv:2110.15211 (cit. on p. 60).

[71] Paolo Nason. "A New Method for Combining NLO QCD with Shower Monte Carlo Algorithms". In: (2004). DOI: 10.1088/1126-6708/2004/11/040. eprint: arXiv:hep-ph/0409146 (cit. on p. 60).

[72] Johan Alwall et al. "MadGraph 5 : Going Beyond". In: (2011). DOI: 10.1007/JHEP06(2011)128. eprint: arXiv:1106.0522 (cit. on p. 60).

[73] Simone Alioli et al. "A general framework for implementing NLO calculations in shower Monte Carlo programs: the POWHEG BOX". In: (2010). DOI: 10.1007/JHEP06(2010)043. eprint: arXiv:1002.2581 (cit. on pp. 60, 91, 178).

[74] Carlo Oleari. "The POWHEG-BOX". In: (2010). DOI: 10.1016/j.nuclphysbps.2010.08.016. eprint: arXiv:1007.3893 (cit. on pp. 60, 178).

[75] Stefano Frixione, Paolo Nason, and Carlo Oleari. "Matching NLO QCD computations with Parton Shower simulations: the POWHEG method". In: (2007). DOI: 10.1088/1126-6708/2007/11/070. eprint: arXiv:0709.2092 (cit. on p. 60).

[76] Torbjörn Sjöstrand et al. "An Introduction to PYTHIA 8.2". In: (2014). DOI: `10.1016/j.cpc.2015.01.024`. eprint: `arXiv:1410.3012` (cit. on pp. 60, 91).

[77] S. Agostinelli et al. "Geant4—a simulation toolkit". In: *Nuclear Instruments and Methods in Physics Research Section A: Accelerators, Spectrometers, Detectors and Associated Equipment* 506.3 (July 2003), pp. 250–303. ISSN: 0168-9002. DOI: `10.1016/s0168-9002(03)01368-8`. URL: `http://dx.doi.org/10.1016/S0168-9002(03)01368-8` (cit. on pp. 60, 91).

[78] CMS Collaboration. *CMSSW Application Framework*. URL: `https://twiki.cern.ch/twiki/bin/view/CMSPublic/WorkBookCMSSWFramework` (cit. on p. 60).

[79] Siona Ruth Davis. *Interactive Slice of the CMS detector*. 2016. URL: `https://cds.cern.ch/record/2205172/` (cit. on p. 63).

[80] CMS Collaboration. "Description and performance of track and primary-vertex reconstruction with the CMS tracker". In: (2014). DOI: `10.1088/1748-0221/9/10/P10009`. eprint: `arXiv:1405.6569` (cit. on pp. 63, 65).

[81] T. Mc Cauley. *Collisions recorded by the CMS detector on 14 Oct 2016 during the high pile-up fill*. 2016. URL: `https://cds.cern.ch/record/2231915` (cit. on p. 64).

[82] P. Billoir and S. Qian. "Simultaneous pattern recognition and track fitting by the Kalman filtering method". In: *Nuclear Instruments and Methods in Physics Research Section A: Accelerators, Spectrometers, Detectors and Associated Equipment* 294.1–2 (Sept. 1990), pp. 219–228. ISSN: 0168-9002. DOI: `10.1016/0168-9002(90)91835-y`. URL: `http://dx.doi.org/10.1016/0168-9002(90)91835-Y` (cit. on p. 64).

[83] CMS Collaboration. "Performance of the CMS missing transverse energy reconstruction in pp data at sqrt(s) = 8 TeV". In: (2014). DOI: `10.1088/1748-0221/10/02/P02006`. eprint: `arXiv:1411.0511` (cit. on p. 68).

[84] CMS Collaboration. "Missing transverse energy performance of the CMS detector". In: (2011). DOI: `10.1088/1748-0221/6/09/P09001`. eprint: `arXiv:1106.5048` (cit. on p. 68).

[85] CMS Collaboration. "Electron and photon reconstruction and identification with the CMS experiment at the CERN LHC". In: (2020). DOI: 10.1088/1748-0221/16/05/P05014. eprint: arXiv:2012.06888 (cit. on pp. 69, 71, 72).

[86] Matteo Cacciari, Gavin P. Salam, and Gregory Soyez. "The anti-k_t jet clustering algorithm". In: (2008). DOI: 10.1088/1126-6708/2008/04/063. eprint: arXiv:0802.1189 (cit. on p. 72).

[87] Gavin P. Salam. "Towards Jetography". In: (2009). DOI: 10.1140/epjc/s10052-010-1314-6. eprint: arXiv:0906.1833 (cit. on p. 72).

[88] CMS Collaboration. *Pileup Removal Algorithms*. 2014. URL: https://cds.cern.ch/record/1751454/ (cit. on p. 73).

[89] Daniele Bertolini et al. "Pileup Per Particle Identification". In: (2014). DOI: 10.1007/JHEP10(2014)059. eprint: arXiv:1407.6013 (cit. on p. 74).

[90] Garvita Agarwal. "Jet Energy Scale and Resolution Measurements in CMS". In: (2023). DOI: 10.22323/1.414.0652. eprint: arXiv:2301.02175 (cit. on p. 76).

[91] CMS Collaboration. "Identification of heavy-flavour jets with the CMS detector in pp collisions at 13 TeV". In: (2017). DOI: 10.1088/1748-0221/13/05/P05011. eprint: arXiv:1712.07158 (cit. on pp. 77, 95, 127).

[92] CMS Collaboration. "Identification of b-quark jets with the CMS experiment". In: (2012). DOI: 10.1088/1748-0221/8/04/P04013. eprint: arXiv:1211.4462 (cit. on p. 78).

[93] Daniel Guest et al. "Jet Flavor Classification in High-Energy Physics with Deep Neural Networks". In: (2016). DOI: 10.1103/PhysRevD.94.112002. eprint: arXiv:1607.08633 (cit. on p. 78).

[94] Emil Bols et al. "Jet Flavour Classification Using DeepJet". In: (2020). DOI: 10.1088/1748-0221/15/12/P12012. eprint: arXiv:2008.10519 (cit. on p. 78).

[95] CMS Collaboration. *Performance of b tagging algorithms in proton-proton collisions at 13 TeV with Phase 1 CMS detector*. 2018. URL: https://cds.cern.ch/record/2627468 (cit. on p. 80).

[96] Mrinal Dasgupta et al. "Towards an understanding of jet substructure". In: (2013). DOI: 10.1007/JHEP09(2013)029. eprint: arXiv:1307.0007 (cit. on p. 81).

[97] Jesse Thaler and Ken Van Tilburg. "Identifying Boosted Objects with N-subjettiness". In: (2010). DOI: 10.1007/JHEP03(2011)015. eprint: arXiv:1011.2268 (cit. on p. 82).

[98] CMS Collaboration. "Identification of heavy, energetic, hadronically decaying particles using machine-learning techniques". In: (2020). DOI: 10.1088/1748-0221/15/06/P06005. eprint: arXiv:2004.08262 (cit. on p. 83).

[99] Huilin Qu and Loukas Gouskos. "Jet tagging via particle clouds". In: *Physical Review D* 101.5 (Mar. 2020). ISSN: 2470-0029. DOI: 10.1103/physrevd.101.056019. URL: http://dx.doi.org/10.1103/PhysRevD.101.056019 (cit. on p. 83).

[100] Nilanjana Kumar and Stephen P. Martin. "LHC search for di-Higgs decays of stoponium and other scalars in events with two photons and two bottom jets". In: (2014). DOI: 10.1103/PhysRevD.90.055007. eprint: arXiv:1404.0996 (cit. on p. 88).

[101] The CMS Collaboration. "Measurement of the Inclusive W and Z Production Cross Sections in pp Collisions at $\sqrt{s} = 7$ TeV". In: (2011). DOI: 10.1007/JHEP10(2011)132. eprint: arXiv:1107.4789 (cit. on p. 90).

[102] J. Alwall et al. "The automated computation of tree-level and next-to-leading order differential cross sections, and their matching to parton shower simulations". In: (2014). DOI: 10.1007/JHEP07(2014)079. eprint: arXiv:1405.0301 (cit. on pp. 91, 178).

[103] CMS Collaboration. "Extraction and validation of a new set of CMS PYTHIA8 tunes from underlying-event measurements". In: (2019). DOI: 10.1140/epjc/s10052-019-7499-4. eprint: arXiv:1903.12179 (cit. on p. 91).

[104] CMS Collaboration. "Event generator tunes obtained from underlying event and multiparton scattering measurements". In: (2015). DOI: 10.1140/epjc/s10052-016-3988-x. eprint: arXiv:1512.00815 (cit. on p. 91).

[105] The NNPDF Collaboration et al. "Parton distributions for the LHC Run II". In: (2014). DOI: 10.1007/JHEP04(2015)040. eprint: arXiv:1410.8849 (cit. on p. 91).

[106] The NNPDF Collaboration et al. "Parton distributions from high-precision collider data". In: (2017). DOI: `10.1140/epjc/s10052-017-5199-5`. eprint: `arXiv:1706.00428` (cit. on p. 91).

[107] G. Buchalla et al. "Higgs boson pair production in non-linear Effective Field Theory with full m_t-dependence at NLO QCD". In: (2018). DOI: `10.1007/JHEP09(2018)057`. eprint: `arXiv:1806.05162` (cit. on p. 91).

[108] CMS Collaboration. "A deep neural network for simultaneous estimation of b jet energy and resolution". In: (2019). DOI: `10.1007/s41781-020-00041-z`. eprint: `arXiv:1912.06046` (cit. on p. 95).

[109] John C. Collins and Davison E. Soper. "Angular distribution of dileptons in high-energy hadron collisions". In: *Physical Review D* 16.7 (Oct. 1977), pp. 2219–2225. ISSN: 0556-2821. DOI: `10.1103/physrevd.16.2219`. URL: `http://dx.doi.org/10.1103/PhysRevD.16.2219` (cit. on p. 102).

[110] CMS Collaboration. *Jet algorithms performance in 13 TeV data*. 2017. eprint: `https://cds.cern.ch/record/2256875` (cit. on pp. 109, 127).

[111] ATLAS Collaboration. "Search for the $HH \to b\bar{b}b\bar{b}$ process via vector-boson fusion production using proton-proton collisions at $\sqrt{s} = 13$ TeV with the ATLAS detector". In: (2020). DOI: `10.1007/JHEP01(2021)145`. eprint: `arXiv:2001.05178` (cit. on pp. 111, 130).

[112] The ATLAS, CMS Collaborations, and The LHC Higgs Combination Group. *Procedure for the LHC Higgs boson search combination in Summer 2011*. 2011. eprint: `TechnicalReportCMS-NOTE-2011-005,ATL-PHYS-PUB-2011-11` (cit. on p. 116).

[113] Thomas Junk. "Confidence Level Computation for Combining Searches with Small Statistics". In: (1999). DOI: `10.1016/S0168-9002(99)00498-2`. eprint: `arXiv:hep-ex/9902006` (cit. on p. 118).

[114] Glen Cowan et al. "Asymptotic formulae for likelihood-based tests of new physics". In: (2010). DOI: `10.1140/epjc/s10052-011-1554-0`. eprint: `arXiv:1007.1727` (cit. on p. 118).

[115] P. D. Dauncey et al. "Handling uncertainties in background shapes: the discrete profiling method". In: (2014). DOI: `10.1088/1748-0221/10/04/P04015`. eprint: `arXiv:1408.6865` (cit. on pp. 122–124).

[116] Frédéric A. Dreyer and Alexander Karlberg. "Vector-Boson Fusion Higgs Pair Production at N³LO". In: (2018). DOI: 10.1103/PhysRevD.98.114016. eprint: arXiv:1811.07906 (cit. on p. 125).

[117] Jon Butterworth et al. "PDF4LHC recommendations for LHC Run II". In: (2015). DOI: 10.1088/0954-3899/43/2/023001. eprint: arXiv:1510.03865 (cit. on p. 125).

[118] Stefano Carrazza et al. "An unbiased Hessian representation for Monte Carlo PDFs". In: *The European Physical Journal C* 75.8 (Aug. 2015). ISSN: 1434-6052. DOI: 10.1140/epjc/s10052-015-3590-7. URL: http://dx.doi.org/10.1140/epjc/s10052-015-3590-7 (cit. on p. 126).

[119] Barbara Jäger et al. "Parton-shower effects in Higgs production via Vector-Boson Fusion". In: (2020). DOI: 10.1140/epjc/s10052-020-8326-7. eprint: arXiv:2003.12435 (cit. on p. 126).

[120] CMS Collaboration. *CMS Luminosity Measurements for the 2016 Data Taking Period.* 2017. eprint: TechnicalReportCMS-PAS-LUM-17-001 (cit. on p. 128).

[121] CMS Collaboration. *CMS luminosity measurement for the 2017 data-taking period at $\sqrt{s} = 13$ TeV.* 2018. eprint: TechnicalReportCMS-PAS-LUM-17-004 (cit. on p. 128).

[122] CMS Collaboration. *CMS luminosity measurement for the 2018 data-taking period at $\sqrt{s} = 13$ TeV.* 2019. eprint: TechnicalReportCMS-PAS-LUM-18-002 (cit. on p. 128).

[123] ATLAS Collaboration. "Combination of searches for Higgs boson pairs in *pp* collisions at $\sqrt{s}$ =13 TeV with the ATLAS detector". In: (2019). DOI: 10.1016/j.physletb.2019.135103. eprint: arXiv:1906.02025 (cit. on pp. 130, 135, 140).

[124] A. M. Sirunyan et al. "Measurements of $t\bar{t}H$ Production and the CP Structure of the Yukawa Interaction between the Higgs Boson and Top Quark in the Diphoton Decay Channel". In: *Physical Review Letters* 125.6 (Aug. 2020). ISSN: 1079-7114. DOI: 10.1103/physrevlett.125.061801. URL: http://dx.doi.org/10.1103/PhysRevLett.125.061801 (cit. on p. 138).

[125] CMS Collaboration. "Combination of searches for Higgs boson pair production in proton-proton collisions at $\sqrt{s} = 13$ TeV". In: (2018). DOI: `10.1103/PhysRevLett.122.121803`. eprint: `arXiv:1811.09689` (cit. on p. 140).

[126] Ulrich Ellwanger, Cyril Hugonie, and Ana M. Teixeira. "The Next-to-Minimal Supersymmetric Standard Model". In: *Physics Reports* 496.1–2 (Nov. 2010), pp. 1–77. ISSN: 0370-1573. DOI: `10.1016/j.physrep.2010.07.001`. URL: `http://dx.doi.org/10.1016/j.physrep.2010.07.001` (cit. on p. 142).

[127] Alexandra Carvalho. *Gravity particles from Warped Extra Dimensions, predictions for LHC*. 2014. eprint: `arXiv:1404.0102` (cit. on p. 142).

[128] Rikkert Frederix and Stefano Frixione. "Merging meets matching in MC@NLO". In: (2012). DOI: `10.1007/JHEP12(2012)061`. eprint: `arXiv:1209.6215` (cit. on p. 178).

[129] CERN. *CERN Yellow Reports: Monographs, Vol 2 (2017): Handbook of LHC Higgs cross sections: 4. Deciphering the nature of the Higgs sector*. en. 2017. DOI: `10.23731/CYRM-2017-002`. URL: `https://e-publishing.cern.ch/index.php/CYRM/issue/view/32` (cit. on p. 179).

[130] A. Tumasyan et al. "Measurement of simplified template cross sections of the Higgs boson produced in association with W or Z bosons in the $H \rightarrow b\bar{b}$ decay channel in proton-proton collisions at $\sqrt{s} = 13$ TeV". In: *Physical Review D* 109.9 (2024). ISSN: 2470-0029. DOI: `10.1103/physrevd.109.092011`. URL: `http://dx.doi.org/10.1103/PhysRevD.109.092011` (cit. on p. 180).

[131] Martín Abadi et al. *TensorFlow: Large-Scale Machine Learning on Heterogeneous Distributed Systems*. 2016. eprint: `arXiv:1603.04467` (cit. on p. 184).

[132] CERN. *CERN Yellow Reports: Monographs, Vol 2 (2017): Handbook of LHC Higgs cross sections: 4. Deciphering the nature of the Higgs sector*. en. 2017. DOI: `10.23731/CYRM-2017-002`. URL: `https://e-publishing.cern.ch/index.php/CYRM/issue/view/32` (cit. on p. 186).

Appendix A

Search for VHbb

Higgs boson decaying into a pair of b quarks ($H \rightarrow b\bar{b}$) has a branching ratio of 58% among all Higgs decays. The Higgs boson has 4 major production modes, namely gluon-gluon fusion (ggF), vector-boson fusion (VBF), associated production with a vector boson (VH), and associated production with a pair of top quarks (ttH) as explained in 2.2. The VH production processes represent the most sensitive production mode for the reconstruction of $H \rightarrow b\bar{b}$ decay. The cross-section of these production modes are not the largest among the Higgs production processes, but due to the leptonic decay modes of vector bosons $Z \rightarrow \nu\nu$, $W \rightarrow l\nu$ and $Z \rightarrow ll$ the triggering and background rejection is more efficient. The Higgs boson can be reconstructed from a pair of b-jets which are identified using b-tagging algorithms. The main challenges in measuring $VH \rightarrow b\bar{b}$ come from background modeling, efficiency in tagging b-jets and measuring its momentum and energy resolution.

A.1 Signal and backgroud processes

A.1.1 Signal

The Feynman diagrams for the signal process are shown in Fig. A.1.

The vector boson in the quark-induced VH process can both be a Z and a W boson. The gluon-induced process is at this order only possible for Z bosons via fermion loops.
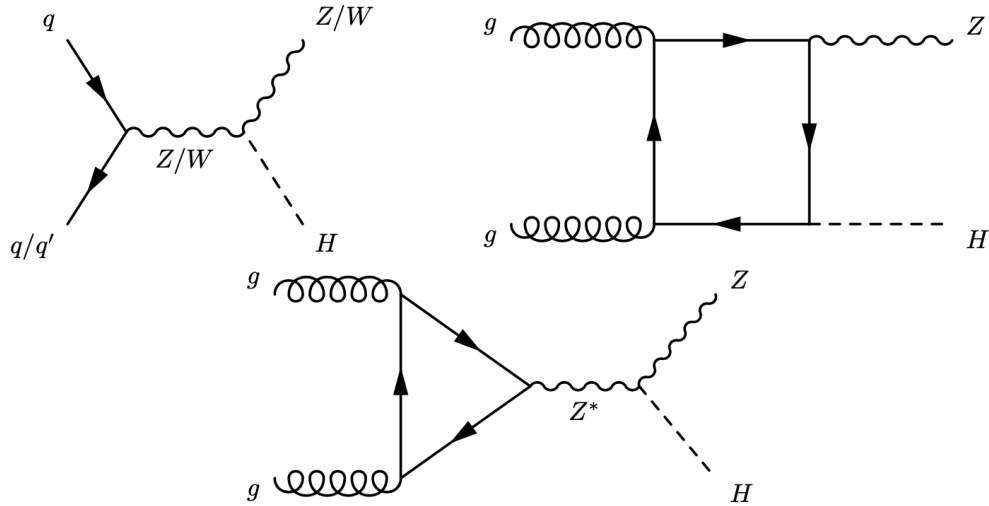
Figure A.1: VH (top left) and ggZH (top right and bottom) process Feynman diagrams.

Through the box-type diagram in figure 4.2 top right, the ggZH process is sensitive also to the coupling to top quarks, which are the dominating fermion contribution in the loop. Following the different decay modes of the vector boson, the analysis is divided into three channels

- 0-lepton (Znn): Z boson decays to two neutrinos

- 1-lepton (Wln): W boson decays to lepton and neutrino

- 2-lepton (Zll): Z boson decays to two leptons (opposite charge, same flavor)

The 1- and 2-lepton channel are further divided into electron and muon channels. Taus are not explicitly reconstructed, but due to the 35% leptonic decay branching ratio, a fraction of events will end up in the electron or muon channels.

A.1.2 Background processes

Final states of VHbb process involves 2 b-jets and 2 leptons (excluding taus). Based on these final states, following processes have similar final state signature and are accounted to be major backgrounds in this analysis:

- **V+jets:** Two quarks or gluons produce a vector boson and radiate off a gluon which can produce a $b\bar{b}$ quark pair, which resembles the $b\bar{b}$ pair from the Higgs decay. It has

a falling distribution in m_{jj} since the jets originate from a mass-less gluon instead of the Higgs boson. In general the V+jets background is divided into three flavors: V+light jets, V+c jets and V+b jets based on counting B- and D-hadrons above 25GeV within detector acceptance ($|\eta| < 2.6$). If multiple hadrons of different flavor are present, the flavor is defined by the heaviest quark.

- **Top quark production:** Most of the times a top quark decays to a W-boson and a b-quark. The consequent decay mode of the W boson defines how this background contributes. The $t\bar{t}$ production with hadronically decaying W bosons contributes to the 0-lepton channel, but the additional jets activity is higher than in VH production. If one of the W-bosons decays leptonically the final state is similar to 1-lepton channel. The final states with both of the W-bosons decaying to leptons contribute to the 2-lepton channel.

  The single-top processes are manifested similarly to the $t\bar{t}$ production, but the kinematics is closer to the signal process, which makes it harder to suppress despite the relatively low production cross-section.

- **Diboson:** The diboson processes WZ and ZZ can produce the same final state as the VH process, when a Z-boson decays to $b\bar{b}$ and the other vector boson follows the leptonic decay mode. The main observable that helps reducing this background is the invariant mass of b-quark pairs, which is peaked around the Z-boson mass.

- **QCD:** The QCD events are abundant at the LHC and the b-quark pairs can be easily produced from the QCD interaction. If other particles in the event are mis-reconstructed, the QCD processes can contribute to all channels in the analysis.

A.2 Analysis strategy

The general strategy of the analysis is to determine a signal strength modifier μ from the observed data by a simultaneous fit of signal and background templates in signal and control regions. The signal region is selected to have a high signal efficiency and the control regions to have a good purity in the individual backgrounds. The templates are derived from a Monte Carlo (MC) simulation. All variations due to detector and calibration effects

₄₁₈₇ are included, either with detailed shape information or as multiplicative normalization
₄₁₈₈ factors. The strengths of each source of variation is steered by nuisance parameters in
₄₁₈₉ the likelihood function. The signal strength modifier μ is implemented in the fit as a free-
₄₁₉₀ floating (unconstrained) parameter. Furthermore, for important background processes,
₄₁₉₁ normalization factors are considered as nuisance parameters in the fit and are set as
₄₁₉₂ free parameters so that the data points from collision reduce the impacts of modeling
₄₁₉₃ uncertainties in simulations.
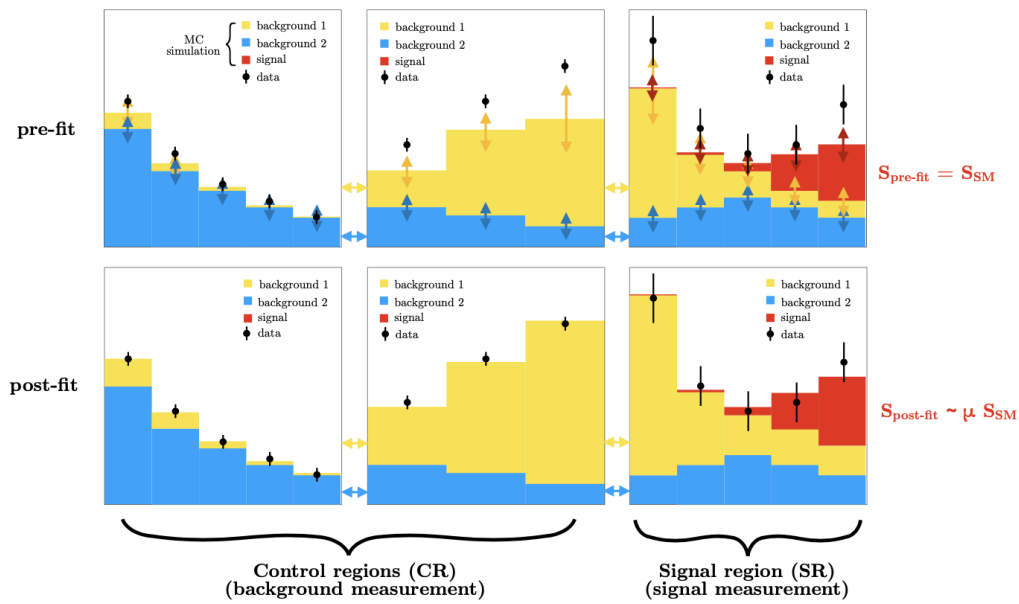
Figure A.2: Simplified schematic of the analysis strategy using a simultaneous fit of
templates derived from MC simulations.

₄₁₉₄ To demonstrate this strategy, an example with two background processes and three regions
₄₁₉₅ of phase space is shown in Fig. A.2, the collision data and simulations pass through a
₄₁₉₆ selection criterion, to create separate templates for the signal and control regions. Then
₄₁₉₇ these templates are simultaneously fitted to the data to extract the signal strength μ,
₄₁₉₈ and the normalization factors for each background contributions. The top row in Fig.
₄₁₉₉ A.2 shows the signal and background predictions before the fit has been run (pre-fit). It
₄₂₀₀ shows some discrepancies between prediction and observation in this example, mostly in
₄₂₀₁ the middle column, where "background 1" dominates. Such discrepancies can originate
₄₂₀₂ from limitations in the simulation. After the fit (post-fit), the results in the bottom row
₄₂₀₃ show the discrepancy has been removed due to the maximum likelihood parameters found
₄₂₀₄ by the fit, in this example scaling up "background 1".

176

The post-fit signal strength modifier μ is called the parameter of interest (POI) and the most-important result of the fit. It denotes the ratio of the observed and the predicted (Standard Model) cross-sections of the signal. The normalization of the signal can not only be affected by μ, but also by other nuisance parameters of the fit, e.g., systematic uncertainties.

To obtain a low uncertainty on the post-fit μ, a good separation of the signal and background templates in the signal region is needed. This is achieved by using the output of a multi-variate classifier as observable for the templates.

A.3 Data Samples and simulated events

A.3.1 Data Samples and trigger requirements

This analysis is performed using the full Run 2 CMS data with the combined luminosity of 137.6 fb^{-1}. In the CMS experiment data is collected using a two-level trigger system, described in Section 3.2.6. For each data taking year a set of High Level Trigger (HLT) paths with the lowest threshold is selected.

In the 0-lepton channel, events are selected with the trigger that requires the presence of MET and MHT ($= |-\Sigma_{jets}\vec{p_T}|$, where jets are required to satisfy $p_T > 30$ GeV and $|\eta| <$ 5.) with thresholds 110 GeV in 2016 and 120 GeV in 2017 and 2018. The MET and MHT are constructed with the jets passing tight identification criteria. In the 1-lepton channel, the presence of an isolated lepton is required. The p_T threshold for the HLT paths used to trigger the isolated electron are 27 GeV in 2016 and 32 GeV in 2017 and 2018. For the muon paths the thresholds are 27 GeV in 2017 data-taking period and 24 GeV in 2016 and 2018.

For the 2-lepton channel, the double-muon and double-electron triggers are used. The p_T thresholds for the leading muon is 17 GeV and 8 GeV for the sub-leading muon. An online requirement on the dimuon invariant mass is applied to remove the contribution from low-mass resonances. For the electron 2-lepton channel, the p_T thresholds are 23 GeV and 12 GeV for the leading and sub-leading electrons, respectively.

A.3.2 Simulated events

The signal samples for the quark induced production of ZH and WH are generated by the PowHeg v2 [73, 74] event generator extended with the MiNLO procedure [64, 80] at NLO accuracy. The gluon induced signal samples on the other hand have leading order accuracy and are produced with PowHeg v2. Signal yields are scaled to an inclusive cross-section calculated up to NNLO [29].

The di-boson samples WZ, ZZ and WW are produced at NLO with the MadGraph5_aMC@nlo [102] using FxFx merging scheme [128]. The $t\bar{t}$ and single-top in t-channel are simulated with PowHeg v2, and for single-top in s-channel and tW production the PowHeg v1 is used.

To reduce the statistical uncertainties from the generation process, events are produced with higher numbers than is expected to appear for that processes in the real collision event. To retrieve the correct number of events, a weight is assigned to each event,

$$w_{\text{event}} = \sigma \times \mathcal{L} \times \frac{w_{\text{generator}}}{\sum w_{\text{generator}}}, \tag{A.1}$$

where the $w_{\text{generator}}$ is assigned by the Monte Carlo generator for each generated event and are not always constant, in some Monte Carlo generators these weights include negative values when next-to-leading order (NLO) accuracies are included.

A.4 Event selection

The signal and control regions are defined as follows, the signal region (SR) enriched in VH($b\bar{b}$), the $t\bar{t}$ control region where $t\bar{t}$ has the highest contribution, the V+HF for the vector boson associated with heavy-flavour jets and the V+LF for the vector boson associated with light-flavour jets. These regions are partitioned according to the STXS framework.

The definition of the boosted region, which has a single fat b-jet instead of the expected two resolved b-jets. Some events can be reconstructed both in the resolved and in the

boosted analysis (called overlap event), therefore those events have to be placed in either the resolved or the boosted regions to avoid double counting. The most efficient scheme is considered where overlap events are assigned to the resolved categories, unless the event would move from the boosted signal region to a resolved control region, then it is assigned to the boosted signal region.

A.4.1   Simplified template cross-section (STXS) bins

The simplified template cross sections (STXS) scheme [129] is designed to lessen the effect of theory dependence in the measurements and to make it simple to compare theoretical models with the observations, provide a consistent scheme for these measurements. The STXS framework offers the best features of signal strength measurements and also provides new features such as identification of a BSM-specific phase space. The STXS kinematic regions, also called bins, are defined at the generator level for each production process. The ultimate goals are to maximise the experimental sensitivity, to minimize the dependence on theoretical uncertainties, and to isolate BSM effects.

In Fig. A.3, the latest recommended categorisation for VH mode is shown. The STXS bins are defined using the transverse momenta of vector boson $p_T(V)$ and the number of additional jets. The VH process is split into three channels $qq \to ZH$, $qq \to WH$ and $gg \to ZH$. Each of them is consequently separated into four $p_T(V)$ regions: 0–75, 75–150, 150–250, >250 GeV. The 150–250 GeV bin is additionally split by the number of additional jets (n_{jet}) with $p_T > 30$ GeV: 0 jets, and at least one additional jet. The $p_T(V)$>250 GeV bin represents the region sensitive to the BSM effects. The dashed boundaries are defined to consider further splitting if possible experimentally. The STXS bins are supposed to be merged by the experiments if a lack of sensitivity for the proposed binning is observed.

A.4.2   Resolved analysis selection

Signal region selection is used to separate the signal from the background while conserving improved signal purity. The reconstructed di-jet invariant mass (m_{jj}), the number of additional jets, and the b-tag discriminator score for the jets in the event are crucial
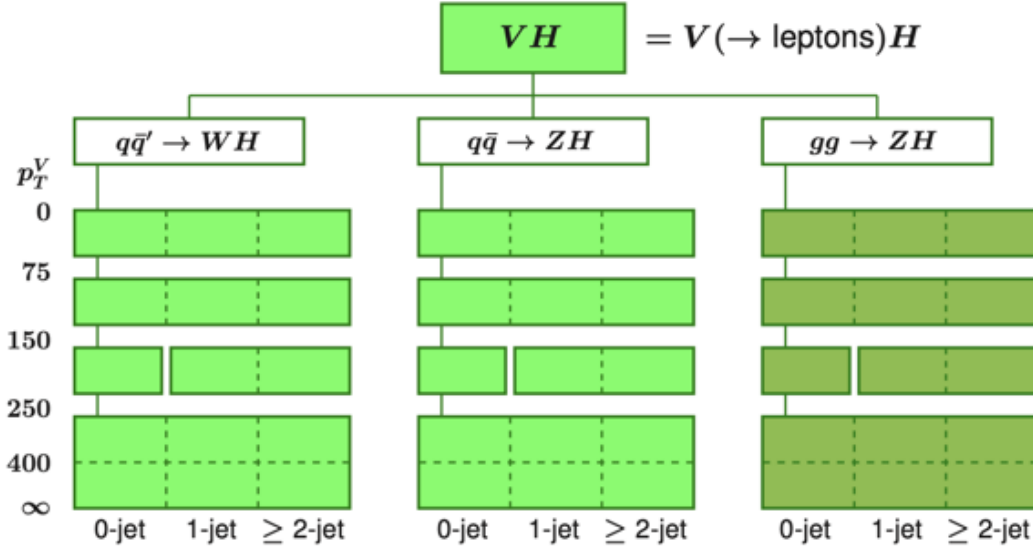
Figure A.3: Overview of the STXS bins for the three VH production modes [130]. The vertical axis reflects the $p_T(V)$ bin ranges and the horizontal axis the number of additional jets.

event variables for identifying signals from the background. The signal region is further divided into several bins with different S/B ratios using an MVA-classifier (DNN) used in the signal region. Therefore, the multivariate classifier is assigned for generating the higher purity signal phase space, while relatively loose cuts are applied for the signal region itself.

A loose channel specific pre-selection is applied in the very beginning of the analysis chain. It is not very specific to the VH signal process but rather to make sure all the needed objects like jets and leptons are present. At the next step the events passing the channel selections are sub-categorised into events from signal regions (SR), defined as the region with enhanced signal efficiency, and the control regions, defined to constrain the leading background and enriched in the corresponding background process. The summary of the selection for signal and control regions for three channels: 0-lepton, 1-lepton, and 2-lepton are given in Tab. A.1, Tab. A.2, and Tab. A.3, respectively. The selection procedure is illustrated in Fig. A.4.

Variable	SR	Z+HF	Z+LF	$t\bar{t}$
Common selection:				
$\min(p_T^{miss}, H_T^{miss})$	>100	-//-	-//-	-//-
p_T^{miss}	>170	-//-	-//-	-//-
$p_\mathrm{T}(\mathrm{j}_1)$	>60	-//-	-//-	-//-
$p_\mathrm{T}(\mathrm{j}_2)$	>35	-//-	-//-	-//-
$p_\mathrm{T}(\mathrm{j, j})$	>120	-//-	-//-	-//-
$\Delta\phi(Z, jj)$	>2.0	-//-	-//-	-//-
$\Delta\phi(\vec{p_T^{miss}}, j)$	>0.5	-//-	-//-	-//-
SR/CR difference:				
N_{aj}	≤ 1	≤ 1	≤ 1	≥ 2
M_{jj}	$\in[90\text{–}150]$	$\notin[90\text{–}150]$	-	-
$btag_{max}$	>medium	>medium	<medium	>medium
$btag_{min}$	>loose	>loose	<loose	>loose
$\Delta\phi(\vec{p_T^{miss}}, \vec{p_T^{miss}}_{trk})$	<0.5	<0.5	<0.5	-
$\min\Delta\phi(\vec{p_T^{miss}}, j)$	-	-	-	$< \pi/2$

Table A.1: Definition of the SR and CRs for the resolved selection in the 0-lepton channel. If the same selection is applied in all SRs and CRs, this is indicated by the -//- symbol in the latter. The M_{jj} and momenta variables have units of GeV.

Variable	SR	W+HF	W+LF	$t\bar{t}$
Common selection:				
$p_\mathrm{T}(\mathrm{j, j})$	>100	-//-	-//-	-//-
$p_\mathrm{T}(\mathrm{V})$	>150	-//-	-//-	-//-
N_al	<1	-//-	-//-	-//-
$p_\mathrm{T}(\mathrm{j}_1)$	>25	-//-	-//-	-//-
$p_\mathrm{T}(\mathrm{j}_2)$	>25	-//-	-//-	-//-
$\Delta\phi(\mathrm{lep}, \vec{p_T^{miss}})$	<2	-//-	-//-	-//-
SR/CR difference:				
$btag_{max}$	>medium	>medium	[loose-medium]	>tight
$btag_{min}$	>loose	-	-	-
M_{jj}	$\in[90\text{–}150]$	$\in[150\text{–}250]$ and <90	<250	<250
N_{aj}	<2	<2	-	>1
$\frac{p_T^{miss}}{\sigma(p_T^{miss})}$	-	>2	>2	-
$\Delta\phi(\mathrm{H, V})$	>2.5	-	-	-

Table A.2: Definition of the SR and CRs for the resolved selection of the 1-lepton channel. If the same selection is applied in all SRs and CRs, this is indicated by the -//- symbol in the latter. The M_{jj} and momenta variables have units of GeV.

Variable	SR	Z+HF	Z+LF	$t\bar{t}$
$p_{\mathrm{T}}(\mathrm{V})$	>75	-//-	-//-	-//-
$\mathrm{btag_{max}}$	>medium	>medium	<loose	>tight
$\mathrm{btag_{min}}$	>loose	>loose	<loose	>loose
$M(\mathrm{V})$	$\in[75\text{–}105]$	$\in[85\text{–}97]$	$\in[75\text{–}105]$	$\in[10\text{–}75]$ and >120
M_{jj}	$\in[90\text{–}150]$	$\notin[90\text{–}150]$	$\in[90\text{–}150]$	-
p_T^{miss}	-	<60	-	-
$\Delta\phi(\mathrm{H},\mathrm{V})$	-	>2.5	>2.5	-

Table A.3: Definition of the SR and CRs for the resolved selection in the 2-lepton channel. If the same selection is applied in all SRs and CRs, this is indicated by the -//- symbol in the latter. The M_{jj}, $M(\mathrm{V})$, and momenta variables have units of GeV.

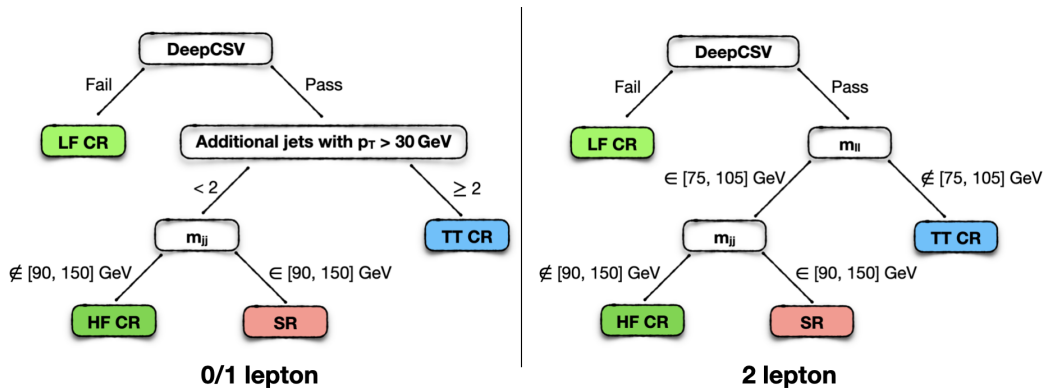
Figure A.4: Left: Resolved 0-lepton and 1-lepton channels selection scheme. Right: Resolved 2-lepton channel selection scheme.

A.4.3 Boosted analysis selection

The vector boson selection in the boosted analysis follows exactly the same procedure as for the resolved analysis described in Section A.4.2. The Higgs boosted decay topology is considered for the vector boson momentum range of $p_T(V) > 250$ GeV in all analysis channels. Boosted analysis is most relevant for high p_T bins of the STXS scheme while reducing multi-jet background events. Selection criteria for the SR and CRs in the boosted topology for 0-, 1-, and 2-lepton channels is given in Tab. A.4. The selection procedure for boosted analysis is illustrated in Fig. A.5.

Variable	SR	V+HF	V+LF	$t\bar{t}$
0-lepton				
DeepAK8bbVsLight	>0.8	>0.8	<0.8	>0.8
m_{SD}	$\in[90\text{--}150]$	$\in[50\text{--}90]$ or $\in[150\text{--}250]$	>50	>50
N_{al}	=0	=0	=0	>0
N_{aj}	=0	=0	=0	>0
1-lepton				
DeepAK8bbVsLight	>0.8	>0.8	<0.8	>0.8
m_{SD}	$\in[90\text{--}150]$	$\in[50\text{--}90]$ or $\in[150\text{--}250]$	>50	>50
N_{al}	=0	=0	=0	>0
N_{aj}	=0	=0	=0	>0
2-lepton				
DeepAK8bbVsLight	>0.8	>0.8	<0.8	>0.8
m_{SD}	$\in[90\text{--}150]$	$\in[50\text{--}90]$ or $\in[150\text{--}250]$	$\in[90\text{--}150]$	>50
$m(V)$	$\in[75\text{--}105]$	$\in[75\text{--}105]$	$\in[75\text{--}105]$	$\notin[75\text{--}105]$

Table A.4: Selection criteria for the SR and CRs in the boosted topology for 0-, 1-, and 2-lepton channels. The DeepAK8bbVsLight designation represents the DEEPAK8 discriminant for the light-quark flavor discrimination node. The m_{SD} and $M(V)$ variables have units of GeV.

A.5 Multivariate discriminants

The signal region selection enriches in signal the phase space. The multivariate analysis techniques allow to further improve the signal versus background discrimination power. Three multivariate methods are used in this analysis: a deep neural networks (DNN) binary classifier for the resolved signal region, a multi-class DNN in the V+HF control
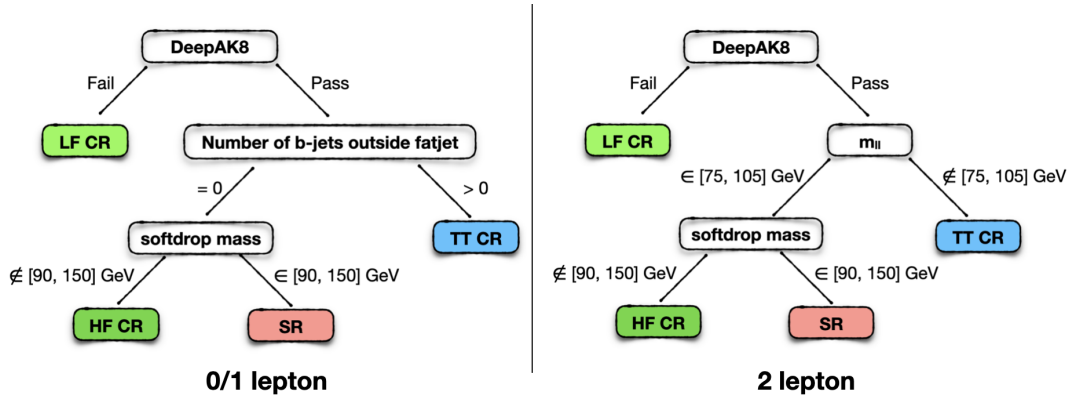
Figure A.5: Left: Boosted 0-lepton and 1-lepton channels selection scheme. Right: Boosted 2-lepton channel selection scheme.

regions to improve the separation of different backgrounds, and a boosted decision tree (BDT) technique for the binary classification in the boosted signal region.

A.5.1   DNN

For the resolved Higgs decay topology, a signal vs. background DNN classifier is trained for each channel separately. The output in the signal region is used in the fit for all the channels. For the 0-lepton and 1-leptons channel V +HF control region, a multi-class DNN classifier is used.

The tensorflow framework [131] was used to train a 6 hidden layer DNN classifier, with each layer having 512, 256, 128, 64, 64 and 64 nodes. For 2-classes DNN all signal processes were grouped into signal class, and all of the background processes into a background class. In the multi-class DNN instead of signal and background output nodes, the classification is performed according to the 5 leading background processes listed in Tab. A.5. A background class is assigned to each event, if the corresponding class probability is the largest.

0	V+udsg
1	V+c
2	V+b
3	Single top
4	$t\bar{t}$

Table A.5: Classes used for the 0/1-lepton multi-DNN classifier.

184

In both 2-class DNN and multi-class DNN the same architecture and the same set of input features are used. The agreement of data and simulation for all of the MVA input variables is studied and found to be sufficient.

Fig. A.6 shows the HFDNN discriminant in the 0- and 1-lepton heavy-flavor CRs, after a maximum likelihood fit to the data. This is a simultaneous fit of all SRs and CRs in the analysis. The DNN score is used as a discriminating variable in each resolved SR, while different strategies are used in the resolved CRs.
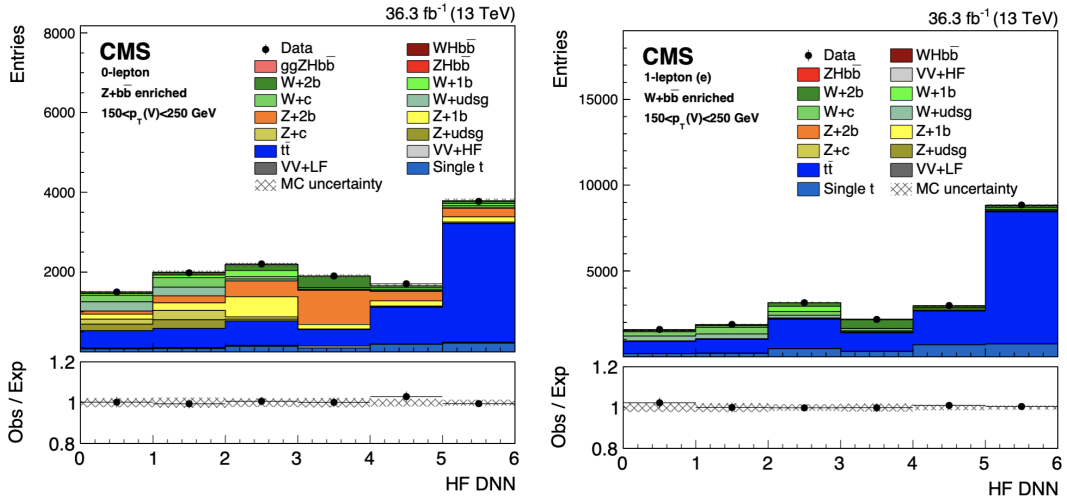
Figure A.6: Distribution of the HFDNN scores in the 0-lepton (left) and 1-lepton, (right) $Z + b$ and $W + b$ heavy-flavor CRs for the 2016 dataset, after the fit to data. The output nodes target enrichment in the V+light-quark (first bin), V+c (second bin), V+b (third bin), $V + b\bar{b}$ (fourth bin), single top quark (fifth bin), and $t\bar{t}$ (sixth bin) backgrounds. The lower plots display the ratio of the data to the MC expectations. The vertical bars on the points represent the statistical uncertainty in the ratio, and the hatched area shows the MC uncertainty.

A.6 Results

The inclusive signal strength extracted from a simultaneous maximum likelihood fit of the SRs and CRs, combining all three data-taking years, is $\mu = 1.15^{+0.22}_{-0.20}$, where the uncertainties include both the statistical and systematic components. The individual signal strengths are $\mu = 1.43 \pm 0.37$, $\mu = 0.68 \pm 0.36$, and $\mu = 1.23 \pm 0.30$ for the 2016, 2017, and 2018 data-taking years, respectively. Figure A.7 shows the signal strengths per analysis channel, as well as the signal strengths split by production mode (ZH or WH).

The p-value compatibility of the individual deviations of the three analysis channels from the SM expectation ($\mu = 1$) is 64%, while the p-value compatibility of the three analysis channels with the inclusive VH, $H \to b\bar{b}$ signal strength is 84%.

The measured signal strengths in the different STXS bins, fitting all data-taking years (2016–2018) are shown in Fig. A.8. These results are interpreted in Fig. A.9 as $\sigma\mathcal{B}$, the product of the production cross sections and the branching fractions for V$\to$ leptons and $H \to b\bar{b}$. To convert the results to measurements of the production cross section alone, theoretical uncertainties that modify the overall cross section of the individual STXS bins, or the inclusive cross section, are removed from the fit. These measured cross sections, along with the SM predictions, are given in Table A.6. The local inclusive observed (expected) significance of the measured ZH and WH signals, over the background-only expectation, is found to be 6.3 (5.6) standard deviations when taking into account all three data-taking years. Examples of post-fit distributions of the DNN output scores in the SRs of the 2018 data set are shown in Fig. A.10 for the 0-, 1-, and 2-lepton channels in the category targeting the $250 < p_{\mathrm{T}}(V) < 400$GeV STXS bin. Figure A.11 shows the distribution of events in all channels, sorted according to the observed value of $\log_{10}$ (S/B), for the three data-taking years combined; here, the signal (S) and background (B) yields are determined from the discriminant scores used in the resolved and boosted analyses.

STXS bin	Expected $\sigma\mathcal{B}$ [fb]	Observed $\sigma\mathcal{B}$ [fb]	Best-fit μ
ZH $75 < p_{\mathrm{T}}(Z) < 150$ GeV	50.0 ± 5.3	71 ± 38	1.4 ± 0.8
ZH $150 < p_{\mathrm{T}}(Z) < 250$ GeV 0 jets	9.0 ± 1.4	3.8 ± 4.1	0.4 ± 0.5
ZH $150 < p_{\mathrm{T}}(Z) < 250$ GeV $\geq$1 jets	10.1 ± 2.2	<0	-0.6 ± 1.0
ZH $250 < p_{\mathrm{T}}(Z) < 400$ GeV	4.5 ± 0.9	6.9 ± 2.2	1.5 ± 0.5
ZH $p_{\mathrm{T}}(Z) > 400$ GeV	0.9 ± 0.1	1.6 ± 0.6	1.8 ± 0.8
WH $150 < p_{\mathrm{T}}(W) < 250$ GeV	24.9 ± 1.8	6 ± 16	0.2 ± 0.7
WH $250 < p_{\mathrm{T}}(W) < 400$ GeV	6.3 ± 0.5	11.9 ± 3.8	1.9 ± 0.6
WH $p_{\mathrm{T}}(W) > 400$ GeV	1.4 ± 0.1	2.7 ± 1.1	1.9 ± 0.8

Table A.6: Predicted and measured values of the product of the cross section and branching fractions in the V(leptonic)H STXS process scheme. The SM predictions for each bin are calculated using the inclusive values reported in Ref. [132]. The uncertainties shown are the combined statistical and systematic components.

Tab. A.7 shows the contribution, in terms of absolute uncertainties, to the uncertainty in the measured inclusive signal strength originating from the various sources of systematic uncertainty. This contribution for a given group of uncertainties is defined as the difference
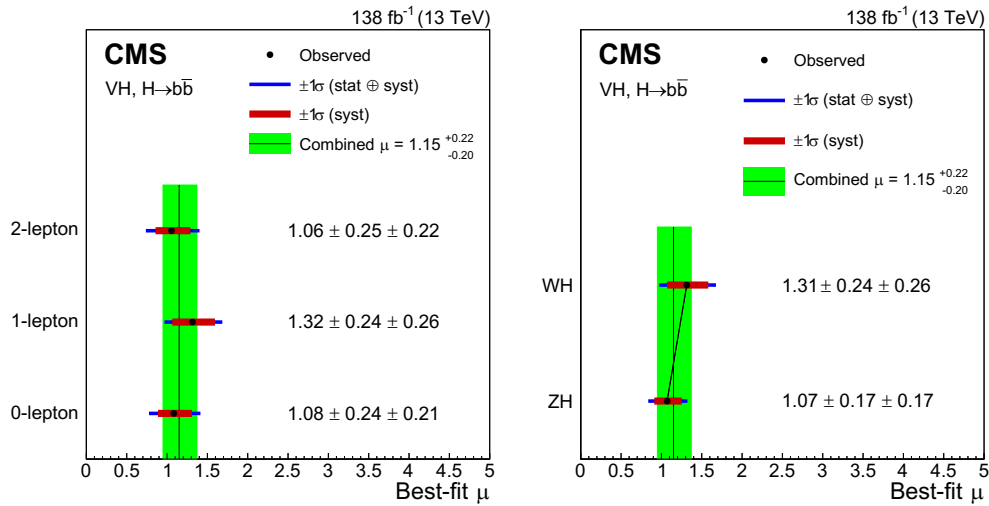
Figure A.7: Signal strengths (points) for the 0-, 1-, and 2-lepton channels (left) and the ZH and WH production modes (right). The horizontal red and blue bars on the points represent the systematic and total uncertainties, respectively. The combined inclusive signal strength is shown by the vertical line, with the green band giving the 68% confidence interval. The results combine the 2016–2018 data-taking years. The first and the second uncertainty values correspond to the statistical and systematic uncertainties, respectively.
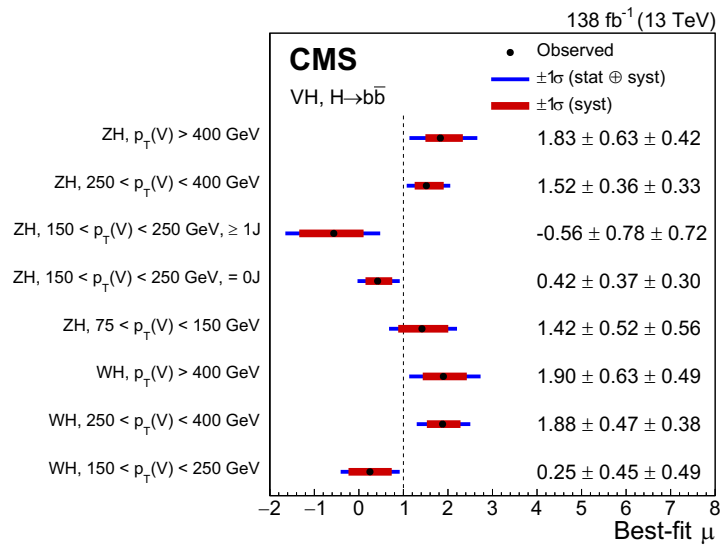
Figure A.8: STXS signal strengths from the analysis of the 2016–2018 data. The vertical dashed line corresponds to the SM value of the signal strength. The first and the second uncertainty values correspond to the statistical and systematic uncertainties, respectively.

in quadrature between the total uncertainty in the signal strength and the uncertainty in the signal strength with the nuisance parameters of the corresponding group fixed to their best-fit values. The total statistical uncertainty is defined as the uncertainty in the signal strength when all the constrained nuisance parameters are fixed to their best-fit values, while the total systematic uncertainty is defined as the difference in quadrature between the total uncertainty in the signal strength and the total statistical uncertainty.

Figure A.9: Measured values of $\sigma\mathcal{B}$, defined as the product of the VH production cross sections multiplied by the branching fractions of V→ leptons and $H \rightarrow b\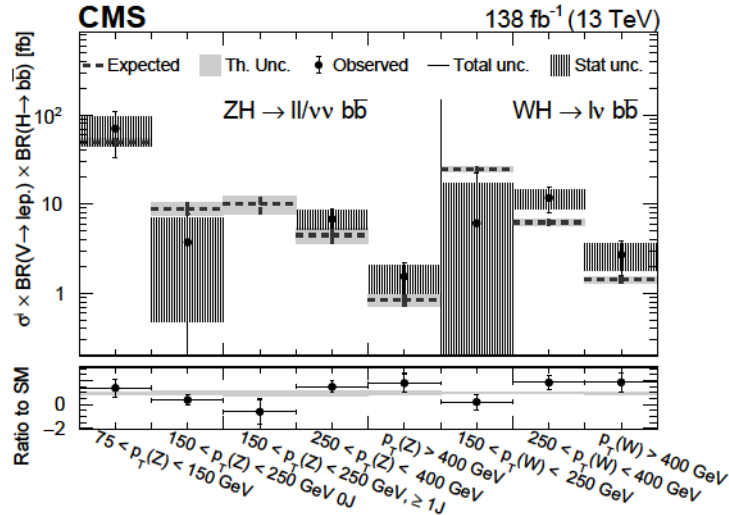bar{b}$, evaluated in the same STXS bins as for the signal strengths, combining all years. In the lower panel, the ratio of the observed results, with associated uncertainties, to the SM expectations is shown. If the observed signal strength for a given STXS bin is negative, no value is plotted for $\sigma\mathcal{B}$ in the upper panel.

Tab. A.7 breaks the total uncertainty down into the following sources.

- Theoretical uncertainties in the signal and background components.

- Limited size of simulated samples.

- Simulation modeling, including uncertainty sources associated with the modeling of the V+jets background components. Additionally, the $p_T(V)$ migration uncertainties are included in this category.

- Experimental uncertainties (b tagging, integrated luminosity, JES and JER, lepton identification, and trigger). The JES and JER components include the dedicated uncertainty in mass scale and smearing that is applied for jets subject to the b jet energy regression.

The limited size of the NLO V+jets samples is the largest contribution to the overall VH, $H \rightarrow b\bar{b}$ signal strength uncertainty.
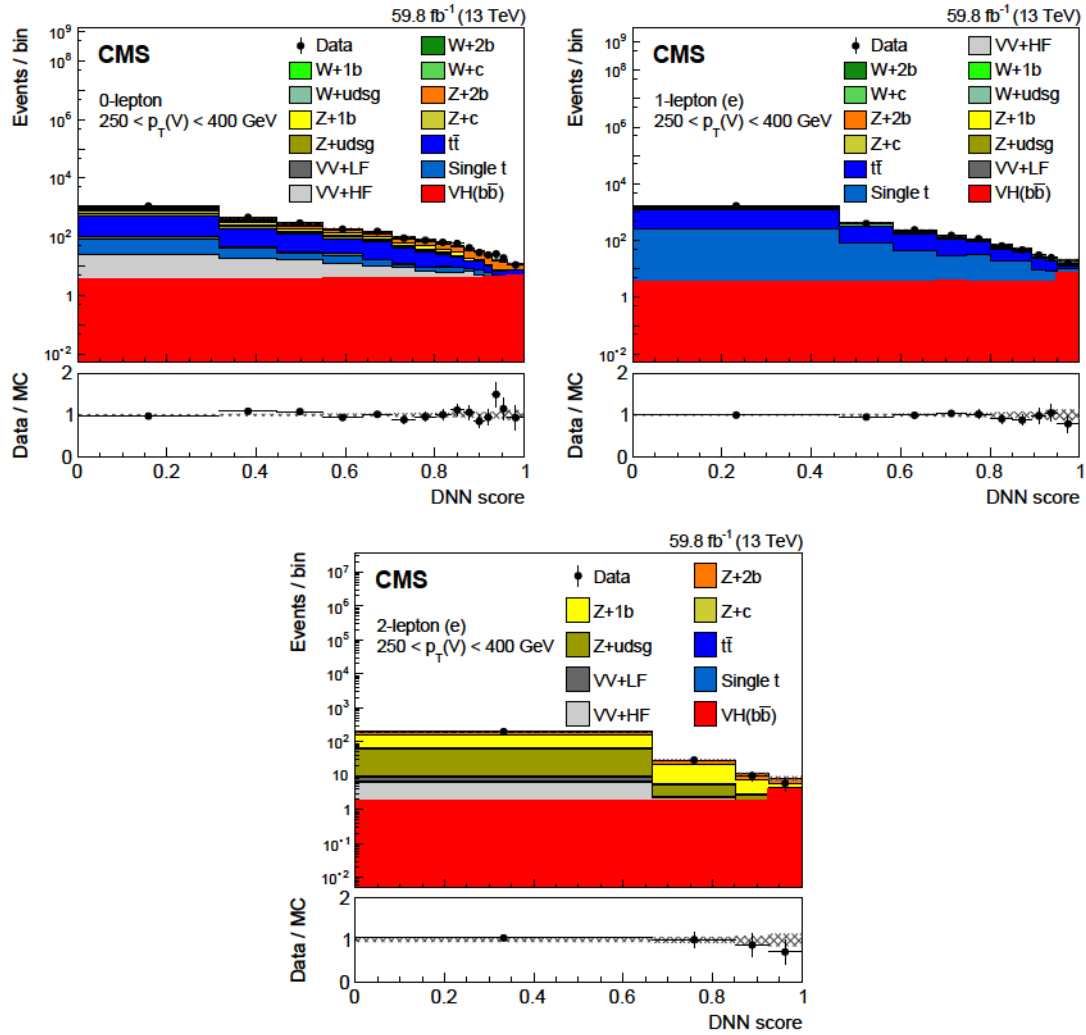
188

Figure A.10: Post-fit distributions of the DNN discriminant in the $250 < p_\mathrm{T}(\mathrm{V}) < 400\,\mathrm{GeV}$ category of the 0-lepton (top left), 1-lepton (top right) and 2-lepton (bottom) channels for the electron final state using the 2018 data set. The background contributions after the maximum likelihood fit are shown as filled histograms. The Higgs boson signal is also shown as a filled histogram, and is normalized to the signal strength shown in Fig. A.8. The hatched band indicates the combined statistical and systematic uncertainty in the sum of the signal and background templates. The ratio of the data to the sum of the fitted signal and background is shown in the lower panel. The distributions that enter the maximum likelihood fit use the same binning as shown here.

A.7 Summary

Measurements are presented of the cross section for the associated production of the 125 GeV Higgs boson and a W or Z boson, where the Higgs boson decays to $b\bar{b}$ and the vector bosons decay to leptons. Proton-proton collision data collected by the CMS experiment during 2016–2018 at $\sqrt{s} = 13\,\mathrm{TeV}$ are used, corresponding to an integrated luminosity of $138\,\mathrm{fb}^{-1}$. Five decay channels are analyzed, and both resolved as well as merged-jet
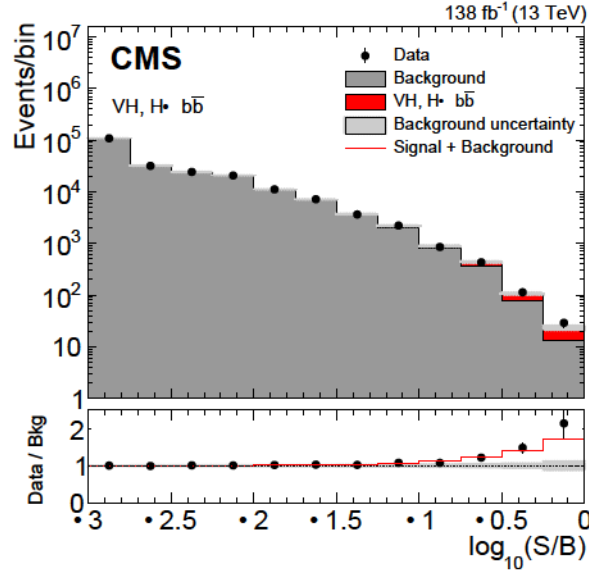
189

Figure A.11: Distributions of signal, background, and observed data event yields sorted into bins of similar signal-to-background ratio, as given by the result of the fit to the multivariate discriminants in the resolved and boosted categories. All events in the signal regions of the 2016–2018 data set are included. The red histogram indicates the Higgs boson signal assuming SM yields ($\mu = 1$) and the sum of all backgrounds is given by the gray histogram. The lower panel shows the ratio of the observed data to the background expectation, with the total uncertainty in the background prediction indicated by the gray hatching. The red line indicates the sum of signal assuming the SM prediction plus background contribution, divided by the background.

	$\Delta\mu$	
Background (theory)	$+0.043$	-0.043
Signal (theory)	$+0.088$	-0.059
MC sample size	$+0.078$	-0.078
Simulation modeling	$+0.059$	-0.059
b tagging	$+0.050$	-0.046
Jet energy resolution	$+0.036$	-0.028
Int. luminosity	$+0.032$	-0.027
Jet energy scale	$+0.025$	-0.025
Lepton ident.	$+0.008$	-0.007
Trigger ($\vec{p}_T^{miss}$)	$+0.002$	-0.001

Table A.7: The sources of systematic uncertainty in the inclusive signal strength measurement and their positive and negative values.

topology are employed in each vector boson decay mode. An additional subcategorization in the transverse momentum of the vector boson and the number of additional jets in the event is applied to maximize the sensitivity of different simplified template cross section bins. The overall signal strength, combining all analysis categories, is found to be $\mu = 1.15^{+0.22}_{-0.20}$. The production of the Higgs boson in association with a vector boson and

decays to bottom quark pairs is established with an observed (expected) significance of 6.3 (5.6) standard deviations.

Curriculum vitae

Education

2019-Current	**PhD** in EXPERIMENTAL HIGH ENERGY PHYSICS, University of Zagreb, Croatia
2015-2017	**Master of Science** in PHYSICS, Major: Nuclear and Particle Physics, The Maharaja Sayajirao University of Baroda, India
2012-2015	**Bachelor of Science** in PHYSICS, The Maharaja Sayajirao University of Baroda, India

Employment History

2019-Current	**Research Assistant** Ruđer Bošković Institute, Zagreb, Croatia
2017-2019	**Scientific Project Assistant** Institute of Physics, Bhubaneswar, India

Research Experience

2019-
Current

PhD Thesis

Search for multiple Higgs boson production in hadronic final states at the Large Hadron Collider

Supervisor: Dr. Dinko Ferenček

Ruđer Bošković Institute, Zagreb, Croatia

OCT 2017 — Jan 2019	**High level trigger development of CMS Experiment at LHC, CERN**
	Supervisor: Dr. Aruna Kumar Nayak
	Institute of Physics, Bhubaneswar, India
2016-2017	[MSc Thesis] **Exotic Hadrons**
	Supervisor: Prof. J. P. Singh
	The Maharaja Sayajirao University, Vadodara, India
SUMMER 2016	**Investigation of CP Violating observables in charged B decay**
	Supervisor: Dr. Jim Libby
	Indian Institute of Technology Madras (IIT-M), Chennai, India
2013-2015	**Procedural Understanding in Physics: Behaviour of soft springs**
	Supervisor: Dr. Rajesh B. Khaparde
	Homi Bhabha Centre for Science Education (HBCSE), TIFR, Mumbai, India

Publications

▷ CMS Collaboration, **Search for non-resonant Higgs boson pair production in final states with two bottom quarks and two photons in proton-proton collisions at $\sqrt{s} = 13$ TeV**, JHEP 03 (2021) 257, DOI 10.1007/JHEP03(2021)257

▷ CMS Collaboration, **Measurement of simplified template cross sections of the Higgs boson produced in association with W or Z bosons in the $H \to b\bar{b}$ decay channel in proton-proton collisions at $\sqrt{s} = 13$ TeV**, Phys. Rev. D 109 (2024) 092011, DOI 10.1103/PhysRevD.109.092011

Workshops and Schools Attended

July 2023	**HHH Workshop** Dubrovnik, Croatia.
Aug. 2021	**Baltic School of High-Energy Physics and Accelerator Technologies (HEP&AT)** Riga Technical University (RTU), Klapkalnciems, Latvia.
Mar. 2021	**Tracker Upgrade DAQ School** online + hardware exercises at Institut Ruđer Bošković, Zagreb, Croatia.
July 2020	**Summer School on Machine Learning in High Energy Physics (MLHEP - 2020)** online by EPFL, Lausanne, Switzerland.
Sep. 2019	**CMS Physics Object School (CMSPOS)** at RWTH, Aachen, Germany.
Nov. 2017	**XI SERC School on Experimental High Energy Physics** at NISER, Khurda, India.
Dec. 2016	**Winter School on Astro-particle Physics (WAPP − 2016)** at Cosmic Ray Laboratory, Ooty, India.
Dec. 2015	**Winter School on Astro-particle Physics (WAPP − 2015)** at Bose Institute, Darjeeling, India.
Nov. 2013	**Refresher Experimental Physics Course** at Indian Academy of Sciences, Bangalore, India.
June 2013	**NIUS Physics(10)** at Homi Bhabha Centre for Science Education, TIFR, Mumbai, India.

Academic Achievements

◇ INnovation in Science Pursuit for Inspired REsearch (INSPIRE) Scholarship Department of Science and Technology, Govt. of India, 2012-2017.

◇ Qualified CSIR-UGC NET Lecturership (Rank - 65), June-2017, Government of India.

◇ Qualified All India Engineering Entrance Examination (AIEEE),

◇ National Means Cum-Merit Scholarship (NMMS), Government of India, 2008-2010.

Skills

Technical Skills

Python, LaTeX, C++, Pandas(Software), Numpy, Awkward Array, Git, Matplotlib, Machine Learning, Data Science, Data Analysis, Statistical Data Analysis

Soft Skills

Independent and critical thinking, Fast learning , Logical Problem-solving, Time Management, Communication, Flexible